Theory And Application Of Auger And Photoelectron Diffraction And Holography

By

Xiang Chen

A Thesis Submitted in
Partial Fulfillment of the
Requirements for the degree of

Doctor of Philosophy
in
Physics

at
The University of Wisconsin-Milwaukee
May 1994

Theory And Application Of Auger And Photoelectron Diffraction And Holography

By

Xiang Chen

A Thesis Submitted in
Partial Fulfillment of the
Requirements for the degree of

Doctor of Philosophy
in
Physics

at
The University of Wisconsin-Milwaukee
May 1994

Dilano K. Saldin Date

Graduate School Approval Date

Theory And Application Of Auger And Photoelectron Diffraction And Holography

By

Xiang Chen

The University of Wisconsin-Milwaukee, 2002
Under the Supervision of Professor Dilano K. Saldin

ABSTRACT

This dissertation addresses the theories and applications of three important surface analysis techniques: Auger electron diffraction (AED), x-ray photoelectron diffraction (XPD), and Auger and photoelectron holography.

A full multiple-scattering scheme for the calculations of XPD, AED, and Kikuchi electron diffraction pattern from a surface cluster is described. It is used to simulate 64 eV $M_{2,3}VV$ and 914 eV L_3VV AED patterns from Cu(001) surfaces, in order to test assertions in the literature that they are explicable by a classical "blocking" and channeling model. We find that this contention is not valid, and that only a quantum mechanical multiple-scattering calculation is able to simulate these patterns well.

The same multiple-scattering simulation scheme is also used to investigate the anomalous phenomena of peak shifts off the forward-scattering directions in photoelectron diffraction patterns of Mg KLL (1180 eV) and O 1s (955 eV) from MgO(001) surfaces. These shifts are explained by calculations assuming a short electron mean free path. Similar simulations of XPD from a CoSi$_2$(111) surface for Co-3p and Si-2p normal emission agree well with experimental diffraction patterns.

A filtering process aimed at eliminating the self-interference effect in photoelectron holography is developed. A better reconstructed image from Si-2p XPD from a Si(001) [2×1] surface is seen at atomic resolution. A reconstruction algorithm which corrects for the anisotropic emitter waves as well as the anisotropic atomic scattering factors is used for holographic reconstruction from a Co-3p XPD pattern from a CoSi$_2$ surface. This new algorithm considerably improves the reconstructed image.

Finally, a new reconstruction algorithm called "atomic position recovery by iterative optimization of reconstructed intensities" (APRIORI), which takes account of the self-interference terms omitted by the other holographic algorithms, is developed. Tests on a Ni-C-O chain and Si(111)($\sqrt{3} \times \sqrt{3}$)B surface suggest that this new method may overcome the twin image problem in the traditional holographic methods, reduce the artifacts in real space, and even separately identify the chemical species of the scatterers.

Dilano K. Saldin   Date

Acknowledgment

I very much enjoyed my time as a graduate student at the University of Wisconsin-Milwaukee. Before starting the next phase of my life, I would like to take this opportunity to thank the following persons who helped me in making this dissertation possible.

I would like to express my sincere gratitude to my advisor, Dilano Saldin, who has profound knowledge and instinct in physics, and created a comfortable and free ambience for me to explore the principles of science as well as to meet the challenges in the New World, and with whom I have learned theories and applications of surface physics and electron holography. I am very glad to have been his student.

Special thanks are extended to Jun Nogami, with whom I have friendly personal and professional relationships, who gave me the encouragement to discover the new continent; Brian Tonner, whose group I collaborated with closely, for many helpful discussions; Dilano Saldin, Jun Nogami and Marija Gajdardziska-Josifovska, who carefully read the draft thesis and made many valuable constructive suggestions; Richard Sorbello and Wilfred Tysoe, who are the committee members of my thesis defense; Donald Beck, whom I liked to talk with in the hallway on Saturdays and Sundays; Niranjani Patel and Nitin Kothari, for friendly collaborations.

I would also like to thank G. R. Harp, J. Zhang, Z. L. Han, and S. Varma, who generously provided me with their experimental results; J. C. Campuzano and Y. Zhou at the University of Illinois at Chicago for friendly cooperations in experiments; Yin Chen and Wei Guo who introduced me to apply for the Ph.D.

program in the Department of Physics at UWM; Margaret Malay, Gerry Graef, Jon Glueckstein, and many other friends who made my stay in Milwaukee more enjoyable.

This dissertation is in memory of my father Ze-bin Chen, a physicist, who was shot dead during the Cultural Revolution in China. I am very grateful to my dear mother, Sue-wen Chen, who brought up her two sons alone, and gave me her love, nurture and encouragement during those very difficult years; and my brother, Ning Chen, who always showed his support and understanding to me. I would also like to thank my father-in-law, Pei-lin Zhang, for his encouragement and support.

Finally, I owe the deepest thanks to my wife, Hong Zhang, for her help and suggestions on figures in my thesis, and for her friendship, love, care and understanding.

Dedication

To my friend and wife Hong.

Contents

List of Tables

List of Figures

Chapter 1

Introduction

The investigation of a solid surface has been an important field of research in science for the last two decades, and will become even more crucial in the next century as the development of modern devices urge more detailed investigations of the properties of solid surfaces when the devices become smaller and smaller. The study of the growth of ultrathin epitaxial films on single-crystal substrates under controlled conditions, the function of a catalyst in a chemical reaction process and the interaction of adatoms with the substrate offer a great challenge to surface science. Surface structure probes such as Low-Energy Electron Diffraction(LEED), Auger Electron Diffraction(AED), X-ray Photoelectron Diffraction(XPD) and Scanning Tunneling Microscopy(STM) are powerful tools to explore solid surfaces. For a surface chemical composition analysis, Auger Electron Spectroscopy(AES), X-ray Photoelectron Spectroscopy(XPS) and Secondary Ion Mass Spectroscopy(SIMS) are sensitive analytical methods.

Surface sensitivity of electron spectroscopy techniques is based on two experimental facts: (1) electrons with kinetic energies in the range of 15 to 1000 eV have a very short inelastic scattering length ($< 10\mathring{A}$) in solid, and (2) the binding energy of a core-level electron is a sensitive function of atomic identity. Therefore, measurements of the kinetic energy of electrons emitted from a solid after the excitation can provide surface specific elemental information. Surface sensitivity of electrons can be illustrated best with a plot of inelastic scattering length of an emitted electron versus its kinetic energy, which is called the “universal” curve [49], as shown in Fig. 1.1 on page 3. A simple explanation of the “universal” curve is for electrons in the energy range 15 to 1000 eV, the dominant electron energy loss mechanism in solids is the excitation of valence band electrons. A general empirical relation for such an inelastic scattering length of an electron in terms of its kinetic energy in a solid can be expressed as:

$$\lambda = AE^{-2} + BE^{1/2} \tag{1.1}$$

where A = 538, B = 0.210, E is in eV, and λ is given in terms of monolayers [4].

X-ray photoelectron diffraction and Auger electron diffraction have been powerful tools for exploring the surface structure information of single crystals and thin films in the past few decades. The atom specificity make XPD and AED invaluable resources in studies of multielement substances which will be amongst the future generation of the new materials.

An x-ray photoemission process occurs when a core-level electron is excited by a x-ray photon, to create a core-hole state and a free photoelectron. A schematic diagram of a photoemission process is shown in Fig. 1.2(a) on page 5. An XPS spectrum can be obtained by illuminating a sample with a monochromatic x-ray flux, and then detecting the photoelectron ejected from the sample as a function of the binding energy, E_c, of a core electron (or kinetic energy, E_{ph}, of the photoelectron). The photoemission process is considered to be *elastic*, and thus the monochromatic x-ray will give rise to a series of photoelectron peaks in XPS which reflect the discrete binding energies of the electrons present in a solid. But some of the photoelectrons may suffer an energy loss which contribute to a higher background in a photoemission peak at high binding energy side. If the photon energy is $h\nu$, and W is the work function of the sample, the kinetic energy of the emitted electron corresponding to this photoemission process is

$$E_{ph} = h\nu - E_c - W.$$

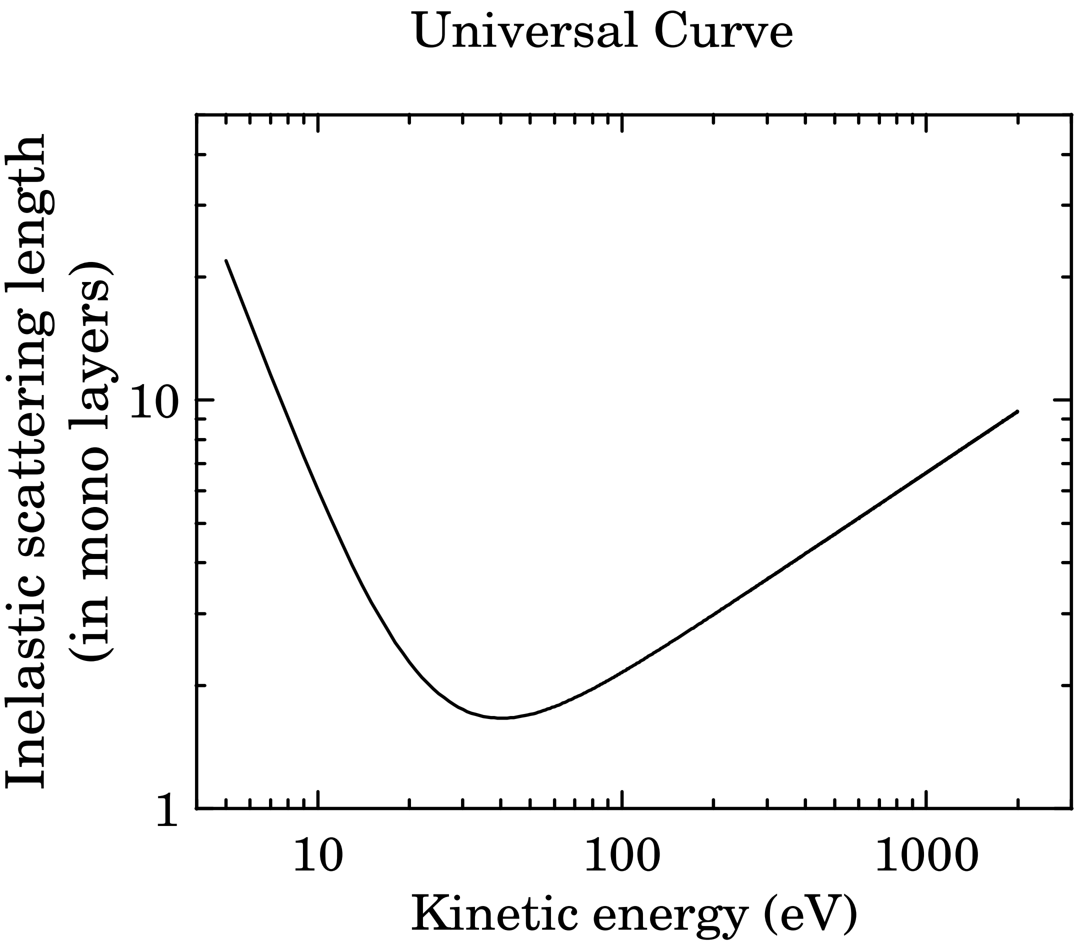

Figure 1.1: Universal curve of electron's inelastic scattering length. A general relation for such an inelastic scattering length of an electron in terms of its kinetic energy in a solid is: $\lambda = AE^{-2} + BE^{1/2}$ where A=538 and B=0.210. A short inelastic scattering length is seen on the graph for the energy range of 15 to 1000 eV which makes electron spectroscopy a surface sensitive tool in this energy range.

It is obvious that in order to observe a particular photoemission line in the spectrum, the photon energy is required to satisfy $h\nu > E_c + W$. A typical photoemission transition rate is approximately 10^{-15} s, which is about the same amount of time for an electron to escape out of the sample. A photoelectron spectrum gives an accurate picture of electronic structure of the solid under investigation.

An Auger process can be realized by exciting a core-hole state in an atom through either an x-ray photoemission or an electron induced process. This ionic state is not stable, and the relaxation of the core-hole state can eject an Auger electron. A schematic diagram of an Auger electron spectroscopy (AES) process is shown in Fig. 1.2(b) on page 5. Specifically, a second electron with less binding energy falls into the excited core-hole state, and transfers its energy, E_2, and angular momentum to a third electron of binding energy E_3, and then this third electron is emitted with a final kinetic energy of

$$E_{aug} = E_c - E_2 - E_3 - W,$$

if we assume that there is no relaxation or hole-hole interaction. This process may also create other core-hole states left by the second and the third electron, and therefore other Auger processes would proceed until the atom is totally relaxed. It can be seen that single Auger emission is a three-step process, i.e., (1) the creation of a core-hole, (2) the excitation of a secondary electron via a radiationless process, and (3) the ejection of an Auger electron. Unlike photoemission excitation, the Auger emission can be caused by either an x-ray photon or an electron beam, and the energy of the emitted electron does not depend on that of the primary beam (x-ray or electron). Since an Auger transition involves atomic inner-shell processes and the transition life-time is much longer than that of a photoemission process, the Auger electron usually has no memory of the process that created the initial

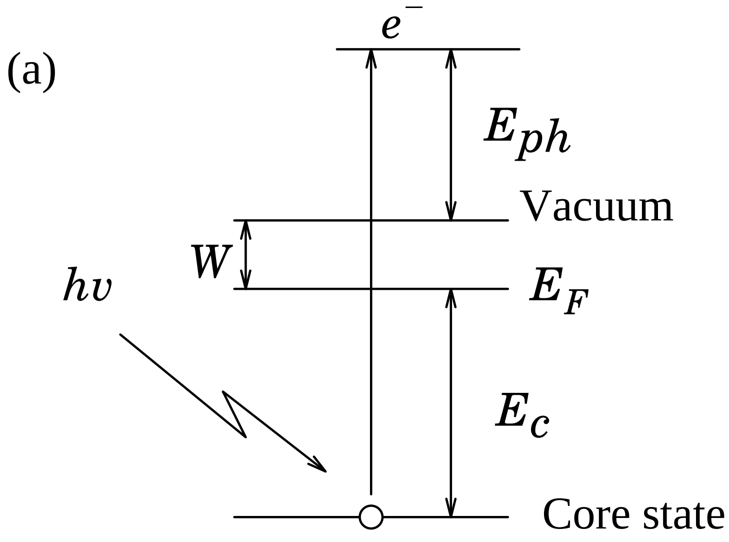

Photoemission process

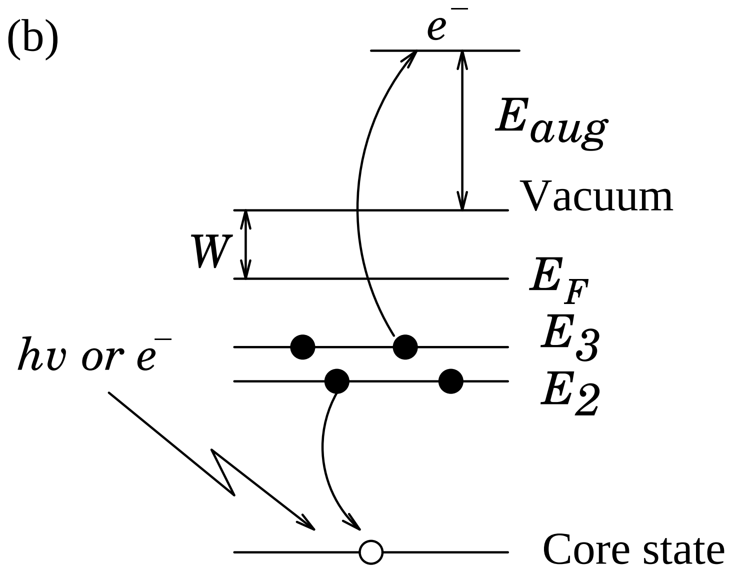

Auger emission process

Figure 1.2: Schematic diagrams of photoemission and Auger emission processes. (a) x-ray excited photoemission process, and (b) x-ray excited or electron beam induced Auger emission process.

core-hole state. Therefore, Auger electron is considered to be emitted isotropically.

As an example, let's look at experimental XPS spectra from a Ta surface, shown in Fig. 1.3 on page 8, which were measured by the author in an assignment in the "surface physics lab" course at the University of Wisconsin-Milwaukee. The experiments were carried out in a VG ESCALAB MARK II system with a base pressure of 9x10^{-10} Torr. Al K_α (1486.6 eV) or Mg K_α (1253.6 eV) radiation was used to excite the Ta sample, and the emitted electrons were collected as a function of binding energy from 1100 eV to 0 eV to obtain the XPS spectra. On Fig. 1.3, we can observe not only transition peaks from Ta, but also from the surface contaminants, O and C. These surface impurities can be removed by an Argon-ion sputtering process. The photoemission peaks observed from Ta are mostly doublets due to non-s core-level transitions. O and C photoemission singlets can also be identified clearly in the spectra. An O Auger KVV transition appears in both spectra. The non-s core-level photoelectrons are doublets and due to the spin-orbit j-j coupling which reflects the "parallel" or "anti-parallel" nature of the spin and orbital angular momentum vectors of the remaining electrons. The relative peak intensities for the doublets are given by the ratio of their respective degeneracies, 2j+1. Atom specificity is clearly shown up in these two XPS spectra, and the core-level photoemission peaks are labeled by Ta-4s, Ta-4$p_{\frac{1}{2}}$, Ta-4$p_{\frac{3}{2}}$, Ta-4$d_{\frac{3}{2}}$, Ta-4$d_{\frac{5}{2}}$, Ta-4f, O-1s, and C-1s. Note that these photoemission peaks appear at the same binding energy positions for both radiations. O-KVV Auger transition peaks are observed at 983 eV and 750 eV for the Al K_α and Mg K_α radiations, respectively, while the kinetic energy of the Auger electrons for both radiations are the same, i.e., 504 eV. This shows that the Auger transition is independent of excitation source. Note that the ghost lines in the Fig. 1.3 curve (a), marked by the arrows, are caused by the Mg K_α source on the Al anode. These peaks correspond to the transitions whose energies are shifted by exactly 233 eV to the lower binding energy end of the same curve.

Better experiment can also distinguish the peaks originating from same atomic ionic states but in different bonding environments. The significance of this is that we can separate the components contributed by the surface atoms from that of the bulk, and thus allowing the technique to become surface sensitive.

The x-ray photoelectron diffraction (XPD) and Auger electron diffraction (AED) from a single crystal surface may provide information about the surface atomic structure. A specific XPS or AES peak can be separated from the spectrum to extract maximum information about the local geometry around an emitter. The emitted photoelectrons will undergo *elastic* and *inelastic* scattering by the surrounding atoms. Fortunately, we can separate the *elastically* scattered photoelectrons from the *inelastically* scattered ones. The area under a specific peak in the spectrum (subtracting a background) represents the diffraction intensity of photoelectrons that are *elastically* scattered in a solid.

Angle-resolved XPD and AED are techniques that measure the angular distribution of the emitted electrons associated with certain peaks in XPS and AES spectra. Two modes are usually used in measuring photoelectron diffraction: (1) measuring the diffraction intensity as a function of the polar and azimuthal angles above the sample, tuning to a specific transition peak with a constant wavelength of the incident x-ray radiation. (2) measuring the diffraction intensity of the same transition peak as a function of electron kinetic energy by varying the incident x-ray wavelength. At high electron kinetic energy, above about 500 eV, angle-resolved photoelectron diffraction patterns show the forward-scattering peaks which can

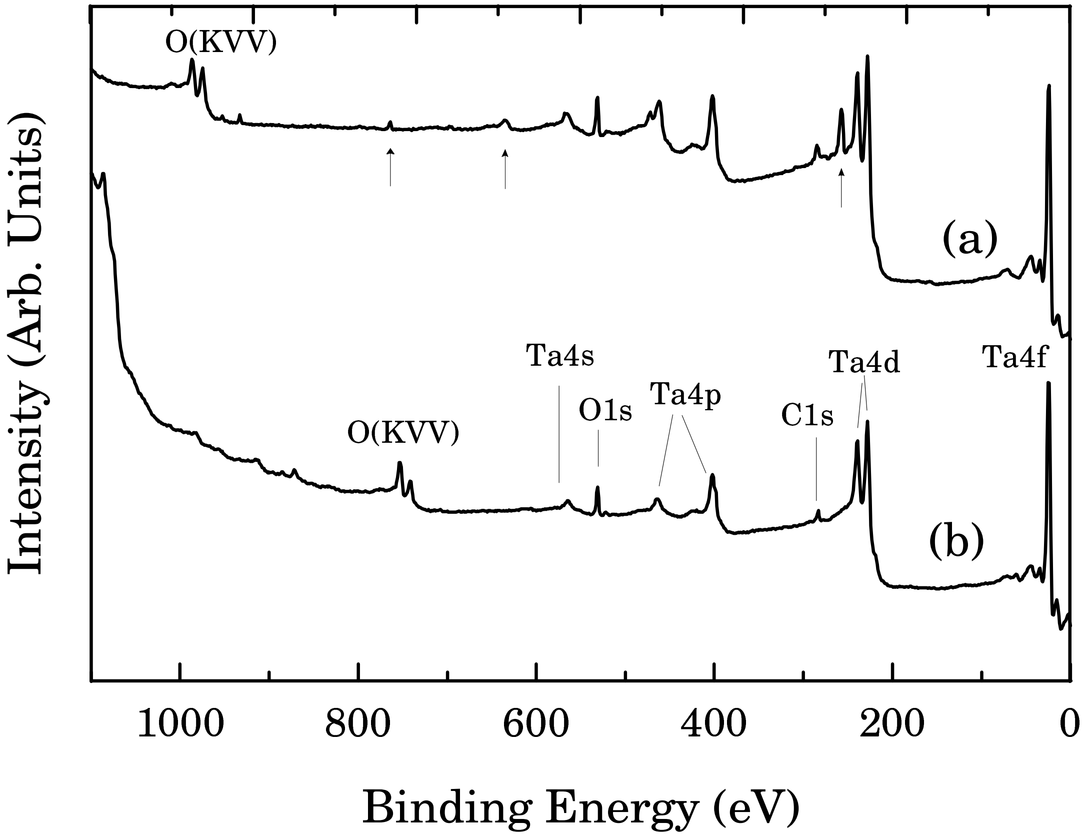

Figure 1.3: Experimental XPS spectra from a Ta surface exited by (a) Al K_α (1486.6 eV), and (b) Mg K_α (1253.6 eV) radiations, and recorded with a pass energy of 50 eV. The photoemission peaks of the same core-levels are at the same binding energy for both radiations, while the same Auger lines should differ by 233 eV on curve (a) and (b) corresponding to the same kinetic energies. The arrows point at the ghost lines in (a) produced by the Mg K_α source on Al anode. These peaks correspond to the transitions whose energies are shifted by exactly 233 eV to the lower binding energy end of the same curve.

be simply interpreted as enhancements of scattering along the projections of the atomic rows. However, those intensity peaks could become local minima at low electron kinetic energy, below about 200 eV, depending on the character of emitter source wave, and this might mislead one in the interpretation of photoelectron or Auger electron diffraction patterns. Also, the forward-scattering analysis gives no information about bond lengths in the surface structure. Therefore calculations are needed to explore the surface structures by using the so-called "trial-and-error" method, in which a model of the structure is first assumed, and then the calculation is carried out to compare with the experiment. The best-fit model is obtained when the calculated pattern and the experimental one are found to have the smallest discrepancy, or error. As the study of photoelectron diffraction has advanced, it has become clear that theoretical calculations beyond single-scattering cluster calculations are required. This become more important when the electron kinetic energy is at the lower end of the "universal" curve, say 40 eV to 300 eV, where full multiple-scattering calculations give much more convincing results.

However, theoretical modeling of photoelectron diffraction with the "trial-and-error" approach results in lengthy computational times, and often it is impossible to explore all surface models for comparison with experiment. This led to the invention of holographic analysis, which allows for a three-dimensional determination of the atom cluster near an emitter at atomic resolution. This straightforward technique also constitutes a direct way of inverting photoelectron diffraction patterns to obtain geometric parameters without prior knowledge of the crystal structure. In recent years, the electron holography has gained much attention and has become a hot topic for the potential of developing into a new powerful tool for the study of a solid surface. The correct interpretation of holographic image formation and reconstruction are crucial to the development of advanced inversion algorithms of holographic analysis at the present time.

Since the use of the optical holography is more popular in science and technology than that of the electron holography, people are more familiar with the former. There are many common features between the two forms of holography, so one may draw an analogy between them. A schematic diagram of formation and reconstruction in optical holography is shown on Fig. 1.4 on page 12. Optical holography is performed mainly by the use of laser light, which provides a light source with extremely long coherent length. Like Gabor's original scheme [3], the optical holography is also a two-step process. A coherent reference wave is incident on a film, and its reflection by the object interferes with the reference wave, and the interference modulation is recorded on the film. A light with the same frequency shining on the developed film will result in a three-dimensional holographic image appearing at the previous object position. If the reference wave is represented by R, and the scattered wave by O, the intensity of the wave-field on this film can be written as:

$$I = |R+O|^2 = |R|^2 + |O|^2 + R^*O + O^*R$$

The holographic image can be reconstructed if a replica of the reference wave, R, shone on the photographic film. Assuming that the wave-field after shining on the film is proportional to the intensity of the interference fringes on the film, the transmitted wave field A is

$$A = IR = |R|^2R + |O|^2R + |R|^2O + O^*R^2$$

If the amplitude of the scattered object wave is assumed to be small compared with that of the reference wave, i.e.,

$$|O| \ll |R|,$$

the square term of the object wave can be omitted, and the $|R|^2O$ term is found to form an image at the object position, O^*R^2 term the object's twin image, and $|R|^2R$ the transmitted wave. The same principle is applied for the electron holography, except that the reference wave might come from the field source (originating from the object) as in the case of photoelectron diffraction.

In the electron holographic interpretation of photoelectron diffraction pattern, electron reference waves are generated in the vicinity of source atoms, and the object waves are produced by the scattering of this radiation by other atoms close to the source atoms. Since the distance between the objects (the nearby atoms and source atom) are small compared to the distance to the detector, the resulting interference pattern could be regarded as a lensless Fraunhofer hologram. Each of the emitting electrons from the source atoms has the same local environment in a single crystal, but devoid of coherence amongst themselves. Thus the interference pattern of each local source can superpose to reinforce the total diffraction pattern. We may extract image information from such a diffraction pattern by means of a the Helmholtz-Kirchoff integral. In many respects, however, an XPD hologram is quite unlike those of conventional optical holography. Electrons are not merely amplitude-reflected from the objects (nearby atoms), but the phases as well as the amplitude of the scattered waves are changed inhomogeneously during the scattering process, and are functions of the electron wave vectors. An electron's nonisotropic scattering factor, and anisotropic emitter wave of a photoemission process are the major factors that determine the formation of faithful XPD holographic reconstructions.

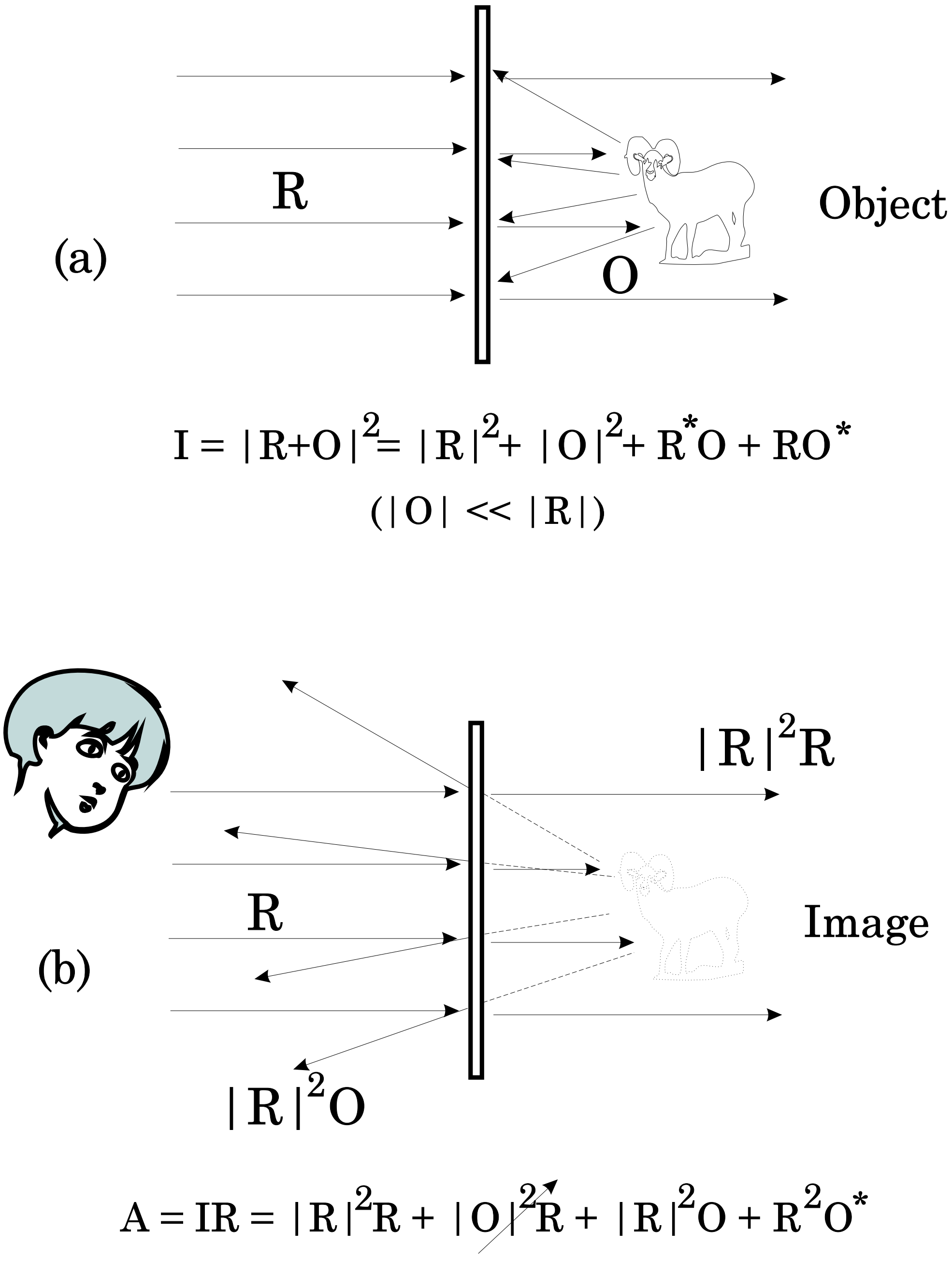

Figure 1.4: Schematic diagram of the optical holographic principle. A coherent laser beam (reference wave) is incident on a film, and the beam reflected by the object interferes with the incident wave forming interference fringes on the film. Light with the same frequency shining on the film will result a three-dimensional holographic image.

In this dissertation, we will focus on the theories and applications of the photoelectron diffraction, Auger electron diffraction, and photoelectron holography. These studies, especially photoelectron holography, are in the frontier of the fast-advancing subject of surface physics today. In chapter 2, the basic theory of electron scattering in a solid is discussed, and a concentric-shell algorithm that performs the full multiple-scattering cluster (MSC) calculations of photoelectron and Auger electron diffraction is proposed. We will apply this MSC calculation to various systems: Auger electron diffraction from a Cu(001) surface in chapter 3, photoelectron diffraction from a MgO(001) surface in chapter 4, experiment-configuration-dependent calculations for core-level photoemission diffraction from a $CoSi_2(111)$ surface in chapter 5. We will discuss hologram formation and reconstruction in photoelectron holography, and an application of holographic analysis to angle-resolved photoelectron diffraction from a Si(001)-[2×1] and a $CoSi_2(111)$ surface in chapter 6. Finally, in chapter 7, we will introduce a robust and new photoelectron holographic algorithm called atomic position recovery by iterative optimization (APRIORI), which makes use of the optimization schemes of linear programming techniques.

Chapter 2

Electron Scattering Theory

2.1 Introduction

Over the past decade angle-resolved x-ray photoelectron diffraction (ARXPD) and Auger electron diffraction (ARAED) have contributed much to the understanding of new surface and thin-film structures. These techniques are complementary in many respects. One of the main features in ARXPD and ARAED is the atom specificity, which plays an important role in the study of the multi-element materials. The atom specificity is the atomic identity of an atom giving rise to identifiable Auger and photoelectron peaks on an x-ray photoelectron spectrum (XPS) or an electron-excited Auger electron spectrum (AES). Furthermore, photoelectron spectra obtained at high energy resolution can be decomposed into peaks originating from atoms in different bonding environments. When combined with angular resolution, such spectral resolution can be used to determine the structural environment of a given kind of atom in a specific chemical state.

Diffuse electron diffraction, such as XPD or AED, occurs when electrons are emitted from atoms near the surface of a crystal through, e.g., a photoemission or Auger emission process, and there is interference between the portion of an outgoing electron wave that passes directly to the detector, and those wave portions that undergo elastic scattering by ion cores in the vicinity of the emitter. There is no coherence between Auger or photoelectron waves emitted from different atoms due to the fact that such emission processes constitute random events that are not correlated in time. What such diffuse electron diffraction probes is the local atomic environment of the excited atom which emits the electron wave. The individual atomic species need not possess an environment with long-range order in order to have intensity modulations. For instance, adsorbates at submonolayer coverages will exhibit diffuse diffraction modulations that are characteristic of the adsorption site, even though there is no long-range order in the adlayer. Also, inclusion of foreign atoms at lattice sites in a given sublattice of a single-crystal specimen will lead to strong Auger and photoelectron intensity modulations, even if the specimen is, in effect, a random alloy. It is precisely the lack of coherence between Auger and photoemission from different atoms that removes the requirement that long-range order be present in order to observe diffraction effects. This is different from the conventional LEED where coherent back-scattering is required in order to observe the coherent diffraction of the elastically scattered electrons. The coherent back-scattering is achieved mainly by the long-range order surface crystal structure of the sample. In a diffuse diffraction pattern, if the kinetic energies of these electrons lie in the high energy range (above 500 eV), forward scattering peaks along the low-index crystallographic direction arise on these diffraction patterns. These peaks provide "fingerprints" of the surface, such as the crystal structure and orientation. However, subtle structural information, regarding tetragonal strain, etc., requires comparison of such diffraction patterns with simulations using a proposed model. On the other hand diffuse electron diffraction patterns with a low electron kinetic energies (below 300 eV) do not have a simple interpretation, and always require comparison with the simulations as part of the data analysis. In general, simulations at low energies require a sophisticated multiple-scattering theory, while at high energies single-scattering can well explain most of the diffraction features, but with some exceptions, such as forward defocusing features on the diffraction patterns.

The advancement of these fields would be greatly aided by the development of efficient methods for the simulation of electron diffraction patterns by computer. Such simulations are useful in the following four aspects: (1) they provide comparisons with the experimental data, allowing the extraction of maximal information from a given measurement, (2) they enable rapid testing of proposed models, sometimes even providing data which, although physically meaningful, are not available in a real world experiment, (3) they can provide simulated data to determine what level of experimental resolution is required before designing the experimental instrumentation, and (4) they will be used as models of "experimental data" to test the various electron holographic algorithms developed for reconstructing three dimensional images at atomic resolution. Usually a proposed new holographic algorithm will be tested first using the simulated data of a simple surface model in order to eliminate some experimental uncertainties and difficulties encountered at present, of a complex structure on the surface. In recent years, the principles of holography have been used to reconstruct three dimensional representations of the relative positions of atoms near a surface from the information on a diffuse electron diffraction pattern. Many electron holography theories have demonstrated the possibility of reconstructing the atom images at atomic resolution. In this chapter, single atom scattering and cluster single scattering theories are discussed first, and then a full multiple scattering theory is introduced in detail.

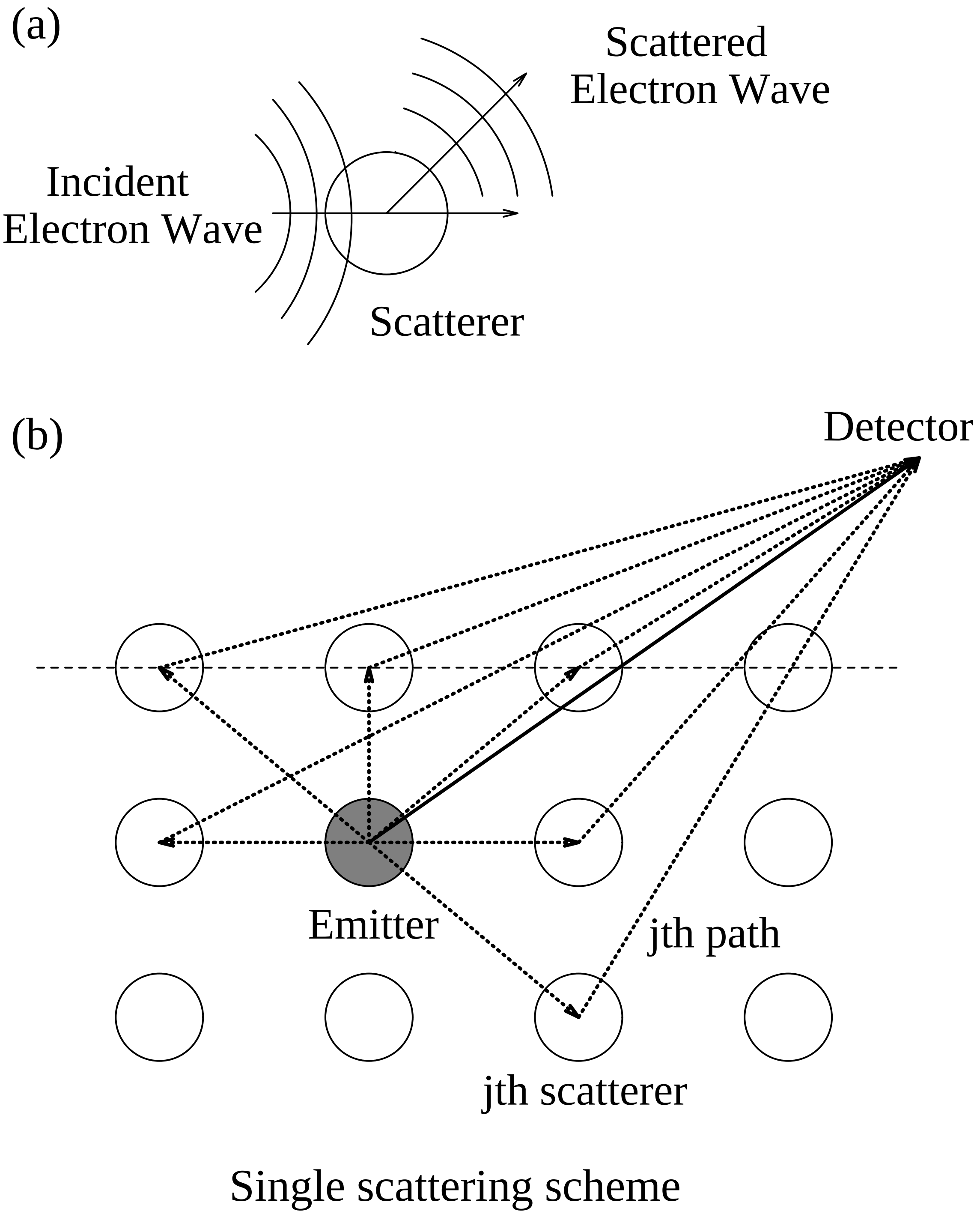

Figure 2.1: (a) Electron wave scattered by an individual atom, and, (b) an electron wave is emitted from an emitter and scattered only once by the surrounding atoms. The overall diffraction intensities are the sum of those scattered waves (dotted lines) and direct emitted wave (solid line).

2.2 Single scattering cluster theory

2.2.1 Electron-atom elastic scattering

Let us first consider a spherical wave

$$j_l(kr)Y_{lm}(\hat{\mathbf{r}})$$

is incident on an atom at the origin, where $j_l(kr)$ is the lth order spherical Bessel function, and Y_{lm} a spherical harmonic function associated with angular momentum quantum numbers l and m. The scattered outgoing wave is generated and takes the form

$$t_l h_l^{(1)}(kr)Y_{lm}(\hat{\mathbf{r}})$$

where $h_l^{(1)}(kr)$ the lth order Hankel function of the first kind, and

$$t_l = e^{\delta_l} sin\delta_l$$

where δ_l is the phase shift due to the scatterer (at the origin) with angular momentum quantum number l, as shown in Fig. 2.1 (a) on page 17.

Let us then consider a simple scattering picture of an electron plane wave ϕ_o which is incident upon a scatterer atom j, when the scattered wave ϕ_j can be written as:

$$\phi_j(\theta_j) = \phi_o f_j(\theta_j)\frac{e^{ikr_j}}{r_j} \tag{2.1}$$

where $f_j(\theta_j)$ is the atomic scattering factor (a complex number), θ_j is the scattering angle if incident electron wave travels along θ_j=0, k the electron wave number, and r_j the emitter-scatterer distance. In the plane-wave or a small-atom approximation, the atomic scattering factor can be calculated using the partial wave method as found in elementary quantum mechanics texts:

$$f_j(\theta_j) = \frac{1}{k}\sum_l (2l+1)e^{i\delta_l^j} sin\delta_l^j P_l(cos\theta_j) \tag{2.2}$$

where $\{\delta_l^j\}$ is a set of phase shifts of the jth scatterer, and $\{P_l(cos\theta_j)\}$ are Legendre polynomial functions. The small-atom approximation is in general accurate for all but nearest neighbors at distances of ≤ 5 $\mathring{A}$ from the emitter.

In the case where the small-atom approximation is not valid, i.e., when the distance between the emitter and the scatterer is not large compared to the size of the scatterer, or the wave number of the electron is small, the shape of an emitted electron wave before scattering by an atom must be taken into account for greater accuracy. Calculations of atomic scattering factors for spherical waves incident over the dimensions of the scattering potential at distances of a few $\mathring{A}$ from the emitter have been performed by McKale *et al.* [5] and Rehr and co-workers [6,**?**,**?**]. A simple curved s-wave scattering factor can be expressed as:

$$f_j^{(s)}(\theta_j, r_j) = \frac{1}{k}\sum_l (2l+1)e^{i\delta_l^j} sin\delta_l^j P_l(cos\theta_j)\sqrt{1+\frac{l(l+1)}{2(kr_j)^2}}e^{il(l+1)/2kr_j} \tag{2.3}$$

It can be seen from Eq. 2.3 that the atomic scattering factor is also a function of the scattering distance r_j, and is significant when r_j or k is small. A large r_j or k in Eq. 2.3 will result in a plane-wave expression which is the same as Eq. 2.2. In Fig. 2.2 on page 21 and Fig. 2.3 on page 22, the small-atom approximation (Eq. 2.2) and more rigorous curved-wave expression of Eq. 2.3 are plotted in scattering phases and amplitudes of the relevant scattering factors of a Cu atom at 914 and 64 eV. It can be seen that differences between the two calculations are observed for the Cu scattering factor both at high and low energy, though more prominently for the low energy curves. At high energy, there are few differences between the two calculations for a high scattering angle, say above 60^o, while substantial differences, for both amplitude and phase, are observed at small scattering angles close to the forward scattering direction on the plots. For the low energy calculations, the Cu atomic scattering factor shows significant differences for the two calculations both in amplitude and phase at all the scattering angles. This indicates the importance of taking the initial state of the emitter wave into account for the diffraction calculation at lower kinetic energies. For the high energy curves, the forward-scattering amplitude $I(0^o)$ versus the back-scattering amplitude $I(180^o)$ is as large as

$$I(0^o)/I(180^o) = 5.68/.0304 = 187$$

while for the low energy curves the radio becomes

$$I(0^o)/I(180^o) = 1.37/.482 = 2.84$$

Relatively speaking, the scattering amplitude for lower kinetic energy is more "uniformly" distributed compared to the forward peaked scattering amplitude at higher energy. The high ratio of the forward to back-scattering amplitude at high kinetic energy is one of the most important features in electron diffraction, and it gives rise to the pronounced peaks in the angular distribution of the diffraction pattern, from which the direction of major bond axes of the adsorbed molecules can be obtained rather directly ("searchlight effect"). The low ratio of the forward to back-scattering amplitude at low kinetic energy complicates the scattering processes where the back-scattering events cannot be neglected, and therefore, a full multiple scattering process must be considered in a dependable calculation.

When the emitted electron wave is other than a simple s wave, the atomic scattering factor can be calculated using a novel high-energy approximation [6]. The atomic scattering factor for a more complicated incident spherical wave takes the form:

$$f_j^{l'}(\theta_j, r_j) = c_{l'}(kr_j)\frac{1}{k}\sum_l (2l+1)e^{i\delta_l^j} sin\delta_l^j P_l(cos\theta_j)c_l(kr_j) \tag{2.4}$$

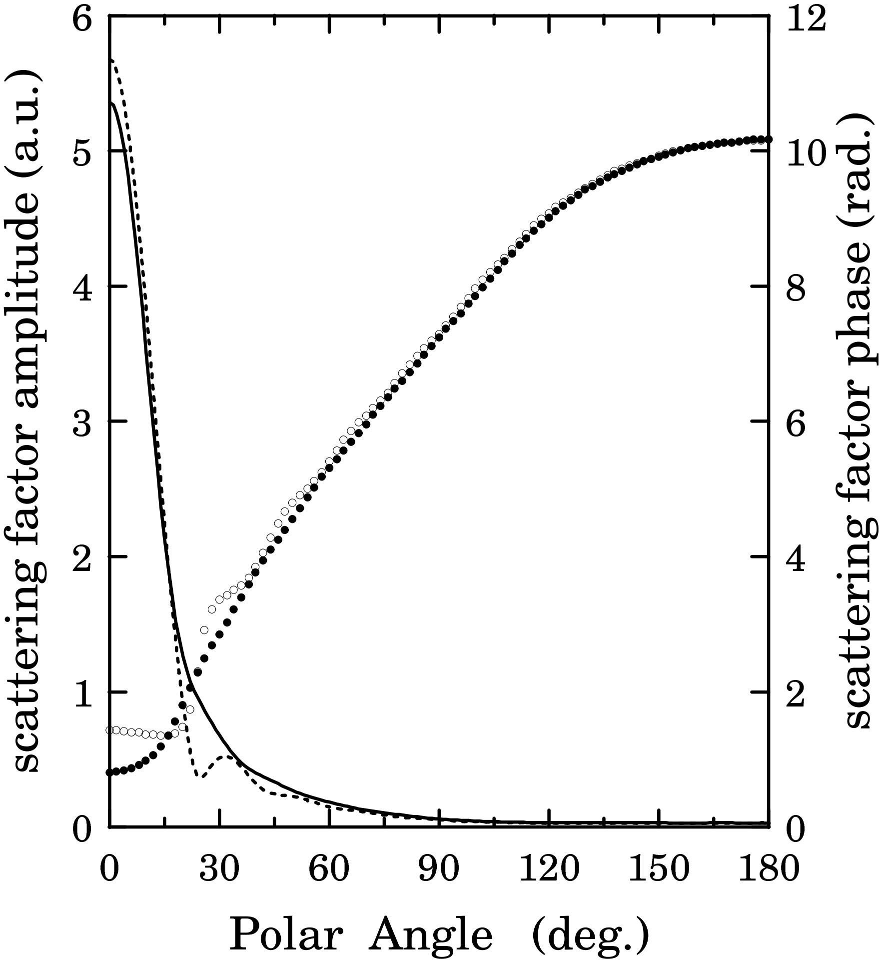

Figure 2.2: Atomic scattering factors of a Cu atom calculated using the plane and spherical wave form. The phase shifts are evaluated at a kinetic energy of 914 eV. The scattering amplitude and phase of a Cu atom are plotted by solid lines and solid circles for the plane-wave calculation of Eq. 2.2 and by dashed lines and open circles for the spherical wave calculation of Eq. 2.3 with an emitter-scatterer distance of 2.55 $\mathring{A}$.

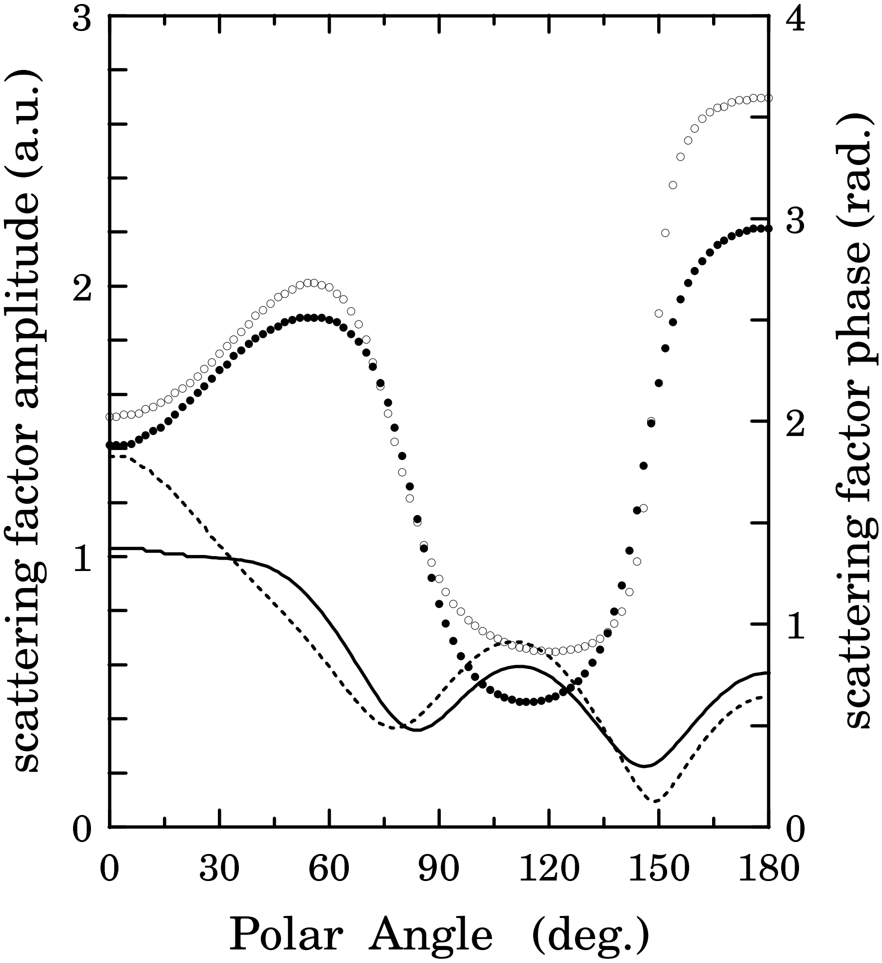

Figure 2.3: Atomic scattering factors of a Cu atom calculated using the plane and spherical wave form. The phase shifts are evaluated at a kinetic energy of 64 eV. The scattering amplitude and phase of a Cu atom are plotted by solid lines and solid circles for the plane-wave calculation of Eq. 2.2 and by dashed lines and open circles for the spherical wave calculation of Eq. 2.3 with an emitter-scatterer distance of 2.55 $\mathring{A}$.

where $c_l(kr_j)$ is the polynomial coefficient of the Hankel function $h_l^{(l)}(kr_j)$. Eq. 2.4 approaches to Eqs. 2.3 and 2.2 at large kr_j, as $c_l(kr_j) \simeq 1$. This indicates that there would be little differences between s wave emitter diffraction and that with a higher angular momentum emitter wave if the electron kinetic energy is higher or the cluster considered is a single crystal with a large nearest-neighbor distance.

2.2.2 Single scattering scheme and formalism

Theoretical simulation of electron diffraction is necessary in order to maximize the information that can be obtained from XPD and AED data. Single scattering cluster(SSC) theory [28,?,?,?,?] has been proved to be a simple and fairly reliable means of interpreting angle-resolved diffuse electron diffraction at high energy for all emission angles except those coinciding with chains of atoms where at least double and triple scattering processes must be considered.

Consider an electron source, with an angular momentum L, at the origin. The emitted wave field takes the form:

$$A_L h_l^{(1)}(kr) Y_L(\hat{\mathbf{k}}),$$

For a scatterer is at the position $\mathbf{r}_j$, the resulting wave-field at the far field in the direction of $\hat{\mathbf{k}}$ can be written as:

$$\psi(\mathbf{k}) = A_L \left(i^{-l} Y_L(\hat{\mathbf{k}}) + \sum_{L'} G_{LL'}(k\mathbf{r}_j) t_{l'} e^{-i\mathbf{k}\cdot\mathbf{r}_j} Y_{L'}(\hat{\mathbf{k}}) \right). \tag{2.5}$$

if we make use of the asymptotic expansion of:

$$h_l^{(1)} \sim i^{-l} \frac{e^{iz}}{iz} \qquad \text{as} \qquad z \to \infty$$

In above expressions, A_L is a complex amplitude, Y_L is a spherical harmonic function, $h_l^{(1)}$ a Hankel function of the first kind, $G_{LL'}$ the element of free-space propagator in an angular momentum representation, $\mathbf{k}$ the wave vector of electrons, $\mathbf{r}$

a position vector, and the atomic t-matrix element

$$t_l = \frac{1}{2}\left(e^{2i\delta_l} - 1\right)$$

where δ_l is the phase shift of a spherical wave of angular momentum l on scattering from the atom. The exact expression of the free propagator Green's function can be written as:

$$G_{LL'}(k\mathbf{r}) = 4\pi \sum_{L''} i^{l-l'-l''} (-)^{m'-m''} h^{(1)}_{l''}(kr) Y_{l'',-m''} \int Y_{lm} Y_{l''m''} Y_{l'',-m'} d\Omega,$$

If

$$kr \gg 1,$$

the Green's function may be approximated by

$$G_{LL'}(k\mathbf{r}) = 4\pi i^{l'-1} \left(\frac{e^{ikr}}{ikr}\right) Y^*_{L'}(\hat{\mathbf{r}}) Y_L(\hat{\mathbf{r}}).$$

This may be regarded as the lowest-order approximation to a "separable" Green's function as defined by Rehr *et al* [8]. Substituting above expression into Eq. 2.5, we may write:

$$\psi(\mathbf{k}) = A_L \left(Y_L(\hat{\mathbf{k}}) + f(\hat{\mathbf{k}}\cdot\hat{\mathbf{r}}_j)\frac{e^{i(kr_j - \mathbf{k}\cdot\mathbf{r}_j)}}{r_j} Y_L(\hat{\mathbf{r}}_j)\right), \tag{2.6}$$

where the common factors i^{-l} are dropped, and the atomic scattering factor takes the "plane-wave" form of

$$f(\hat{\mathbf{k}}\cdot\hat{\mathbf{r}}_j) = \frac{4\pi}{ik}\sum_{L'} Y^*_{L'}(\hat{\mathbf{r}}_j) Y_{L'}(\hat{\mathbf{k}}),$$

and by making use of

$$P_{l'}(\hat{\mathbf{k}}\cdot\hat{\mathbf{r}}_j) = \frac{4\pi}{2l+1}\sum_{m'} Y^*_{L'}(\hat{\mathbf{r}}) Y_{L'}(\hat{\mathbf{k}}),$$

we end up with

$$f(\hat{\mathbf{k}} \cdot \hat{\mathbf{r}}_j) = \frac{1}{k} \sum_{l'} (2l' + 1) t_{l'} P_{l'}(\hat{\mathbf{k}} \cdot \hat{\mathbf{r}}_j).$$

More accurate approximation of $\psi(\mathbf{r})$ in Eq. 2.6 can be calculated using higher-order separable Green's functions [8], which results in more accurate atomic scattering factors, such as the "spherical-wave" form [79,**?**] which has been already discussed in Sec 2.2.1.

If the emitted electron wave takes a more complicated form, and can be expanded in a linear combination of the spherical harmonic functions in the angular momentum representation, e.g.,

$$\phi(\mathbf{k}) = \sum_{L} a(k, L) Y_L(\hat{\mathbf{k}}),$$

where $a(k, L)$ is a complex number and a function of k and L, and more than one scatterer is involved in the scattering process, i.e., scatterers $\mathbf{r}_j$ j =1, 2, 3,..., the resulting wave field could be expressed as:

$$\psi(\mathbf{k}) = \phi(\mathbf{k}) + \sum_{j} \left(f(\mathbf{k}, \mathbf{r}_j) \frac{e^{i(kr_j - \mathbf{k} \cdot \mathbf{r}_j)}}{r_j} \phi(\mathbf{r}_j) \right). \tag{2.7}$$

The first term in Eq. 2.7 is the reference wave of the emitter that directly goes to the electron detector at the far field, the second summation term represents all the scattered waves. We can then write the diffracted intensity, $I(\mathbf{k})$, as:

$$I(\mathbf{k}) = \left| \phi(\mathbf{k}) + \sum_{j} \left(f(\mathbf{k}, \mathbf{r}_j) \frac{e^{i(kr_j - \mathbf{k} \cdot \mathbf{r}_j)}}{r_j} \phi(\mathbf{r}_j) \right) \right|^2. \tag{2.8}$$

A schematic diagram of the single-scattering scheme is shown in Fig. 2.1 (b) on page 17 where the total kinematic diffraction amplitude is seen to be the sum of the direct emitted wave and the waves $\phi_i(\mathbf{k})$ scattered once by each of the surrounding atoms around the emitter. Note that in order to carry out the calculation correctly, the summation should include all the important scatterers surrounding the emitter.

The attenuation of the electron wave traveling through a solid may suffer considerable damping, and the inelastic scattering length, λ, of the electron contributes to the diffraction process through a damping factor of $e^{-L/2\lambda}$ for the scattered and the direct waves.

Vibrational attenuation of interference effects is also potentially important, and can be included in a standard way by multiplying each scattered wave by its associated temperature-dependent Debye-Waller factor:

$$\begin{aligned} W_j(T) &= exp\left[-\Delta k^2 \overline{U_j^2(T)}\right] \\ &= exp\left[-2k^2(1-cos\theta_j)\overline{U_j^2(T)}\right] \\ &= exp\left[-2k^2(1-cos\theta_j)\frac{\hbar^2 T}{m\Theta_T^2 k_B}\right] \end{aligned} \tag{2.9}$$

where Δk is the magnitude of the change in wave vector produced by the scattering, $\overline{U_j^2(T)}$ the temperature-dependent one-dimensional mean-squared vibrational displacement of atom j with respect to the emitter, Θ_T the Debye-Waller temperature, $\hbar$ Planck's constant, and k_B Boltzmann's constant. The physical meaning of the quantity, $\frac{\hbar^2 T}{m\Theta_T^2 k_B}$, is the mean-square displacement of the scatterers, and a typical value of this in a Cu single crystal is 0.0065 $\mathring{A}^2$ [29].

At this level of approximation, $\overline{U_j^2(T)}$ is assumed to be isotropic in space and any correlations in the movements of near-neighbor atoms are neglected. However, the electron scattering is significant only when θ_j is close to zero. Then $(1-cos\theta_j)$ factor in the argument of Eq. 2.9 suggests that W_j is very close to unity for all important scattered waves. So, vibrational effects are, to first order, not very important in forward-scattering dominated XPD, although important to the backscattered diffraction modes. Another alternate method of accounting for vibrational effects is to assume some probability distribution of atom positions due to vibration and then to sum separate weighted diffraction intensities for all possible combinations of atom positions. This leads to

$$I(\mathbf{k}) = \left| e^{-L/2\lambda} + \sum_j \frac{f_j(\theta_j, r_j)}{r_j} W_j e^{-L_j/2\lambda} e^{ikr_j(1-cos\theta_j)} \right|^2$$
$$+ \sum_j \frac{|f_j(\theta_j, r_j)|^2}{r_j^2} \left(1 - W_j^2\right) e^{-L_j/\lambda}. \tag{2.10}$$

Here the attenuation caused by the inelastic scattering length λ is assumed to be isotropic and approximated by the factor $e^{-L/2\lambda}$, where L is the distance that electron travels in a solid. In the first summation of Eq. 2.10, the interference between scattered and unscattered wave portions is expressed in terms of a structure factor $kr_j(1 - cos\theta_j)$. The second $\sum_j$ corrects the absolute squared term for the incorrect inclusion of Debye-Waller attenuations in terms involving a product of a scattered wave with itself [30,**?**]. That is, in expanding the absolute value squared, only products involving unlike waves as $\phi_o \phi_j^*$ or $\phi_j \phi_l^*$ $(l \neq j)$ should include Debye-Waller factors of W_j or $W_j W_l$, respectively. The $(1 - W_j)$ factor in the second summation is thus necessary to yield overall correct products of the form $\phi_j \phi_j^*$ without any W_j^2 factor. The second sum is termed the thermal diffuse scattering term and it is usually quite small with respect to the overall XPD modulations due to the fact that W_j is close to unity for strong scatterers.

Refraction at the surface needs to be considered when the detector is at grazing angle. The correction for the refraction can only affect the polar angle of the outgoing electron wave passing through the solid/vacuum interface, and the corrected polar angle is

$$\theta' = acos\left[\sqrt{\frac{E_k - V_o}{E_k}} cos\theta\right]. \tag{2.11}$$

where V_o is the inner potential which equals to a potential step across the vacuum and the solid. E_k is the electron kinetic energy outside the solid. It can be seen that this correction can be negligible in the high kinetic energy range except at grazing angle.

The simple concept and convenient computation formula of SSC theory makes it very attractive for interpretation of diffuse electron diffraction data. However, the limitations of the single scattering model must be kept in mind to avoid erroneous structural conclusions. As shown in Fig. 2.2 the relatively small phase shifts in the high energy range at low scattering angles constitute an universally constructive interference along this scattering direction in which direction a forward scattering peak can be formed. An overall reduction in diffraction intensity relative to what is predicted with single scattering theory along this direction would be observed if more than two scatterers are found along this direction, and this "forward defocusing" effect will cause a breakdown of the SSC theory. As shown in Fig. 2.3 the low ratio of forward to back-scattering amplitude suggests that multiply scattered waves arise and contribute much to the final diffraction modulations at low energy. This indicates that Eq. 2.10 is valid only for an electron kinetic energy greater than 500 eV, and that multiple scattering must be considered as the kinetic energy drops significantly below 500 eV. For low energies, the explicit inclusion of the differential photoelectron cross section and integration over the photon electric field polarization vector becomes important for an accurate description of the diffraction process [25]. Similarly, the use of bulk Debye temperatures for surface atoms and neglect of correlated vibrations can become a source of error for energies in the order of 100 eV [26]. Finally, the finite size of the analyzer aperture must be considered in the calculations in order to achieve a result similar to experiment. This task is performed by averaging the intensities over the small solid angles subtended by the detector aperture. Simulations of this sort also allow one to determine what level of angular resolution is desired in a diffraction experiment.

2.3 Multiple scattering cluster theory

2.3.1 Multiple scattering scheme

The major reason for the breakdown of the single scattering cluster (SSC) theory is the fact that the scattered waves could be scattered again by other atoms in the cluster and that these scattered waves (scattered more than once) also contribute to the final diffraction modulations. It has been shown that for high kinetic energy, the principal failure of SSC theory is an overestimation of the forward-scattering intensity along close-packed, low-index directions [27] where the multiple scattering results in a considerable attenuation known as the "defocusing" effect. A simple picture to explain this is that a secondary scattering site acts to reduce the total scattered-wave amplitude along the chain via a weak Coulomb interaction. This interaction occurs as the portion of the wave that is forward scattered by the atom directly adjacent to the emitter passes through the potential centered on the secondary scattering site. This phenomenon cannot be modeled without using multiple scattering theory. In the low kinetic energy range, the back scattered waves are relatively strong and contribute much to the overall diffraction modulations, and multiple scattering theory is needed in this case also to correctly explain the experimental data.

The history of multiple-scattering calculations for angle-resolved photoemission can be traced at least as far back as the work of Liebsch [9] in 1974. Pendry [10] proposed a theory for angle-resolved valence-band photoemission and Tong and co-workers [12,?,?] proposed a corresponding treatment for photoemission from molecular orbitals and atomic core states. All these schemes rely on a computational machinery of low-energy electron-diffraction (LEED) theory for evaluating the multiple electron scattering in ordered atomic structures. Full multiple scattering theory based on the short inelastic scattering length of low and medium energy electrons in solids to restrict the multiple scattering of the Auger electron or photoelectrons to a cluster of atoms localized around the emitter will be discussed in this Chapter. The advantage of this technique is the relaxation of the requirement of translational symmetry in the layers of atoms parallel to the surface. Such cluster techniques have been developed by Barton and co-workers [16,**?**], Fritzsche [18], and Friedman and Fadley [19]. In these schemes all the interatom propagation of the electrons is represented by Green's functions which relate the amplitudes of a spherical-wave expansion of the wave field about another point. The evaluation of these Green's function turns out to be major limiting factor in the speed of such calculations. Therefore, fast approximate schemes such as the Taylor-series magnetic quantum number expansion (TS-MQNE) [16], the reduced angular momentum expansion (RAME) [18], and the separable Green's functions of Rehr and Albers [8,**?**] have been employed to speed up the calculations.

2.3.2 Multiple scattering formalism

The exact multiple-scattering cluster scheme of by Saldin, Harp, and Chen [32] to calculate Auger, photoemission and Kikuchi diffraction patterns is introduced here. This multiple-scattering cluster scheme is based on dividing a cluster into a series of concentric shells, with an origin chosen at the source atom, as shown in Fig. 2.4 on page 32. In this way, a convenient computational algorithm for intra- and inter-shell processes can be applied to treat the multiple scattering problem. Within each shell, atoms are located at approximately the same distance from the emitter, i.e., atoms within the same shell have distances from the emitter which differ by less than 1.00 a.u. An advantage of such a classification of the cluster into a series of concentric sub-shells is the removal of the requirement of translational symmetry of the atomic structure near the surface. This multiple-scattering cluster scheme restricts consideration of the multiple-scattering of the electrons (with a short inelastic-scattering length) to a cluster of atoms localized around the emitter. This is a good approximation when the energy of the electrons is in the range of 40 eV and up to about 1000 eV.

The basis for the scattering by the cluster is a set of spherical waves. A set of multiple scattering equations based on waves centered on each individual atom in the cluster, is transformed to a single center expansion only at the end of the calculation. As shown in Fig. 2.4, when an atom emits electrons by Auger or photoemission processes, the resulting wave-field could be written as the following linear combination, with amplitudes $A_L^{(0)}$, of outgoing spherical waves:

$$\sum_L A_L^{(0)} h_l^{(1)}(kr) Y_L(\hat{\mathbf{r}}) \tag{2.12}$$

where $(lm) \equiv L$ are angular momentum quantum numbers, $\mathbf{r}$ is a position vector with respect to an origin at the emitter, and k the wave-number of the emitted electrons. The extent of the propagation of such a wave through a material will depend on the fairly short inelastic scattering length, and hence be restricted to a localized cluster of atoms surrounding the emitter.

For an isolated atom, it is known from dipole transition theory that when a core-level photoelectron is emitted from this atom, the ejected photoelectron wave

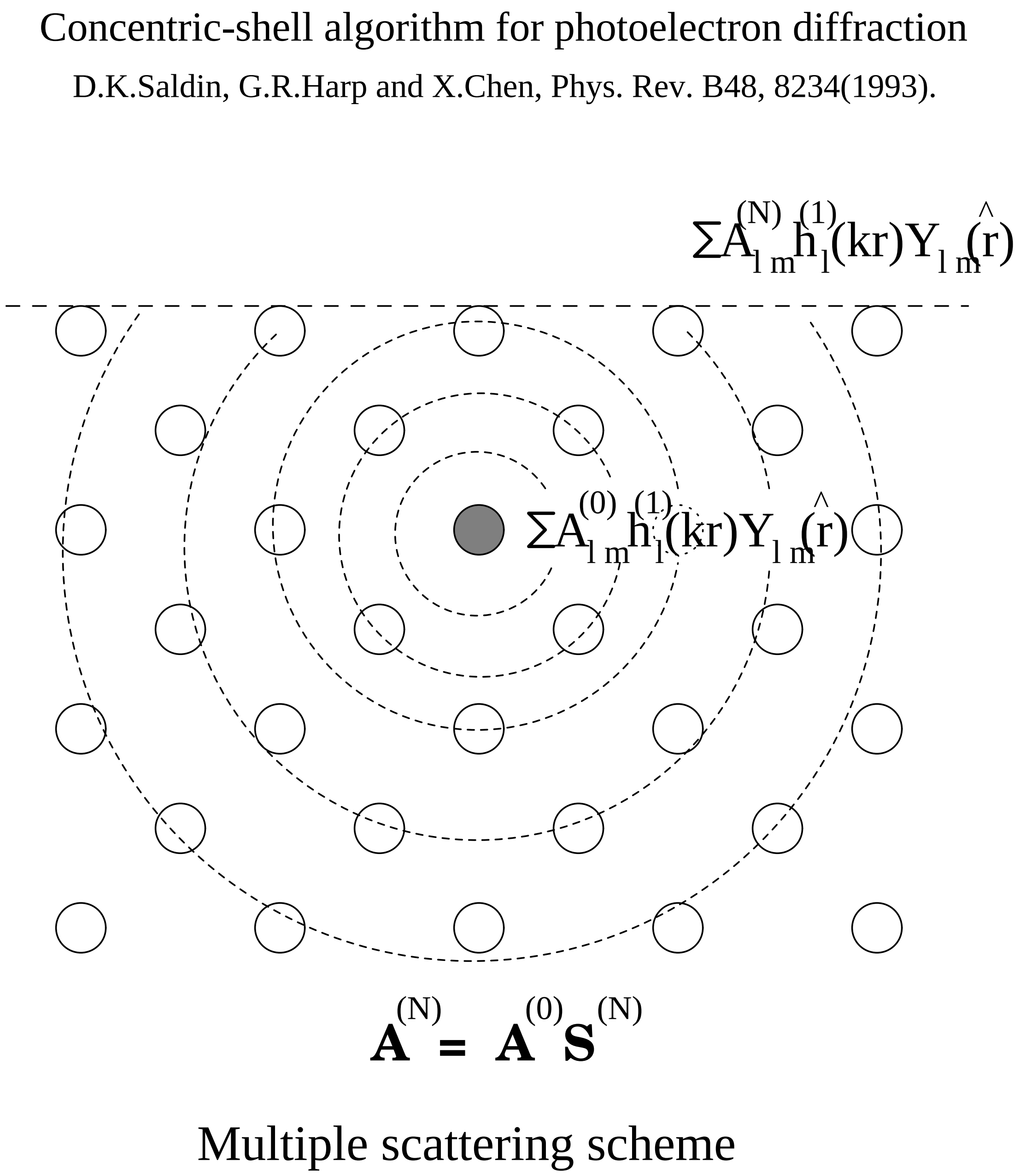

Figure 2.4: An electron wave is emitted from an origin and is scattered by the surrounding atoms. Multiple scattering processes arise when those scattered waves are scattered again in the cluster and contribute to the final diffraction pattern.

function, $\psi_a(\mathbf{r})$, may be written:

$$\psi_a(\mathbf{r}) = \int d\mathbf{r}' G_a^+(\mathbf{r}, \mathbf{r}'; E)\Delta(\mathbf{r}')\psi_{l_o m_o}(\mathbf{r}') \tag{2.13}$$

where $\psi_{l_o m_o}(\mathbf{r}')$ is the core state wave function of angular momentum quantum numbers, l_o and m_o, and, $\Delta(\mathbf{r}')$ is the photon-electron interaction operator.

The Green's function takes the form:

$$G_a^+(\mathbf{r}, \mathbf{r}'; E) = -ik \sum_{lm} R_l(r_<, E) R_l^{(+)}(r_>, E) Y_{lm}(\hat{\mathbf{r}}) Y_{lm}^*(\hat{\mathbf{r}}') \tag{2.14}$$

where the $r_>$ and $r_<$ are defined as:

$$\text{if } r > r' \text{ then } r_> = r,\ r_< = r',$$
$$\text{if } r < r' \text{ then } r_< = r,\ r_> = r',$$

and $R_l(r, E)$ and $R_l^{(+)}(r, E)$ are the regular and irregular solutions, respectively, of the radial Schrödinger equation for the exciting atom such that $R_l(r, E)$ matches onto

$$R_l(r, E) \sim j_l(kr) cos\delta_l - n_l(kr) sin\delta_l$$

at the muffin-tin boundary, and $R_l^{(+)}(r, E)$ matches onto

$$R_l^{(+)}(r, E) \sim h_l^{(1)}(kr) e^{i\delta_l}$$

at muffin-tin radius. Substituting Eq. 2.14 into Eq. 2.13 we obtain:

$$\psi_o(\mathbf{r}) = \sum_{lm} A_{lm}^{(0)} h_l^{(1)}(kr) Y_{lm}(\hat{\mathbf{r}}) \tag{2.15}$$

where

$$A_{lm}^{(0)} = -ik \int d\mathbf{r}' R_l(r', E) Y_{lm}^*(\hat{\mathbf{r}}') \Delta(\mathbf{r}') \psi_{l_o m_o}(\mathbf{r}') \tag{2.16}$$

is essentially the matrix element for the core-level photoemission transition.

When the atom is in the environment of a cluster where many other atoms are present, the wave field $\psi(\mathbf{r})_o$ is modified by the multiple scattering by that cluster.

For computational convenience we divide the cluster into a series of N concentric shells centered at the emitter. We also suppose that the total electron wave field between the q-th and the $(q{+}1)$-th shells takes the same form as Eq. 2.12, but with expansion coefficients $A_L^{(q)}$, which are collectively represented by the vector $\mathbf{A}^{(q)}$. Thus the task of determining the electron wave-field emerging to some external detector after multiple scattering with all atoms of the cluster is effectively one of evaluating the vector $\mathbf{A}^{(N)}$, representing the corresponding expansion coefficients of the wave-field propagating outwards from the N-th shell.

Consider a surface containing a lager number of atoms of the same species. The photoemitted wave from one atom makes its way out of the surface after scattering many times from its nearby atoms before it emerge from the surface. Suppose that it is possible to combine the scattering matrices of the shells together to construct an "out-out" scattering matrix of the whole cluster $S^{(N)}_{lm,l'm'}$. The wave which finally emerge after all the multiple scattering can be written:

$$\psi(\mathbf{r}) = \sum_{lm}\sum_{l'm'} A^{(0)}_{lm} S^{(N)}_{lm,l'm'} h^{(1)}_{l'}(kr) Y_{l'm'}(\hat{\mathbf{r}})$$

where, as expected, there are more wave $l'm'$ components than lm components since the outer radius of the cluster is large. The amplitude $A^{(n)}$ are those of the outgoing spherical waves finally emerging from a cluster of N shell, and

$$A^{(N)}_{lm} = \sum_{l'm'} A^{(0)}_{lm} S^{(N)}_{lm,l'm'}$$

or it can be written in a vector form, i.e., the elements of the vector $\mathbf{A}^{(N)}$ may be computed from known values of $\mathbf{A}^{(0)}$ [20,**?**]:

$$\mathbf{A}^{(N)} = \mathbf{A}^{(0)}\mathbf{S}^{(N)} \tag{2.17}$$

where the matrix $\mathbf{S}^{(N)}$ may be evaluated by the following pair of coupled recursion relations:

$$\mathbf{S}^{(q+1)} = \mathbf{S}^{(q)}(\mathbf{I} - \mathbf{T}^{OI}_{q+1}\mathbf{J}^{IO}_{q})^{-1}(\mathbf{I} + \mathbf{T}^{OO}_{q+1}) \tag{2.18}$$

and

$$\mathbf{J}^{IO}_{q+1} = \mathbf{T}^{IO}_{q+1} + (\mathbf{I} + \mathbf{T}^{II}_{q+1})\mathbf{J}^{IO}_{q}(\mathbf{I} - \mathbf{T}^{OI}_{q+1}\mathbf{J}^{IO}_{q})^{-1}(\mathbf{I} + \mathbf{T}^{OO}_{q+1}) \tag{2.19}$$

where $\mathbf{J}^{IO}_{q}$ is the "in-out" reflection matrix of the cluster consisting of the central atom plus the first q shells. With the starting conditions

$$\mathbf{S}^{(0)} = \mathbf{I} \tag{2.20}$$

and

$$\mathbf{J}^{IO}_{0} = \mathbf{t}_c \tag{2.21}$$

where $\mathbf{t}_c$ is the t-matrix of the emitter atom. In the above expressions, the elements of the scattering matrices $\mathbf{T}^{OO}_{q}$, $\mathbf{T}^{OI}_{q}$, $\mathbf{T}^{II}_{q}$ and $\mathbf{T}^{IO}_{q}$ of the q-th shell are given by

$$T^{OO}_{qLL'} = \sum_{iL_i}\sum_{jL_j} g^{oi}_{LL_i} T^{ij}_{L_iL_j} \tilde{g}^{jo}_{L_jL'}, \tag{2.22}$$

$$T^{OI}_{qLL'} = \sum_{iL_i}\sum_{jL_j} g^{oi}_{LL_i} T^{ij}_{L_iL_j} g^{jo}_{L_jL'}, \tag{2.23}$$

$$T^{II}_{qLL'} = \sum_{iL_i}\sum_{jL_j} \tilde{g}^{oi}_{LL_i} T^{ij}_{L_iL_j} g^{jo}_{L_jL'}, \tag{2.24}$$

and

$$T^{IO}_{qLL'} = \sum_{iL_i}\sum_{jL_j} \tilde{g}^{oi}_{LL_i} T^{ij}_{L_iL_j} \tilde{g}^{jo}_{L_jL'}, \tag{2.25}$$

where $g^{ij}_{LL'}$ and $\tilde{g}^{ij}_{LL'}$ are propagators from atom i of position vector $\mathbf{r}_i$ to atom j of position vector $\mathbf{r}_j$ in the q-th shell defined in the Appendix. The superscript o

in the propagators represents the central emitter atom. A schematic diagram of interpretations of scattering matrices $\mathbf{S}^{(q)}$, $\mathbf{J}_q^{IO}$, $\mathbf{T}_q^{OO}$, $\mathbf{T}_q^{OI}$, $\mathbf{T}_q^{II}$ and $\mathbf{T}_q^{IO}$ are shown in Fig. 2.5 on page 37.

The intra-shell multiple scattering is represented by the elements $T^{ij}_{L_iL_j}$ of the matrix

$$\mathbf{T} = \mathbf{H}^{-1}. \tag{2.26}$$

where $\mathbf{H}$ is the real-space Korringa-Kohn-Rostocker (KKR) matrix also defined in the Appendix.

With $\mathbf{S}^{(N)}$ calculated by this algorithm, making use of the asymptotic expansion of the Hankel functions

$$\lim_{z\to\infty} h^{(1)}_{l'}(z) = (-i)^{l'+1} z^{-1} \mathrm{e}^{iz} \tag{2.27}$$

and neglecting some common constant factors, the angular distribution of the far-field intensity of a photoelectron or Kikuchi diffraction pattern can be evaluated from

$$I_p(\mathbf{k}) = \left| \sum_L A_L^{(0)} \sum_{L'} S^{(N)}_{LL'} (-i)^{l'} Y_{L'}(\hat{\mathbf{k}}) \right|^2 \tag{2.28}$$

where $S^{(N)}_{LL'}$ are the elements of the matrix $\mathbf{S}^{(N)}$. In the evaluation of $I_p(\mathbf{k})$ in Eq. 2.28 we have allowed for the interference between the angular momentum channels L of the emitted electron. The coefficients $A_L^{(0)}$ can be evaluated from the matrix elements of the atomic excitation process, be it photoexcitation (for photoelectron diffraction) or quasi-elastic scattering of an incident plane wave (for Kikuchi diffraction).

In the case of Auger emission the initial-state angular momentum channels are mutually incoherent and the angular distribution of an Auger diffraction pat-

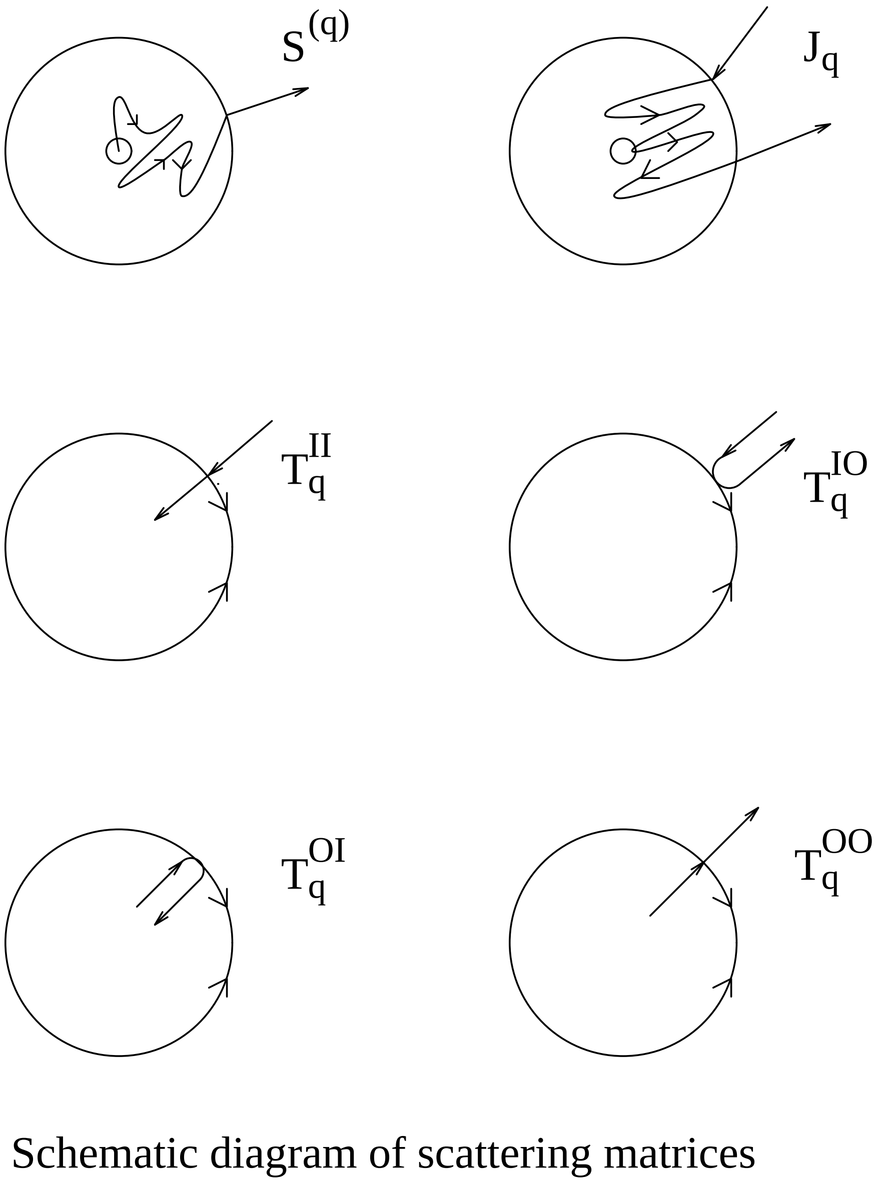

Figure 2.5: Schematic diagram of interpretations of scattering matrices. $\mathbf{S}^{(q)}$, $\mathbf{J}_q^{IO}$, $\mathbf{T}_q^{OO}$, $\mathbf{T}_q^{OI}$, $\mathbf{T}_q^{II}$ and $\mathbf{T}_q^{IO}$ are defined as cluster scattering, cluster "in-out" reflection, "in-out", "out-in", "in-in" and "in-out" shell scattering matrix, respectively.

tern should instead be evaluated from an expression of the form

$$I_A(\mathbf{k}) = \sum_L \left| A_L^{(0)} \sum_{L'} S_{LL'}^{(N)} (-i)^{l'} Y_{L'}(\hat{\mathbf{k}}) \right|^2 \tag{2.29}$$

where the $A_L^{(0)}$ are now related to the matrix elements for Auger transitions.

In the next two sections, we are going to perform tests on model atomic clusters to check the convergence of our calculations with respect to various parameters, and to verify the justification of the approximations, such as, truncating the angular momentum quantum number expansions, the forward-scattering approximation, the back-scattering approximation and single-scattering limitations.

Quantitative comparisons of diffraction patterns are made using a mean square difference reliability R-factor defined as

$$R = \frac{\sum_i \mid P_i^{(1)} - P_i^{(2)} \mid^2}{\sum_i \mid P_i^{(1)} + P_i^{(2)} \mid^2} \tag{2.30}$$

Of the two diffraction patterns to be compared, the reference pattern, $P^{(1)}$, is chosen to be the one which is the better approximation. The summation is taken over all the available data points on the patterns. Based on previous results [22], we expect that R$\sim$0.1 is the minimum R-factor to be expected for the comparison between calculations and experiment. We therefore assume that any approximation which changes the calculated diffraction pattern such that the R-factor is less than or equal to R= 0.001 is a more than adequate approximation. All the calculations involve Cu atoms in a geometry corresponding to the face-centered-cubic (fcc) (001) orientation. The electron kinetic energy is 914eV, which is the energy of the Cu LVV Auger electron. The atomic scattering processes take into account angular momentum quantum numbers up to $l = l_{max} = 16$. Note that this parameter was checked for convergence via a calculation involving 13 Cu atoms. An R-factor analysis comparing a calculation with $l_{max} = 16$ and $l_{max} = 20$ resulted in R=0.02, showing the computations to be converged to an degree much better than the expected agreement between calculation and experiment. All calculations above assume an inner potential with real and imaginary parts of -15eV and -4eV, respectively. The zero temperature phase shifts are corrected by a Debye-Waller factor [11] assuming a Debye temperature of 320K and a sample temperature of 300K.

2.3.3 Finite Angular Resolution

The number of partial waves needed to describe a cluster scattering is a function of the radius, R (in atomic units), of the cluster, and electron kinetic energy, E (in Hartree units):

$$l_{out} \simeq R\sqrt{2E}$$

where l_{out} is the maximum angular momentum quantum number that is used in a cluster calculation. But at relatively high energy ranges for a large cluster calculation the l_{out} can be as large as 160 for a cluster size of 10 $\mathring{A}$ at 1000 eV. Such a large l_{out} in a cluster calculation can take a huge size of the computer memory and long cpu time. For an actual cluster calculation the time scales approximately as l_{out}^4. Fortunately, a smaller l_{out} can be used in a cluster calculation for a large size of a cluster at high electron energy due to the experimental limitation of the finite detector aperture.

In an actual apparatus, the electron detector integrates over some finite solid angle when making an angle-resolved measurement. For the purposes of our argument, and without loss of generality, we may choose a polar axis passing through the center of the detector with an aperture solid angle of $\Delta\Omega$. Then the experimentally-measured intensity, I_{exp}, would be related to the theoretical intensity $I_{th}(\hat{\Omega})$ by the equation

$$I_{exp}(0,0) = \int_{\Delta\Omega} I_{th}(\hat{\Omega}) d\hat{\Omega} = \int_{\phi=0}^{2\pi} \int_{\theta=0}^{\theta_m} I_{th}(\theta, \phi) \sin\theta d\theta d\phi \tag{2.31}$$

where we have assumed that the analyzer aperture is circular with angular half-width θ_m. From Eq. 2.28 it can be seen that a theoretical photoemission intensity may be written

$$\begin{aligned} I_{th}(\theta,\phi) &= \mid \sum_L A_L^{(N)} (-i)^l Y_L(\theta,\phi) \mid^2 \\ &= \sum_{L'} \sum_{L''} A_{L'}^{(N)} A_{L''}^{(N)*} (-i)^{l'-l''} Y_{L'}(\theta,\phi) Y_{L''}^*(\theta,\phi) \\ &= \sum_{L'} \sum_{L''} A_{L'}^{(N)} A_{L''}^{(N)*} (-i)^{l'-l''} \sum_{l=|l'-l''|}^{l'+l''} \sum_{m=-l}^{l} < L''|L'L > Y_{lm}^*(\theta,\phi) \end{aligned} \tag{2.32}$$

where

$$A_L^{(N)} = \sum_{L'} A_{L'}^{(0)} S_{L'L}^{(N)}$$

and

$$< L''|L'L >= \int Y_{L''}^* Y_{L'} Y_L d\Omega, \tag{2.33}$$

a Clebsch-Gordon coefficient. Substituting Eq. 2.32 into Eq. 2.31 and performing the integrals over θ and ϕ, we find

$$\begin{aligned} I_{exp}(0,0) = 2\pi \sum_{l'} \sum_{l''} (-i)^{l'-l''} \sum_{m'} A_{l'm'}^{(N)} A_{l''m'}^{(N)*} \\ \sum_{l=|l'-l''|}^{l'+l''} < l''m'|l'm'; l\ 0 > \left(\frac{2l+1}{4\pi} \right)^{\frac{1}{2}} Q(l) \end{aligned} \tag{2.34}$$

where

$$Q(l) = -\int_1^{\cos\theta_m} P_l(\cos\theta) d(\cos\theta). \tag{2.35}$$

Noting that the Legendre function $P_l(z)$ may be represented by the hypergeometric function $F(-l, l+1, 1; (1-z)/2)$,

$$P_l(z) = F(-l, l+1, 1; (1-z)/2)$$

or

$$P_l(cos\theta) = \frac{\Gamma(1)}{\Gamma(-l)\Gamma(l+1)} \sum_{n=0}^{\infty} \frac{\Gamma(n-l)\Gamma(n+l+1)}{\Gamma(n+1)} \frac{(\frac{1-cos\theta}{2})^n}{n!}$$

substituting its series expansion into Eq. 2.35 and performing the integral over $\cos\theta$ yields

$$Q(l) = \sum_{n=0}^{\infty} \frac{(-)^n \Gamma(l+n+1)}{(n!)^2 \Gamma(l-n+1) 2^n} \frac{\xi^{n+1}}{(n+1)}$$

where Gamma function $\Gamma(n+1)$ equals $n!$, and then

$$\begin{aligned} Q(l) = \xi + \frac{(-l)(l+1)}{(1!)^2 2}\left(\frac{\xi^2}{2}\right) + \frac{(-l)(-l+1)(l+1)(l+2)}{(2!)^2 2^2}\left(\frac{\xi^3}{3}\right) + \cdots \\ \cdots + \frac{(-l)(-l+1)\cdots(-l+n-1)(l+1)(l+2)\cdots(l+n)}{(n!)^2 2^n}\left(\frac{\xi^{n+1}}{n+1}\right) + \cdots \end{aligned} \tag{2.36}$$

where

$$\xi = 1 - \cos\theta_m. \tag{2.37}$$

The quantity $Q(l)$ may be evaluated numerically from the series expansion Eq. 2.36 for different aperture sizes as specified by θ_m. The results are shown on Figure 2.6. It can be noted that $Q(l)$ drops off with increasing l, and the more sharply the larger the aperture size. In fact, for a typical experimental aperture semi-angle of $\theta_m = 2.5^o$, Figure 2.6 indicates that the contributions of the terms in Eq. 2.34 with values of l greater than about 120 are likely to be negligible. Note that the maximum value of l in the sum in Eq. 2.34 is $l' + l''$ ($= l_m$, say). For a given value of l_m, l' can take values between 0 to l_m, while l'' correspondingly varies from l_m to 0. However, since the lower limit of the sum over l in Eq. 2.34 is $|l' - l''|$, it is clear that the number of allowed terms in the sum over l is greatest when $l' \simeq l'' \simeq l_m/2$. That is, for the highest appreciable value of $l_m \simeq 120$, the most significant contributions to I_{exp} will come from terms with $l' \simeq l'' \simeq 60$. For lower values of l_m the dominant terms will have even lower values of l' and l''.

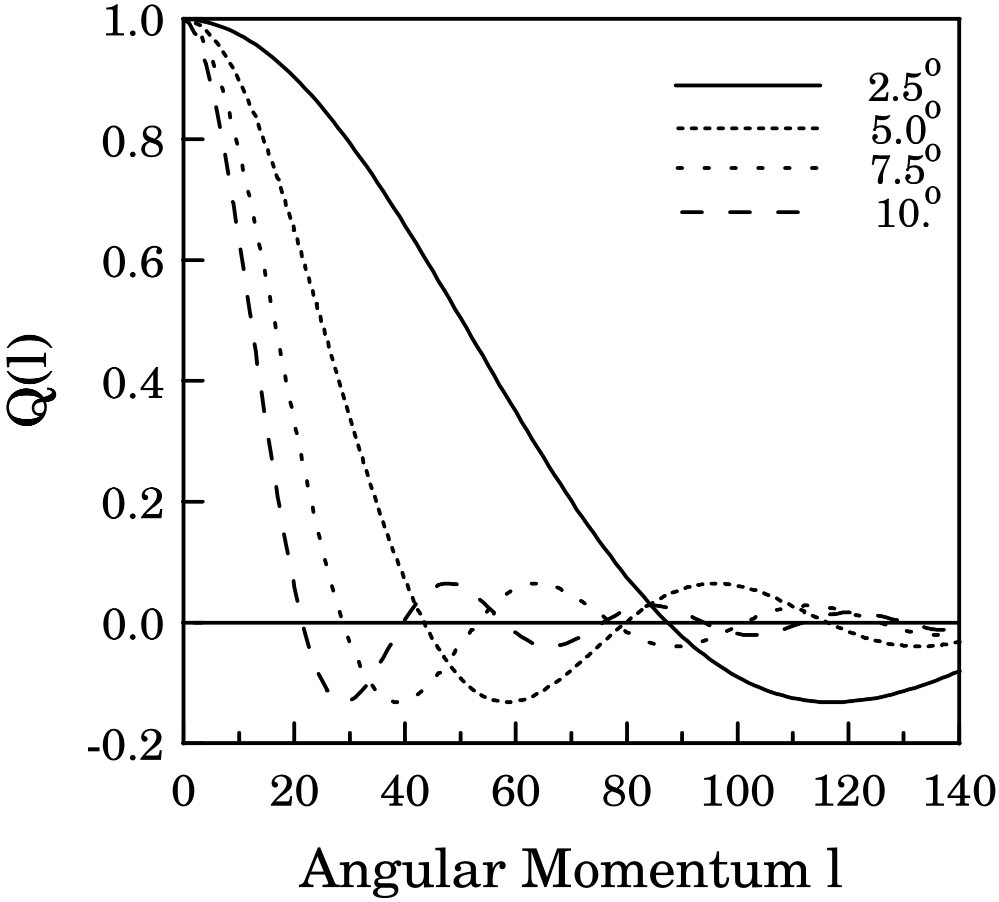

Figure 2.6: Theoretical relative contributions, $Q(l)$ of angular momenta to an experimental photoelectron diffraction pattern for different half-angle θ_m=2.5, 5.0, 7.5, and 10.^{o} of the detector aperture.

Thus, it may be concluded that an experimental diffraction pattern, measured by a detector of aperture with a semi-angle of 2.5^o, could be simulated with reasonable accuracy by restricting the angular momentum quantum numbers of the single-center expansions Eq. 2.28 and Eq. 2.29 to

$$l', l'' < l_{out} \simeq 60. \tag{2.38}$$

It should also be noted, that a mere truncation of the angular momentum expansion at $l', l'' = l_{out}$ is not sufficient to reproduce a finite experimental angular resolution in a calculated diffraction pattern. The reason is found in the gradual decrease of $Q(l)$ with l, as seen on Figure 2.6. The corresponding gradual attenuation of the spherical-wave amplitudes $A_L^{(N)}$ is not accounted for by just a sharp cut-off at $l = l_{out}$. The theoretical diffraction patterns also need to be convolved with an aperture function representing the detector.

Now let's test the assertions about the adequacy of truncating the angular momentum expansions of wave-fields for finite experimental detector apertures. The results of two calculations for the case of a Cu atom emitter in the second layer from the surface of a Cu(001) single crystal are shown in Fig. 2.7 on page 44. In addition to the electron emitter, the atomic cluster contained 160 scattering atoms, with the outermost atomic shell having a radius of $10.6\mathring{A}$. One calculation, (a), was performed using $l_{out} = 60$, a value large enough for a detector aperture of semi-angle 2.5^o according to the argument above. The other, (b), used $l_{out} = 82$, which should be large enough for a detector of perfect angular resolution shown in Fig. 2.6. For the reasons explained above that both patterns were convolved with a Gaussian of angular variance $\sigma = 2.5^o$, representing an experimental angular resolution of 2.5^o, FWHM. The diffraction patterns from these two calculations displayed in Figure 2.7 are indistinguishable to the eye. An R-factor comparison

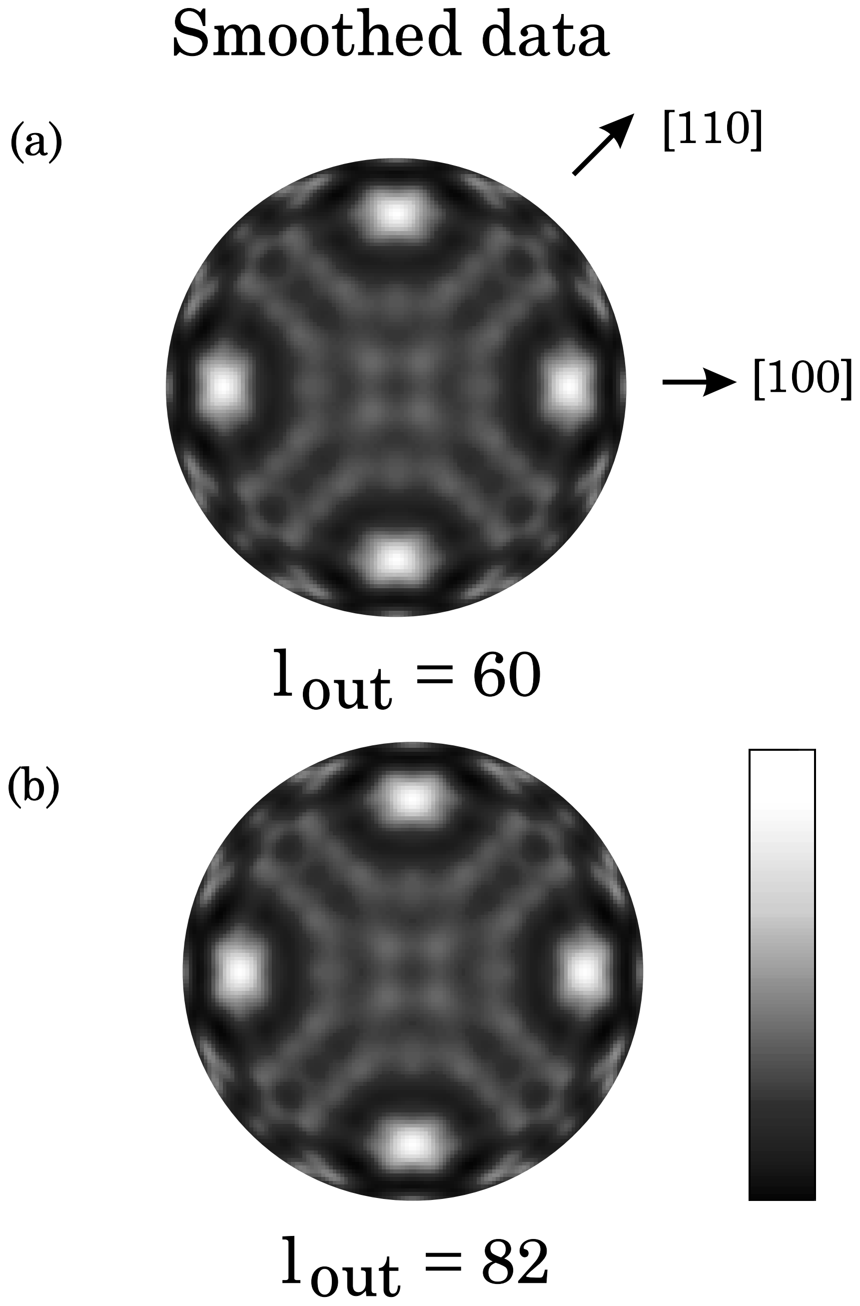

Figure 2.7: Auger diffraction calculation at an electron kinetic energy of 914 eV from a Cu emitter in the second layer of a Cu(001) surface using an angular momentum quantum number up to (a) $l_{out} = 60$, and (b) $l_{out} = 82$ with a detector aperture semi-angle of 2.5 ^{o}. These patterns are virtually identical with an R-factor of 0.0006.

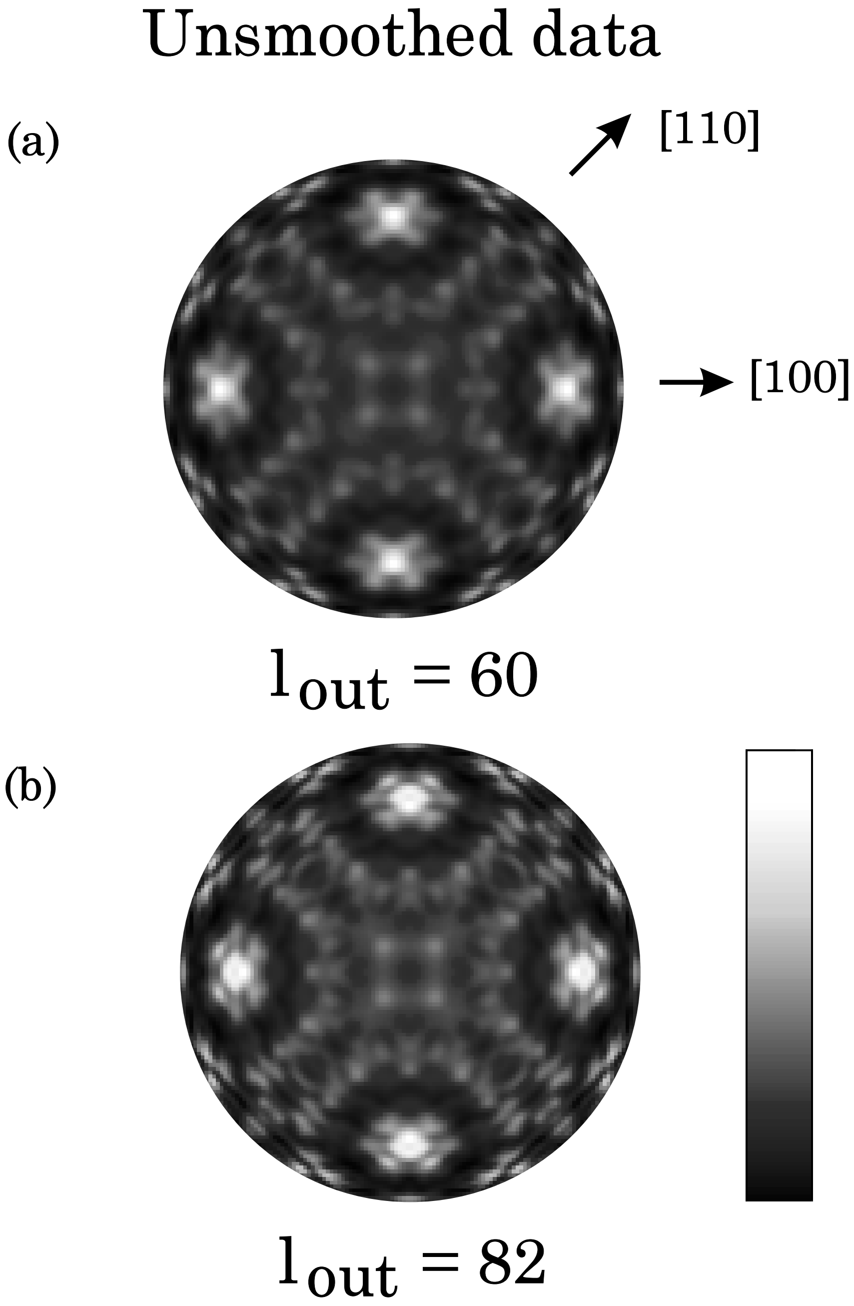

Figure 2.8: Auger diffraction calculation at an electron kinetic energy of 914 eV from a Cu emitter in the second layer of a Cu(001) surface using an angular momentum quantum number up to (a) $l_{out} = 60$, and (b) $l_{out} = 82$ without smoothing. Some difference can be observed between the two patterns with the higher l_{out} calculation (b) giving rise to more fine details in the diffraction pattern.

of the two patterns results in R = 0.0006, which is within our criterion for a valid approximation. Also shown on Fig.2.8 are the calculated diffraction patterns of $l_{out} = 60$ and $l_{out} = 82$ but without smoothing process. It is shown that considerable differences, are observed between the two patterns for the peak intensities and some fine fringes. The $l_{out} = 82$ pattern exhibits more fine details compared to the one with l_{out}=60. Those fine differences will be smoothed out if a finite aperture is present in the calculation of even larger l_{out} of 82.

2.3.4 The Forward-Scattering Approximation

For sub-surface emitters, a very convenient approximation to the full multiple-scattering scheme of Section 2.3.2 may be found. This takes advantage of the unique geometry of the concentric shells, yields calculated diffraction patterns practically indistinguishable from those from a full multiple-scattering calculation, and affords about an order of magnitude speed-up of the calculation.

The approximation is based on the fact that when a medium-energy electron is incident upon an atom, it is most likely to be scattered with a small angle close to the direction of its initial path, as is now well attested to in numerous publications, e.g. [15]. It is possible to exploit this forward-scattering behavior in the CSA in two ways: 1) by neglecting intra-shell multiple scattering, and 2) by the successive transmission approximation to inter-shell multiple scattering. The successive transmission approximation assumes that an outward traveling spherical wave incident on an atomic shell has a negligible backward scattered (i.e. inward traveling) component.

Intra-shell multiple scattering can be turned off by neglecting the intra-shell propagators $g^{ij}_{L_iL_j}$ in Eq. 8.7 above. This is equivalent to making the approximation:

$$T^{ij}_{L_iL_j} \approx t_{i,L_i}\delta_{ij}\delta_{L_iL_j}. \tag{2.39}$$

in Eq. 2.22-2.25.

The inclusion of only forward scattering in the inter-shell multiple scattering is accomplished by setting the *out-in* scattering matrices, $\mathbf{T}^{OI}_q$, equal to zero. Then the scattering matrix of the entire cluster takes on the particularly simple form:

$$\mathbf{S}^{(N)} \simeq (\mathbf{I}+\mathbf{T}^{OO}_0)(\mathbf{I}+\mathbf{T}^{OO}_1)\cdots(\mathbf{I}+\mathbf{T}^{OO}_N). \tag{2.40}$$

Note that both these simplifications, which together we term the forward-scattering approximation, avoid the matrix inversion operations necessary for the evaluation of full multiple scattering (see equations Eq. 2.18,Eq. 2.19, and Eq. 2.26 above), thus substantially reducing the computational time requirements. Nevertheless, the forward-scattering approximation includes all single-scattering events and all significant multiple-scattering pathways, particularly those which do not contain scattering angles greater than about 90^o.

In order to test the validity of the forward-scattering approximation, two calculations were performed, and the results are displayed in Figure 2.9. Both computations were for the case where a Cu atom emitter in the fourth layer of a Cu(001) single crystal. The calculations assumed an l=0 angular momentum of the initial emitted electron wave, and an electron energy of 914 eV. In Figure 2.9, the diffraction pattern labeled (a) utilized the forward-scattering approximation described above, and (b) the full multiple scattering algorithm of Section 2.3.2. The results of the two calculations appear identical to the eye. The R-factor relating the two diffraction patterns is as small as R=0.00025, demonstrating the

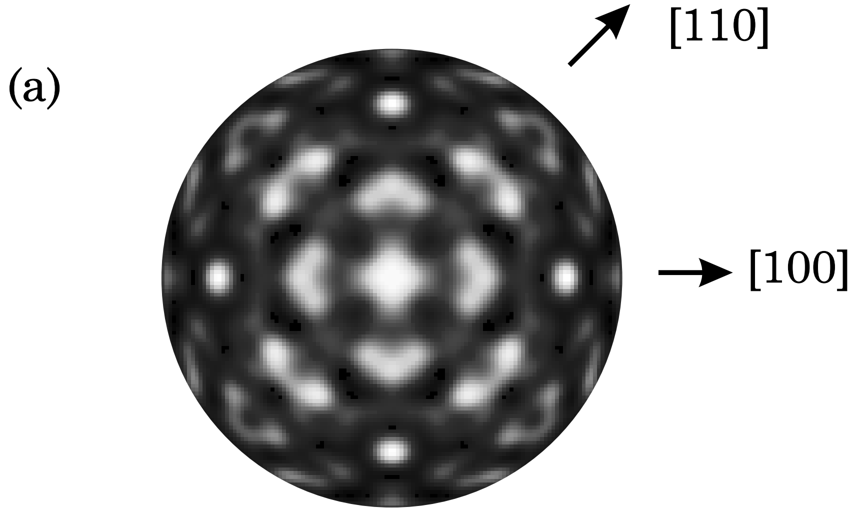

Forward scattering calc.

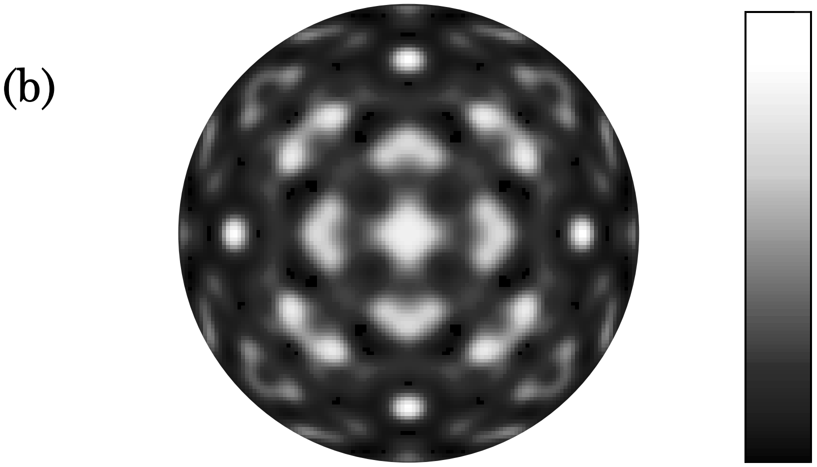

Multiple scattering calc.

Figure 2.9: Comparison of Auger electron diffraction cluster calculations at an electron kinetic energy of 914 eV for a Cu emitter in the 4th layer of a Cu(001) orientation. Pattern (a) is the result using the forward scattering approximation, and (b) is the result using the full multiple scattering. These patterns are virtually identical, with an R-factor of 0.00025.

excellence of the forward-scattering approximation for such electron kinetic energies. A single scattering calculation was also conducted and compared with the full multiple scattering result, as shown in Fig.2.10 on page 50, using a same cluster and parameters as above. It is easily seen on Figure that pattern (a) and (b) are significantly different, especially on the magnitude of the peak intensities between the two patterns, and a poor R-factor value of 0.189 indicates the break down of single scattering theory in this calculation.

2.3.5 Conclusions

We have described an algorithm for the calculation of the angular distributions of Auger, photoelectron, and Kikuchi diffraction patterns which is capable of including *exactly* the multiple scattering of the emitted electrons by a cluster of atoms surrounding the emitter. The size of the cluster is chosen to include all scattering paths which make a significant contribution to the diffraction pattern. The central quantity calculated is the single-center transmission matrix **S** of the cluster in an angular momentum basis. Once calculated, the angular variation of the diffraction pattern may be computed on an arbitrarily fine angular grid, simulating real experimental conditions, such as, the geometry of the analyzer, the x-ray incident beam and the sample position, the polarization of the x-ray photon, etc., with very little extra expenditure of effort. The same is true for calculating the diffraction patterns from different emitted electron states, a feature which we used to advantage recently [22] in determining the angular momentum state of Auger electrons by using a reliability (R) factor to compare an experimental diffraction pattern with simulated patterns due to various emitted electron states.

We have demonstrated that the maximum angular momentum quantum num-

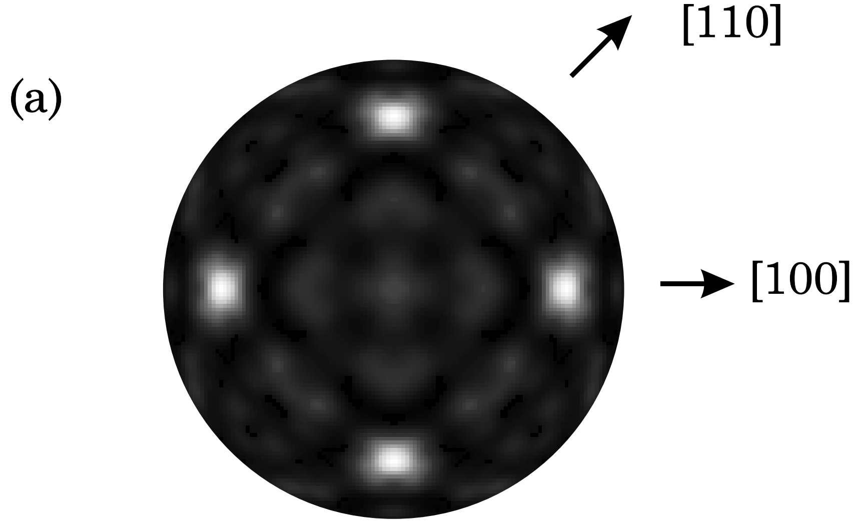

Single scattering calc.

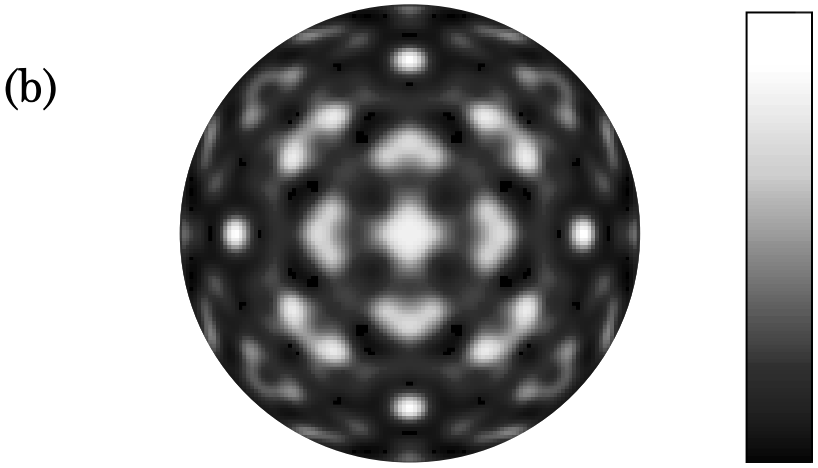

Multiple scattering calc.

Figure 2.10: Comparison of Auger electron diffraction calculations at an electron kinetic energy of 914 eV for Cu emitter in the 4th layer of a Cu(001) orientation. Pattern (a) is the result using the single scattering approximation, and (b) is the result using the full multiple scattering. Significant differences are observed between the two patterns with a poor R-factor of 0.189.

ber that is needed to carry out the calculation is l_{out}=60 for a high kinetic energy of 914 eV for a Cu emitter at the forth layer in a Cu single crystal. Any calculation of using more than $l_{out} > 60$ will result in more fine fringes in the diffraction modulations, but the R-factor (between the pattern using l_{out}=60 and that for l_{out}=82) will be very small (0.0006) after smoothing by a finite aperture semi-angle. The forward-scattering approximation of our algorithm was also tested by neglecting intra-shell multiple scattering and using the successive transmission approximation to the inter-shell multiple scattering. The R-factor for this approximation is as small as 0.0025. The single scattering cluster calculation for the same Cu cluster was carried out with the similar parameters, and a poor R-factor of 0.189 shows a significant breakdown of SSC at this energy range.

Finally, the full multiple scattering calculation of Auger diffraction from a Cu(001) surface is shown on Fig. 2.11 together with an experimental Auger KLL diffraction pattern measured by G. R. Harp *et al.* [22]. The calculated diffraction pattern contained contributions from Cu emitters in the first, second, third, fourth and fifth layers of a Cu(001) single crystal, and an f-wave emitter (angular momentum quantum number of 3) was assumed for an f-wave dominated Cu Auger KLL emission. It is demonstrated that the calculation agrees very well with the experiment and reproduces all the forward scattering features of the experiment.

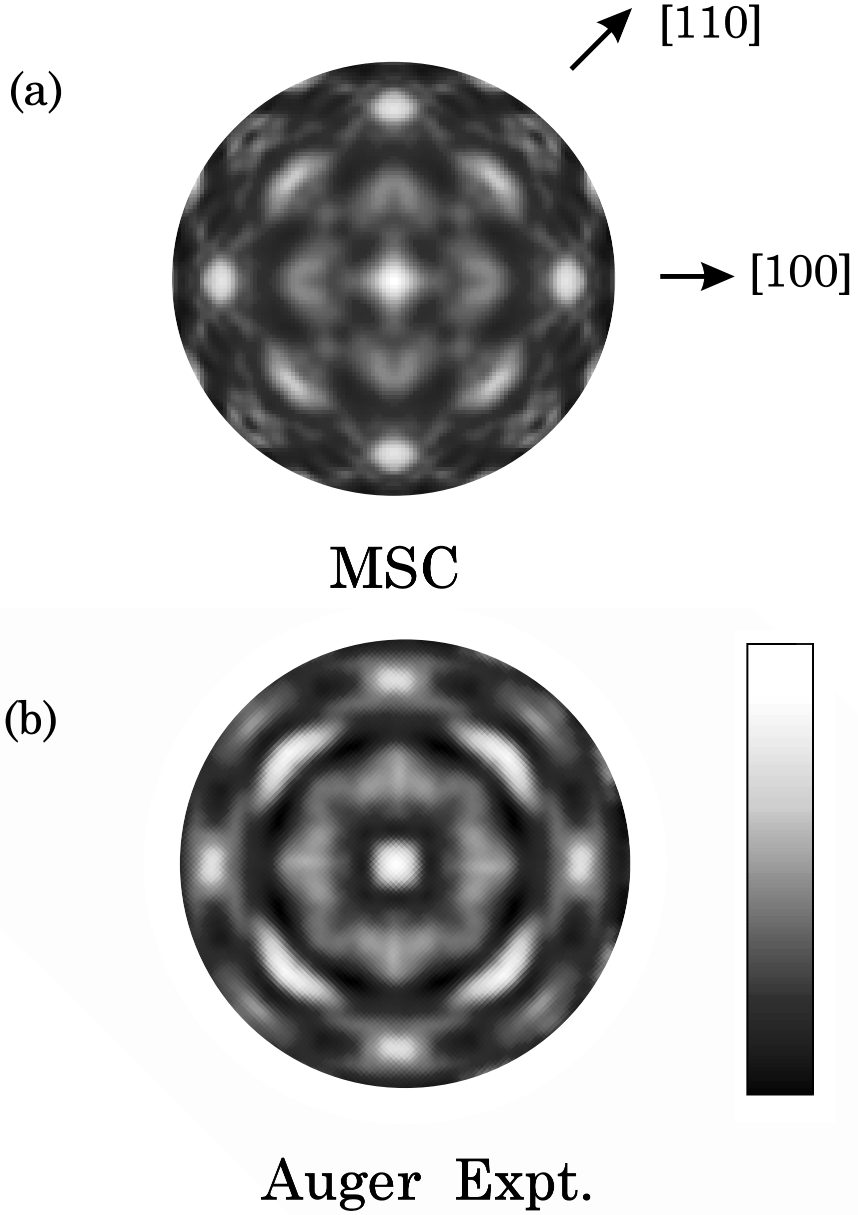

Figure 2.11: Theoretical simulation and experiments of Auger KLL diffraction from Cu(001) surface, (a) full multiple scattering calculation of f-wave emitter, and (b) experiment of Auger KLL diffraction from a Cu(001) surface measured by G. R. Harp.

Chapter 3

The Interpretation Of Angular Distribution Of Auger Electrons From Cu(001) Surface

3.1 Introduction

Auger electron and photoelectron diffraction become widely accepted as popular techniques for determining surface structures, and have proved to be sensitive tools for determination of an environment around an emitting atom. The correct interpretation of the angular distribution of Auger electron and x-ray photoelectron transitions is based on the quantum mechanical theory of electron wave scattering and interference inside the solid. This picture was challenged by Frank *et al.*'s classical "blocking" model [36] which emphasizes an electron's classical particle features in a solid. Many recent experiments and theoretical speculations raised interesting discussions on what kind of features a diffraction pattern shows at the projections of internuclear directions in the pattern. In Frank *et al.*'s experimental work [1] shown on Fig. 3.1 on page 54, complete angular intensity distributions of Auger electrons emitted from a Cu(001) surface both at the low energy 64 eV ($M_{23}VV$ transition) and the high energy 914 eV (L_3VV transition) were measured, and they showed totally different features in the patterns. It was found that the intensity is a minimum along the [001] direction in the low energy pattern, while the intensity reaches a maximum along the same direction in the high energy diffraction. Along this direction there is an atom (the next-nearest neighbor atom) directly above the emitter. In this chapter we will seek to examine the causes of the great difference in the diffraction intensity distributions at low and high electron energies . This phenomenon of the intensity minimum at low energy seems

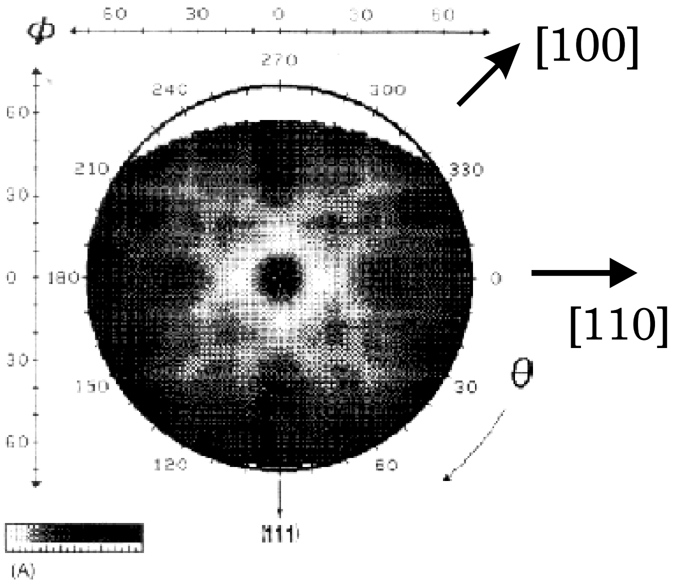

$M_{23}VV$ 64 eV

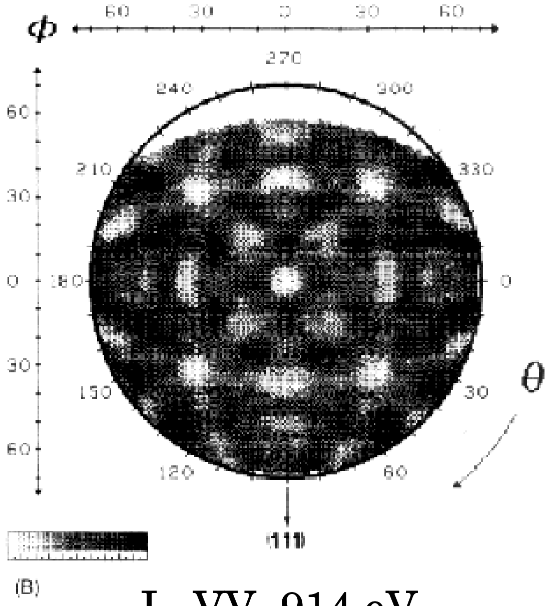

L_3VV 914 eV

Figure 3.1: Complete Auger angular distributions from Cu(001) surface at 64 eV $M_{23}VV$ and 914 eV L_3VV transition lines. Note the intensity shows minimum along the [001] direction in the low energy pattern, while intensity reaches a maximum along the same direction in high energy diffraction.

quite the contrary to the results for high electron kinetic energy where forward-scattering theory can give a satisfactory explanation to many electron diffraction experiments [22]. In order to solve this contradiction, Terminello and Barton [37] compared the Auger electron diffraction pattern of the $M_{23}M_{45}M_{45}$ Auger transition with the photoelectron diffraction of Cu $3p_{3/2}$ photoemission from a Cu(001) surface for a similar energy of 56.6 eV. In their experiments, the Auger pattern show an intensity minimum at the normal direction [001] while the photoelectron diffraction shows a maximum along the same direction. This evidence strongly suggests that the character of the emitter source waves plays an important role in the resulting diffraction. A single-scattering model has been used to explain the above phenomena [40,**?**] and preliminary results were obtained, but a full multiple scattering theory is still needed in order to reach a convincing conclusion.

In this chapter, we address some of the recent controversies regarding the interpretation of Auger electron diffraction patterns by simulating those from the 64 eV $M_{2,3}VV$ and the 914 eV L_3VV lines from a Cu(001) surface. The lower-energy Auger electron diffraction pattern, in particular, is found to be strongly dependent on the angular momentum l of the emitted Auger electrons, which is in agreement with the observations of some other authors. However, it was found that *both* peaks and dips are observed on the *same* diffraction pattern at the projections of different atomic rows, indicating that the angular momentum of the source wave cannot be the only determinant of these features. The distance of the scatterer from the source, as well as overlap and interference effects from scatterers in other atomic rows are equally important determining factors. On comparing our simulations with the experimental diffraction patterns, it was found that, for an $l = 3$ source wave (f-wave emitter), the simulations agree remarkably well with the data from both Auger lines.

3.2 Interpretation of Auger angular distribution and Blocking model

Auger electron diffraction has proved to be a powerful and convenient tool for the investigation of the structures of surfaces and thin films [33,?,?,?]. When the electron ejected by the atomic emission process has an energy of the order of 500 eV or above, the diffraction pattern tends to be dominated by strong peaks at the projections of atomic rows radiating from a source atom in a crystalline sample, as a result of the strong forward-scattering nature of atomic scattering factors. Thus, crystallographic information may be gleaned from such a diffraction pattern even without the need for theoretical simulations of the patterns. In addition the specificity of the diffraction patterns to the chemical species of the emitter enables the structure around each different type of atom to be deduced independently.

When the ejected electrons are emitted at lower energies, the interpretation of the diffraction patterns is much more complex. From their observations of low-energy Auger diffraction patterns from Pt and Cu surfaces, Frank *et al.* [36,?] have claimed that forward-scattering directions are dominated by dips of intensity according to a classical "blocking" or "silhouette" model. They indicated in their paper that the anisotropic Auger diffraction patterns from the surfaces *have been mistakenly attributed to anisotropic emission from individual atoms, to diffraction, to multiple scattering or to a combination of these effects* in previous works. They claimed that the measured angular distribution of Auger electrons at 65 eV kinetic energy emitted from a bare Pt(111) surface, as shown in Fig. 3.2 on page 57 [36], contains the "silhouettes" of near-surface atoms "back lit " by Auger emission

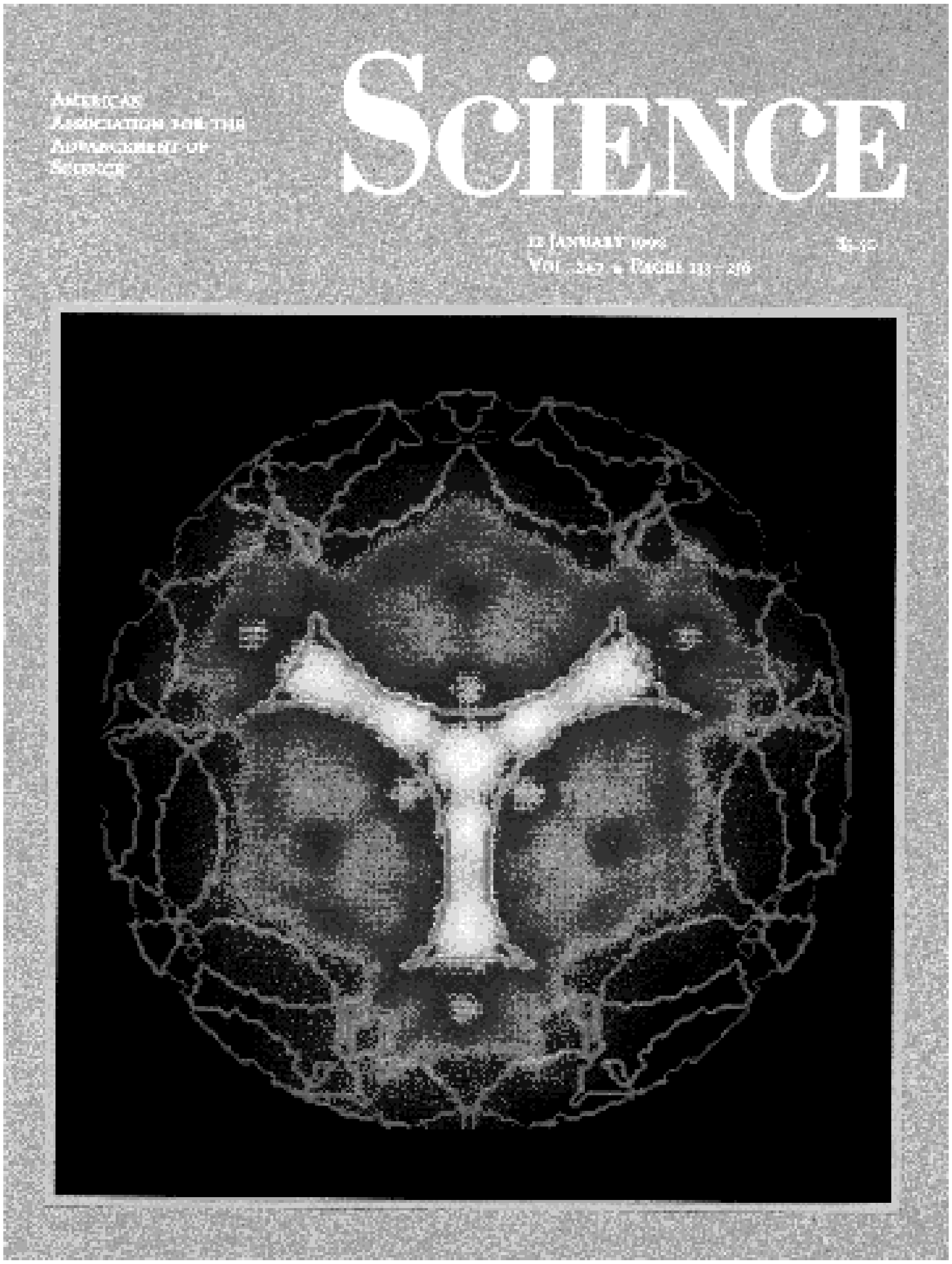

American
Association for the
Advancement of
Science

SCIENCE

Figure 3.2: The experimental Auger electron angular distribution from a Pt(111) surface at 65 eV measured by Frank *et al.* [36]. Theoretical simulation contours based on “blocking” model show the “Y”-shaped region in the center from which the authors claimed that Auger electrons behave like classical particles in a solid.

originating from atoms deeper in the solid. They further proposed the "blocking" model, a theory based upon isotropic Auger electron emission from atomic point-emitters and scattering by spherical atomic scatterer of uniform cross section. All the Pt atoms near the surface act as emitters and scatterers, or in other words, the emitters were assumed to be located in the first, second, third layer, and so on, and the atoms above the emitters were assumed to block the emitted Auger electrons from reaching the detector, thereby causing the angular variations in the diffraction pattern. Accordingly, the simulation multiplies the attenuation due to each scatterer encountered along the path to the detector, and sums the contributions from all layers of atoms. Theoretical simulation contours based on the "blocking" model show the "Y"-shaped region in the center and agrees "well" with the experiment on Fig. 3.2, and with this evidence the authors inferred a considerable breakdown of the quantum mechanical theory in the solid for the Auger electron, and that a classical picture of Auger electron can "well" explain the experiment. The best agreement between experiment and their theory occurs when the radii of the scatterers were taken to be 60 to 90 percent of their atomic radii, and the scatterers 40 percent transparent.

In fact, as have been pointed out by others, there is no reason to doubt the ability of a proper quantum mechanical theory to explain all the observed phenomena at both high and low energies. An explanation of the forward-scattering dips observed by Frank *et al.* [36,**?**] has been given by Barton and Terminello [37,**?**], in terms of the extra angular momentum barrier at the emitting atom as seen by an ejected electron of high angular momentum. Idzerda and Ramaker [39] and Greber *et al.* [40] have simulated such diffraction patterns with single-scattering model. However, low energy electrons are known to suffer strong multiple scattering, and it is important to examine its effects on such diffraction patterns. We present here the results of our full multiple-scattering simulations of the 64 eV $M_{23}VV$ and the 914 eV L_3VV Auger diffraction pattern from a Cu(001) surface and compare them with the experimental Auger angular distribution, measured by Frank *et al.* [1] as shown on Fig 3.1 on page 54. The simulations in the following sections are performed by the full multiple-scattering concentric-shell algorithm developed recently by Saldin, Harp and Chen [32]. We compare our simulations with both the experimental diffraction patterns of Frank *et al.* [1], and the simulations by those authors of the same patterns, based on their "shadowing" or "blocking" model. The implications of our calculations on the recent controversies regarding the interpretation of Auger diffraction patterns in general will also be discussed.

3.3 Simulation of Auger electron diffraction patterns from a Cu(001) surface

The concentric shell algorithm developed by Saldin, Harp and Chen [32], employs a muffin-tin model of the internal potential of the solid. The phase shifts were calculated by the MUFPOT program, from atomic potentials taken from the book by Moruzzi, Janak and Williams [41]. The multiple scattering of an electron emitted from each inequivalent atom near the surface was evaluated separately by constructing a cluster of atoms around each emitter divided into a set of concentric shells. Up to 16 atomic shells containing 396 scattering atoms were included in our calculation. Emitters in layers deep within the solid contribute less to the diffraction pattern, due to the small inelastic scattering length of the electrons. For our simulations we took account of emitting atoms in the first five layers from the surface.

In the case of a Cu(001) surface all atoms in any particular layer have identical local surroundings and an electron emitted from any one of them would give rise to the same diffraction pattern. Emitters in different layers generate different patterns. The contribution to the final diffraction pattern from an atom in layer J from the surface is taken as

$$I_A^J(\mathbf{k}) = \sum_l \sum_m |A_{lm}^{(0)} \sum_{l'm'} \mathcal{S}_{lm;l'm'}^{(N)}(J)(-i)^{l'} Y_{l'm'}(\hat{\mathbf{k}})|^2 \exp\{-a(J)/\lambda \cos(\theta)\} \tag{3.1}$$

where the amplitudes, $A_{lm}^{(0)}$, of the emitted waves of different magnetic quantum numbers m corresponding to a particular azimuthal quantum number l are taken to be equal, and represented by $A_l^{(0)}$. Taking a pure f-wave emitter for the Auger electron diffraction simulation, for example, the initial wave functions are composed of 7 components, they are $Y_{3\bar{3}}$, $Y_{3\bar{2}}$, $Y_{3\bar{1}}$, Y_{30}, Y_{31}, Y_{32}, and Y_{33}. We assigned each wave component, Y_{3m}, equal weight, i.e.,

$$A_{lm}^{(0)} = A_l^{(0)} = \delta_{l3}$$

and the total intensity arising from those initial wave functions will be the intensity summation of each component, i.e. added incoherently. This is consistent with the usual assumption that in Auger emission, the final ejected electron has lost any memory of the initial excitation process, and thus emerges from an atom with an overall isotropic angular distribution. The emitted waves of angular momentum components l, m are taken to be incoherent with respect to each other. The quantities $\mathcal{S}_{lm;l'm'}^{(N)}(J)$ are the elements of the transmission matrix of a cluster of N concentric shells around an emitter in the J th layer from the surface, and Y_{lm} is a spherical harmonic function. The exponential factor represents the inelastic attenuation of an Auger electron emitted from an atom in the J th layer of depth $a(J)$ from the surface, λ the electron's inelastic scattering length, and θ the angle between **k** and the surface normal.

Angular wave functions of the emitted Auger electron, with the angular momentum quantum number of l=0, 1, 2, and 3, and m=-l, ..., l, which represents the s, p, d, and f orbitals, are listed on Table 3.1 on page 62, and the corresponding electron density distributions in the x-z and y-z planes are shown in Fig. 3.3 on page 63.

3.3.1 The 64 eV $M_{2,3}VV$ Auger pattern

The quantities $A_{lm}^{(0)}$ (=$A_l^{(0)}$) in Eq. 3.1 are the matrix elements of the atomic Auger process. We are unaware of any calculations of these quantities for the 64 eV Cu $M_{2,3}VV$ Auger line, and accordingly simulate several different model Auger diffraction patterns taking the quantities A_l individually equal to unity with all the others zero. That is we used a full multiple-scattering theory to simulate separately the Auger diffraction patterns arising from emitted electrons initially in angular momentum states of $l = 0$, 1, 2, 3, 4 or 5, corresponding to s, p, d, f, g and h-wave emitters, respectively. The results of the simulations are shown on Fig. 3.4 on page 65. The upper panel on Fig. 3.1 on page 54 displays the corresponding experimental diffraction pattern, measured by Frank et al., and reproduced from their paper [1]. Comparison of the measured Auger angular distribution with the simulations shows that none of the patterns agree well with the measured data, except that for the f-wave emitter, which agrees extraordinarily well. It is shown that the simulation with an f-wave emitter produces a major dip along sample normal direction and dips along most low-index crystallographic directions, except along <101> directions where peaks appear. It is also shown that different source waves produce totally different diffraction patterns at low energy, and that

Table 3.1: Angular wave functions of s, p, d, and f orbitals in angular momentum representation

L= (lm)	Orb. Type	Spherical Harmonic Function $Y_{lm}(\theta, \phi)$	$r^l Y_{lm}(\theta, \phi)$
00	s	$1/\sqrt{4\pi}$	$1/\sqrt{4\pi}$
10	p	$\sqrt{3/4\pi} cos\theta$	$\sqrt{3/4\pi} z$
1±1	p	$\mp\sqrt{3/8\pi} sin\theta e^{\pm i\phi}$	$\mp\sqrt{3/8\pi}(x \pm iy)$
20	d	$\sqrt{5/16\pi}(3cos^2\theta - 1)$	$\sqrt{5/16\pi}(2z^2 - x^2 - y^2)$
2±1	d	$\mp\sqrt{15/8\pi} cos\theta sin\theta e^{\pm i\phi}$	$\mp\sqrt{15/8\pi}(x \pm iy)z$
2±2	d	$\frac{1}{2}\sqrt{15/8\pi} sin^2\theta e^{\pm 2i\phi}$	$\frac{1}{2}\sqrt{15/8\pi}(x \pm iy)^2$
30	f	$\frac{1}{4}\sqrt{7/\pi}(5cos^3\theta - 3cos\theta)$	$\frac{1}{4}\sqrt{7/\pi}(2z^2 - 3x^2 - 3y^2)z$
3±1	f	$\mp\frac{1}{8}\sqrt{21/\pi}(5cos^2\theta - 1)sin\theta e^{\pm i\phi}$	$\mp\frac{1}{8}\sqrt{21/\pi}(4z^2 - x^2 - y^2)(x \pm iy)$
3±2	f	$\frac{1}{4}\sqrt{105/2\pi} sin^2\theta cos\theta e^{\pm 2i\phi}$	$\frac{1}{4}\sqrt{105/2\pi}(x \pm iy)^2 z$
3±3	f	$\mp\frac{1}{8}\sqrt{35/\pi} sin^3\theta e^{\pm 3i\phi}$	$\mp\frac{1}{8}\sqrt{35/\pi}(x \pm iy)^3$

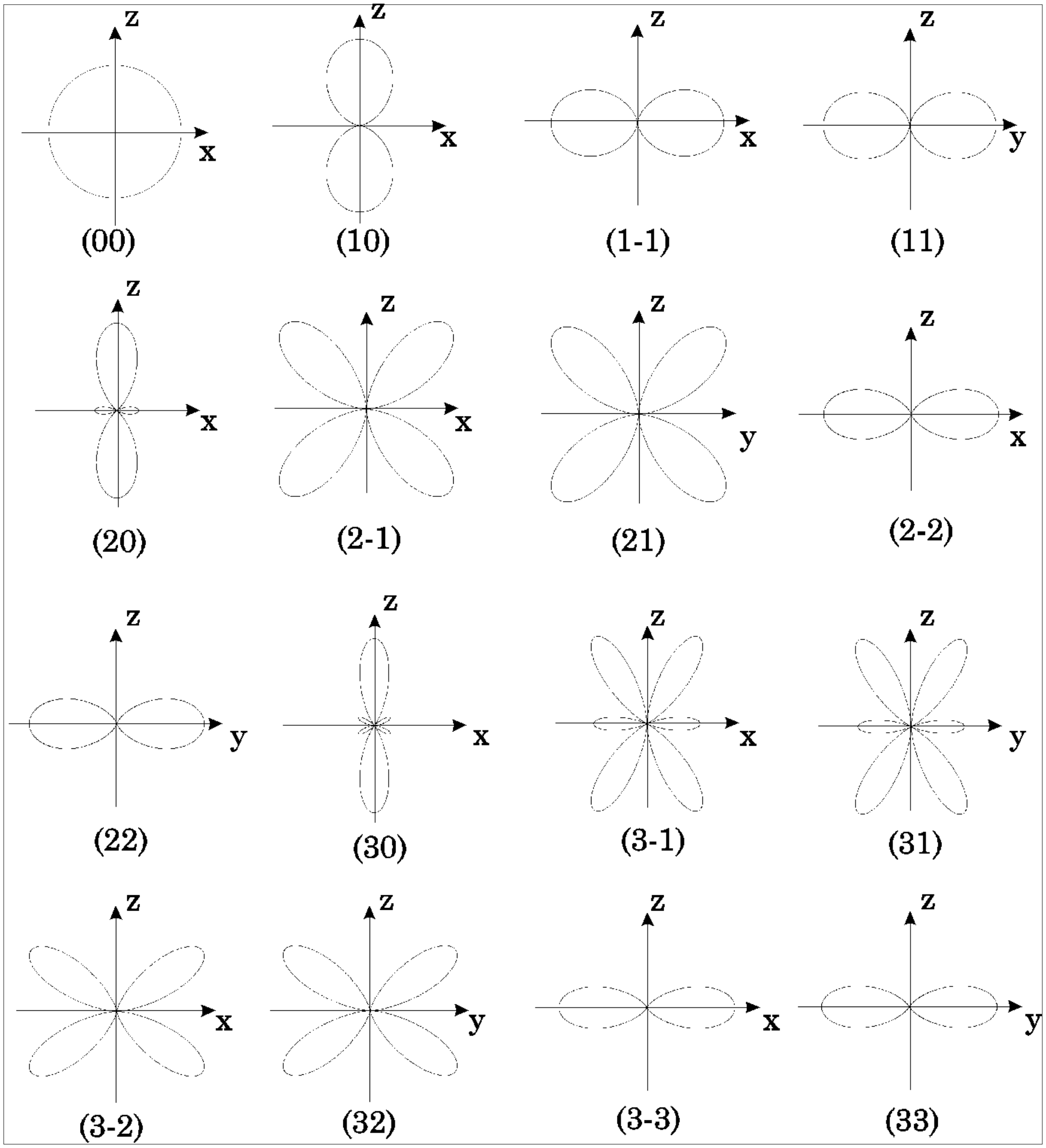

Figure 3.3: Schematic diagrams of angular wave functions of s, p, d, and f orbitals in Table 3.1, where the angular momentum quantum numbers are shown within the parentheses. Note the above wave function plots are of the intensity and shown along the x-z plane and the y-z plane.

is why there is no direct correlation of electron diffraction pattern with the surface structure as for the high energy diffraction patterns.

On the question of whether the diffraction pattern should manifest a peak or a dip in the direction normal to the surface, our simulations clearly bear out the conclusions of Barton and Terminello [37,?] that this is a function of the angular momentum of the emitted electron, with the lower angular momenta (the s, p and d) appearing to show a region of relatively high intensity in this direction, while the f, g and h angular momenta clearly displaying significantly lower intensity in these directions.

However, we find evidence that the angular momentum of the emitted wave is not the only factor determining whether a peak or dip appears at the projection of an atomic row radiating from the emitter. This is most clearly illustrated by Fig. 3.5 on page 66, which depicts polar-angle profiles of the f-wave diffraction pattern along the [100] and [110] azimuths. It reveals the intensity minimum at the projection of the [001] surface normal and close to those of the [103], [112] and [111] atomic rows, but a maximum close to the [101] projection. It should be noted that the latter peak is also present on the corresponding experimental diffraction pattern of Frank *et al.* [1], shown on Fig. 3.1, although not commented upon by those authors.

From these observations, one may immediately draw several conclusions:
(1) that the 64 eV Cu(001) Auger diffraction patterns of Frank *et al.* [1] are reproducible almost exactly by an elastic multiple-scattering theory, without the need for the “shadowing” or “blocking” mechanism postulated by those authors.
(2) there does not seem to be a general rule about whether, in the direction of a scatterer, one would expect an intensity peak or a dip.

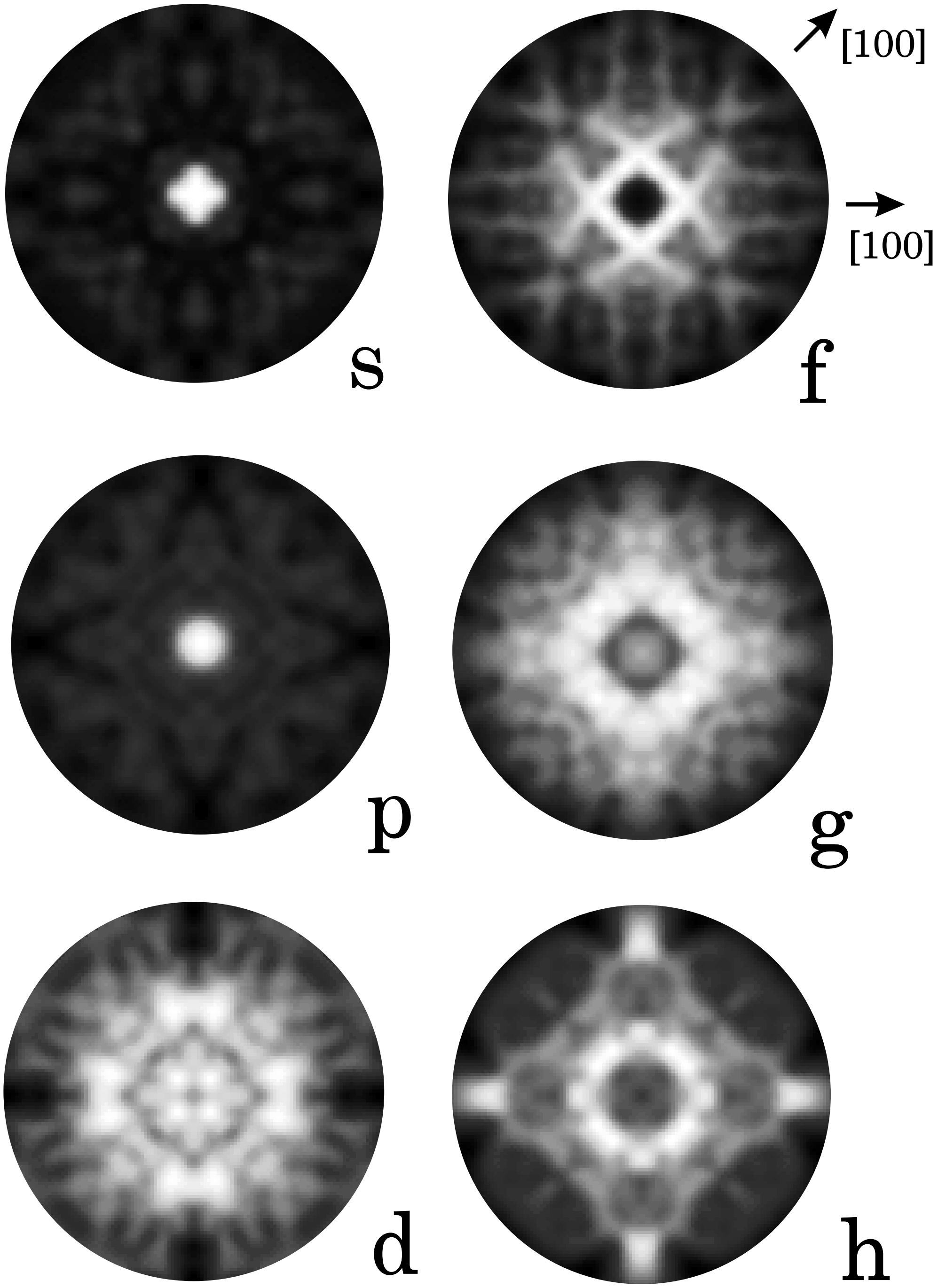

Figure 3.4: Full multiple-scattering simulations of the electron diffraction from Cu(001) surface at 64 eV for emitted Auger electrons of angular momentum l=0, 1, 2, 3, 4, or 5 (corresponding to s-, p-, d-, f-, g-, or h-wave emitters, respectively). Note the differences between the simulated patterns are pronounced for the different emitter waves, and the 64 eV $M_{23}VV$ experiment measured by Frank *et al.* [1] as shown in the upper panel on Fig. 3.1, was reproduce by f-wave simulation.

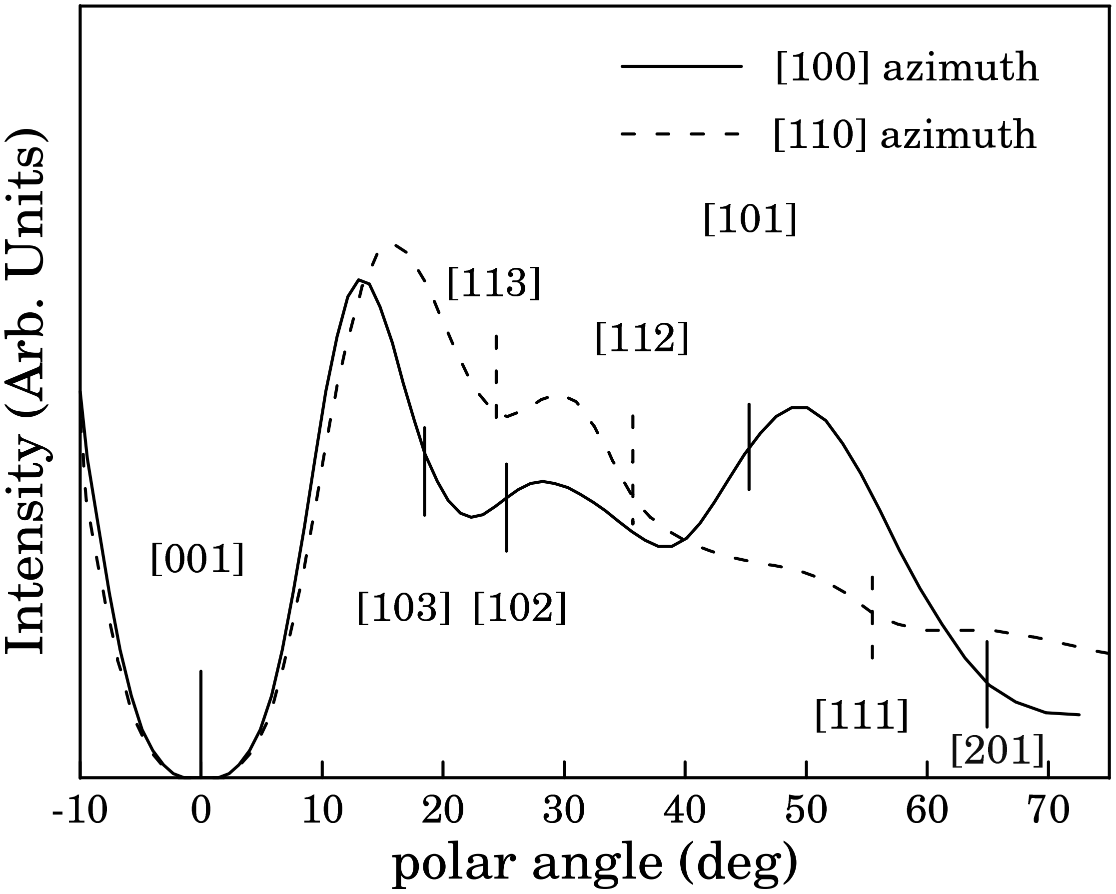

Figure 3.5: Polar-angle profiles of the 64 eV f-wave simulation of Fig. 3.4 along two major azimuths of [100] and [110] directions. Note that a large dip is observed at [001] direction and some other intensity dips close to the projections of most low index atomic rows, but a peak close to the [101] projection which is along the emitter-nearest-neighbor-atom direction.

(3) in agreement with the conclusions of Barton and Terminello [37,?] we find that a factor determining a peak or a dip is the angular momentum of the emitted electron.

(4) but it appears that the latter is not the only determining factor, for a dip appears on the diffraction pattern at the projection of the surface normal, but not at that corresponding to nearest-neighbor vectors in the structure.

In trying to understand these rather complicated results, we first check whether they are particularly a consequence of the fact that electrons of such energies must be expected to suffer rather large amounts of multiple scattering. Accordingly, we re-calculate the diffraction patterns of Fig. 3.4. with the same computer programs, but with the multiple scattering switched off (i.e. diffraction patterns which would be expected on the basis of kinematical, or single scattering of the same Auger electrons). The results are shown on Fig. 3.6 on page 68. It will be seen that although, as expected, there are noticeable differences between the corresponding patterns of Figs. 3.4 and 3.6, the kinematic simulated pattern is also a function of the angular momentum of the source wave, and the patterns with higher angular momenta also show an intensity dip in sample normal direction. Thus, the general conclusions (1) to (4) above remain valid, even for the single-scattering pattern.

3.3.2 The 914 eV $L_{23}VV$ pattern

The paper by Frank *et al.* [1] also contains measured diffraction patterns, from a Cu(001) surface, of the 914 eV $L_{2,3}VV$ Auger line, as shown on the lower panel of Fig. 3.1, together with the results of their simulations of these patterns on a classical particle channeling model. As in the case of 64 eV $M_{2,3}VV$ diffraction

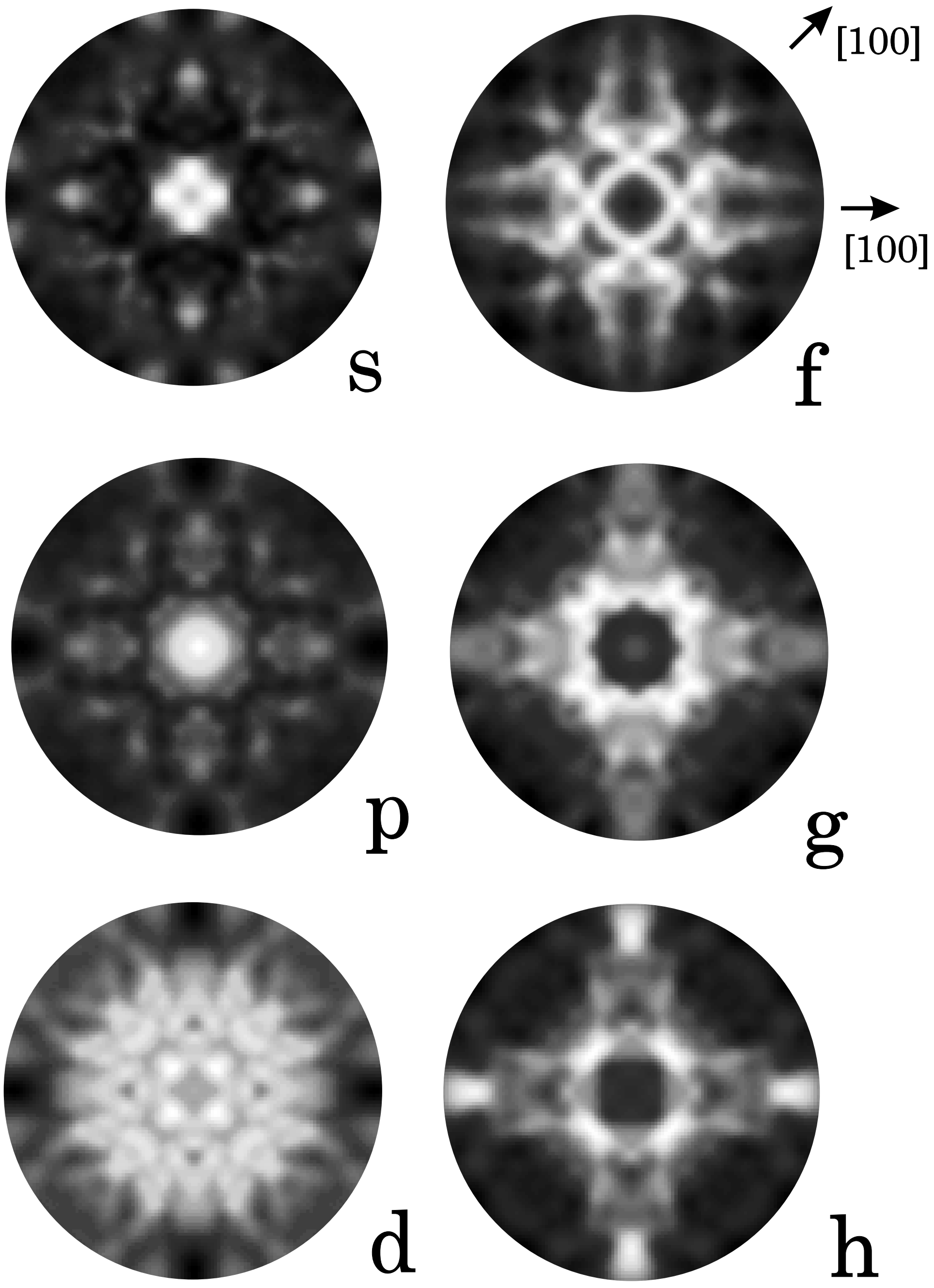

Figure 3.6: Simulations of the electron diffraction from Cu(001) surface at 64 eV for emitted Auger electrons of angular momentum l=0, 1, 2, 3, 4, or 5 (corresponding to s-, p-, d-, f-, g-, or h-wave emitters, respectively), for only single-scattering processes were allowed. They are quite different from the full multiple-scattering simulations shown in Fig. 3.4.

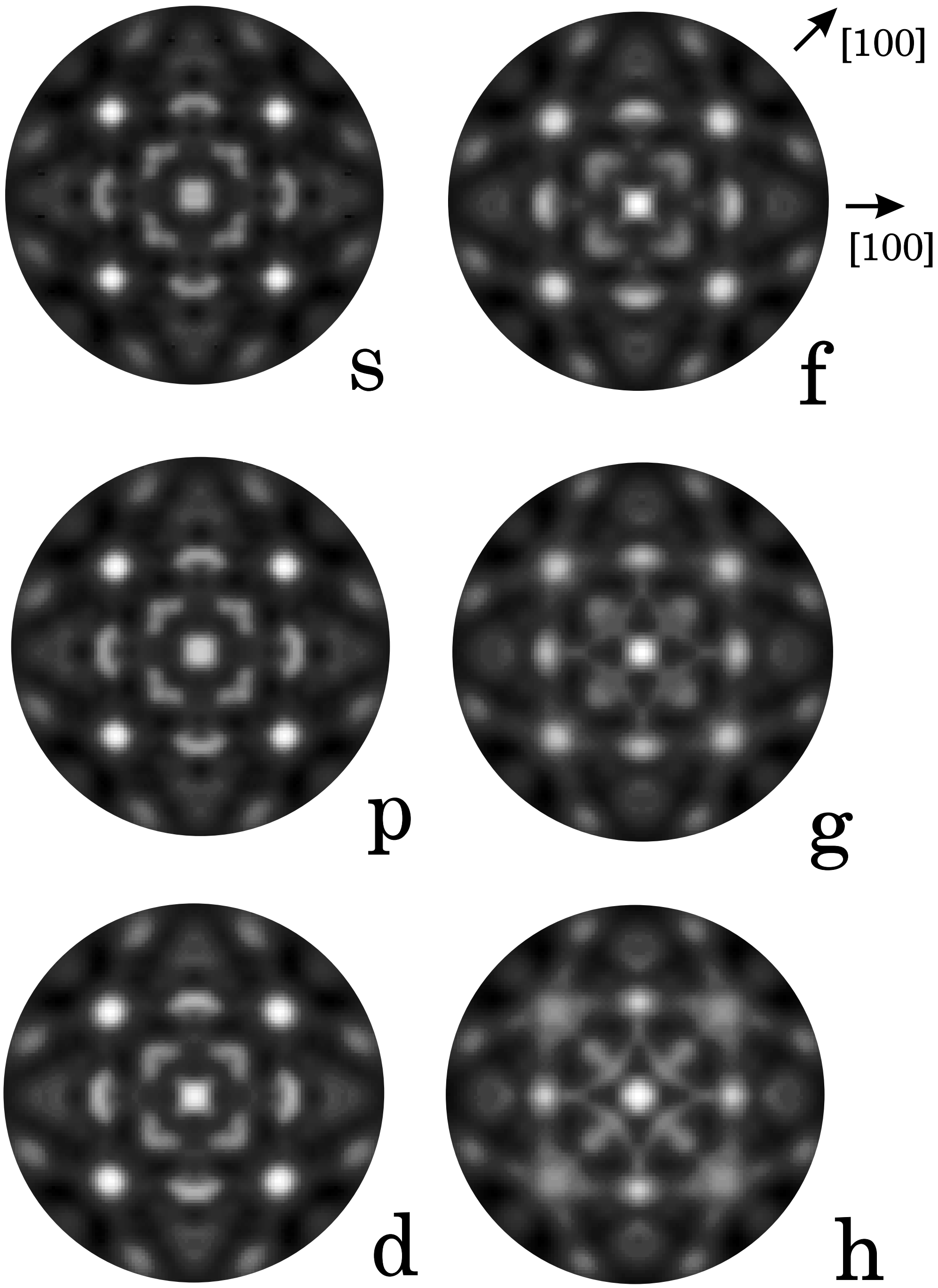

Figure 3.7: Full multiple-scattering simulations of the electron diffraction from a Cu(001) surface at 914 eV for emitted Auger electrons of angular momentum l=0, 1, 2, 3, 4, or 5 (s-, p-, d-, f-, g-, or h-wave emitters, respectively). The differences between the simulated patterns are much less pronounced than those of Fig. 3.4.

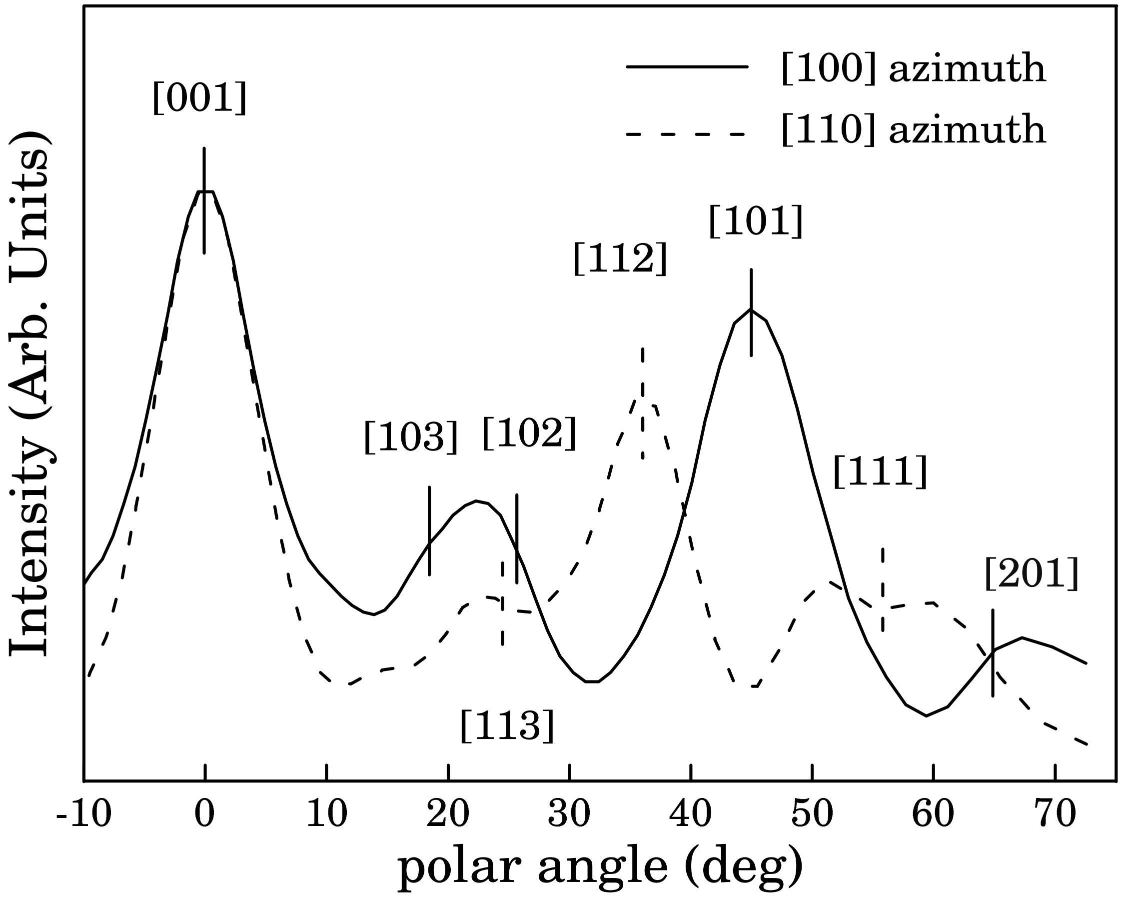

Figure 3.8: Polar-angle profiles of the 914 eV f-wave diffraction simulation of Fig. 3.7 along the two major azimuths of [100] and [110]. Intensity peaks are seen close to the projections of all low-index rows which shows the main feature of the electron forward-scattering theory.

pattern discussed above, we have performed multiple-scattering calculations for Auger electron diffraction from the Cu(001) surface at 914 eV, as shown Fig. 3.7 on page 69, assuming six different choices of emitted electron angular momenta, namely: l=0, 1, 2, 3, 4 and 5, corresponding to s, p, d, f, g and h-waves, respectively. It will be seen that, unlike the low-energy Auger patterns of Fig. 3.4, all the simulated diffraction patterns of Fig. 3.7 are dominated by the strong forward-scattering of the atomic scattering factors at such energies, and the projections of all the crystal atomic rows appear to be illuminated by spots of high intensity. This is a feature also of the experimental Auger angular distribution from a Cu(001) surface from 914 eV $L_{2,3}VV$ Auger line also measured by Frank *et al.* This is clearly illustrated by the plot of the intensity of the f-wave diffraction pattern along two major azimuths [100] and [110], as shown on Fig. 3.8 on page 70. It is seen that the diffraction intensity is peaked at along all the low-index crystallographic directions in the sample.

Due to the dominance of the forward-scattering effect, however, the variations between the different diffraction patterns of Fig. 3.7 are much less pronounced than those of the low energy patterns of Fig. 3.4. In fact, the angular distribution of the 914 eV L_3VV Auger transition from a Cu(001) surface has also been measured by Tonner and co-workers [22], and we have compared their measured diffraction pattern with our simulations by means of the reliability (R) factor

$$R(l) = \frac{\sum_i [E_i - S_i(l)]^2}{\sum_i E_i^2} \tag{3.2}$$

where the E_i represent the experimental data and $S_i(l)$ the simulated data for the Auger emitter of angular momentum l. The summations were taken over all available experimental data points i. Fig. 3.9 on page 72, shows that a minimum in the R-factor plot is found for the l=3 source angular momentum state.

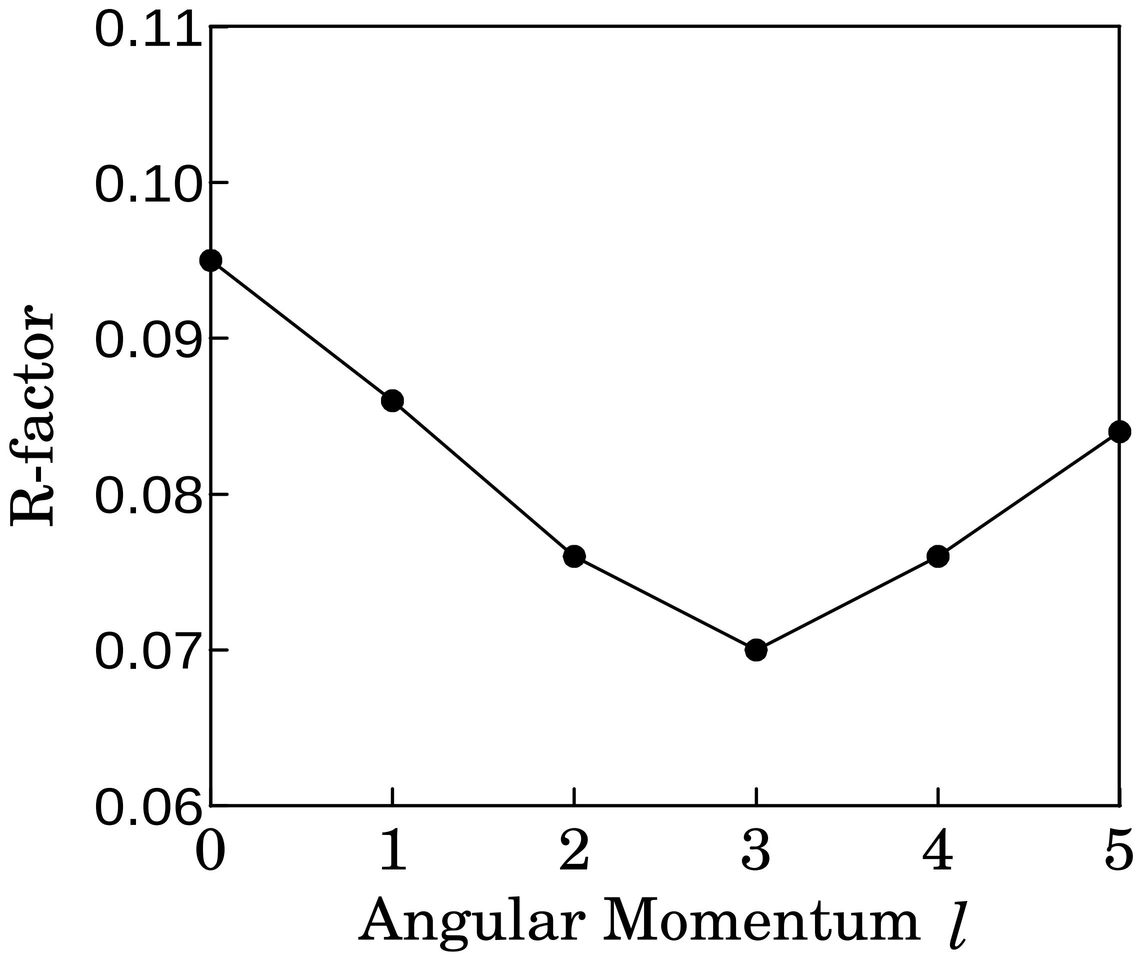

Figure 3.9: R-factor comparison of the experimental Auger L_3VV electron diffraction and the simulations for the different source waves of angular momenta l=0, 1, 2, 3, 4, and 5. The minimum (best fit) is seen for the f-wave emitter (l=3).

3.4 Discussion

3.4.1 Comparison with experimental patterns and simulations of Frank *et al.*

On Fig. 3.10 on page 75, we reproduce for a closer comparison, the experimental Cu(001) 64 eV $M_{2,3}VV$ Auger diffraction (upper panel) of Frank *et al.* [1], their simulation of "blocking" model (lower right panel) of the same pattern, also from the same paper, and our multiple-scattering simulation (lower left panel) for the f-wave emitter at 64 eV. It is obvious that the multiple-scattering cluster model agrees much better with the experimental data at this low energy. It should be noted that in our 64 eV f-wave Auger electron diffraction simulation, pattern shows mostly dips along the low-index crystallographic directions, except for a peak that apears close to the [101] direction which joins the emitter and the nearest neighbor atom direction. This intensity enhencement is also found on the measured experimental pattern at low energy. On Fig. 3.11 on page 76 we show the corresponding comparisons for the 914 eV L_3VV Auger patterns with the experimental pattern and "channeling" model simulation by Frank *et al.*, and our multiple-scattering simulation, shown on the upper panel, lower right, and lower left, respectively. In our simulations of both energies, we used *exactly* the same computer program for the simulation of both Auger diffraction patterns. Thus the differences between the two multiple-scattering simulated patterns are ascribable *only* to the different energies of the Auger electrons in the two cases, while the "blocking" model has to be supplemented by including a "channeling" effect to obtain the high energy angular distribution pattern instead of the "back" lit effect at low energy.

From both Fig. 3.10 and Fig. 3.11, we can draw an obvious conclusion that multiple-scattering simulations reproduce all the features of the experiments. For the low energy Auger diffraction pattern, the correctly chosen source wave angular momentum of the emitter is crucial, while for high energy Auger diffraction pattern an s-wave emitter simulation could reproduce fairly well the experiment, but an f-wave source simulation would result in a the smallest R-factor when compared with the experiment. We can also see that although the "blocking" model simulation at low energy could barely "reproduce" some features of the experiment, namely the center dip, it failel to predict the <101> peaks at the projections of the emitter-nearest-neighbor directions, in the low energy experiment. The "channeling" model simulation at high energy totally fails to reproduce the experimental diffraction pattern.

3.4.2 Dominance of the f-wave channel for the two diffraction patterns examined

As mentioned above, both the 64 eV $M_{2,3}VV$ and the 914 eV L_3VV Auger diffraction patterns appear to be best simulated by source waves of $l = 3$ or f-wave character. We point out that this is consistent with the earlier findings of several different groups.

For example, Weissmann and Müller [42,43] have drawn attention to the fact that the angular momentum l of an Auger electron emitted from an atom is subject to selection rules summarized by the relations

$$|l_i - |l_j - l_k|| \quad \leq \quad l \quad \leq \quad l_j + l_k + l_i \tag{3.3}$$

and

$$l_j + l_i + l_k + l = \text{even} \tag{3.4}$$

where l_i represents the angular momentum quantum number of the initial core

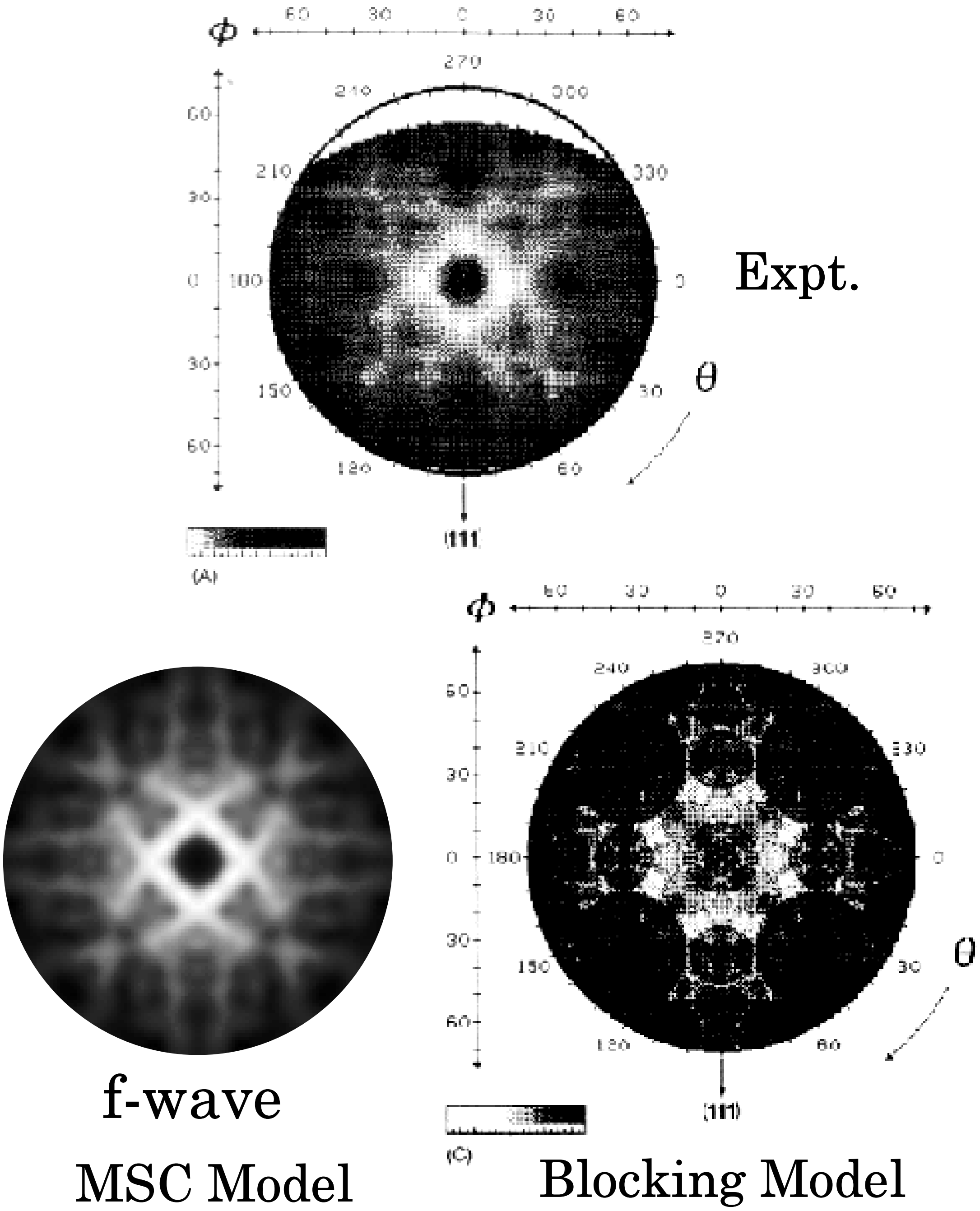

Figure 3.10: Comparison of the measured Cu(001) 64 eV $M_{23}LL$ Auger electron angular distribution of Frank *et al.* [1](upper panel) with their blocking model simulation(right pattern in lower panel), and our f-wave multiple-scattering cluster simulation(left pattern in lower panel).

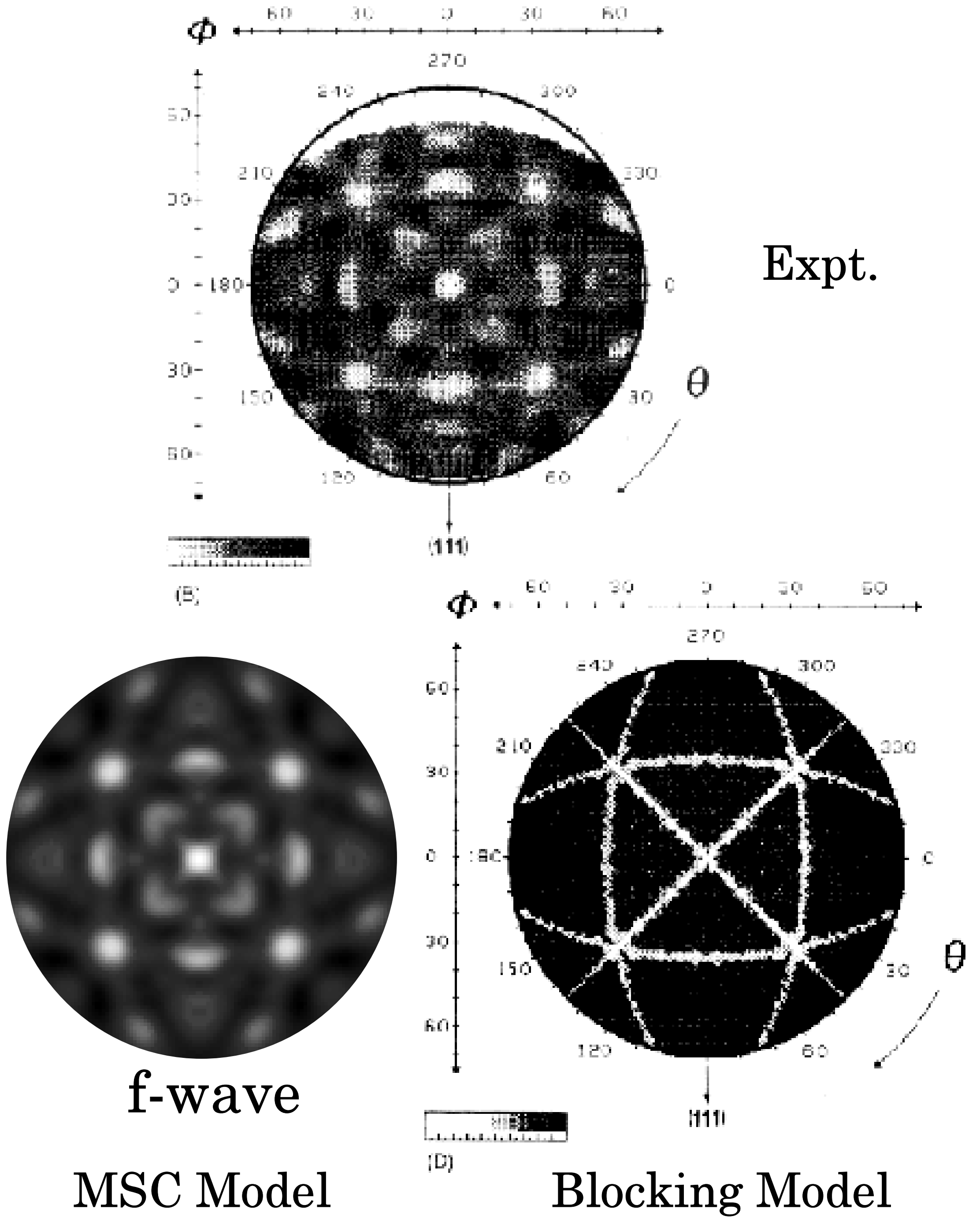

Figure 3.11: Comparison of the measured Cu(001) 914 eV K_3LL Auger electron angular distribution of Frank *et al.* [1](upper panel) with their blocking model simulation(right pattern in lower panel), and our f-wave multiple-scattering cluster simulation(left pattern in lower panel).

hole, and l_j, l_k represent those of the final-state holes, and l that of the emitted wave. In the cases of either an $L_{2,3}VV$ or an $M_{2,3}VV$ Auger transition, the initial core hole is a p-state, and corresponds to an $l_i = 1$ state. In the case of both transitions considered here, the final-state holes are primarily associated with the transition-metal d states which tend to be localized on the atomic sites. Thus we may take $l_j = l_k = 2$. On substituting these values into (3.3) and (3.4), some simple arithmetic shows that the angular momentum of the ejected Auger electron may take on only one of the following allowed values:

$$l = 1, \quad 3 \text{ or } 5. \tag{3.5}$$

In his comparisons of line profiles of measurements of the 64 eV $M_{2,3}VV$ Cu(001) Auger diffraction pattern with his model calculations, Davis [44] also found best fit for a source wave with $l = 3$.

A theoretical calculation [39] using proper radial matrix elements and the table given by Cherkendorff [45] shows that the f-wave source contributes over 95 % to the $M_{23}VV$ line. Also the calculations by Aberdam et al. [46] of the Auger matrix elements for the corresponding Ni $M_{2,3}VV$ line indicate that the amplitudes $A_3^{(0)}$ are overwhelmingly dominant over those of the other angular momentum components.

3.4.3 Factors influencing the existence of peaks or dips at projections of atomic rows

On Fig. 3.12 on page 79 we compare our optimum simulations of the 64 eV $M_{2,3}VV$ (upper panel) and the 914 eV L_3VV (lower panel) Auger diffraction patterns from a Cu(001) surface. Also shown on the simulated patterns are crosses marking the positions of the projections of all atomic rows emanating from an emitter.

Peaks are found close to all the crosses on the simulation of the high-energy pattern, whereas there appears to be no general rule for the low-energy one. For example, there is the now famous, and prominent, dip at the center of the pattern, arising mainly from the scattering of a source wave from a second-nearest neighbor along the [001] direction. In contrast, at the positions represented by the dark crosses on the low-energy pattern (at the projections of the [101], $[\bar{1}01]$, [011], and $[0\bar{1}1]$ directions), peaks in intensity are seen.

Our simulations of the 64 eV $M_{2,3}VV$ Auger diffraction pattern with source waves of different angular momenta have lent support to the general conclusions of Barton and Terminello [37,**?**] that the angular momentum of the source wave is an important determinant of the appearance of a peak or a dip along the direction of a particular atomic row on a low-energy Auger or photoelectron diffraction pattern. However, the appearances of *both* dips and peaks along projections of different atomic rows on the *same* diffraction pattern clearly indicates that this cannot be the *sole* factor.

To test the contention of Barton and Terminello [37,**?**] that, on a simple source-scatterer model, the angular momentum of the source wave is a determinant of the form of extremum in the forward-scattering direction, we reproduce on Fig. 3.13 on page 81 our calculated polar-angle plots of diffraction patterns formed by Auger sources of s to h angular momentum character and a Cu atom scatterer placed 2.55 $\AA$ (corresponding to the first-nearest neighbor distance, such as exists along the [101]-type rows in an f.c.c. structure) from the emitters. It will be seen that, as suggested by Barton and Terminello [38], a maximum in the forward-scattering direction from the s, p and d sources turns into a minimum for the f-,

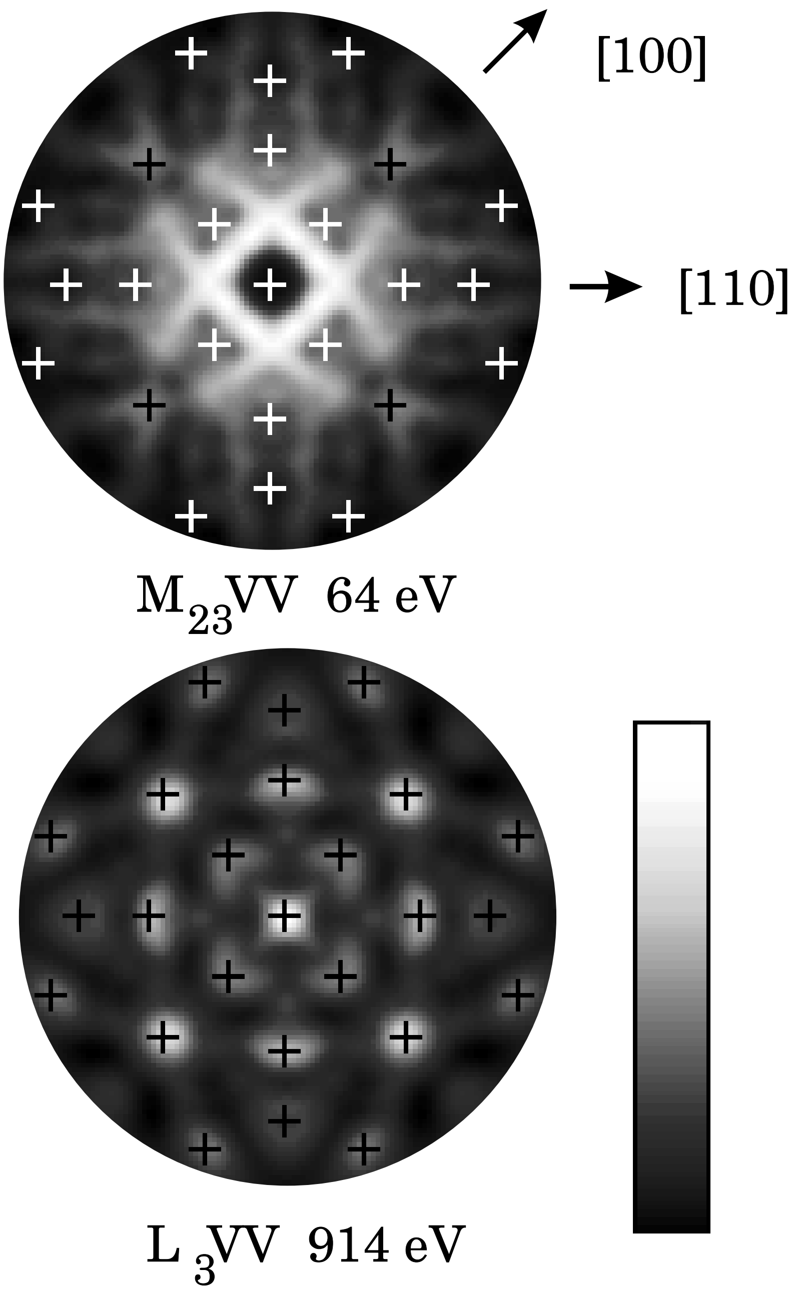

Figure 3.12: Auger electron diffraction patterns of f-wave simulations from Cu(001) of 914 eV and 64 eV. The crosses mark the projections of the crystal's low-index atomic rows. Note that intensity peaks match the crosses on the 914 eV pattern. On the 64 eV pattern most crosses are associated with intensity dips, except the peaks at the projections of the <101> directions(dark crosses). Of particular interest is the fact that the latter peaks are also found on the corresponding measured pattern of Frank *et al.* [1], reproduced in Fig. 3.1.

g- and h-wave sources.

If the calculations were repeated for a Cu atom placed 3.61 Å from the source, corresponding to the next-nearest neighbor distance, which separates atoms along e.g. the surface normal direction, a similar trend is seen (on Fig. 3.14 on page 82): namely that a peak in the forward-scattering direction for the lower angular momenta is replaced by a peak for the higher ones. However, a true minimum in this direction is only seen for the source with very highest angular momentum considered, namely the h-wave (although the central peak from the f-wave source is clearly lower in intensity than the first high-intensity ring that surrounds it).

The distance dependence of the nature of the extremum in the forward-scattering direction on the single-scatterer model is most clearly shown on Fig. 3.15 on page 84, in which similar polar-angle distributions are plotted for an f-wave Auger source and a range of source-scatterer distances including that for the nearest-neighbor (marked with the star) and the next-nearest neighbor one (marked by the square). A true minimum is seen only for the nearest-neighbor distance, but a global maximum in the forward-scattering direction is seen only for source-scatterer distances in excess of about 4 Å, which is beyond even the second-nearest neighbor distance. Although this distance dependence was not explicitly commented on by Barton and Terminello [38], it is consistent with their semi-classical expression

$$\phi = k_{l,r} r = kr + \frac{(l+1/2)^2}{2kr} - \frac{(l+1/2)\pi}{2} \tag{3.6}$$

for the cumulative phase acquired by an emitted electron of angular momentum l at distance r from an atom. (In the above expression, k represents the electron's wavelength at an infinite distance from the atomic potential). Thus the angular-momentum dependent centrifugal potential contributes both a constant,

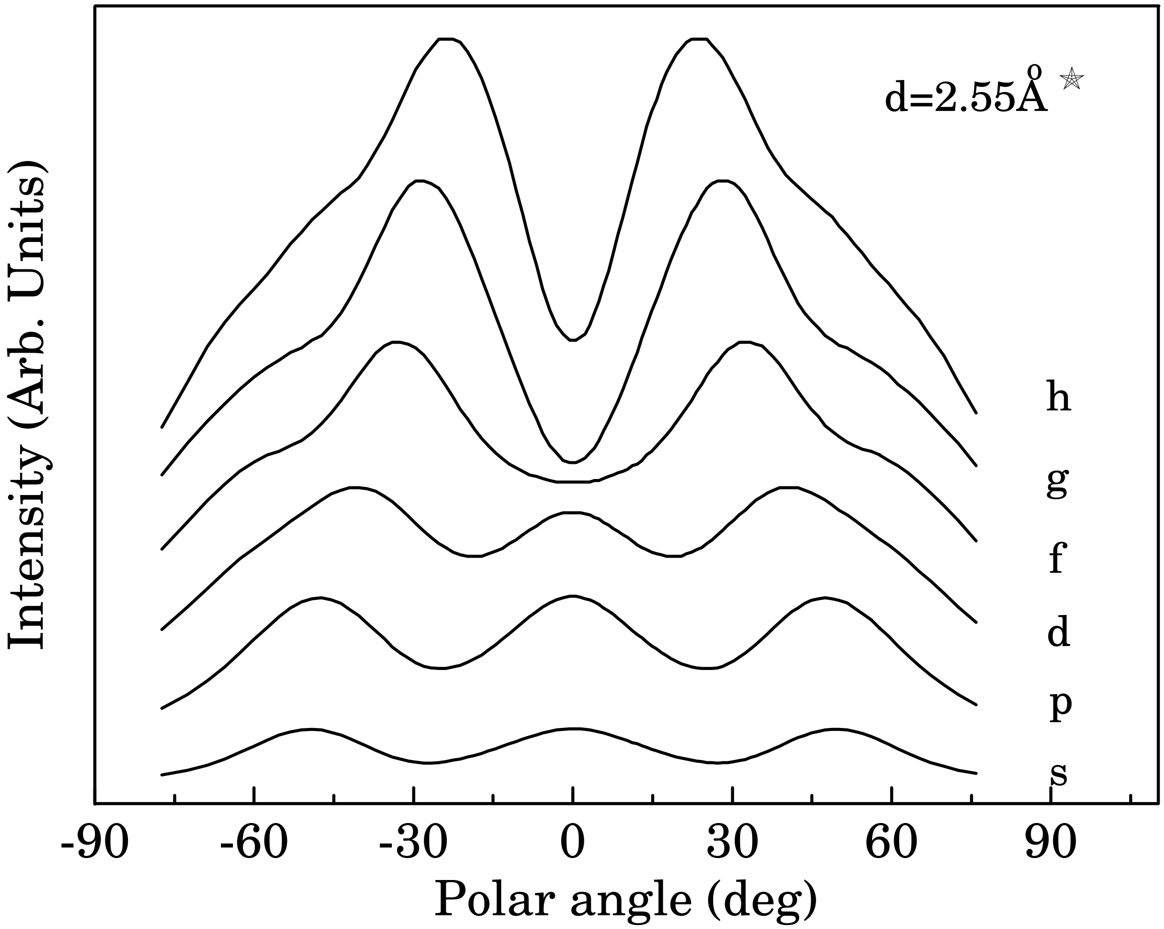

Figure 3.13: Intensity variation on a 64 eV $M_{23}VV$ Auger diffraction pattern due to a single Cu atom scatterer, placed 2.55 $\mathring{A}$ from electron emitters of s-, p-, d-, f-, g-, and h-wave character, as a function of the polar angle, measured from the emitter-scatterer axis. Observe the dips in the forward-scattering direction (at zero polar angle) for the high angular momenta.

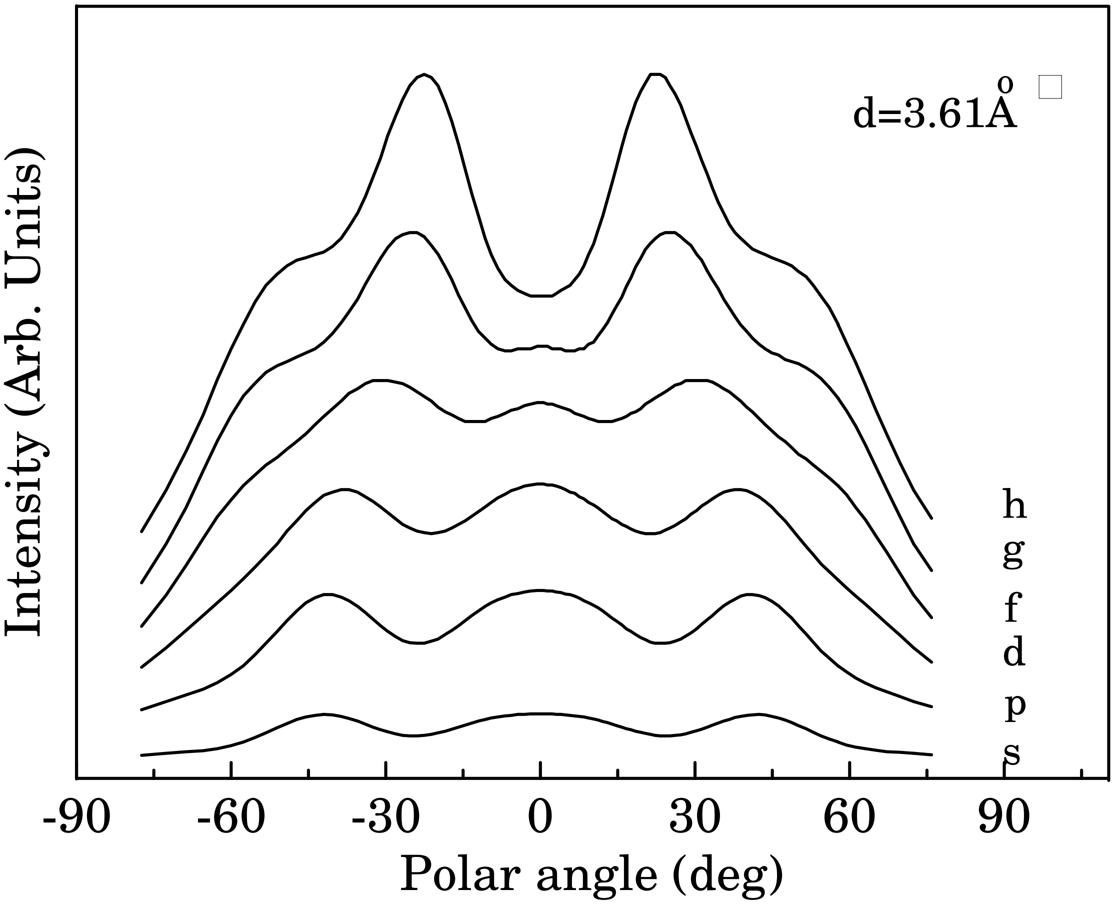

Figure 3.14: Intensity variation on a 64 eV $M_{23}VV$ Auger diffraction pattern due to a single Cu atom scatterer, placed 3.61 $\mathring{A}$ from electron emitters of s-, p-, d-, f-, g-, and h-wave character, as a function of the polar angle, measured from the emitter-scatterer axis. A pronounced forward-scattering dip is seen to develop at rather higher angular momenta.

represented by the third term on the right-hand-side of Eq. 3.6, and also a distance-dependent term (the second term). Since the diffraction pattern is determined by the interference between the direct wave from the emitter and that after scattering by the nearby atom, the third term cannot be a cause of the angular-momentum dependence of the pattern. To put it another way, if the cumulative phase due to the angular momentum barrier is the same for the direct and scattered waves there will be no effect on the interference pattern between the two. The second term in Eq. 3.6 above vanishes as $r \rightarrow \infty$ and thus does not contribute to the far-field phase of the direct wave. However, it makes a non-zero contribution to the phase ϕ at the position of the scatterer, and this is reflected in the far-field phase of the *scattered wave*. It is this dependence of the latter phase on the distance of the scatterer from the emitter which is responsible for the differences between the polar-angle profiles of Fig. 3.15.

However, it is important to note that the results of these single-scatterer calculations do not explain all the observations on either the 64 eV experimental patterns of Frank et al. [1] or our f-wave simulation of it shown on Fig. 1 (which is in very good agreement with the former). On these diffraction patterns a *peak* is seen at the projections of the rows containing the *nearest-neighbor* distances (the [101]-type directions at 45^o to the surface normal), while a *dip* is seen at the projection of the surface normal (containing the *next-nearest neighbor* distances), which is contrary to the distance-dependent trend in Fig. 3.15.

Thus, the true explanation of the peaks and dips on the much-discussed 64 eV $M_{2,3}VV$ Cu(001) Auger diffraction pattern must lie in the overlap and interference of the diffraction from the simultaneous presence of many scatterers [47,**?**]. Note, that the essential features of the peaks along the [101]-type directions and the dip

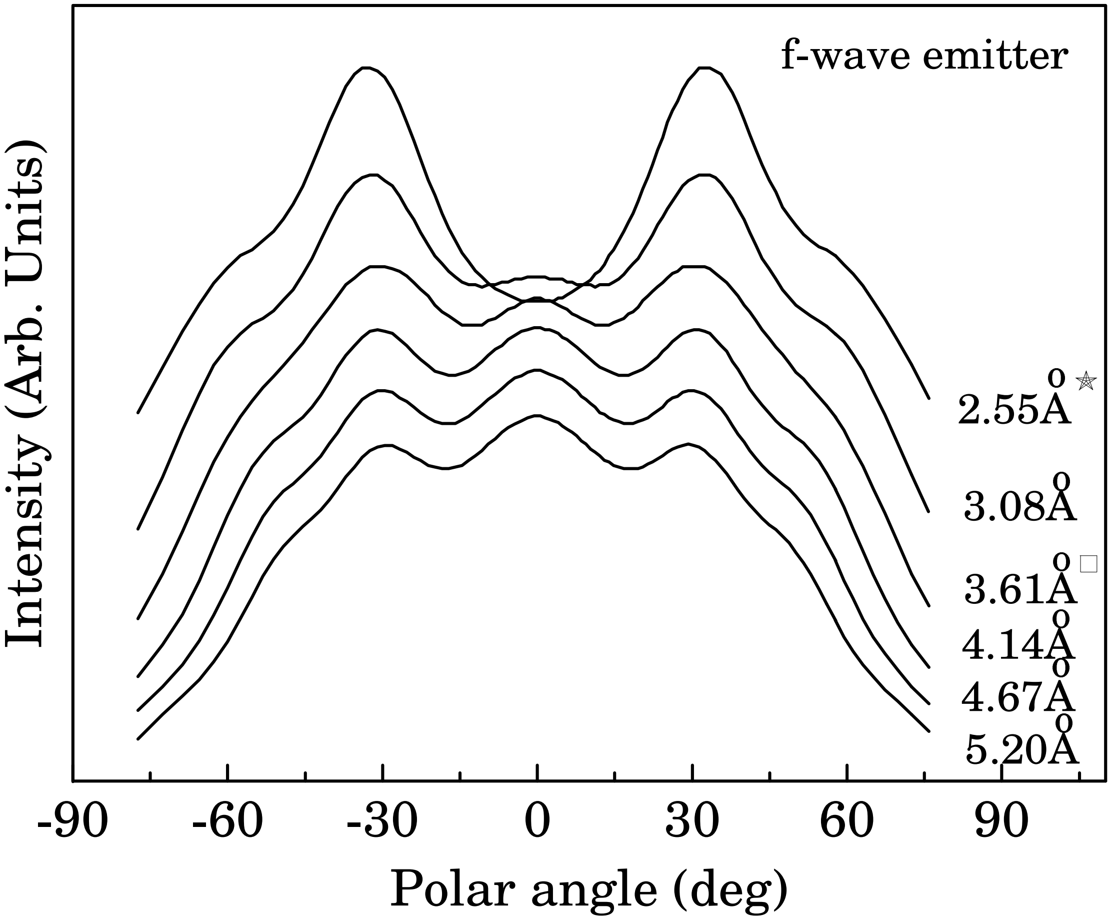

Figure 3.15: Same polar angle plots as in Fig.3.13 and 3.14, except that here the intensity variation are examined as a function of the emitter-scatterer distance, for the f-wave emitter. Notice that a forward-scattering dip at low emitter-scatterer distances turns into a peak for greater distances.

at the projection of the surface normal is present even in the single-scattering (but with several scatterers and sources) diffraction pattern of Fig. 3, and that it is not necessary to invoke *multiple scattering* for an explanation.

3.5 Conclusions

We have employed the full multiple-scattering concentric-shell algorithm of Saldin et al. [32] to simulate the 64 eV $M_{2,3}VV$ and the 914 eV L_3VV Auger diffraction patterns from a Cu(001) surface, and have compared these patterns with the published experimental data and computer simulations of Frank et al. [1] of the same Auger patterns. Our simulations agree much better with the experimental data of those authors than their own simulations, provided the Auger electrons are assumed to be emitted from each atom into an $l = 3$ angular momentum state. These results are consistent with earlier work [37,?], which have also suggested that Auger electrons from these particular transitions are emitted into f-wave channels.

However, we find that the angular momentum of the emitted electron is not the *sole* factor determining the appearance of either a peak or a dip at the projection of a particular atomic row in a crystal. On the contrary, we find that other factors, such as the inter-atomic distances along a particular row, and the existence of overlap and interference between diffraction from different, and not necessarily collinear, atoms in a complex structure can have as important an effect. By comparing our simulations with ones assuming only single-scattering we are also able to demonstrate that multiple-scattering has a noticeable effect on the diffraction patterns.

It is particularly gratifying to find that *exactly* the same theory reproduces the very different appearances of the high and low energy diffraction patterns. The theory treats essentially elastic scattering of the emitted Auger electrons, with an exponential attenuation of the elastic intensities with path length, due to the finite inelastic scattering length, in the standard fashion of usual multiple-scattering calculations.

CHAPTER 4

Anomalous Shifts Of Forward Scattering Peaks In Photoelectron Diffraction Patterns From MgO(001) Surface

4.1 Introduction

The structure of clean MgO(001) surface has been the subject of many investigations over the past two decades. The interest of studying MgO surfaces is due to its technological use as a substrate for thin film growth and as an important refactory material. The initial interest in this surface, however, was motivated by predictions that the anions and cations undergo different relaxations due to their differing polarizabilities. Theoretical predictions of the size and even existence of such a differential relaxation and rumpling has been the subject of some debate for a long time. Extensive experiments were conducted on MgO surfaces using surface sensitive techniques, such as Low Electron Energy Diffraction (LEED), Reflection High Energy Electron Diffraction (RHEED), Electron Energy Loss Spectroscopy (EELS), Extended Energy Loss Fine Structure (EELFS), He^+ diffraction, Impact Collision Ion Scattering Spectroscopy (ICISS), Extended Fine Auger Structure (EXFAS), Photoelectron Spectroscopy (XPS, UPS), and Angle-Resolved X-ray Photoelectron or Auger Electron Diffraction (ARXPD, ARAED), to explore its surface information in different aspects. Controversies over the amount of rumpling and relaxation for this surface still exist, and the reported values of the rumpling vary between 1 and 8% [54,55], and relaxation values between -15% and 3% [54,55].

An early study of MgO(001) surfaces cleaved in the air was carried out by

Legg, Prutton and Kinniburgh [50] in 1974 using the LEED technique. It has been shown that the relaxation of the top layer on the surface was very small, being at most 3% of its bulk interlayer spacing. On the other hand, Welton-Cook and Prutton [51] indicated that the MgO(001) surface should not be relaxed but might be rumpled to a degree of 5% by a shell model calculation of the surface energy.

A LEED study by T. Urano and T Kanaji [52] in 1983 showed that the surface of MgO(001) prepared by (1) cleaving a MgO single crystal in the air, (2) then heating to 300 ^{o}C, (3) heating under an oxygen environment to remove surface carbon contamination. These experiments result in similar LEED I-V curves of the diffraction beams of (10), (11), and (20) spot. Theoretical modeling has been conducted, allowing the first layer to be adjusted, the result shows that theoretical curves with no relaxation or with the smallest relaxation of (2.5%) in the calculation fit the above three experiments best.

A RHEED experiment for elastic diffraction of 10 keV electrons incident on the MgO(001) surface along the [010] azimuth, was done by P. A. Maksym [53] in 1985. It was concluded from this experiment that the most likely value of the outermost layer spacing is close to the bulk layer spacing, and the upper limit of any deviation from the bulk spacing was found to be an expansion of 3%. This is consistent with the accepted LEED results of previous studies. It was also shown that the RHEED intensities are insensitive to rumpling when the incident beam azimuth lies in one of the [n10] directions with n being even, while they are very sensitive to rumpling when it lies in other directions.

But a large inward relaxation of the topmost layer of 15% ± 3% with respect to the distance in the bulk and a small rumpling surface were observed by ICISS technique conducted by H. Nakamatsu, A. Sudo, and S. Kawai [56,**?**] in 1988-1989.

The electronic structure of MgO surface was also studied by V. E. Henrich, G. Dresselhaus, and H. J. Zeiger [60] using the EELS technique in the early 80's. In their experiment, the primary electron energy, E_p, was varied in a range between 100 eV and 2000 eV, and it was possible to unambiguously separate bulk and surface features in loss spectra. Both surface and bulk Mg intraionic and O-to-Mg interionic transitions have been studied and found to be associated with the excited-state spectra of free Mg^{2+}.

The structure, the microtopography and the cleanliness of MgO(001) surfaces were investigated by a combination of thermal helium scattering, surface decoration and Auger spectroscopy [58]. It has been shown that the microstructure depends strongly on the surface preparation technique. MgO surfaces obtained by cleavage under UHV are clean, and present a high coefficient for coherent He^+ reflection, while annealed MgO surfaces show a lower coefficient of coherent He^+ reflection. An explanation of this might be that the cleaved surfaces have a low number of defects while annealed surfaces present a high number of defects. The large difference in number of defects on a clean and annealed surfaces was also found by Varma et al. [59] using Angle-Resolved X-ray Photoelectron (ARXPD) and Auger Electron Diffraction (ARAED) experiments, where the ARXPD and ARAED data were from a cleaved MgO surface and a sputtered & annealed one. Substantial differences in shape and intensity of the diffraction peaks are observed for diffraction patterns from the cleaved sample and that from the sputtered & annealed one. The Mg KLL ARAED pattern and the O 1s ARXPD one from the cleaved sample show additional fine structures which are an indication of a higher degree of order on the sample surface than that of sputtered & annealed one. Theoretical simulations using a multiple scattering algorithm show that a defect free surface model of MgO(001) can well reproduce the experimental electron diffraction patterns taken from the cleaved sample, while simulations do not agree very well with those from the sputtered & annealed surface. This also indicates that there is a low density of defects on the cleaved surface.

ARXPD has been proved to be a very powerful surface technique in investigating the atomic arrangements of metal surfaces and thin films with metal substrates, while there have been few ARXPD studies of insulator surfaces. Anomalous electron diffraction patterns were first observed from an ionic insulator surface of MgO(001) by Varma et al [59] from the Mg KLL Auger line (1180 eV) and the O 1s core-level photoemission line (955 eV). Two significant anomalies were observed. Firstly, the intensity maxima of the electron diffraction data do not always match the low-index crystallographic directions. This is contrary to the observations for metal surfaces where, along the low index directions, there always exist the forward-scattering peaks in the range of high electron kinetic energies. Secondly, the diffraction patterns produced by Mg KLL Auger and O 1s photoemission do not contain peaks at the projection of exactly the same directions even though they occupy equivalent crystallographic sites in bulk MgO. Large relative peak shifts are found between these two patterns.

In this chapter, a full multiple scattering method was used to calculate the electron diffraction patterns of Mg KLL and O 1s emission from a flat and rumpled MgO(001) surfaces. A detailed MgO(001) surface rumpling model was discussed and used in the multiple scattering calculation of the electron diffraction. The electron inelastic scattering length was found to play an important role in the explanation of the peak shifts in the diffraction pattern, and it was shown that a short inelastic scattering length could cause the shifting of Mg and O peaks off their low index crystallographic directions. The magnitude and direction of the shifting are in line with the observations from the experiments. Simulations were also done on Mg s and d-wave emitters, and by comparing them with the experiment, it was shown that the s-wave emitter is dominant in the Mg KLL Auger transition.

4.2 MgO surface model and electron diffraction experiments

A MgO bulk crystal is a rocksalt-structured ionic crystal which takes a simple cubic structure of Mg and O atoms occupying alternative lattice position and each atom is surrounded by 6 nearest neighbor atoms with opposite species as shown in Fig. 4.1 on page 93. Its lattice constant is 4.21 $\AA$ with a Mg-O bonding length of 2.10 $\AA$. In a MgO compound, magnesium loses two electrons and becomes a Mg^{2+} cation, and oxygen gains two and becomes an O^{2-} anion. In the ionic structure of MgO, the ionic radii of Mg^{2+} and O^{2-} are 0.65 and 1.46 $\AA$ respectively, very different from the radii of neutral Mg and O of 1.72 and 0.65 $\AA$, respectively.

Fig. 4.2 on page 94, shows a bulk terminated MgO rocksalt (001) surface viewed along [100] and [011] directions with smaller filled circles representing Mg atoms and bigger open circles for O atoms. Some polar angles radiating from a Mg atom along low-index crystallographic directions are marked in the figure, and listed on Table 4.1. Due to an identical local environment, atomic rows radiate from the O atom in the same directions. A rumpled MgO(001) surface model is shown in Fig. 4.3 on page 95, in which surface cations (Mg atoms) and anions (O atoms) undergo different relaxations, which anions moving into the vacuum relative to the cations. The degree of rumpling of the surface depends on the separation of the cations and anions in the outermost surface. A net inward or

Table 4.1: Low-index directions of a bulk terminated MgO(001) surface

[001]	[103]	[102]	[101]	[302]	[201]	[112]	[111]	[332]
0^o	18.4^o	26.6^o	45.0^o	56.3^o	63.4^o	35.3^o	54.7^o	64.8^o

outward motion of the surface cations and anions will result in a relaxation of the surface. A large rumpling on the surface may not necessarily mean a large relaxation, and *vise versa*, a large relaxation does not necessarily indicate a large rumpling on the surface. The low-index crystallographic directions in a bulk do not necessarily pass the center of those surface cations or anions, as shown in Fig. 4.3.

Completed ARXPD patterns have been measured in the same scan from sputtered & annealed and cleaved MgO(001) surfaces for O 1s core-level photoemission and Mg KL_2L_3 Auger emission by B. Tonner's group [59]. Fig. 4.4 on page 96 shows the electron diffraction patterns from a sputtered & annealed MgO(001) surface and that on Fig. 4.5 on page 97 from a cleaved surface. The experiments were carried in a VG ESCALAB MARK II system using the Al K_α (1486.6 eV) radiation with a base pressure of $9x10^{-11}$ Torr. The x-rays are assumed to be unpolarized. The angular resolution of the electron analyzer was less than 3^o. The diffraction intensity distributions were measured in a geometry with a fixed angle of 75^o between the incident x-ray source and the electron analyzer direction. The polar angle θ was scanned by rotating the sample normal direction relative to the detector, and the changes in azimuthal angle ϕ were realized by rotating the sample along its normal direction.

There are two significant anomalies observed in these experiments. The first

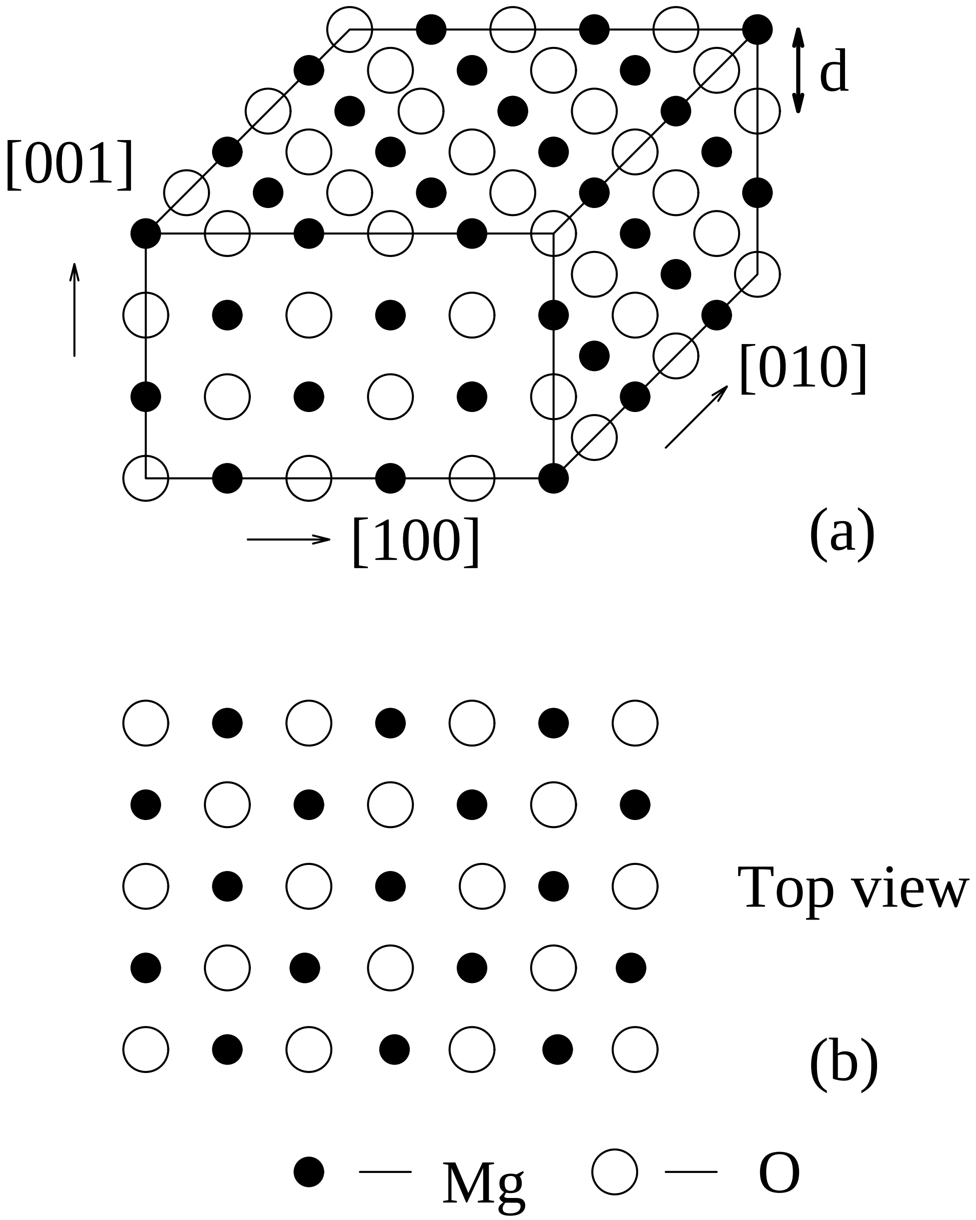

Figure 4.1: MgO rocksalt surface model: (a) three dimensional view of the rocksalt structure, and, (b) top view of (001) surface. The bulk interlayer spacing d equals 2.10 $\mathring{A}$. Filled and empty circles represent Mg and O atoms, respectively.

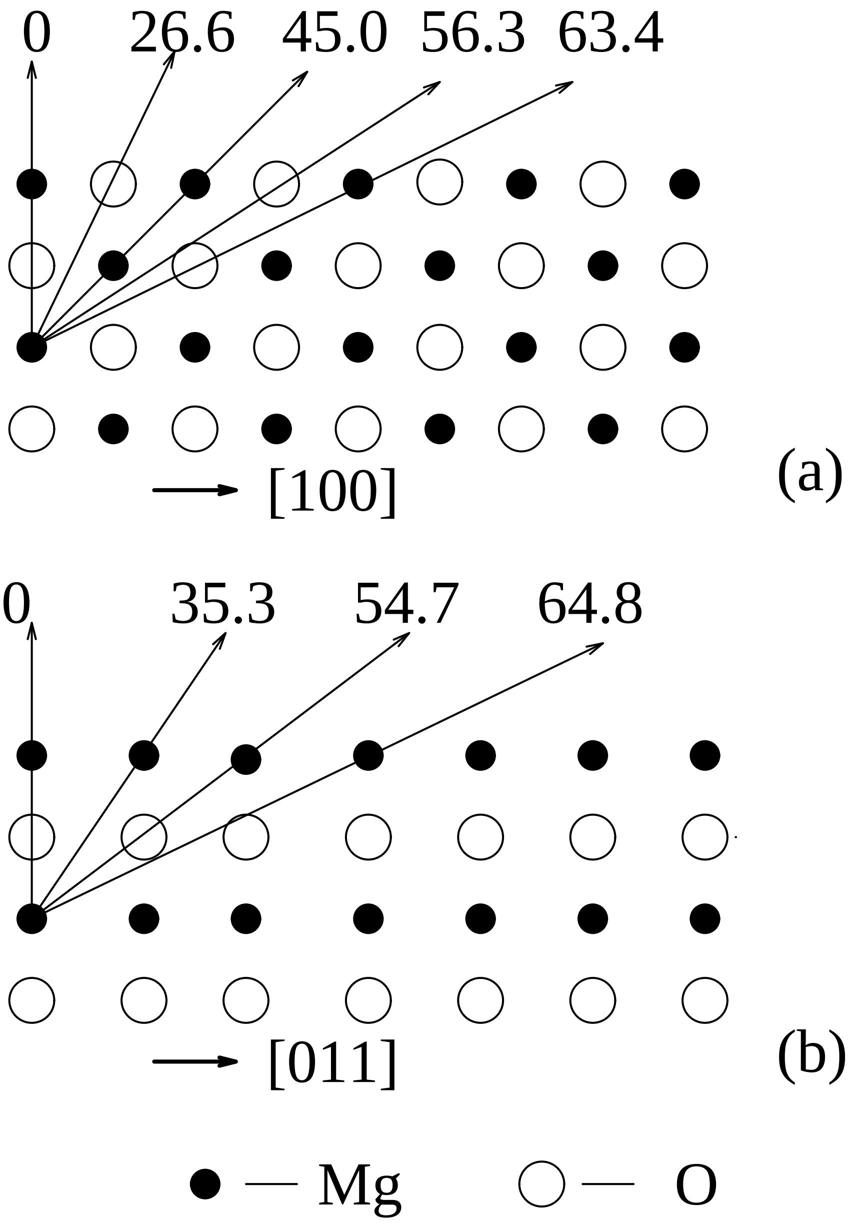

Figure 4.2: MgO bulk terminated surface model, a side view along (a) the [100] direction, and, (b) the [011] direction of the rocksalt (001) surface structure.

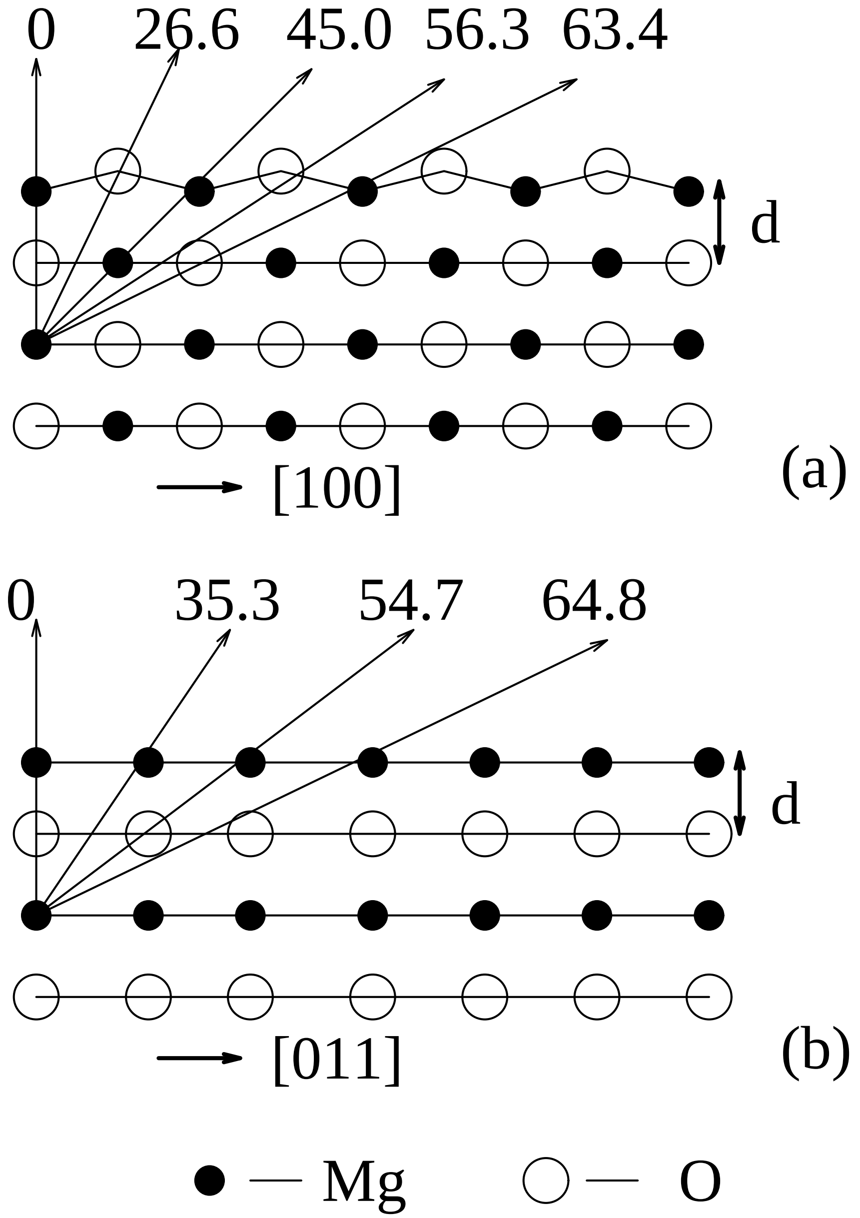

Figure 4.3: MgO rumpled surface model, a side view along (a) the [100] direction, and, (b) the [011] direction of the rocksalt (001) surface structure. In this model, surface O atoms move towards the vacuum relative to the surface Mg atoms, and the bulk interlayer spacing d and low-index crystallographic directions are also marked as a reference.

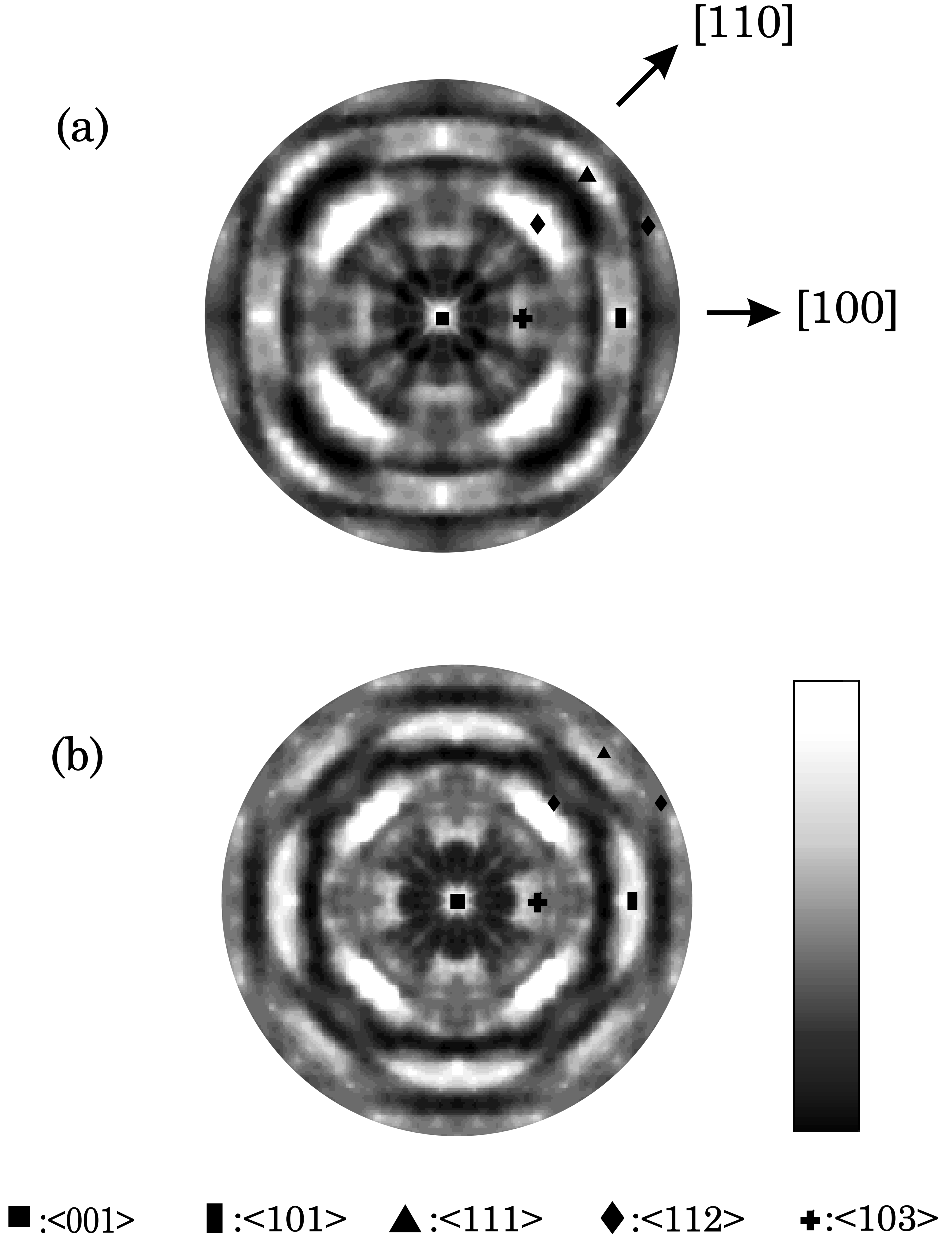

Figure 4.4: Angle-resolved diffraction patterns of (a) Mg Auger KLL (1180 eV), and, (b) O 1s photoemission (955 eV) from a sputtered & annealed MgO(001) surface measured from the same scan by S. Varma et al [59]. The patterns are plotted as a function of a uniform $\mathbf{K}$ grid with $\mathbf{K}_{\|}=0$ (where the subscript "$\|$" indicates component parallel to the surface) at the center of the patterns. The locations of the major low-index crystallographic directions are marked by different symbols.

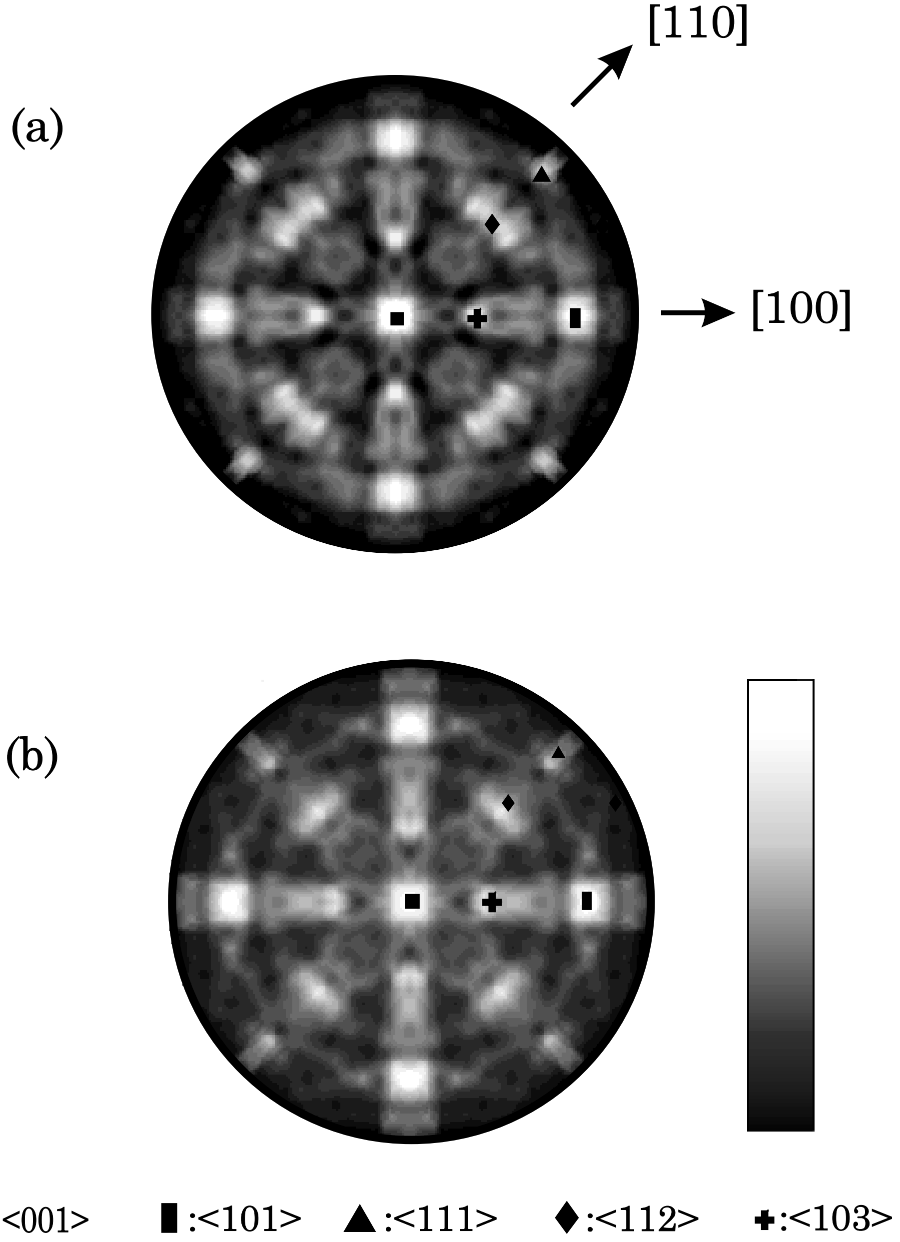

Figure 4.5: Angle-resolved diffraction patterns of (a) Mg Auger KLL (1180 eV), and, (b) O 1s photoemission (955 eV) from a cleaved MgO(001) surface from the same scan as measured by S. Varma et al [59]. The locations of the major low-index crystallographic directions are also shown.

is that some diffraction intensity peaks shift off the forward-scattering directions to a lower polar angle, such as the O peak near the [201] direction. The polar angle of this [201] direction is 63.4^o, while the observed O peak in the electron diffraction patterns is 60.0^o. The second is that peak positions in the diffraction patterns measured from the Mg KLL Auger and the O 1s core-level photoemission lines are not matched, despite a similar local environment occupied by Mg and O. Some O 1s peaks have a larger shift than that produced by the Mg Auger diffraction, e. g. the Mg and O peaks near the projections of the [111], [112], and [201] directions for both the cleaved and sputtered & annealed experiments. Above anomalies have no simple explanation on the forward-scattering theory [72] that has been successfully applied to metal surfaces. Thus those anomalous features must be associated with some intrinsic feature of this insulator.

4.3 Full multiple scattering calculation of electron diffraction from MgO(001) surfaces

4.3.1 Theoretical modeling of the MgO structure

The theoretical calculation of electron diffraction from MgO(001) surface was carried out by using a concentric shell cluster multiple scattering algorithm developed by D. K. Saldin, G. R. Harp, and X. Chen [32] and described in detail in Chapter 2 on page 14. The approach is basically based on the classification of the cluster into a series of concentric shells centered at the origin (emitter position). The shells contain atoms of approximately the same distance from the origin. Intershell and Intrashell scattering matrix can be evaluated with the aid of a pair of recursion relations developed by Saldin and Pendry [21].

Before carrying out any cluster calculation, the atomic and electronic structure of MgO(001) surface has to be examined carefully. The MgO(001) surface clusters used in the calculation were the unrumpled MgO(001) surface shown in Fig. 4.2 and rumpled surface structure shown in Fig. 4.3. From these two cluster models, the atoms in the first five outermost surface layers (a total 250 scattering atoms) are included in the multiple scattering calculations, the outermost atomic shell being 11 $\mathring{A}$ from the emitter. These clusters are big enough for a full convergence of the scattering calculation, because the radius of the outermost shell distance is larger than the electron inelastic length, which is in the order of 8 $\mathring{A}$.

Electron wave functions of Mg, Mg^{2+}, O, and O^{2-} atoms were obtained by a Hartree-Fock-Slater self-consistent program [61] and then used as an input in the MUFPOT program developed by J. Pendry and co-workers [11] to calculate the atomic potentials in an ionic $Mg^{2+}O^{2-}$ and a neutral MgO structure. In the MUFPOT program, an averaged statistical exchange parameter α of 0.73680 was assumed for both $Mg^{2+}O^{2-}$ and MgO system (exchange parameter α for free O and Mg atoms were reported to be 0.74447 and 0.72913 respectively in reference [62]). The phase shifts of ionic Mg^{2-} and O^{2-} atoms at kinetic energies of 1180 eV and 955 eV were then calculated by taking a muffin-tin radius of 0.65 $\mathring{A}$ for Mg^{2+} atom and 1.46 $\mathring{A}$ for O^{2-} atom. Phase shifts of neutral Mg and O atoms were also evaluated at 1180 eV and 955 eV with both neutral atoms having the same muffin-tin radius of 1.06 $\mathring{A}$ in the solid. The plots of the amplitude and phase of the atomic scattering factors of Mg, Mg^{2+}, O, and O^{2-} for a high electron energy of 1180 eV are shown in Fig. 4.6 on page 101 and in Fig. 4.7 on page 102. Atomic scattering factors of Mg^{2+} and Mg atoms are calculated using a spherical wave form [79]

$$f(\theta, r) = \frac{1}{k} \sum_{l=0}^{22} (2l+1) sin\delta_l e^{i\delta_l} P_l(cos\theta) c_l(kr) \tag{4.1}$$

where δ_l is the phase shift, and $P_l(cos\theta)$ a Legendre polynomial, and $c_l(kr)$ the polynomial coefficient of Hankel function $h_l^{(1)}(kr)$ [8], and r the distance between the scatterer and emitter, and k wave number of the electron. There is very little difference between the scattering factor at energy 1180 eV and 955 eV due to the very small energy dependence of the phase shifts at high energies.

A simple criterion

$$l = kR$$

can be used to estimate the angular momentum quantum number l that is needed to fully describe a scattering process, where k is wave number and R the atomic radius. It can be obtained from this criterion that, at 1180 eV, l=24 and 12 for O^{2-} and Mg^{2+} respectively, and l=17 for both neutral O and Mg atoms; at 955 eV l=22 and 11 for O^{2-} and Mg^{2+} respectively, and l=16 for both neutral O and Mg atoms. Despite the large differences in ionic radii, for high electron energies the atomic scattering factors of Mg^{2+} and O^{2-} were found to differ in amplitude in the forward-scattering direction (0^o) by 10%, and to have nearly the same half-width of about 20^o. This is also true for the atomic scattering factor of neutral Mg and O atoms. It is shown in Fig. 4.6 and 4.7 that neutral atoms of Mg and O have larger scattering strength than the ionic atoms, and that there are relatively large changes in scattering phase between the neutral and ionic atoms of the same species along forward-scattering direction.

In this calculation, the atomic scattering factors for Mg, Mg^{2+}, O and O^{2-} atoms sum over angular momenta up to l=22. However, there are only small differences beyond l=16 for the Mg, Mg^{2+}, O and O^{2-} scatterers. Due to the fact

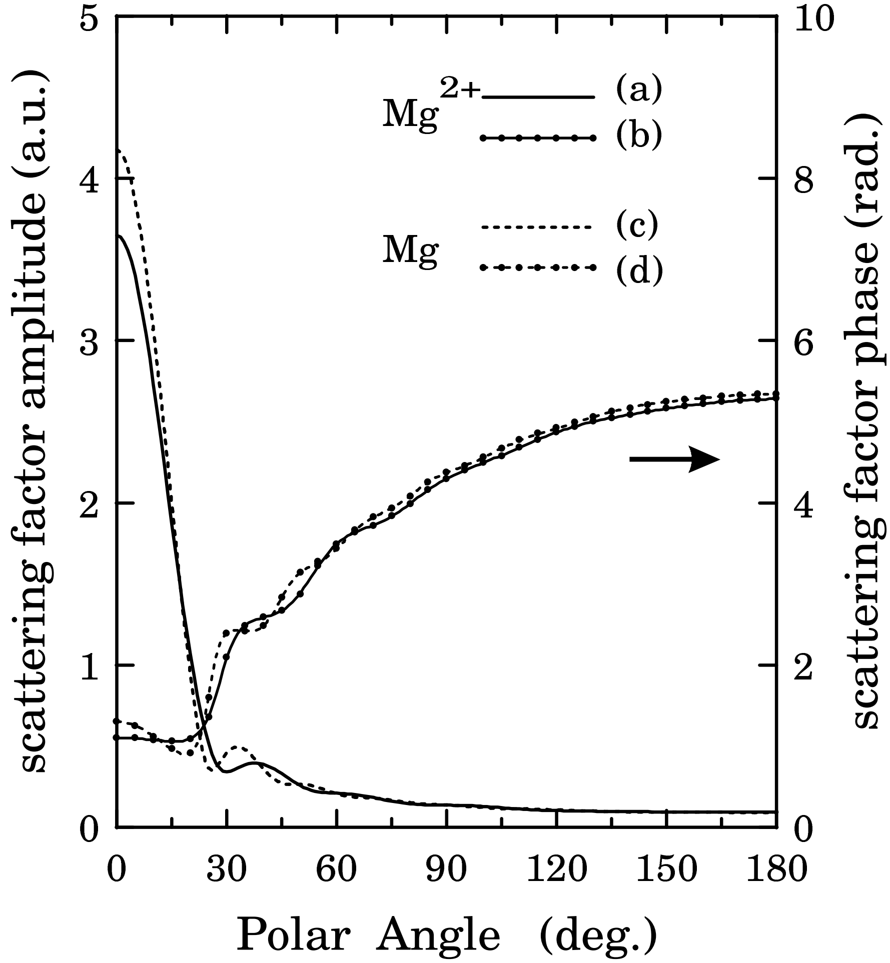

Figure 4.6: Atomic scattering factors of Mg^{2+} and Mg atoms calculated using the spherical wave form [79], where the phase shifts are evaluated by a MUF-POT program at an energy of 1180 eV with input electron wave functions obtained from a Herman-Skillman self-consistent program. The scattering-factor amplitude and phase of an ionic Mg^{2+} atom are plotted by curves (a) and (b), respectively, and the scattering-factor amplitude and phase of a neutral Mg atom are plotted by curves (c) and (d), respectively.

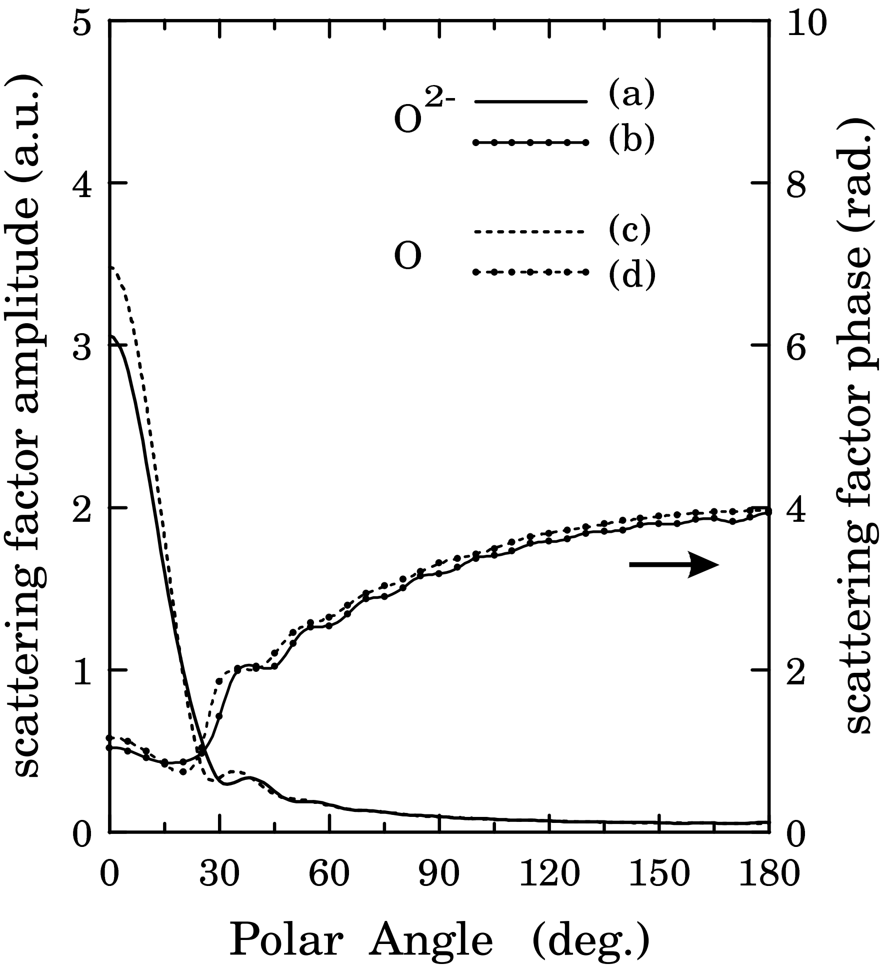

Figure 4.7: Atomic scattering factors of O^{2-} and O atoms calculated at 1180 eV. The scattering-factor amplitude and phase of the ionic O^{2+} atom are plotted by curves (a) and (b), respectively, and the scattering-factor amplitude and phase of a neutral O atom are plotted by curves (c) and (d), respectively.

that the MgO single crystal is a hard and rigid solid, we could infer that the atomic structure of MgO is stable or that the bonding between Mg and O is strong, so the Debye temperature, T_D, could be very high. Taking T_D=1600^{o}K or above, and the sample temperature T to be 300^{o}K, for example, and comparing the atomic scattering factor with that of the sample temperature at zero Kelvin, it was found that the atomic scattering factors of the above two cases were almost identical. This infers that phase shifts at a sample temperature of a zero Kelvin is the limit of the phase shifts at very high Debye temperature. Therefore zero Kelvin sample temperature was used for the calculation of phase shifts of Mg and O.

4.3.2 Simulation of electron diffraction from MgO(001) surface

The results of the multiple scattering simulations of Mg KLL Auger and O 1s core-level photoemission lines will be discussed in this section for the flat and rumpled MgO(001) surface models. First of all, the initial forms of the Mg and O emitted waves should be determined. Due to the dipole selection rule, the O 1s core-level (angular momentum quantum number l=0) photoemission was assumed to be emitted into an l=1 state, whereas in the Mg KLL Auger transition, an s-wave emitter was assumed first. This is generally a good approximation when the kinetic energy of an electron is large (above 600 eV). Due to the Auger transition selection rule [43], a possible Auger d-wave emitter could be involved in this transition and it will generate a similar diffraction pattern to that of an s-wave but with small differences [72] which will be discussed in Section 4.3.4. It was assumed in all the calculations that a real part of inner potential energy is -11.4 eV inside the MgO solid, and an adjustable imaginary part of the inner potential energy ranges from 0 eV to 16 eV. The later is associated with the electron inelastic scattering length at the lower end of the universal curve [63] around 1000 eV.

The scattering matrix $\mathbf{S}^{(N)}$ can be calculated by using the concentric shell algorithm program described in Chapter 2. Once the scattering matrix $\mathbf{S}^{(N)}$ is obtained, it will then be used in the diffraction intensity calculation simulating different experimental conditions.

The angular distribution of the far-field intensity with electron wave number $\mathbf{k}$ due to the O 1s transition with an emitter located at the Jth layer below the surface can be expressed in terms of $\mathbf{S}^{(N)}$ as:

$$I^J_{XPD}(\mathbf{k}) = |\sum_L \sum_{L'} \mathbf{S}^{(N)}_{L'L} \mathbf{A}^{(0)}_{LL_c} (-i)^{l'} Y_{L'}(\hat{\mathbf{k}})|^2 \exp\{-d_J/\lambda cos\theta\} \qquad (4.2)$$

where L represents (lm), l angular momentum quantum number and m the magnetic quantum number, $\mathbf{A}^{(0)}_{LL_c}$ is the transition amplitude from core-state L_c to the final emittering state L, $\mathbf{K}$ is the electron wave vector, and λ is the inelastic scattering length of an electron in a solid. The resulting wave-fields involve waves that are mutually coherent if they originally come from the same core-level state L_c, and mutually incoherent if they are emitted from different core-states. In the case of O 1s photoemission, there is only one 1s core-state and the final emitting state is a p-state.

The angular distribution of the far-field intensity for the Mg KLL Auger transition lines can be expressed as:

$$I^J_{AED}(\mathbf{k}) = \sum_L |\sum_{L'} \mathbf{S}^{(N)}_{L'L} \mathbf{A}^{(0)}_{L} (-i)^{l'} Y_{L'}(\hat{\mathbf{k}})|^2 \exp\{-d_J/\lambda cos\theta\} \qquad (4.3)$$

where the matrix $\mathbf{A}^{(0)}_L$ represents the transition amplitude of a final Auger electron in state L $(=lm)$, and the amplitudes of the emitted waves of different magnetic quantum number m corresponding to a particular azimuthal quantum number l

are taken to be equal, and $\mathbf{A}_L^{(0)}$ will be replaced by $\mathbf{A}_l^{(0)}$. This is consistent with the usual assumption that in Auger emission, the final ejected electron has lost any memory of the initial excitation process, and thus emerges from an atom with an overall isotropic angular distribution. The emitted waves of angular momentum components lm are taken to be incoherent with respect to each other. The exponential factor in both equations represents the inelastic attenuation of an photoelectron or Auger electron emitted from an atom in the Jth layer of depth d_J from the surface, λ is the electron's inelastic scattering length, and θ the angle between $\hat{\mathbf{k}}$ (pointing from sample to the detector direction) and the surface normal.

In the case of a MgO(001) surface all atoms of the same species in any particular layer have identical local surroundings, and an electron emitted from any one of them would give rise to the same diffraction pattern. Emitters in different layers generate different patterns, and the final diffraction pattern will account for the contributions from all layers. Due to time constraints, the diffraction intensities from just the first five layers below the surface were calculated, and the total intensity summation was carried out by putting more weight on the intensity of the fifth layer. The reason for doing this is that diffraction intensities from deeper layers result in a similar diffraction pattern due to a similar local environment as the emitter goes deeper into the bulk, but with a different damping factor due to the different path that electron travels through a solid to reach the detector. In the MgO(001) simulations, only small changes in intensity profiles were found between those from 4th layer and 5th layer emitters as shown in Fig. 4.11 on page 116. With this evidence, therefore, we can make a further approximation that the diffraction intensities from the emitters below the 5th layer have the same intensity distributions as that of 5th layer, except for an extra attenuation factor.

A simple algorithm shows that the effective intensity contributed by the fifth layer and all subsequent layers can be expressed as:

$$I_{eff}^{5-\infty} = I^5 + I^6 + I^7 + I^8 + \cdots$$

$$= I^5 + I^5 exp\{-d/\lambda cos\theta\} + I^5 exp\{-2d/\lambda cos\theta)\} + \cdots$$

$$\cdots + I^5 exp\{-nd/\lambda cos\theta\} + \cdots$$

Therefore,

$$I_{eff}^{5-\infty} = I^5 (1 - exp\{-d/\lambda cos\theta\})^{-1} \tag{4.4}$$

The expression of $(1 - exp\{-d/\lambda cos\theta)\})^{-1}$ was taken as the weight factor, which is a function of the polar angle θ, for a total diffraction intensity summing over an infinite number of layers below the 5th layer. Eq. 4.4 is held for the x-ray excited electron diffraction circumstance where the photon penetration depth is much larger than that of the electron inelastic scattering length in the solid. Therefore, emitters in each layer have the same possibility to be excited, and contribute equally to the diffraction intensity except to a damping factor due to the electron meam free path. However, for an electron excited Auger electron diffraction, the penetration depth, $\lambda_{ext}^{\perp}$ (along the sample normal direction), of the external electron beam is usually shorter than or equivalent to that of the electron escape length. The emitters in the deeper layers have less chances to be excited, therefore the intensity contributed by the 5th layer and all subsequent layers should be:

$$I_{eff}^{5-\infty} = I^5 + I^6 + I^7 + I^8 + \cdots$$

$$= I^5 + I^5 exp\{-d/\lambda cos\theta - d/\lambda_{ext}^{\perp} cos\theta\} + I^5 exp\{-2d/\lambda cos\theta - 2d/\lambda_{ext}^{\perp} cos\theta\} + \cdots$$

$$\cdots + I^5 exp\{-nd/\lambda cos\theta - nd/\lambda_{ext}^{\perp} cos\theta\} + \cdots$$

Therefore,

$$I_{eff}^{5-\infty} = I^5(1 - exp\{-d/\lambda cos\theta - d/\lambda_{ext}^{\perp}cos\theta\})^{-1} \tag{4.5}$$

and we take $(1 - exp\{-d/\lambda cos\theta - d/\lambda_{ext}^{\perp}cos\theta\})^{-1}$ as the weigth factor here. Noted that when adding the intensities of the 1st to 5th layer, the extra damping factor of $exp\{-d_J/\lambda_{ext}^{\perp}cos\theta\}$ due to the external electron beam should also be considered.

In the first calculation, the flat MgO(001) surface model of Fig. 4.2 on page 94 was used, and the diffraction patterns for the Mg emitter at the energy of 1180 eV and the O emitter at 955 eV shown on Fig. 4.8 (a) and (b) on page 109 were obtained. The diffraction patterns of both Mg and O emitters reveal a similar forward-scattering feature, different only in small details. In comparison with the experimental diffraction patterns of Fig. 4.4 and Fig. 4.5, the calculated diffraction patterns from a flat MgO(001) surface are in much better agreement with the cleaved MgO(001) electron diffraction experiments than the experimental diffraction patterns from the sputtered & annealed MgO(001) surface. In general, the peak positions from the calculations match nicely with the experiments from both cleaved and sputtered & annealed surfaces, however, the peak shapes and intensity distributions of the cleaved MgO experiments are much closer to the simulations for both Mg KLL and O 1s emitters. This suggests that the cleaved MgO(001) surface is closer to a perfect surface or has a lower number of surface defects than that of the sputtered & annealed surface. The high number of defects on a sputtered MgO surface has also been discovered by Duriez et al in the He$^+$ ion scattering experiments [58].

Some important features in the experimental diffraction patterns are reproduced by the calculated diffraction patterns, and they are: The extremum is observed along [001] direction for the O 1s emitter from the cleaved and sputtered

& annealed MgO(001) surface, although is much more prominent in the multiple scattering simulations; The "$\mho$" shaped features that appear near the [013], $[0\bar{1}3]$, [103], and $[\bar{1}03]$ directions of the Mg KLL pattern from the cleaved experiment; Some of forward-scattering peaks are toward the lower polar angle for both Mg KLL and O 1s emitters; Peak shifts between the Mg KLL and O 1s emitters are found, e.g. the [111] peak of the O 1s shifts as much as 3.3^o more than that of the Mg KLL emitter; Other forward-scattering directions in the diffraction simulations, such as [103], [101], and [001] of both Mg and O emitters, remain unchanged along the low-index crystallographic directions.

In order to see if the relative peak shifts toward the low polar angle, as seen in the experiments, could also be due to the rumpling on the MgO(001) surface, in the second calculation, the rumpled MgO(001) surface model in Fig. 4.3 was assumed and the corresponding calculated diffraction patterns are shown in Fig. 4.9 on page 110 for both the Mg KLL and the O 1s emissions. The rumpling model used for the calculation assumes that the surface Mg atoms remain at their bulk terminated positions and O atoms move into the vacuum by 0.2 $\AA$, that is a rumpling of 10 % and relaxation of 5% at the surface. The Mg and O atoms below the second layer remain at their positions as they were in the bulk.

It is shown that the calculated diffraction patterns from a rumpled MgO(001) surface produce a similar diffraction patterns as those from a flat surface. Quantitative evaluations on the diffraction patterns have been done to reveal the differences between those theoretical simulations from a flat and a rumpled surface, and it was found that the peak shifts between those diffraction patterns are within 0.5^o. Actually, peak shifts of a rumpled surface are toward the center of the patterns, although along the right direction, but much less than the measured values of 3 to

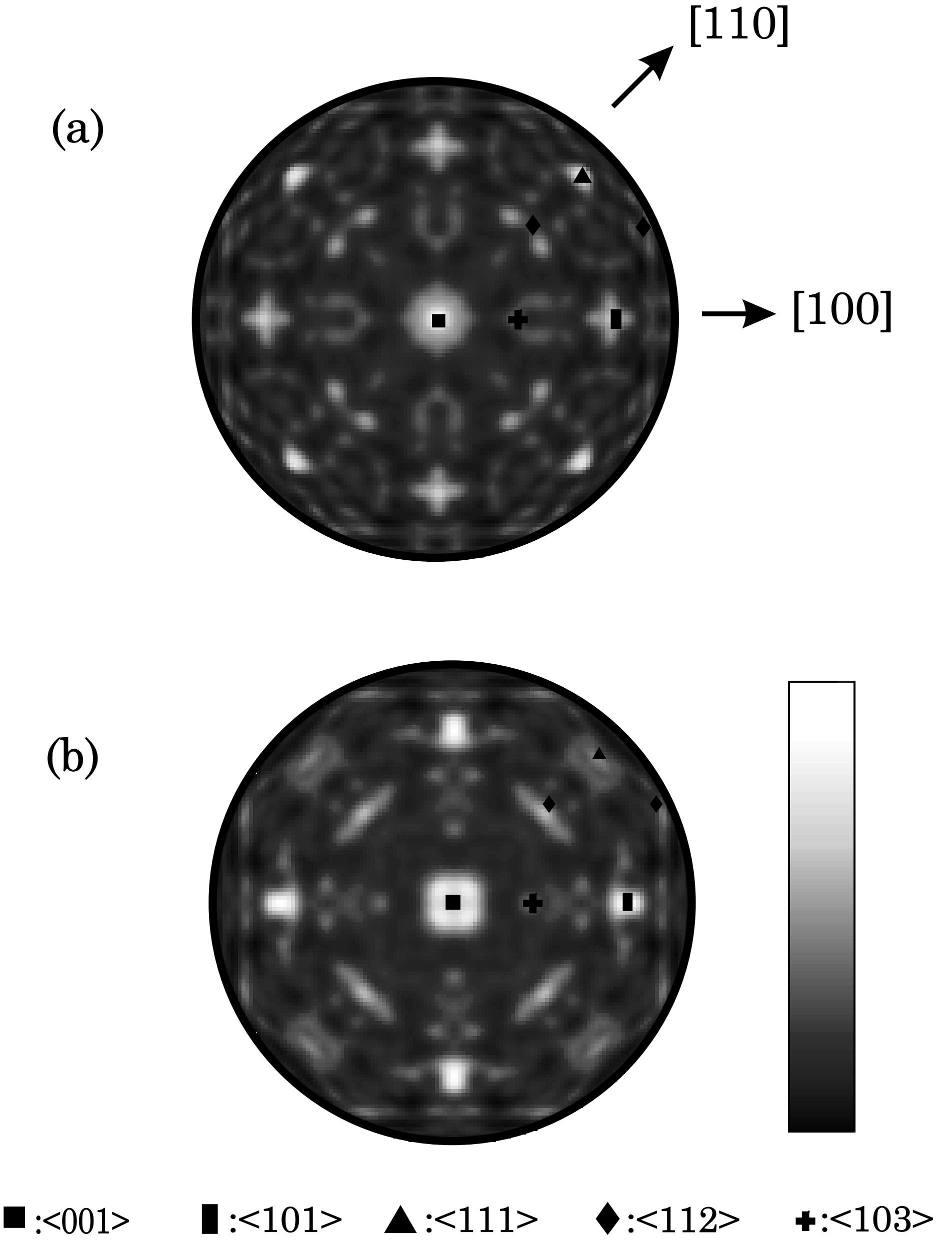

Figure 4.8: Calculated diffraction patterns due to (a) Mg KLL Auger (1180 eV) s-wave emitter, and, (b) O 1s photoemission (955 eV) from a flat MgO(001) surface. The patterns are plotted as a function of a uniform $\mathbf{k}$ grid with $\mathbf{k}_{||}=0$ (where the subscript "$||$" indicates component parallel to the surface) at the center of the patterns. The major low-index crystallographic directions are indicated by different symbols.

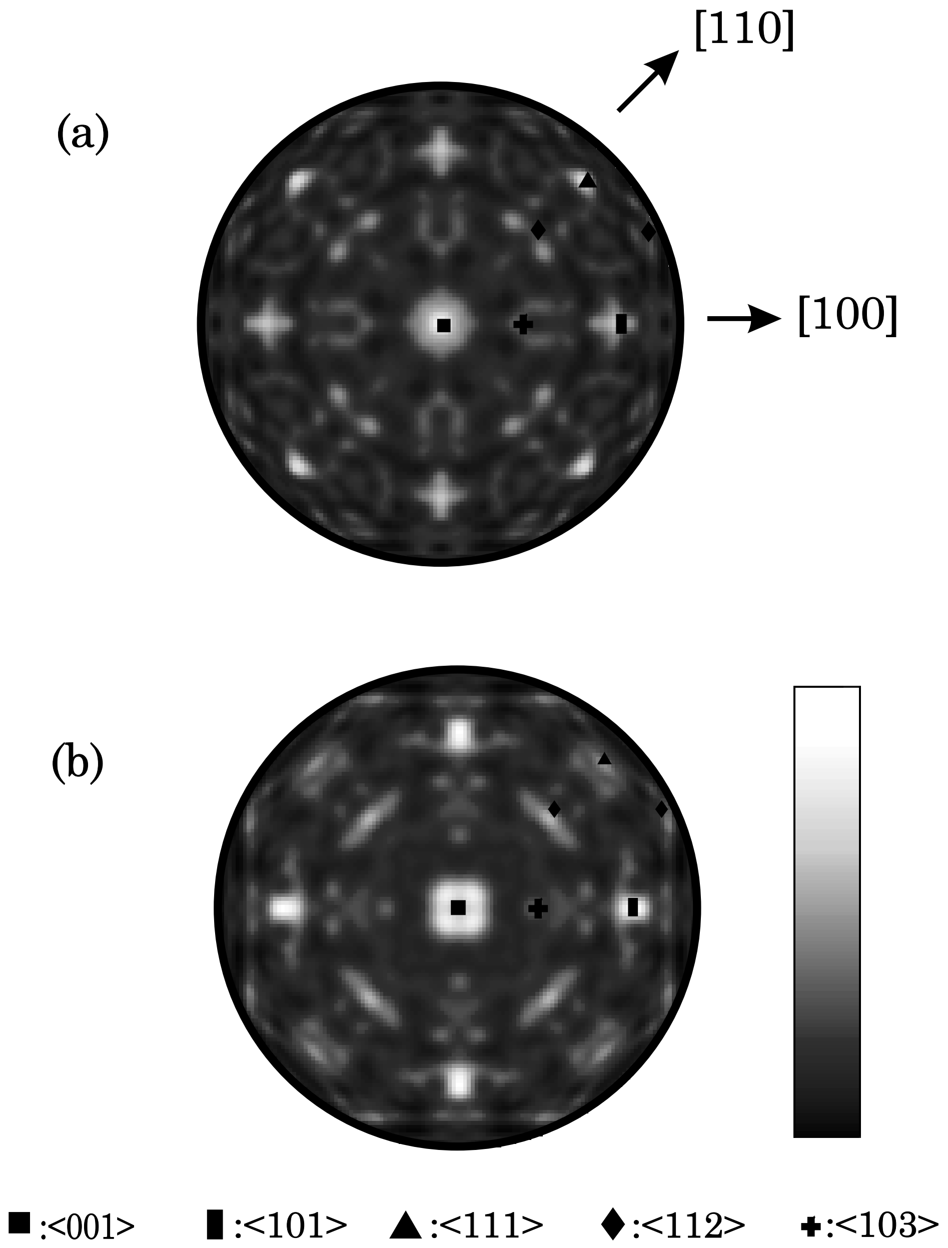

Figure 4.9: Calculated diffraction patterns of (a) Mg KLL Auger (1180 eV) s-wave emitter, and, (b) O ls photoemission (955 eV) from a rumpled MgO(001) surface. The major low-index crystallographic directions are marked by different symbols.

5 ^{o} shifts in the experiments. This indicates that the peak shifts in the diffraction patterns may not be caused by the rumpling of the MgO(001) surface. The reason for the insensitivity of electron diffraction to a rumpled MgO(001) surface is that the diffraction pattern produced by the emitter close to the surface does depend heavily on the rumpling model. The sensitivity to the rumpling decreases as the emitter goes into the bulk where the local structure is essentially the same as that from the flat surface. The overall intensities are made up of those from the surface and the bulk, and the bulk to surface ratio of the electron diffraction intensity derived from Eq. 4.4 is approximately:

$$\text{bulk to surface ratio} \approx \frac{\exp\{-d/\lambda\}}{1-\exp\{-d/\lambda\}} \approx 3.5 \tag{4.6}$$

where d=2.1 $\mathring{A}$ and λ=8 $\mathring{A}$ were taken. It is assumed that the pattern of the first layer is featureless (which is not true for the intensity at large polar angle), the second layer intensity is considered to be the surface component, and all the intensity below the third layer constitutes the bulk component. Due to the large ratio of bulk to surface diffraction intensity of the MgO(001) solid, such a large rumpling of 10 % and relaxation of 5% at the surface cannot be easily detected by electron diffraction experiments of this energy range.

Polar plots along the two major azimuths of [100] and [110] from the multiple scattering simulations due to the Mg and O emitters from the flat MgO(001) surface, and the electron diffraction experiments of the Mg KLL and O 1s photoemission from the cleaved MgO(001) surface are shown in Fig. 4.10 on page 115. Points of agreement between the simulations and the experimental patterns are (1) both the O 1s and Mg KLL [112] peaks are shifted toward lower polar angle by 3 to 5^o, and the sharp peak of the O pattern and the smooth peak of the Mg one are reproduced, (2) the O 1s curve shows a dip at [001] direction, and Mg KLL curve

Table 4.2: Forward scattering directions of electron diffraction from MgO(001) surface

Direction	Line	Bulk	Expt. (shifts)	Theory (shifts)
[001]	Mg KLL	0	0 (0)	0 (0)
	O 1s	0	0 (0)	0 (0)
[103]	Mg KLL	18.4	18.4 (0)	18.4 (0)
	O 1s	18.4	18.4 (0)	18.4 (0)
[101]	Mg KLL	45.0	46.0 (-1)	46. (-1)
	O 1s	45.0	46.0 (-1)	45. (0)
[201]	Mg KLL	63.4	63 (0)	63. (0)
	O 1s	63.4	60 (3)	60.5 (3)
[111]	Mg KLL	-54.7	-54.7(0)	-55. (0)
	O 1s	-54.7	-51.0(3.7)	-51.5 (3.3)
[112]	Mg KLL	-35.3	-32.3(3)	-33 (2.3)
	O 1s	-35.3	-30.5(4.8)	-31.8 (3.5)

doesn't, (3) the [101] peak for the Mg emitter is broader and lower than that of the O, and this Mg peak has a shoulder while the O peak doesn't, (4) there are two peaks in the Mg curve between [001] and [101] peaks, while there are three peaks in the O curve at the same region, (5) the [111] O peak is asymmetric and shifted to a lower polar angle by 5^o, while the Mg peak remains along the [111] direction. Forward scattering angles are listed in Table 4.2 for the experimental and calculated electron diffraction patterns from the Mg KLL and O 1s emitters together with the low-index crystallographic directions of the bulk MgO.

There are some small peaks that appear on the experimental patterns, such as the one at 10^o along [110] azimuth, but it can not be reproduced in the calculated diffraction curve. This minor discrepancy could be due to the approximation that emitters in only five layers are explicitly calculated (with the contributions from the remaining layers approximated). Diffraction intensity differences between the fifth and deeper layer contributions might be the reason for the missing peaks. A layer-by-layer decomposition of from the calculated electron diffraction intensities are plotted along two major azimuths [100] and [110] in Fig. 4.11. Few differences between the diffraction intensity curves of layers 4 and 5 have been observed, which is the rationale behind the approximation described by Eq. 4.4 A very smooth diffraction intensity distribution around the normal direction (0^o) is seen on the curve contributed by the first layer. As the emitter goes deeper into the bulk, the number of minor peaks between [001] and [112] along [110] azimuth increases and the shapes of the peaks are also changed. These low polar angle peaks are mainly along the higher index crystallographic directions whose footprints show up when the emitter locates deeper into the bulk, and a calculation of containing more layers of atoms below the surface could simulate these missing peaks at low polar angles.

4.3.3 The role of the inelastic scattering length in electron diffraction

There still remains a question to be answered: why the forward-scattering peaks in the electron diffraction patterns of the MgO(001) surface do not always correspond to the low-index crystallographic directions, even though our calculated diffraction patterns reproduce the experimental results. It is well known that Mg and O atoms in the rocksalt MgO solid have a similar local environments with just different surrounding species. What then is the main reason that causes the shifting between the forward-scattering peaks due to the Mg and O emitters? Fig. 4.8 and Fig. 4.9 show that very small peak shifts (within 0.5 ^{o}) were observed between the diffraction patterns from flat and rumpled MgO surfaces, which is much less than the measured peak shifts of 3 to 5 ^{o}. This evidence strongly suggests that the shifts of the peak positions in the Mg and O diffraction patterns are not sensitive to the surface rumpling, and the observed peak shifts may not be due to the rumpling of the MgO(001) surface.

It will be demonstrated in this section that a short electron inelastic scattering length could be the reason that causes the peak shifts in diffraction patterns. In order to do this, a series of calculations of electron diffraction of Mg and O emitters from flat and rumpled MgO(001) surfaces have been performed by taking the imaginary part of the electron energy, E_i, to be 0, 4, 8, 12, and 16 eV. It can be easily shown that the electron inelastic scattering length is

$$\lambda = \frac{\sqrt{2E}}{E_i}$$

in Hartree atomic units, so the corresponding inelastic scattering length of an electron ranges from infinity to about 8 $\mathring{A}$.

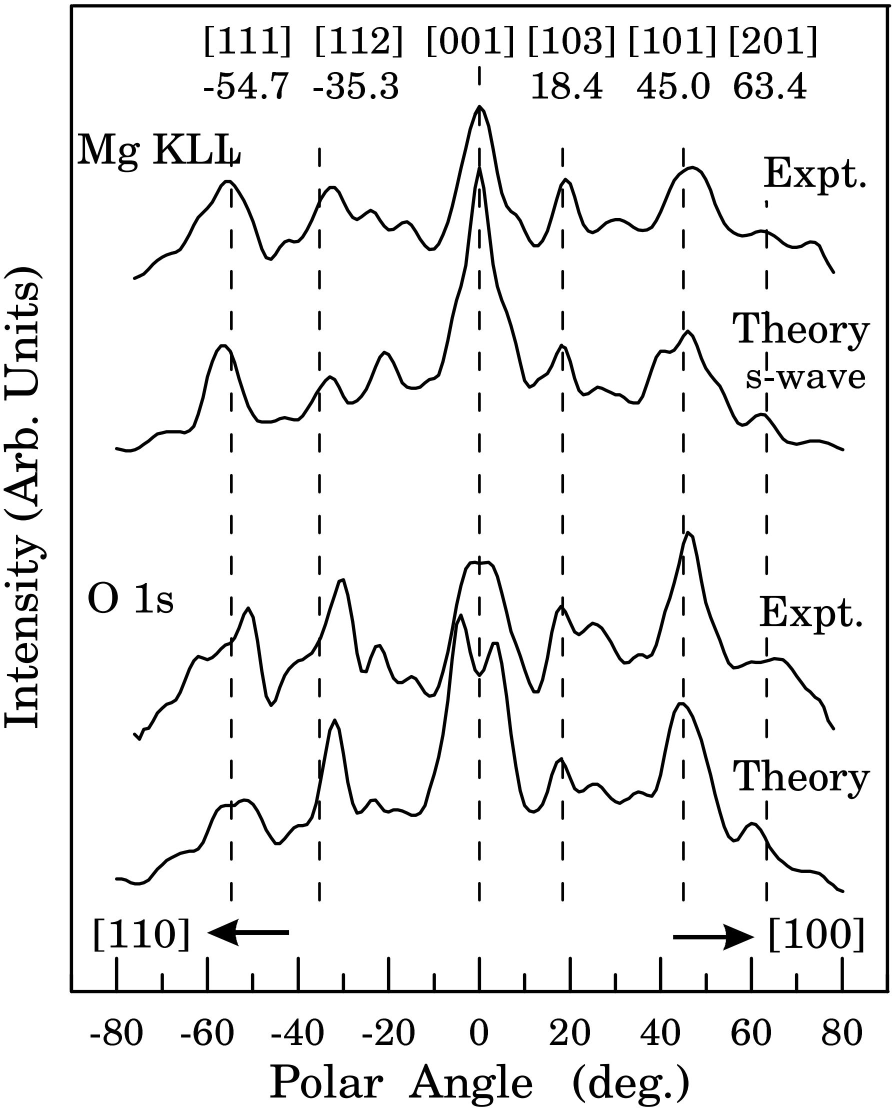

Figure 4.10: Multiple scattering calculations of electron diffraction are plotted along two major azimuths of [110] and [100] and compared with the experiments of Mg *KLL* and O 1s curves from a cleaved MgO(001) surface.

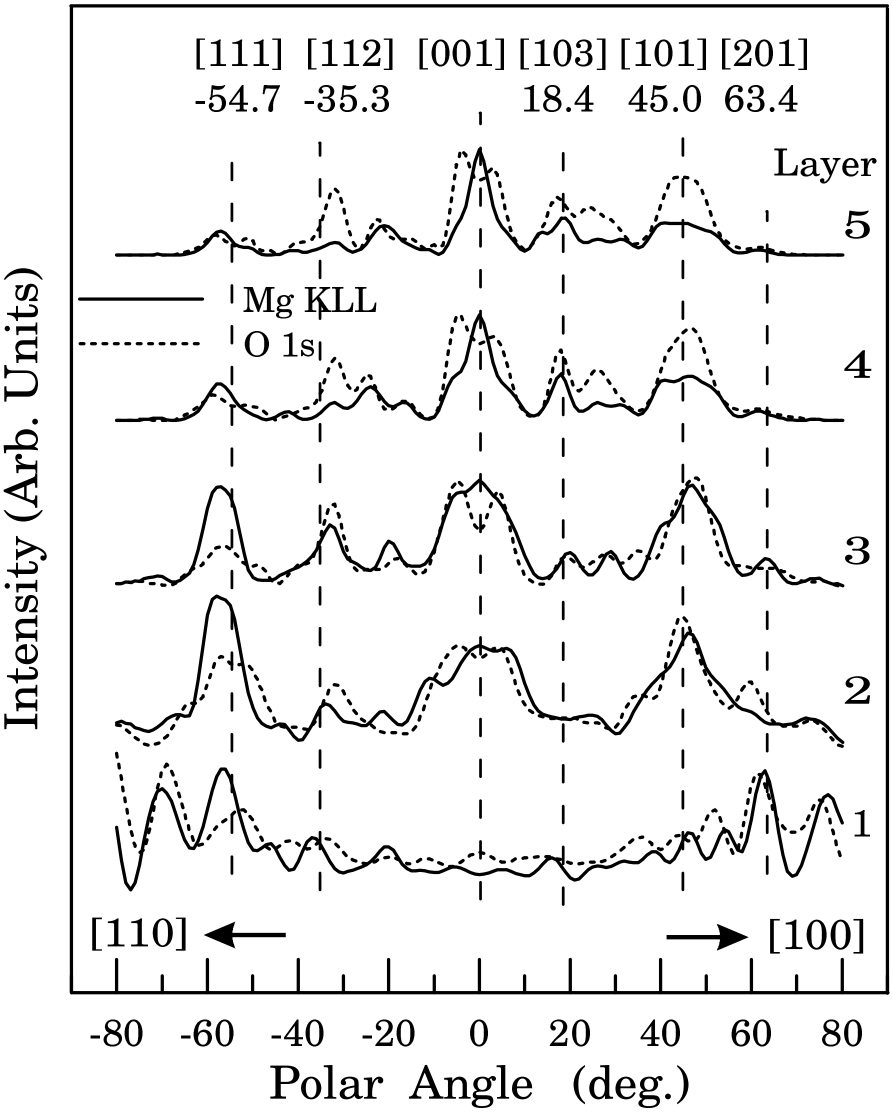

Figure 4.11: Calculations of a layer-by-layer decomposition of the diffraction intensities of the Mg and O emitters from a flat MgO(001) surface. The plots are along two major azimuths of [110] and [100] of layers 1 to 5. Solid lines represent the Mg emitter and the dashed line the O emitter.

Calculations of the diffraction intensity along two major azimuths of [110] and [100] are shown in Fig. 4.13 on page 121 for the Mg emitter, and Fig. 4.14 on page 122 for the O emitter for the different inelastic scattering lengths. The experimental results for both emitters are also shown on the top panel of the plot for a closer comparison. It can be seen on the diffraction curves for the Mg emitter in Fig. 4.13 that as the imaginary part of energy is increased from curve (a) to curve (e) (or the inelastic scattering length of the electron is decreased), most of the diffraction intensity peaks gradually change in shape and position, such as the peaks at [101] and [103] for both flat and rumpled surfaces, but the peak at [111] changes dramatically from a narrow peak and off the [111] direction by -4^o (at a larger polar angle position) to a broader one and peaked at the [111] crystallographic direction. By comparing with the experimental electron diffraction from the Mg KLL line, one can find that the curve (e) with an inelastic scattering amplitude of 8 $\mathring{A}$ fits the experimental result best. Similar trends can also be observed in Fig. 4.14, of an O 1s emitter, that the shape of [111] peak changes dramatically to an asymmetric shape and only curve (e) in Fig. 4.14 is a close fit to the O 1s experimental curve. This is also true for the [101] peak for both Mg and O emitters. In general, the calculated diffraction patterns of Mg and O emitters from flat and rumpled surfaces are a little different in the shapes and positions of the diffraction intensity profiles for long inelastic scattering lengths, whereas differences become distinctive as the inelastic scattering length decreases. This is consistent with the general knowledge that a shorter inelastic scattering length of an electron makes an electron diffraction pattern more sensitive to the surface. Further measurements of electron diffraction due to Mg and O emitters at lower energies, a region of a shorter inelastic scattering length, should be conducted to check the flat and rumpled MgO surface models. From the above conclusions one could infer that the anomalous differences between the Mg KLL Auger and the O 1s core-level photoelectron diffraction are due much more to the short inelastic scattering length in the insulating MgO material, and that the forward-scattering feature in the electron diffraction is only valid for the case of metals where the inelastic scattering length is relatively large.

A very simple intuitive picture, as shown in Fig. 4.12 on page 120, could explain part of the shifting of the forward-scattering peaks off their low-index crystallographic directions, and toward lower polar angles. At an infinite or long electron inelastic scattering length, for example, and under an assumption that there is a scattered atom or row of atoms at a large polar angle position corresponding to an emitter at the origin, the forward-scattering peak will be formed along the chain connecting by the emitter and scatterer(s) if diffraction interferences from other atoms in the cluster are weak. However for a short inelastic scattering length, the forward-scattering peak will become asymmetric due to the path difference that electron travels in the solid. The path length at lower polar angle side of this low-index crystallographic direction is shorter than that at the higher angle side of this direction, and it will experience a smaller damping than that at the higher angle, and therefore, the forward-scattering peaks will be moved to a lower polar angle as has been observed by both experiments and theoretical calculations. While in a large cluster, the interference from other atoms could be strong, and the scattering peak might be off the forward-scattering direction due to the multiple scattering diffraction from atoms along other rows and planes, so the changes in the position of the peaks are very difficult to predict just by using this simple picture. This could be the reason that some forward-scattering peaks are not altered and remain at same forward-scattering directions when the elastic scattering length is changed in Fig. 4.13 and 4.14. Calculations for electron energies of 1180 eV and 955 eV are consistent and suggest that the electron inelastic scattering length in a MgO crystal is short and at the lower end of the universal curve for this energy range.

4.3.4 Electron diffraction of s and d-wave emitters from a MgO surface

In the previous section, an s-wave was used in the calculation of electron diffraction from a MgO(001) surface. It is often assumed [65] that an emitted Auger electron an s-wave due to the isotropy of Auger emission. However, considerable differences on the diffraction patterns could still be observed if the initial emitter wave was changed to one of high angular momentum, such as the case of electron diffraction of the Cu L_3VV Auger line from Cu(001) surface [72].

In a review paper [43] of the calculations of Auger transition matrix elements, Weissmann and M*ü*ller have shown that the possible values of the angular momentum l of the ejected Auger electron wave are determined by the selection rules[64]:

$$|l_i - |l_j - l_k|| \leq l \leq l_i + l_j + l_k$$

$$l + l_i + l_j + l_k = even \tag{4.7}$$

where l_i represents the angular momentum quantum number of core hole, and l_j and l_k represent those of the final state holes. For the Mg KL_2L_3 transition, l_i=0, l_j=1, and l_k=1, and the final possible angular momenta of the ejected Auger electron waves are l=0 or 2 corresponding to an Auger s or d-wave emitter.

As pointed out before in reference [72] Auger or photoelectron diffraction

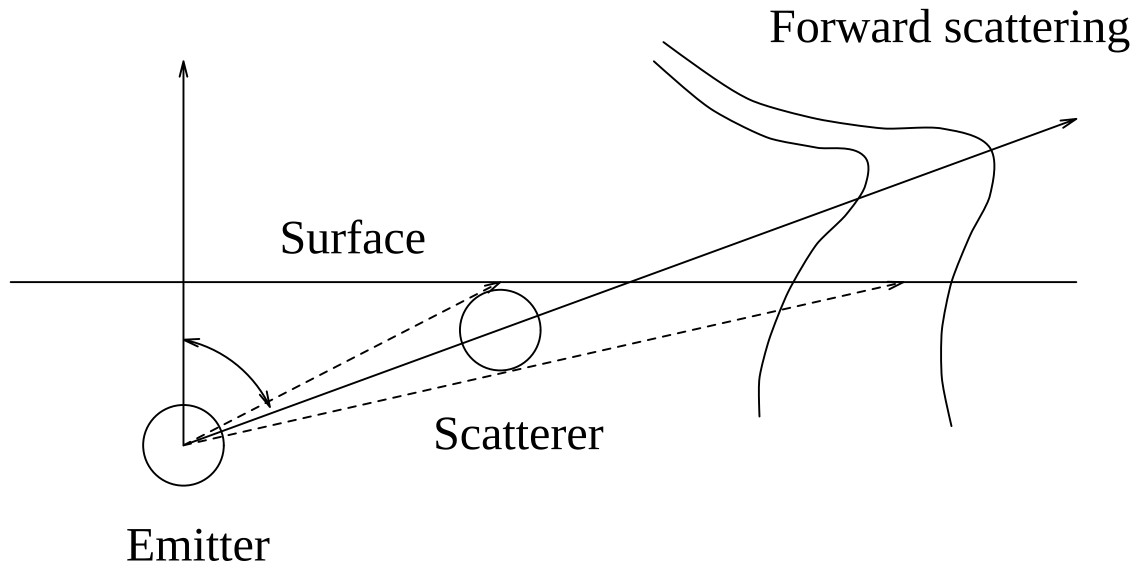

Figure 4.12: Scheme of forward-scattering peak shift. For a short inelastic scattering length, the forward-scattering peak will become asymmetric due to the path difference that electron travels in the solid. The path length at lower polar angle side of this low-index crystallographic direction is shorter than that at the higher angle side of this direction, and it will experience a smaller damping than that at the higher angle.

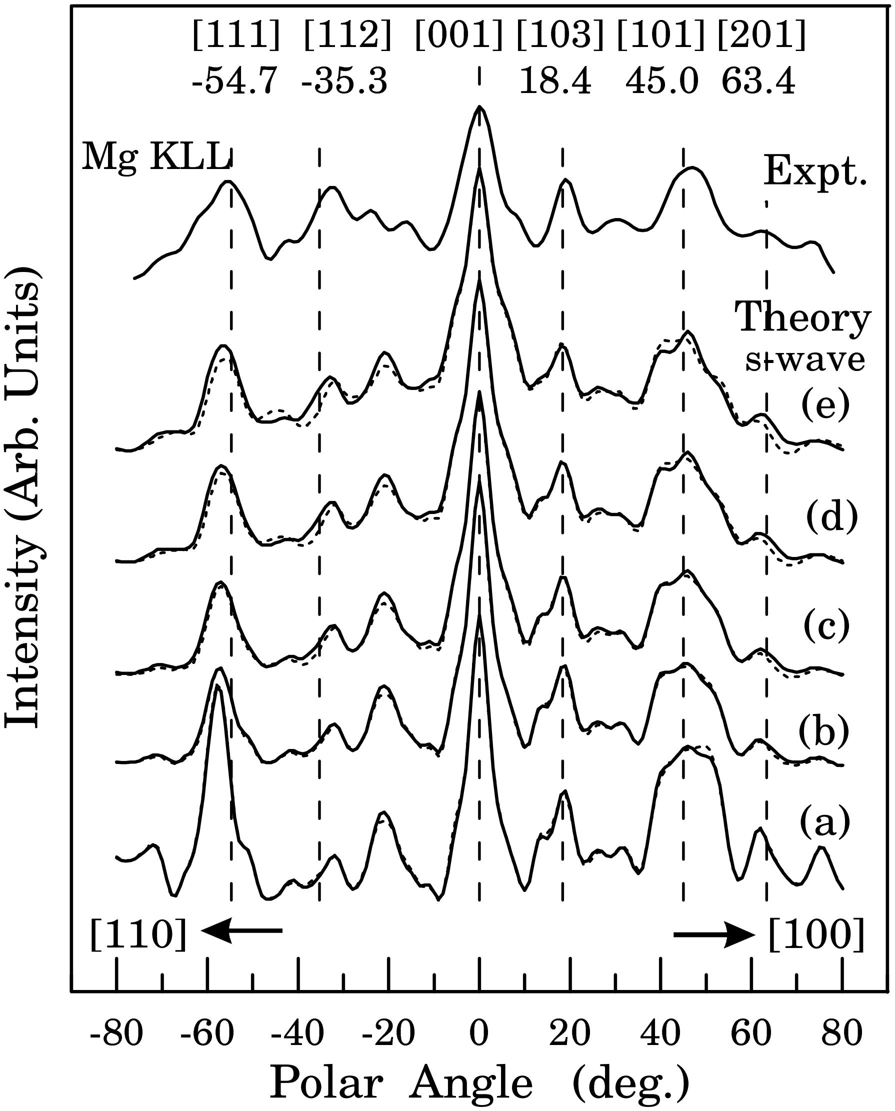

Figure 4.13: Multiple scattering calculations of Mg Auger *KLL* diffraction from flat and rumpled MgO(001) surfaces with an imaginary part of the electron energy of (a) 0 eV, (b) 4 eV, (c) 8 eV, (d) 12 eV, and (e) 16 eV. The experimental result for the Mg Auger *KLL* line is also plotted on the top panel for a closer comparison. Curves drawn in solid lines are the calculations from a flat MgO(001) surface, and in dashed lines the calculations from a rumpled surface.

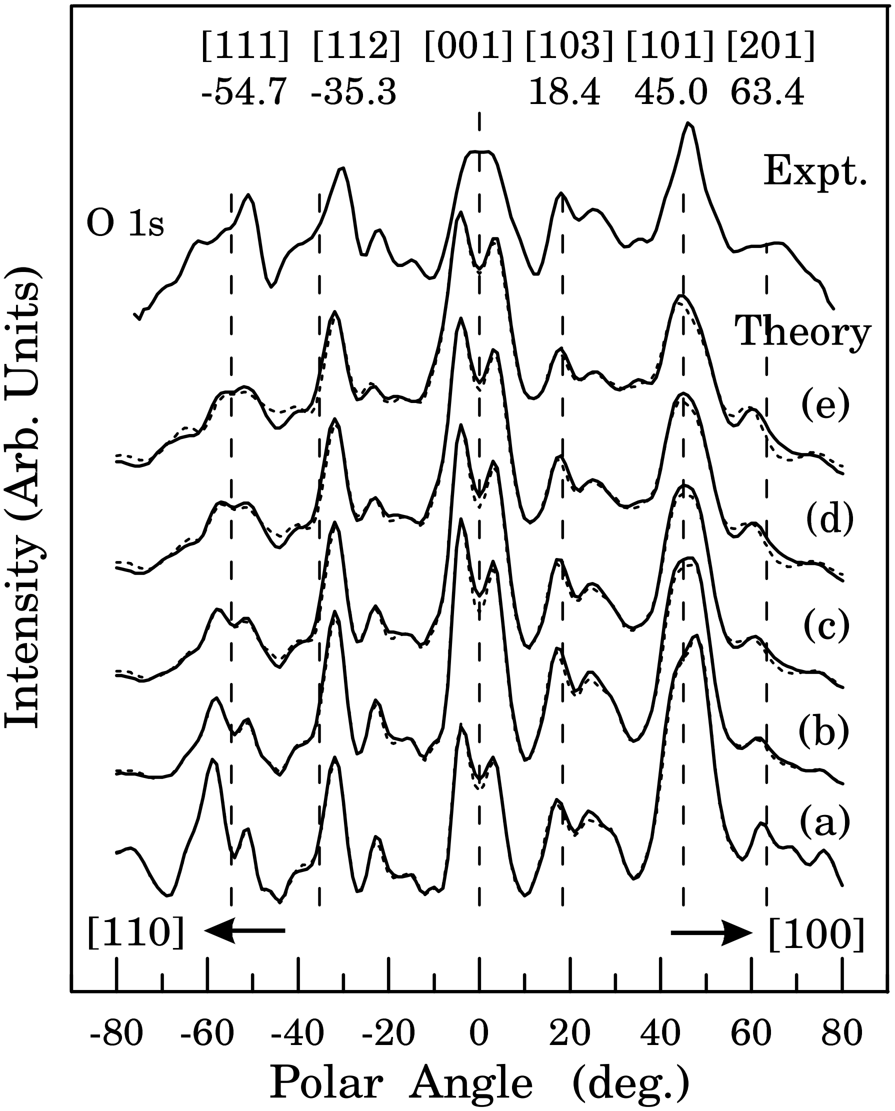

Figure 4.14: Multiple scattering calculations of O 1s photoemission diffraction from flat and rumpled MgO(001) surfaces with an imaginary part of electron energy of (a) 0 eV, (b) 4 eV, (c) 8 eV, (d) 12 eV, and (e) 16 eV. The experimental result of O 1s photoemission is plotted on the top panel for a closer comparison. Curves drawn in solid lines are the calculations from a flat MgO(001) surface, and in dashed lines the calculations from a rumpled surface.

patterns from metal surfaces of high electron kinetic energy will form forward-scattering peaks along low-index crystallographic directions, but diffraction patterns of different angular momenta of the Auger emitter wave will result in detailed differences in the diffraction patterns. This is especially true when the kinetic energy of the free Auger electron is in the low energy range, but not so obvious at high energy [72]. Our primary goal here is to calculate the electron diffraction patterns of s and d-wave emitters, and to compare them with experiments.

The results of the calculations of Auger diffraction patterns for a d-wave emitter from a flat and a rumpled MgO(001) surface are shown in Fig. 4.15 on page 125. Very similar diffraction patterns are produced from both flat and rumpled surfaces, and they are also close to those calculated patterns in Fig. 4.8 (a) and Fig. 4.9 (a) for the s-wave emitter. This result is not unexpected for the high electron kinetic energy range, as firstly, it is known that the electron diffraction at this energy range is not sensitive to the rumpling of a MgO surface, and secondly, the diffraction patterns calculated for either an s or a d-wave emitter will result in a similar forward-scattering pattern as pointed out before.

In order to have a closer comparison, electron diffraction patterns calculated using an Auger s and d-wave emitter are plotted together in Fig. 4.16 on page 126, along with the experimental electron diffraction of the Mg KLL line. All the forward-scattering peaks from both simulations in Fig. 4.16 match the experimental pattern nicely, but the shapes and positions of the forward-scattering peak in the s-wave simulation agrees better with the experiment than that of the simulation from the d-wave emitter. The major result is that along the [013] direction (also [013], $[\bar{1}03]$, and $[0\bar{1}3]$ directions) the "Ʊ" shaped forward-scattering peak in the s-wave simulation (b) matches a similar "Ʊ" shaped peak on the experimental pattern (a), while the simulation of the d-wave emitter (c) shows a "=" shaped peak along this direction. The arrows on the electron diffraction patterns on Fig. 4.16 are pointed at the [013] peaks. From selection rules Eq. 4.7, one can see that the Mg KLL transition could produce either s or d-wave emitters, and that the final Auger electron wave could be a mixed state of s and d-wave. However, the evidence of Fig. 4.16 strongly suggests that this Auger transition is dominated by the s-wave emitter.

4.3.5 Conclusions

Auger and photoelectron diffraction angular distribution profiles from MgO(001) surfaces have been studied. In general, there is coincidence between the low-index crystallographic directions and the forward-scattering maxima on a diffraction pattern. However, anomalous phenomena of the peak shifts off the forward-scattering direction have been observed in the diffraction patterns of Mg KLL Auger and O 1s photoemission lines from a sputtered & annealed and a cleaved MgO(001) surface. This is in contradiction to the previous expectation that for high electron kinetic energies forward-scattering peaks on the electron diffraction patterns should be found at the projections of the low-index crystallographic directions.

Theoretical calculations of electron diffraction have been performed on flat and rumpled MgO(001) surfaces, and the results show that diffraction patterns do not differ very much between flat or rumpled MgO surfaces, even when a highly rumpled surface structure of 10 % rumpling and 5 % relaxation has been used in the calculations. A simple calculation shows that the bulk to surface ratio of diffraction intensities in a MgO solid is about 3.5, which means that the diffraction patterns contain more structural information about the bulk than that about the

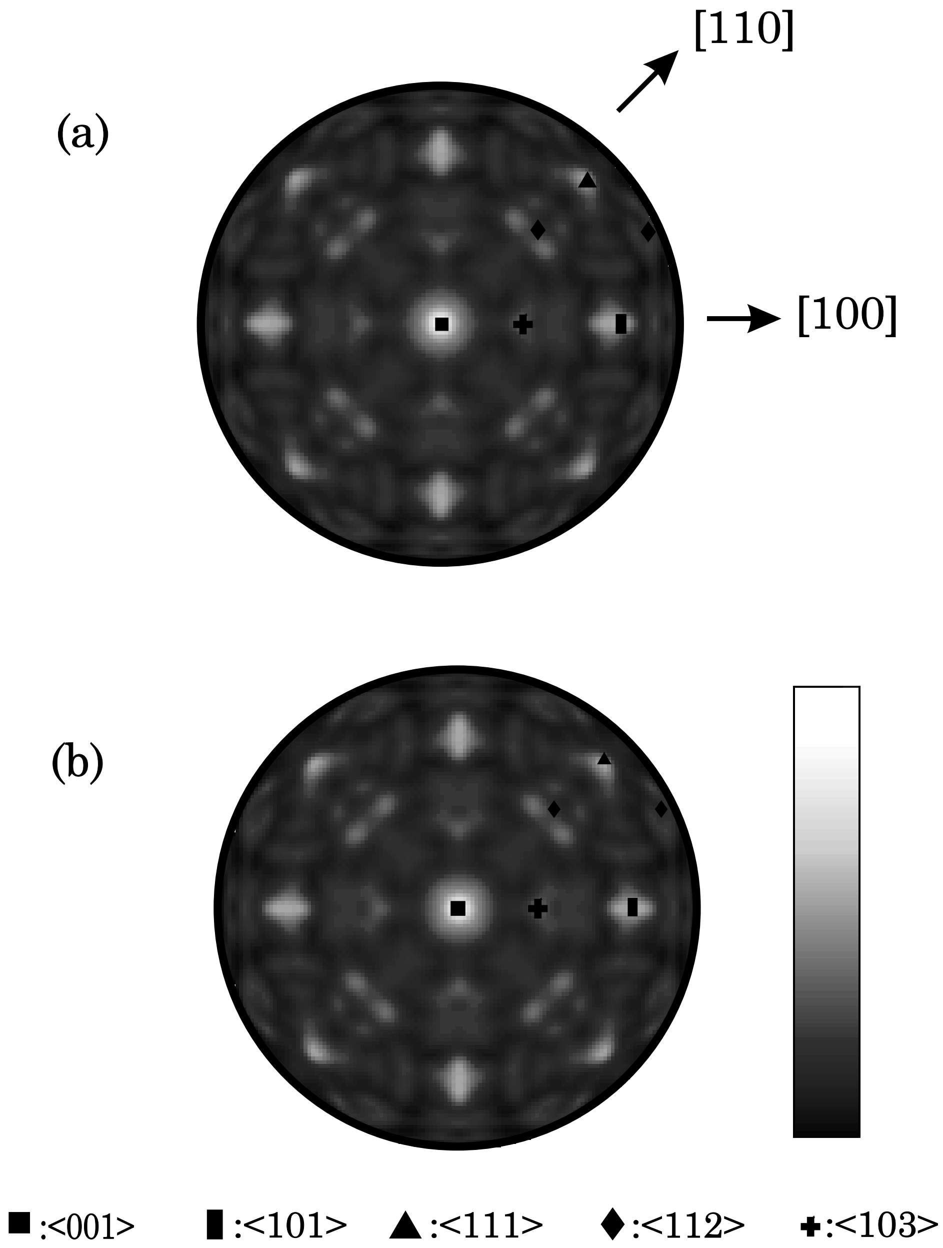

Figure 4.15: Calculated diffraction patterns of the Mg *KLL* Auger (1180 eV) d-wave emitter from (a) a flat, and, (b) a rumpled MgO(001) surface. The major low-index crystallographic directions are indicated by different symbols.

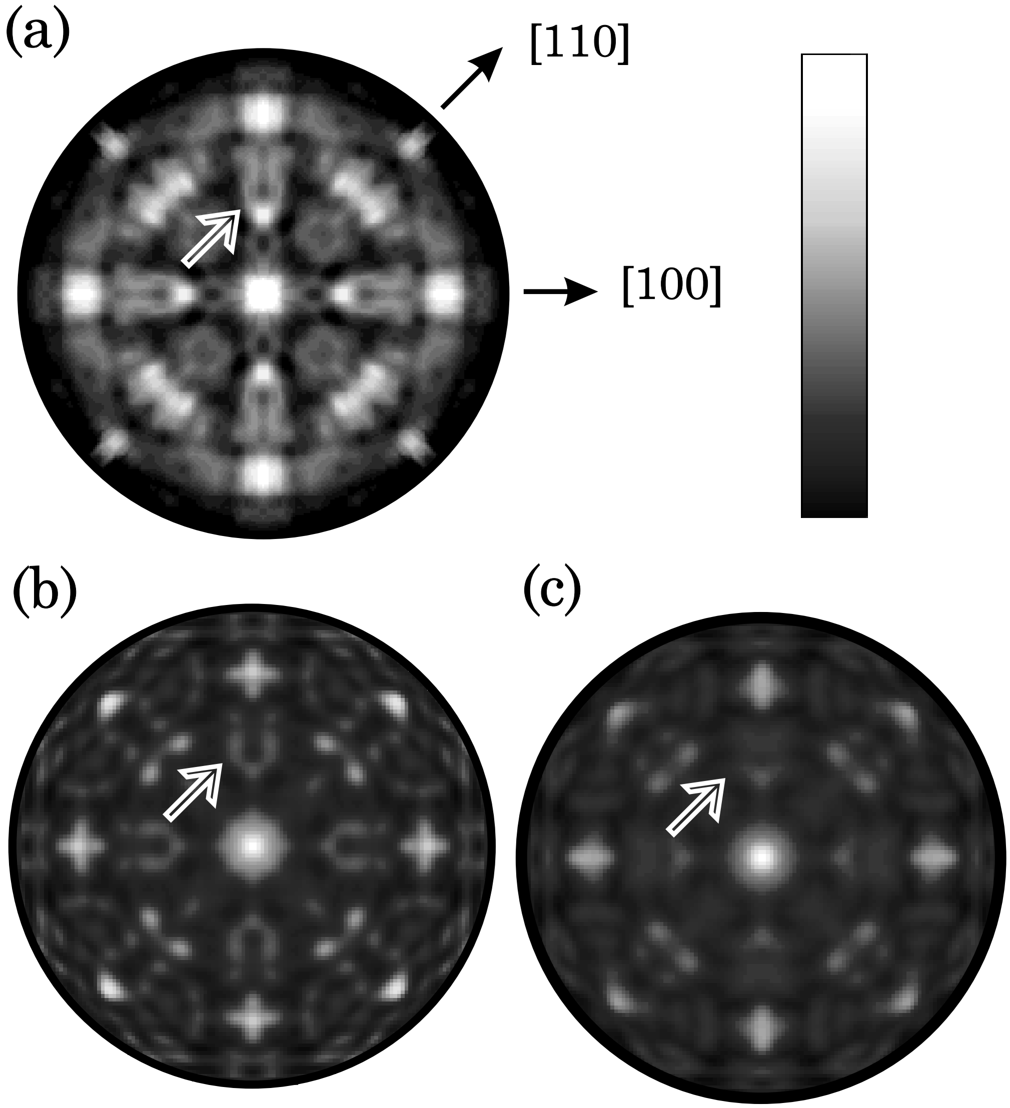

Figure 4.16: Comparison between the experimental electron diffraction pattern from a cleaved MgO(001) surface and the calculations using s and d-wave emitters at 1180 eV from a flat MgO(001) surface model. (a) Experimental diffraction pattern of the Mg KLL line, (b) Simulation of an s-wave emitter, (c) Simulation of a d-wave emitter. The arrows are pointed at peaks along the [013] direction. The simulation due to the s-wave emitter in pattern (b) reproduces the “℧” shaped peak in the experimental pattern (a), while the simulation of the d-wave emitter in pattern (c) shows a “=” shaped peak along this direction.

surface structure. This also indicates that the peak shifts toward lower polar angles are not necessarily caused by the rumpled surface structure of MgO(001).

Good agreement between the experimental electron diffraction patterns of the Mg KLL and the O 1s lines from a cleaved MgO(001) surface and calculated diffraction patterns due to a Mg s-wave emitter and an O final p state have been obtained. Those points of agreement include: (a) that some of the diffraction peaks are shifted toward a lower polar angle by 3 to 5^o compared to their forward-scattering directions, with O 1s peaks moving much more than those of Mg Auger KLL, e.g. the peaks at [111] and [112]. (b) that some of the diffraction peaks of both the Mg and O emitters move by the same amounts toward lower angles, e.g. the peaks at [101]. (c) that some of the peaks remain along their low-index crystallographic directions, e.g. the Mg and O peaks at [101] and [103]. (d) that the diffraction pattern of O 1s shows a central dip at its origin.

It was found that a short electron inelastic scattering length of about 8 $\AA$ at 1000 eV in the MgO crystal is one of the major factors that causes the shifts of the forward-scattering peaks in diffraction pattern, and this short inelastic length is at the lower end of the universal curve. A series of calculations show that a smaller inelastic scattering length can move those peaks off their forward-scattering directions to lower polar angles, and give a good overall intensities fit to the experimental intensities at both energies of 1180 eV and 955 eV. It is also shown that a short inelastic scattering length in the electron diffraction from a MgO surface can well reproduce those peak shifts accurately, and that the forward-scattering model will not be too accurate in the case where the solid has a short electron inelastic scattering length, such as an insulator like single crystal MgO. Observed differences in shape and position between Mg KLL and O 1s peaks are partly due to the differences between the different atomic scattering factors of Mg and O atoms.

Diffraction profiles were also studied from the two differently-prepared surfaces of MgO. Although similar in crystallography, there are substantial differences in the detailed shape and intensity of the forward-scattering peaks between the two experimental patterns. It is shown that the electron diffraction experiment performed on the cleaved MgO surface is in much better agreement with the calculations of a defect free MgO surface model, while the diffraction experiment on the sputtered & annealed surface are less accurately reproduced by the theoretical calculations. This fact suggests that the cleaved MgO surface has a fewer number of defects than that of the sputtered & annealed surface, and that this is consistent with the He^+ scattering experiments [58].

Since the Auger transition rule shows that the final ejected Auger electron wave could be an s, d or in a mixed state of s and d waves, a possible d-wave emitter cannot be excluded in the calculations. Theoretical calculations have been conducted on electron diffraction for the Mg d-wave emitter, and compared with the s-wave simulation and the experimental electron diffraction of Mg KLL Auger line. It was found that s-wave simulation agrees better with the experiment than that of d-wave although the patterns are quite similar. We conclude that in the Mg KLL Auger transition, a final electron wave of angular momentum l=0 dominates.

Calculations were also done on electron diffraction from a MgO(001) surface, assuming that neutral Mg and O atoms exist in a MgO solid. The radii of neutral Mg and O were assumed to be 1.06 $\mathring{A}$, and their atomic scattering factors were plotted in Fig. 4.6 and Fig. 4.7. Little difference was found between the diffraction patterns calculated using ionic Mg^{2+} and O^{2-} atoms and results of neutral Mg and O atoms. The similarity of the calculated electron diffraction patterns from both ionic and neutral atoms were mainly due to the similar scattering strength in their atomic scattering factors, as there are only about 10% different in the forward-scattering direction, and they are almost the same at angles larger than 70^o.

CHAPTER 5

The Simulation Of Experimental Photoelectron Diffraction From A $CoSi_2(111)$ Surface

In this chapter we discuss the practical details of performing a photoelectron diffraction calculation to simulate a real experimental diffraction pattern. Such considerations include calculating the transition probability from the atomic core-state of an emitter atom, which is assumed to be excited by a polarized x-ray photon, the angular momenta of the emitter waves, and the interference among those waves in a multiple scattering process. The dipole selection rule for core-level photoexcitation shows that the final free states of the photoelectrons are s and d waves for the Co-3p and Si-2p core-state, and from quantum mechanical principles, some of the emitted waves will be mutually coherent and some will be incoherent amongst themselves in the resulting diffraction. The coherent or incoherent superpositions of those emitted waves are subject to the conditions that they come from the same angular momentum quantum core-state. In this chapter, simulations of XPD from a $CoSi_2(111)$ surface at both high and low energies are performed, and the results prove the importance of considerating of final state interference as well as the details of the experimental setup in the calculation of the diffraction patterns. It will be seen that experimental configuration-dependent simulations give much more convincing results than a calculation using only an s-wave emitter, and this is most clearly the case when the photoelectron energy is low.

5.1 Introduction

Because of its quite perfect and sharp interface with a Si crystal and many favorable features for the fabrication of hetero-epitaxial systems, metallic di-silicides are considered important both in experimental and theoretical work. In this field, $CoSi_2$ has attracted more attention in recent decades due to its structural compatibility with a Si and relatively high electric conductivity. Numerous studies [66,?,?] have been concerned with the quality of the epitaxial-growth kinetics of $CoSi_2$ ultrathin films on a Si surface, especially the $CoSi_2$/Si(111) interface morphology and the characterization of the $CoSi_2$(111) surface crystallography. The small mismatch with Si crystal tends to make a $CoSi_2$ ultrathin film grow easily on Si surface, and has wide applications in microelectronic devices such as Schottky junctions, and hetero-junction or double hetero-junctions with Si.

Electron diffractions, such as x-ray photoelectron diffraction (XPD) and Auger electron diffraction (AED), are useful tools for the understanding of crystal geometries. Recent controversies regarding the interpretation of the Auger electron diffraction pattern measured by Frank *et al.* [72], have contributed much to the understanding of the importance of the electron source waves. We have already shown, in Chapter 3, that in full multiple scattering simulations of AED from a Cu(001) surface at high and low energies, the source wave of the Auger electron emitter plays an important role in the resulting diffraction patterns at low energy. For the high energy electron diffraction, the patterns are dominated by forward-scattering peaks, but they are not very sensitive to the character of the source waves. In this chapter, diffraction patterns of angle-resolved Co-3p XPD at higher energy and Si-2p normal emission at low energies from a $CoSi_2$(111) surface are calculated using a full multiple scattering scheme by taking account of experimental conditions under which the XPD data were measured. In the Co-3p or Si-2p photoemission process, the resulting emitted wave-fields would be mainly composed of s and d waves due to the dipole transition selection rule. Different emitted wave angular momenta will affect features in the diffraction patterns, as will the orientations of the x-ray polarization directions in an actual experimental setup.

5.2 Multiple scattering of the core-level photoelectron diffraction

5.2.1 Multiple scattering theory for photoelectron diffraction

We will briefly recount, here, the forms of a source wave and subsequent scattered waves in a photoemission process. Initially an electron is emitted from a core-level by a photoemission process, and a component of resulting wave-field in an angular momentum basis could be expressed by:

$$A^{(0)}_{LL_c} h^{(1)}_l (kr) Y_L(\hat{\mathbf{k}}) \tag{5.1}$$

where $A^{(0)}_{LL_c}$ is the initial amplitude of the emitting wave originating from bound core-state $|n, L_c\rangle$ to final free state $|\epsilon,\mathrm{L}\rangle$, where n is the principal quantum number of the core-states and ϵ is the kinetic energy of the free electron, $L \equiv (lm)$, l is the angular momentum quantum number and m the magnetic quantum number, $\mathbf{r}$ is a position vector with respect to the emitter at the origin, $h^{(1)}_l$ the Hankel function of order l, $Y_L(\hat{\mathbf{k}})$ a spherical harmonic function and $\mathbf{k}$ the wave-number of the emitted electrons.

It has already been shown [21] that the final components of the outgoing wave can be expressed as:

$$\mathbf{A}^{(N)} = \mathbf{S}^{(N)}\mathbf{A}^{(0)} \tag{5.2}$$

where the matrix $\mathbf{A}^{(N)}$ represents the corresponding expansion coefficients of the wave-field propagating outwards from the N-th shell with matrix element of $A^{(N)}_{LL_c}$. The scattering matrix $\mathbf{S}^{(N)}$ can be calculated by using our concentric shell algorithm program. With $\mathbf{S}^{(N)}$ evaluated by this algorithm, a component of wave-field outgoing from the N-shell cluster can be evaluated from:

$$A^{(N)}_{LL_c} h^{(1)}_l(kr) Y_L(\hat{\mathbf{k}}) = \sum_{L'} \mathbf{S}^{(N)}_{LL'} \mathbf{A}^{(0)}_{L'L_c} h^{(1)}_l(kr) Y_L(\hat{\mathbf{k}}) \tag{5.3}$$

where $S^{(N)}_{LL'}$ are the elements of the scattering matrix $\mathbf{S}^{(N)}$. The angular distribution of the far-field intensity could be expressed in the form:

$$I_{\mathbf{XPD}}(\hat{\mathbf{k}}) = \sum_{L_c} | \sum_{L} \sum_{L'} S^{(N)}_{LL'} A^{(0)}_{L'L_c} (-i)^l Y_L(\hat{\mathbf{k}})|^2 \tag{5.4}$$

The summation over L_c is due to the quantum mechanical principle that the resulting wave-fields would involve waves that are mutually coherent if they originally come from the same core-state, and mutually incoherent if they are emitted from different core-states. The $\mathrm{A}^{(0)}_{LL_c}$ would be the dipole transition matrix element for an atomic photoexcitation process if the wavelength of the x-ray is considerably larger than the radius of the emitter. The detailed calculation of $\mathrm{A}^{(0)}_{LL_c}$ are discussed in Sec. 5.2.2.

5.2.2 Dipole transition in Sample Reference Frame and Laboratory Reference Frame

In order to transform spherical harmonics from a reference frame labeled by $\mathbf{a}'=(x', y', z')$ to another specified by $\mathbf{a}$=(x,y,z). One can define a rotation matrix

[18]:

$$D^{(l)}_{m^{'},m}(\mathbf{a},\mathbf{a}^{'}) = e^{im^{'}\gamma+im\alpha} d^{(l)}_{m^{'},m}(\beta) \tag{5.5}$$

where α, β and γ are the Eulerian angles, and are defined by the following relations.

$$cos\beta = sin\theta_2 sin\theta_1 cos(\phi_2-\phi_1) + cos\theta_2 cos\theta_1$$

$$sin\alpha sin\beta = sin\beta_2 sin(\phi_2-\phi_1)$$

$$cos\alpha sin\beta = sin\beta_2 cos\theta_1 cos(\phi_2-\phi_1) - cos\theta_2 sin\theta_1$$

$$sin\gamma sin\beta = -sin\theta_1 sin(\phi_2-\phi_1)$$

$$cos\gamma sin\beta = -cos\theta_2 sin\theta_1 cos(\phi_2-\phi_1) + sin\theta_2 cos\theta_1$$

The $d^{(l)}_{m^{'},m}(\beta)$ are determined by

$$d^{(l)}_{m^{'},m}(\beta) = \left(\frac{(l+m^{'})!(l-m^{'})!}{(l+m)!(l-m)!}\right)^{1/2} (cos(\beta/2))^{m^{'}+m}$$

$$(sin(\beta/2))^{m^{'}-m} P^{(m^{'}-m,m^{'}+m)}_{l-m^{'}}(cos\beta) \tag{5.6}$$

where $P^{m,n}_l(x)$ are the Jacobi polynomials. The $d^{(l)}_{m^{'},m}(\beta)$ obey the symmetry relations

$$d^{(l)}_{m^{'},m}(\beta) = d^{(l)}_{-m,-m^{'}}(\beta)$$
$$d^{(l)}_{m^{'},m}(\beta) = (-)^{m+m^{'}} d^{(l)}_{m,m^{'}}(\beta)$$

and can be calculated for $m^{'} \geq 0$ and $\mid m \mid \leq m^{'}$ by using the following recurrence relations:

$$b_{l+1,m} b_{l+1,m^{'}} d^{(l+1)}_{m^{'},m}(\beta) = (2l+1)((l+1)cos\beta - mm^{'}/l) d^{(l)}_{m^{'},m}(\beta)$$

$$-((l+1)/l) b_{l,m} b_{l,m^{'}} d^{(l-1)}_{m^{'},m}(\beta)$$

where $b_{l,m} = \sqrt{l^2 - m^2}$, and the initial values are:

$$d^{(m')}_{m',m}(\beta) = 2^{-m'} \left(\frac{(2m')!}{(m'+m)!(m'-m)!}\right)^{1/2} (cos(\beta/2))^{m'+m} (sin(\beta/2))^{m'-m}$$

and

$$d^{(m'+1)}_{m',m}(\beta) = \left(\frac{(2m'+1)}{(m'+m+1)(m'-m+1)}\right)^{1/2} ((m'+1)cos\beta - m)d^{(m')}_{m',m}(\beta)$$

By combining above equations, one end up with,

$$D^{(l)}_{m'm}(\theta,\phi) = e^{-im\phi}\left(\frac{(l+m')!(l-m')!}{(l+m)!(l-m)!}\right)^{\frac{1}{2}} \frac{(cos(\theta/2))^{m'+m}}{(sin(\theta/2))^{m'-m}} P^{(m'-m,m'+m)}_{l-m'}(cos\theta) \tag{5.7}$$

where the Eulerian angle α, β and γ are set to be θ, ϕ and zero respectively.

Since Eq. 5.4 is expanded in an angular momentum representation, *i. e.*, the bases are a set of spherical harmonic functions of lm, it will be useful to define a matrix, $\mathbf{D}(\theta,\phi)$, whose elements are given by Eq. 5.7. In an actual simulation process, we first calculate scattering matrix $\mathbf{S}$, then store it for later use in the simulations under different experiment configurations. With this rotation matrix, $\mathbf{D}(\theta,\phi)$, one can easily transform a transition matrix $A'^{(0)}_{LL_c}$ in a coordinate system (x', y', z') to another matrix $A^{(0)}_{LL_c}$ in a reference (xyz) by using:

$$\mathbf{A}^{(0)} = \mathbf{D}(\theta,\phi)\mathbf{A}'^{(0)} \tag{5.8}$$

With the aid of the above equation, we can include the experimental configuration in the calculations by connecting the laboratory reference frame (defined by the x-ray polarization) with sample reference (defined by crystal geometry). The modes of conducting the angle-resolved electron diffraction (ARED) experiments, such as (1) with fixed x-ray incident beam, moving the electron analyzer in a plane which passes through the sample normal to scan the polar angles, and rotating the sample about its normal to obtain the azimuthal scan ϕ, (2) with a fixed angle between x-ray beam and electron analyzer, and rotating the sample to scan the polar and azimuthal angles, and (3) with fixed relative positions of the x-ray incident beam and the sample, moving the electron analyzer to scan the whole hemisphere, etc., could also be used in the calculations of the intensity of Eq. 5.4 along any direction $\hat{\mathbf{k}}$. The procedure to conduct the experimental configuration-dependent simulation is to calculate and store the cluster scattering matrix $\mathbf{S}$ first. One may choose the photon polarization direction as the z-axis, defining laboratory reference frame, and calculate the transition matrix $\mathbf{A}'$, and then use Eq. 5.8 to convert matrix $\mathbf{A}'$ to matrix $\mathbf{A}$ in a sample-oriented reference frame. Finally one may use Eq. 5.4 to calculate the intensity at a given $\hat{\mathbf{k}}$ direction.

5.3 Co-3p angle-resolved XPD from a CoSi$_2$(111) surface

5.3.1 CoSi$_2$(111) bulk and surface geometry

The structure of $CoSi_2$ is of CaF_2 structure type with a lattice constant of 5.367 $\AA$, and the unit cell of a bulk crystal of $CoSi_2$, is shown in Fig. 5.1 on page 137. The Si atoms form a simple-cubic (sc) lattice, while Co atoms sit on a face-centered-cubic (fcc) structure with twice the lattice constant of the Si lattice. The geometric structure of $CoSi_2$(111) consists of an alternate sequence of one Co layer for every two Si layers along the [111] direction, while its surface is terminated with only one Si layer on the top of the outermost surface Co layer, as shown in Fig. 5.2 on page 138. A wide variety of experimental techniques and extensive theoretical calculations [70,?,?] have been used to determine the surface structure of this material. A recent low energy electron diffraction (LEED) analysis

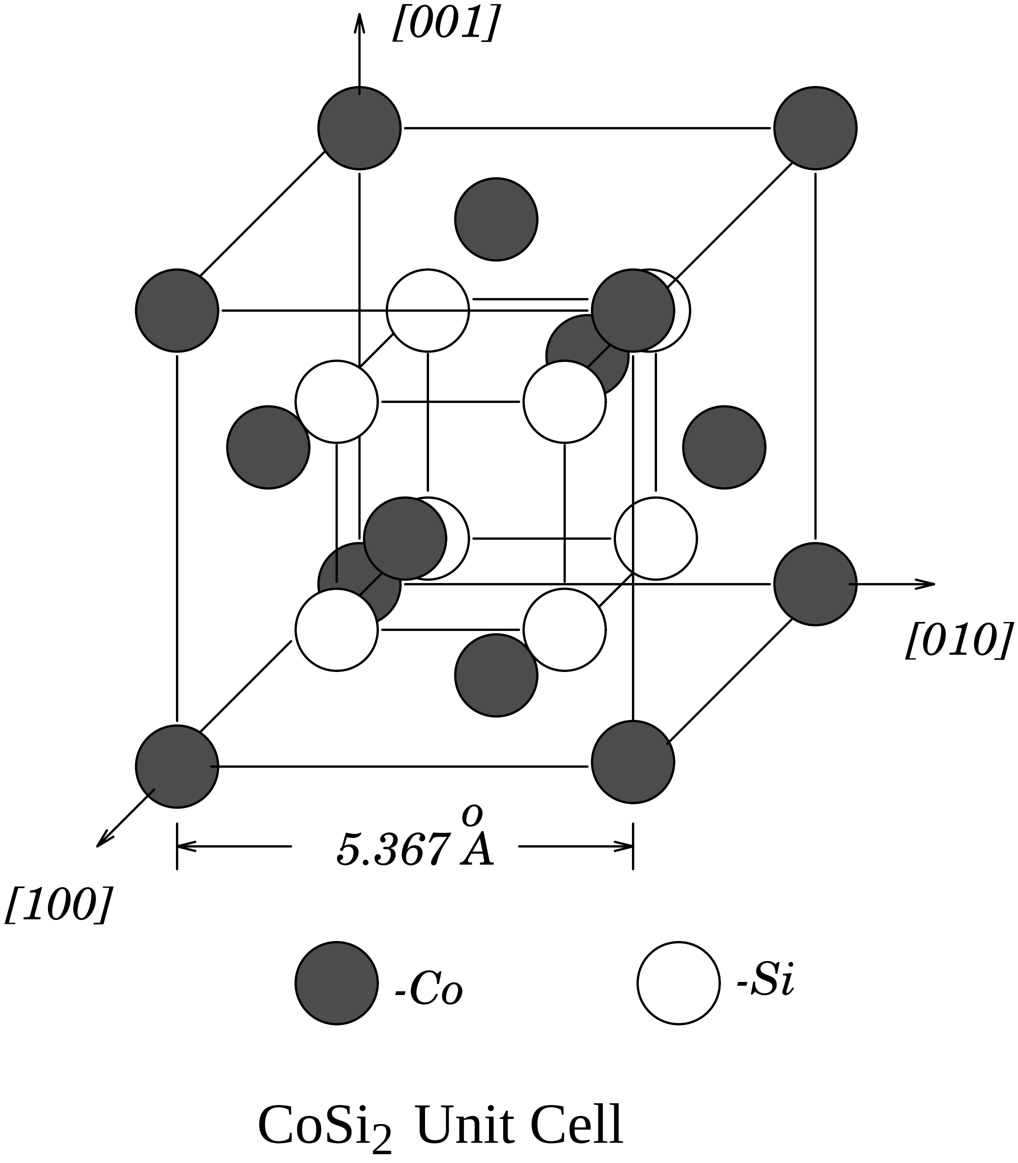

Figure 5.1: Diagram of a unit cell of $CoSi_2$ single crystal. In this cell, the Si atoms form a simple-cubic (sc) lattice, and Co atoms sit on a face-centered-cubic (fcc) structure with twice the lattice constant of Si lattice.

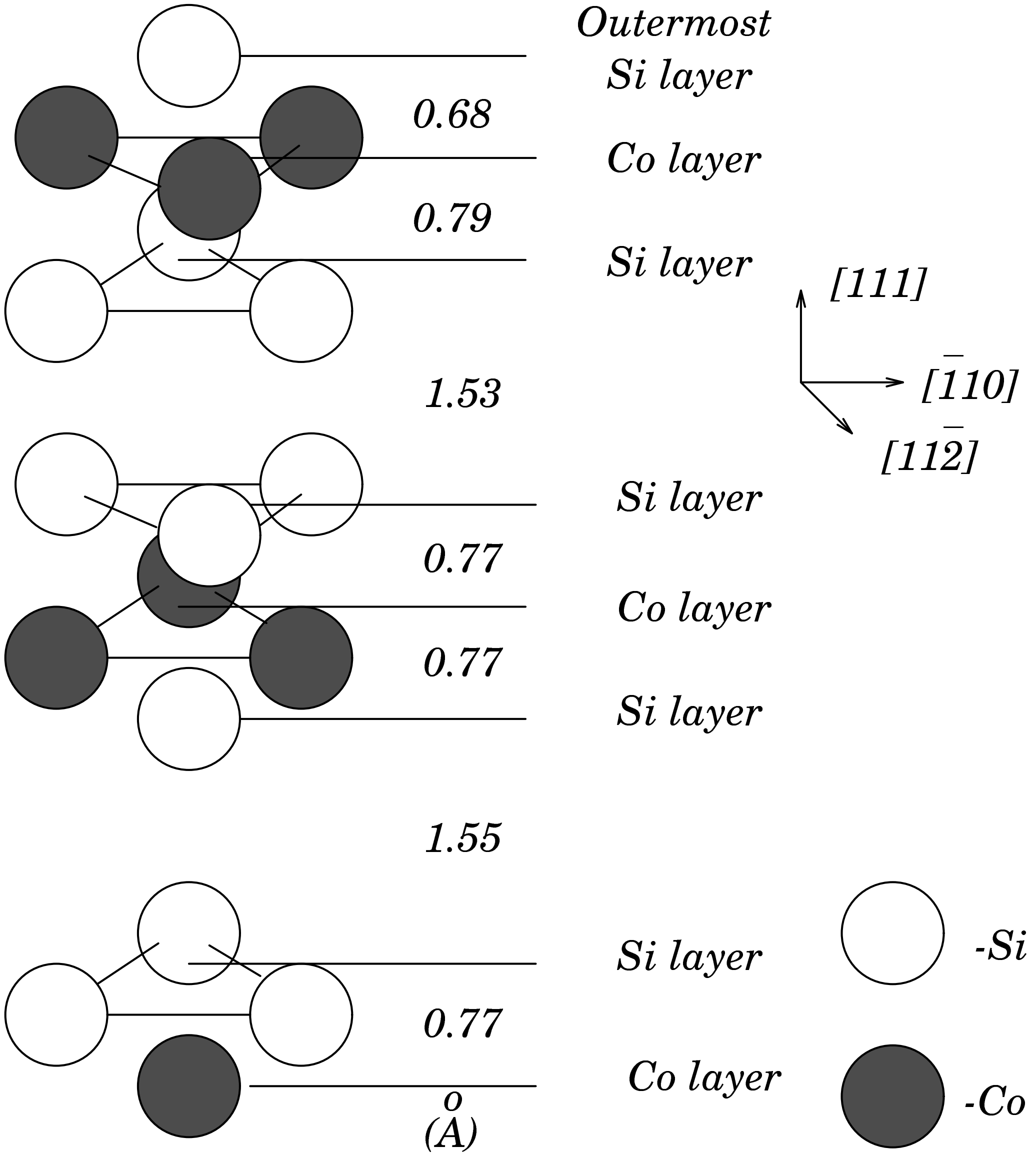

Figure 5.2: Perspective view of the stacking of the surface layers, of $CoSi_2(111)$. An alternate sequence of one Co layer for every two Si layers is seen. The surface is terminated with one Si layer on the top of the outermost Co layer. The interlayer spacings for this surface model comes from reference [68].

[68] shows that the interlayer spacing of the first few surface layers are different from the bulk. Compared with the bulk structure, the first interlayer spacing is contracted by 12%$(-0.09\mathring{A})$, the second one expanded by 2.6%$(+0.02\mathring{A})$ and the third one contracted by 1.3%$(-0.02\mathring{A})$, respectively, and the atoms in deeper layers remain at their bulk positions. In our simulations of the photoelectron diffraction from $CoSi_2(111)$ surface, we make use of this surface model to carry out a cluster calculation of the scattering matrix **S**.

5.3.2 Angle-resolved Co-3p XPD experiment

In the angle-resolved Co-3p XPD experiment, the configuration of the experiment is a fixed x-ray incident beam and sample position, with the electron analyzer rotated to scan the whole hemisphere to vary the θ and ϕ. The x-ray beam is incident on the (111) surface of the $CoSi_2$ sample along the $[\bar{1}10]$ azimuth at a fixed angle of 67.5^o from the surface normal, as shown in Fig. 5.3 one page 140. The polarized photon energy is 750eV, and the polarization direction is along $[\bar{1}10]$ azimuth and off the surface normal by 22.5^o. If we choose a sample reference frame with the $[\bar{1}10]$ direction the x-axis, $[11\bar{2}]$ the y-axis and [111] (surface normal) the z-axis, the photon polarization vector $\hat{\mathbf{e}}$ would be along the $\theta = 22.5^o$ and $\phi = 0.0^o$ direction in this coordinate system. The $CoSi_2$ sample has the size of 1.5x7x11 mm^3, and x-ray Laue diffraction shows that the surface is aligned perpendicular to the (111) direction to an accuracy of 0.8^o. In this experiment, the analyzer was tuned to collect the Co-3p transition peak in the XPS spectrum with photoelectron kinetic energy of 695 eV. Angle-resolved electron diffraction intensities were recorded by moving the analyzer through only one-sixth of the whole collection hemisphere over the sample surface. The resulting electron diffraction pattern is

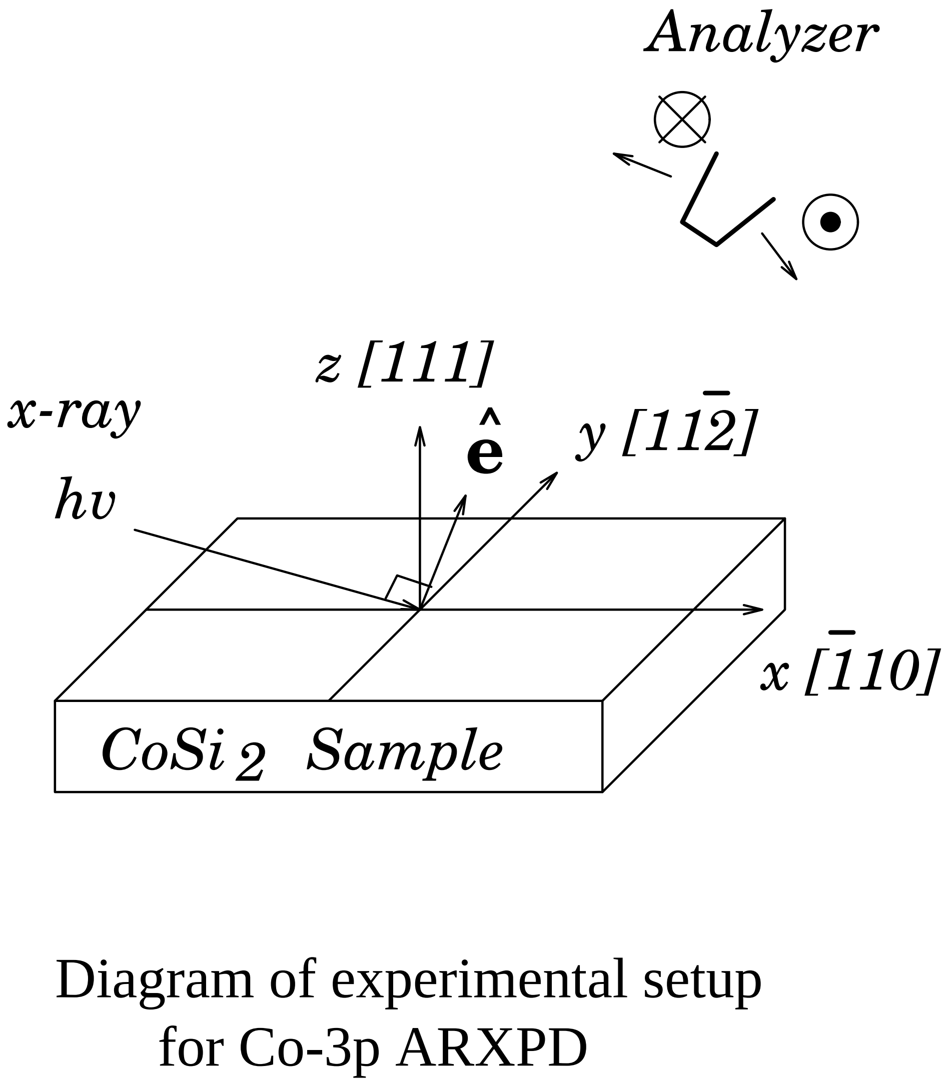

Figure 5.3: Schematic diagram of Co-3p XPD experimental setup. Sample orientation coordinates are defined as x, y, and z, along the [$\bar{1}$10], [11$\bar{2}$] and [111] directions, respectively. The x-ray incidence angle and sample position are fixed, and the angle-resolved electron diffraction pattern is obtained by moving the analyzer through the collection hemisphere above the surface.

shown on Fig. 5.4 on page 142, where the polar angles are plotted ranging from zero at the centers to 90^o at the pattern's edge, and projected on the equatorial plane with the center at $(K_x, K_y) = (0, 0)$ and uniform ΔK_x and ΔK_y, where K_x and K_y are the wave vector of the photoelectron along x and y-axis. The actual angle-resolved diffraction were measured from only one-sixth of hemisphere above the sample surface, and the entire pattern was then generated by symmetry operations of reflection and rotation to cover the whole hemisphere. It is shown that the diffraction pattern is dominated with forward-scattering peaks which is a typical features of high energy electron diffraction. It is known that a Si atom sits directly above Co emitters in the cluster model of $CoSi_2(111)$, and the center peak on the diffraction pattern is caused by forward-scattering by this atom. It was found that the center peak has a local minimum, which is the characteristic feature of a Si atom at high electron energy. We will show later that the symmetry operations to obtain the whole pattern throughout the hemisphere might not be correct for this configuration of the experimental setup, although the single crystal sample has a three-fold symmetry.

5.3.3 Calculation of Co-3p transition matrices

In a central field approximation, the electron spin-orbital wave function can be characterized by four quantum numbers n, l, m and m_s, where m_s is the spin quantum number. For a simple dipole transition theory, we can usually omit the quantum number m_s. As defined in Sec. 5.2, $A^{(0)}_{LL_c}$ represents the transition amplitude from core-state $|n, L_c\rangle$ to final free state $|\epsilon, L\rangle$ (ϵ=695eV). From a dipole approximation, transition matrix element $A^{(0)}_{LL_c}$ is proportional to [69],

$$< \psi_f|\hat{\Delta}|\psi_c >

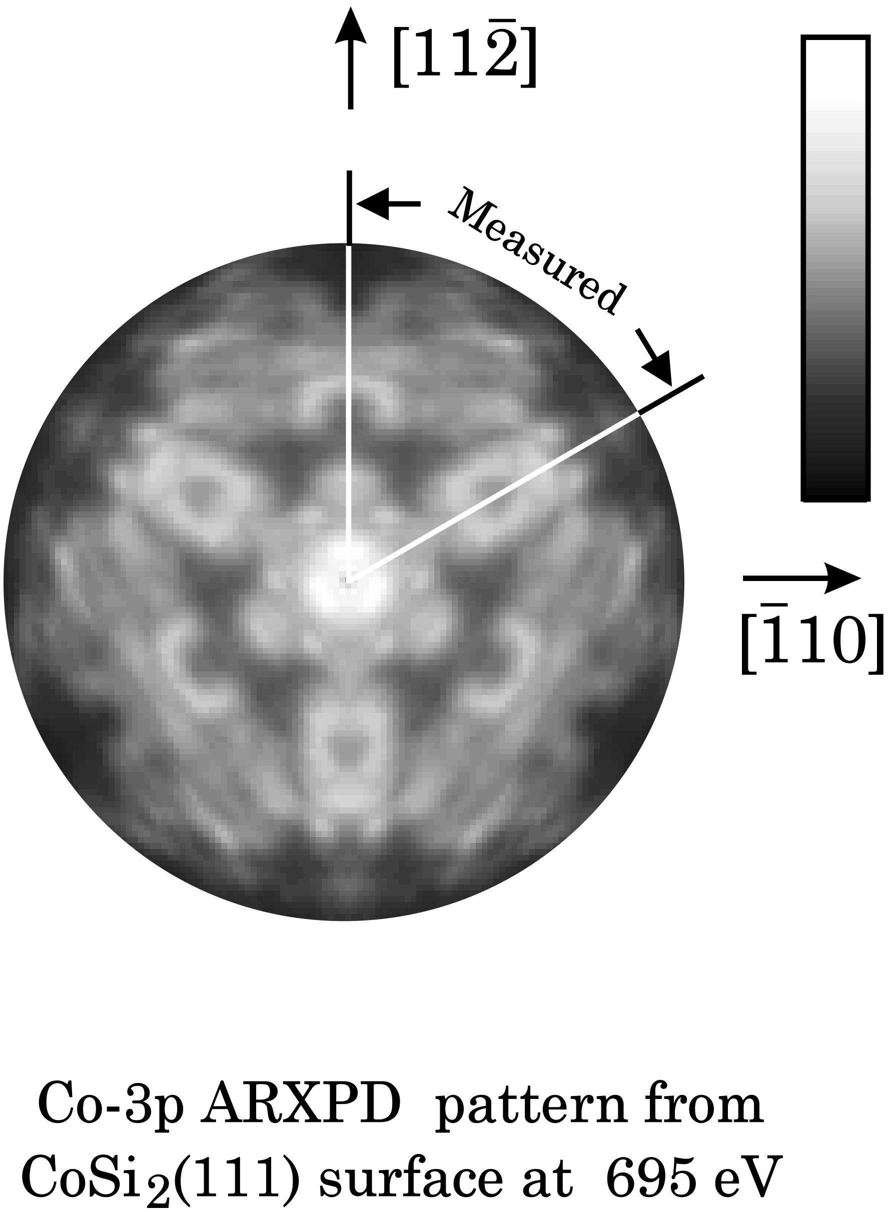

Figure 5.4: Experimental pattern of Angle-resolved Co-3p XPD with photoelectron kinetic energy of 695 eV from CoSi$_2$(111) surface. The actual measurements were performed over only one-sixth of whole hemisphere above the sample surface normal, and the pattern was obtained by symmetry operations of reflection and rotation to cover the whole hemisphere.

as defined in Eq. 2.16 on page 33, where ψ_c and ψ_f are the core-state and final state of the photoelectrons respectively, and $\hat{\Delta}$ is the photon-electron interaction operator, and can be written in the momentum, potential and position form of

$$\hat{\Delta} = \frac{i\hbar e}{mc}\mathbf{A} \cdot \nabla,$$

$$\hat{\Delta} = \frac{ie^2}{\omega mc}\mathbf{A} \cdot \nabla V(\mathbf{r}),$$

and

$$\hat{\Delta} = \frac{ie^2\omega}{c}\mathbf{A} \cdot \mathbf{r}$$

respectively, where m is the mass of a free electron, e the unit charge of an electron, c speed of the light in the vacuum, $\mathbf{A}$ electromagnetic radiation vector potential, ∇ the gradient vector operator, and $\mathbf{r}$ position vector operator. If we choose a laboratory reference frame defined by x', y' and z', where the z'-axis is along the polarization vector $\hat{\mathbf{e}}$ of the incident x-ray beam, as shown in Fig. 5.3, we could choose the position form of photon-electron interaction as:

$$\hat{\Delta} \propto \hat{\mathbf{e}} \cdot \mathbf{r}' \propto z' = r' cos(\theta')$$

if we omit a constant here, we can define:

$$A'^{(0)}_{LL_c} = \langle L|cos(\theta')|L_c\rangle\langle R(r', \epsilon, l)|r'|R_{31}(r')\rangle e^{i\delta_l} \tag{5.9}$$

where the core-state radial wave function of $R_{31}(r')$ is a solution of the radial Schrödinger equation of a cobalt atom. $R(r', \epsilon, l)$ is a solution of the radial Schrödinger equation within the muffin-tin sphere for an energy of ϵ, and matching on to the function $j_l(kr')cos(\delta_l) - n_l(kr')sin(\delta_l)$ at the muffin-tin radius, where j_l and n_l are spherical Bessel and Hankel functions respectively, the wave number k equals $\sqrt{2\epsilon}$, and δ_l is a phase shift. Now we can evaluate the angular and radial part of the transition matrix separately. Note that the initial states are bound states whereas the final emitting states are unbound states, with electron kinetic energy of ϵ and angular momentum quantum number of L.

Initially, the $|3L_c>$ core-state is assumed to equally populate the cobalt $|31\bar{1}>$, $|310>$ and $|311>$ core-states, so the angular matrix element, $\langle L|cos(\theta^{'})|L_c\rangle$, can be calculated analytically by using the following relations [73],

$$cos(\theta)Y_{lm} = a_{l,m}Y_{l+1,m} + a_{l-1,m}Y_{l-1,m},$$

$$sin\theta e^{i\phi}Y_{lm} = b_{l-1,-m-1}Y_{l-1,m+1} - b_{l,m}Y_{l+1,m+1},$$

and

$$sin\theta e^{-i\phi}Y_{lm} = -b_{l-1,m-1}Y_{l-1,m-1} + b_{l,-m}Y_{l+1,m-1},$$

where

$$a_{l,m} = \sqrt{\frac{(l+1)^2 - m^2}{(2l+1)(2l+3)}}$$

and

$$b_{l,m} = \sqrt{\frac{(l+m+1)(l+m+2)}{(2l+1)(2l+3)}}$$

respectively. Therefore, we obtain

$$cos(\theta)Y_{10} = \sqrt{4/15}Y_{20} + \sqrt{1/3}Y_{00},$$

$$cos(\theta)Y_{11} = \sqrt{1/5}Y_{21},$$

and

$$cos(\theta)Y_{1\bar{1}} = \sqrt{1/5}Y_{2\bar{1}}.$$

The non-zero elements of the matrix $\langle L|cos(theta^{'})|L_c\rangle$ give that the angular momenta of the emitted states of $l = 0$ and 2, which corresponds to s and d wave emitters respectively. The radial matrix element, $\langle R(r^{'}, \epsilon, l)|r^{'}|R_{31}(r^{'})\rangle$, can be evaluated numerically by the MUFPOT program, and the results of the radial matrix elements for s and d emitting waves are:

$$\langle R(r', \epsilon, l_s)|r'|R_{31}(r')\rangle = 2.502$$

and

$$\langle R(r', \epsilon, l_d)|r'|R_{31}(r')\rangle = 7.050$$

Some common factors are dropped in the above two expressions. Combining the angular and radial parts of the transition matrix elements, we end up with only four non-zero elements:

$$A'^{(0)}_{2\bar{1},1\bar{1}} = 3.153e^{i\delta 2},$$

$$A'^{(0)}_{00,10} = 1.444e^{i\delta 0},$$

$$A'^{(0)}_{20,10} = 3.641e^{i\delta 2},$$

and

$$A'^{(0)}_{21,11} = 3.153e^{i\delta 2}$$

By using Eq. 5.8, we can calculate the matrix element $A^{(0)}_{LL_c}$ which is transition amplitude represented in the sample reference frame, for any tilt of the polarization direction of the x-ray photon. In order to simulate the diffraction pattern of Fig. 5.4 with experimental setup of Fig. 5.3, θ and ϕ are chosen to be 22.5^o and 0.0^o respectively in Eq. 5.7.

5.3.4 Simulations of Co-3p ARXPD from CoSi$_2$(111) surface

The cluster scattering matrix $\mathbf{S}^{(N)}$ is calculated using a cluster surface model, as shown in Fig. 5.1 and Fig. 5.2, centered at a Co emitter, where twelve shells ($N = 12$) of 430 atoms (with a cluster of radius 12 $\AA$) are included. With transition matrix $\mathbf{A}^{(0)}$ evaluated by the method of Sec. 5.3.3, we could obtain an experimental configuration-dependent simulation of $CoSi_2(111)$ Co-3p ARXPD by using Eq. 5.4. Due to the limited inelastic length of an electron in a solid, we could include only the contributions of Co emitters in the first few layers. In Fig. 5.5 on page 147, the electron diffraction patterns contributed by 2nd, 5th, and 8th layer emitters are shown on the upper, middle, and lower panels respectively. In these simulations, the polar angles are plotted ranging from zero at the centers to 90^o at the edges, and projected on the equatorial plane with center at $(K_x, K_y) = (0, 0)$ and uniform ΔK_x and ΔK_y, where K_x and K_y are the components of the wave vector of the photoelectron along the x and y axes.

Considering that the x-ray penetration depth in a sample is very large, the chances for the excitation of Co atoms are almost same through out the sample. The major damping factor for an electron wave reaching the detector is due to the limited electron mean free path that confines the electrons emitted by the Co atoms located at the deeper layers. It is assumed here that electrons emanating from much deeper layers would have a small effect on the final diffraction pattern. This is seen to be justified by estimating that the escape length of the next Co emitter layer (11th layer from the surface) is much larger than the average electron inelastic scattering length in the solid. Also the comparison of the pattern produced by the emitter at the 5th layer and that of the 8th layer, in Fig. 5.5 (middle and lower panels), shows that the major features on the patterns will remain the same if the calculation continues on for deeper layer emitters.

It can be seen from Fig. 5.5 that the diffraction features from 2nd layer is quite different from that produced by the emitters in the 5th and 8th layer which have Si scatterer(s) directly above the emitters. It is interesting to see that our simulations for the 5th and 8th layer emitters show a strong center peak with a crater on top,

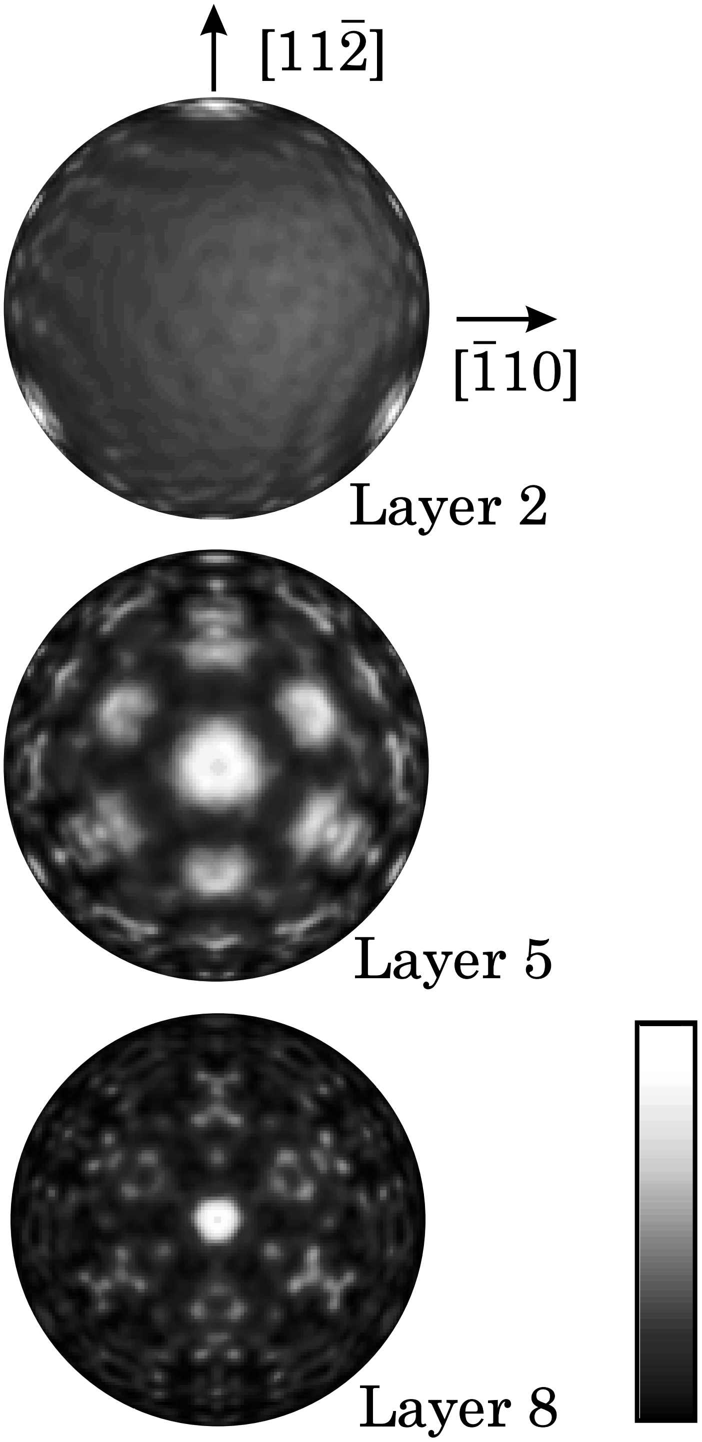

Figure 5.5: The simulations of Co-3p XPD from a $CoSi_2(111)$ surface assuming that the Co emitter is at the 2nd, 5th and 8th layer respectively. Note that the simulated patterns are not three fold symmetric due to the photon polarization direction pointing in the (θ, ϕ)=(22.5^o, 0.0^o) direction.

and this feature was reproduced by the Co-3p XPD experiment. One of the important result of these simulations is that an experimental configuration-dependent calculation gives an overall asymmetric angle-resolved diffraction pattern, although a three-fold symmetric cluster was used in the calculation. This asymmetry of the photoelectron diffraction pattern is different from the Auger electron diffraction pattern where the Auger electron emission is isotropic due to its loss of memory of its initial core-hole state. The simulations indicate the presence of a smoothly-varying envelope which is peaked at the (θ, ϕ)=(22.5^o, 0.0^o) direction, that of the photon polarization vector $\hat{\mathbf{e}}$. This asymmetrical intensity distribution is the direct result of the dipole transition, where the final free electron states tend to peak along the photon polarization direction. The simulations for the 2nd, 5th, and 8th layer emitter in Fig. 5.5 clearly show this feature. The conclusion can be easily drawn: for this experimental configuration, a three-fold symmetry operation cannot be used to expand a part of the photoelectron diffraction pattern to whole one, even though the sample surface is three-fold symmetric.

The final pattern, shown on the lower panel of Fig. 5.6 on page 149, is the sum of the diffraction intensities contributed by the Co emitters located at the 2nd, 5th and 8th layer below the surface with a proper damping factor. The weight of diffraction intensity from the 8th layer is enhanced to account for the contributions from Co emitters below the 8th layer, as has been discussed in Chapter 4. For a direct comparison with the simulation, we also show the measured diffraction pattern of the angle-resolved Co-3p XPD pattern from a $CoSi_2$(111) surface on the upper panel of Fig. 5.6. The experiment was conducted for only one-sixth of the whole hemisphere, and then "three-fold" symmetry operations was used to expand to the whole pattern. The comparison shows that the simulated pattern is

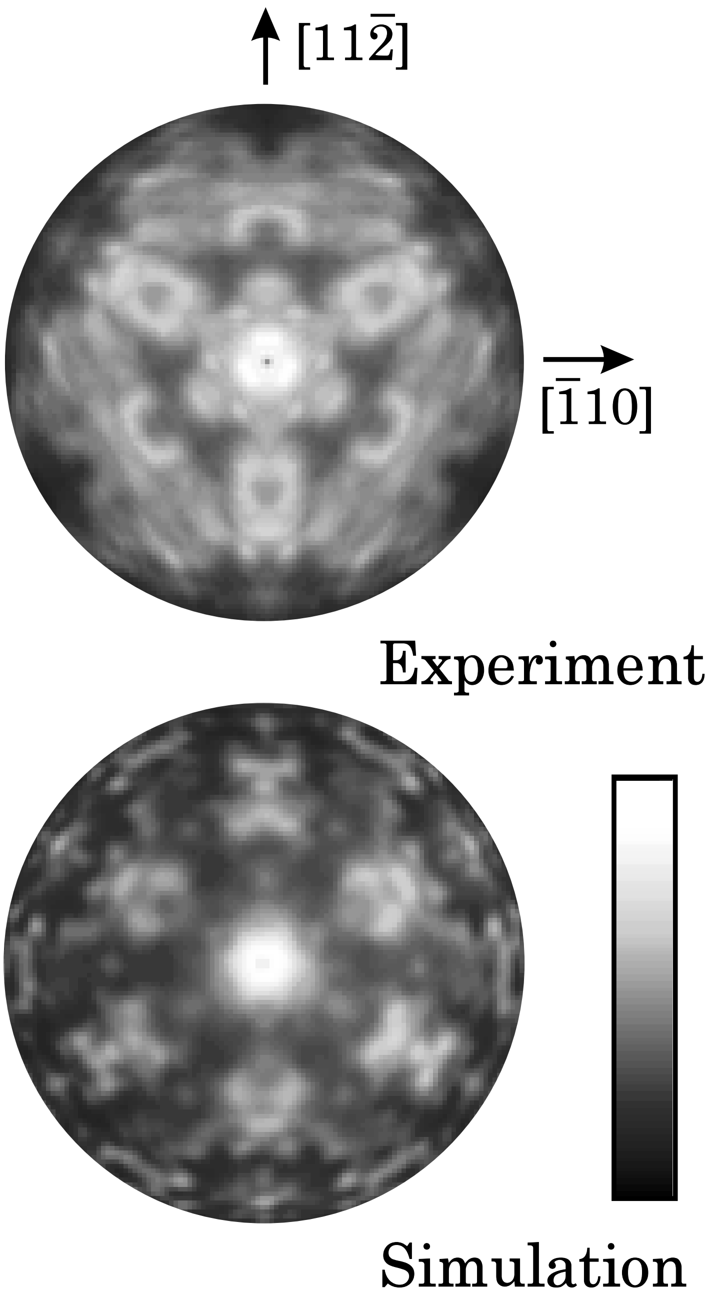

Figure 5.6: The experiment and simulation of the angle-resolved Co-3p XPD from CoSi$_2$(111) surface. Upper panel pattern is the experimental diffraction pattern with only one-sixth of the pattern measured, and then expanded by the symmetry operations. The simulated pattern is not threefold symmetric, and this infers that this symmetry operation is not appropriate for the above experimental pattern.

in general close to the experimental one and reproduces almost all the diffraction structures well, including some fine features. In the center of both experimental and simulated patterns, the patterns show a local minimum, although in the $CoSi_2(111)$ cluster model there is a Si atom directly above Co emitter. Again, it is seen that although the simulation in Fig. 5.6 shows the forward-scattering peaks in a "three fold" symmetry pattern, an envelope peaked at the (θ, ϕ)= (22.5^o, 0.0^o) direction can be seen.

5.4 Si-2p normal emission diffraction from $CoSi_2$ (111) surface

5.4.1 Si-2p normal emission experiment

The experiment on the surface Si-2p normal emission diffraction from $CoSi_2(111)$ was carried out in a similar configuration to that described for the angle-resolved Co-3p XPD experiment, but with a fixed detector at normal direction and a tunable x-ray source to vary the kinetic energy, ϵ, of the photoelectron to get the I-ϵ curve. This mode is similar to a LEED I-V curve measurement, except that the electron sources are the surface Si emitters and only the normal diffraction component is measured. As shown in Fig. 5.7, the x-ray beam is incident along the $[\bar{1}10]$ azimuth at a fixed angle of 67.5^o from the surface normal, the photon polarization direction is along $[\bar{1}10]$ azimuth and off the surface normal by 22.5^o. In the experiment, the photon energy was changed from 125 eV to 216 eV, the analyzer was fixed along the sample normal direction and tuned to collect photoelectrons within surface component of Si doublets ($2p_{1/2}$ and $2p_{3/2}$ peaks) in the XPS spectrum. In the Si-2p XPS spectrum, the peaks are composed of surface

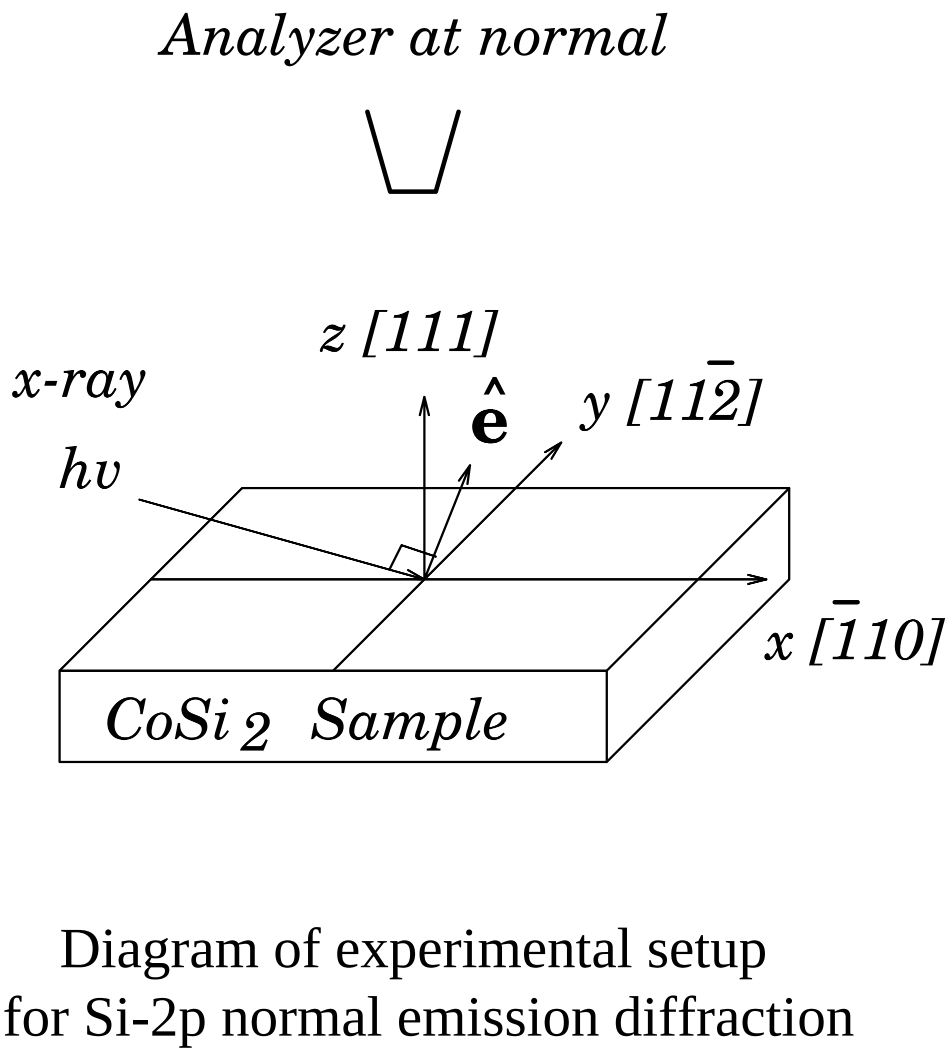

Figure 5.7: Schematic diagram of the Si-2p normal emission experimental setup. The sample orientation coordinates are defined as x, y, and z are along the [$\bar{1}$10], [11$\bar{2}$] and [111] directions, respectively. The mode of collecting the I-ϵ curve is by fixing the incident x-ray beam and sample position and analyzer at the sample normal direction, and changing the x-ray wavelength and tuning the analyzer to the Si-2p peaks.

and bulk components. Four peaks related to Si-2p photoemission were observed in the spectrum. Being careful and able to distinguish and separate them would result in a maximum extraction of surface information from the experiment. One way to do so is to make use of the theoretical result to eliminate some uncertainty in the experiment. Due to the principle of the spin-orbit interaction, the possible states are those with total angular momentum $J = \pm\frac{1}{2}$ for the $2p_{1/2}$ state, and $J = \pm\frac{1}{2}, \frac{3}{2}$ for the $2p_{3/2}$ state. Hence, the probability of a p electron in the $2p_{1/2}$ state is half of that in the $2p_{3/2}$ state. By considering these theoretical results, the separation of the surface and bulk components could be done by fitting two Gaussian doublets with branching ratio chosen to be 0.5 for both surface and bulk components, the separation of the peaks for the doublets set to be 0.62 eV for the bulk component, and no constraint for the surface component. It is assumed here that there is much more freedom on the orbitals of the atoms at the surface than those in the bulk. The result of the Si-2p normal emission experiment is shown in Fig. 5.8 on page 153.

5.4.2 Calculation of Si-2p transition matrices

In a laboratory reference frame, the transition matrix $\mathbf{A}^{'(0)}(\epsilon)$ with matrix element of $\langle L|cos(\theta^{'})|L_c\rangle\langle R(r^{'},\epsilon,l)|r^{'}|R_{21}(r^{'})\rangle e^{i\delta_l}$ may be evaluated in a similar way of using the MUFPOT program described in Sec. 5.3.3. The non-zero elements of the angular matrix will result in final emitted waves of $l_s = 0$ (s-wave emitter) and $l_d = 2$ (d-wave emitter), and the radial matrix element, $\langle R(r^{'},\epsilon,l)|r^{'}|R_{21}(r^{'})\rangle$, will be a function of the energy, ϵ, and should be calculated for each energy. Typical values of radial matrix elements around $\epsilon = 60$ eV are calculated to be:

$$\langle R(r^{'},\epsilon,l_s)|r^{'}|R_{21}(r^{'})\rangle = 1.742$$

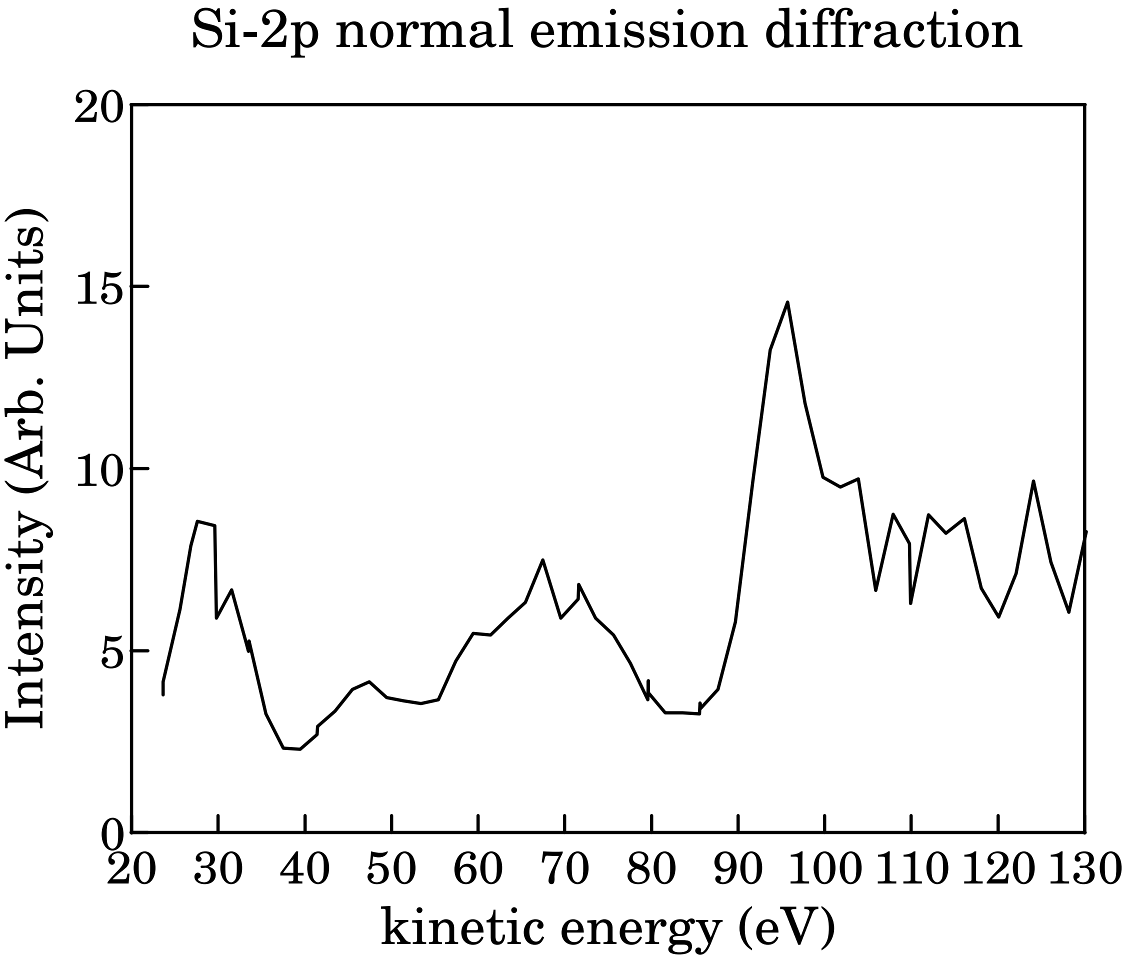

Figure 5.8: Experimental I-ϵ curve of Si-2p photoemission from $CoSi_2(111)$ surface with electron kinetic energy of ranging from 20 to 130 eV. The I-ϵ curve is obtained by fixing the incident x-ray beam and sample position, and analyzer at the sample normal direction, and changing the x-ray wavelength and tuning the analyzer to the Si-2p peaks.

and

$$\langle R(r^{'}, \epsilon, l_d)|r^{'}|R_{21}(r^{'})\rangle = 6.378$$

where $R_{21}(r^{'})$ is a bound solution of the radial Schrödinger equation of a silicon atom, and some common constant factors are dropped in the above expressions. We can evaluate the quantity $\mu(\epsilon)$, which is defined as the ratio between the final s-wave and d-wave in the photoemission process by

$$\mu(\epsilon) = \frac{\langle R(r^{'}, \epsilon, l_s)|r^{'}|R_{21}(r^{'})\rangle}{\langle R(r^{'}, \epsilon, l_d)|r^{'}|R_{21}(r^{'})\rangle}$$

In Fig. 5.9 on page 155, a plot $\mu(\epsilon)$ versus kinetic energy of the photoelectron ϵ is given, which shows that $\mu(\epsilon)$ does not change very much in this energy range (20 eV to 130 eV). For a simple approximation, $\mu(\epsilon)$ can be taken as a constant number, and chosen as $\mu(60\text{ eV})$ for this energy range. The physical meaning of this is the assumption of a constant transition rate ratio between s and d wave emitters in this kinetic energy range.

5.4.3 Simulations of Si-2p normal emission

For a full multiple scattering calculation, a cluster centered at the surface Si emitter was used to obtain the scattering matrix $\mathbf{S}^{(N)}(\epsilon)$ at energy ϵ, where five shells ($N = 5$) of 33 atoms were included in the cluster. The maximum radius of this cluster was 7 $\AA$ which is larger than the electron inelastic scattering length, 6 $\AA$, in this energy range. This ensured a convergence of the calculations. The transition matrix $\mathbf{A}^{(0)}(\epsilon_o)$ in a sample reference frame was evaluated in the same way in Sec. 5.3.3 where the θ and ϕ were chosen to be 22.5 and 0 ^{o} respectively. An experimental configuration-dependent diffraction intensity along $CoSi_2(111)$

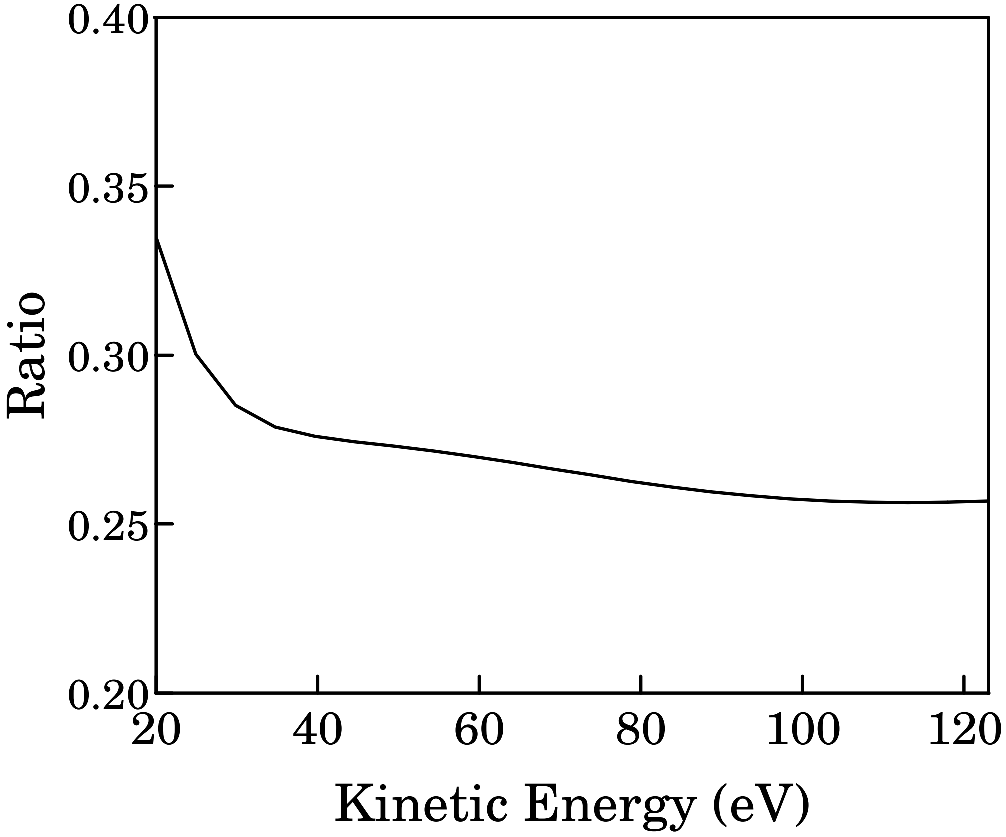

Figure 5.9: Ratio of transition amplitude of an s- to d-wave emitter in Si-2p photoemission. The ratio, $\mu(\epsilon)$, is that of the radial matrix element of $\langle R(r', \epsilon, l_s)|r'|R_{21}(r')\rangle$ verses $\langle R(r', \epsilon, l_d)|r'|R_{21}(\{r'\})\rangle$, where $l_s = 0$ and $l_d = 2$.

surface normal can be obtained by using the expression:

$$I_{\mathbf{XPD}}(\epsilon) = \sum_{L_c} |\sum_{L} \sum_{L'} S^{(N)}_{LL'}(\epsilon) A^{(0)}_{L'L_c}(\epsilon_o)(-i)^l Y_L(0,0)|^2 \tag{5.10}$$

Note that the intensity in Eq. 5.10 is a function of the electron kinetic energy. In the simulations, we first calculated accurately with Eq. 5.10 the electron diffraction intensities in the sample normal direction which accounts for the contribution from both s- and d-wave emitters of the Si-2p transition where the transition matrix element, $A^{(0)}_{L'L_c}(\epsilon_o)$, include electron waves of angular momentum quantum numbers of 0 and 2. We then repeated the simulation except with a pure s-wave emitter and compared it with the more complicated simulation of mixed s- and d-wave emitters to see the impact of a simplified s-wave emitter in this energy range. In Fig. 5.10 on page 157, the simulations of Si-2p normal emission from a $CoSi_2(111)$ surface with contributions only from the Si-2p surface components in the XPS spectrum is shown as a function of the kinetic energy of the photoelectron. The mixed s- and d-wave emitter simulation is drawn as a solid line, the s-wave emitter simulation is shown as a dashed line, and the experimental results for surface component of Si-2p normal emission is plotted with the long-dashed line.

Excellent agreement between the experiment and the simulation using mixed s and d wave-fields in the range of 20 eV and up to 90 eV is achieved, and no good agreement was found between the experiment and the simulation using only a pure s wave-field. These results show that the photoelectron final state plays an important role in this low energy diffraction. In the higher energy range (above 90 eV), the Si Auger $L_3M_1M_{23}$ and $L_3M_{23}M_{23}$ transitions appear in the spectrum and are mixed with the Si-2p's doublets, and hence it is difficult to separate them in the experiment. The resulting intensities will be increased sharply due to the presence of Si Auger emission. This explains the fact that at higher energies (above

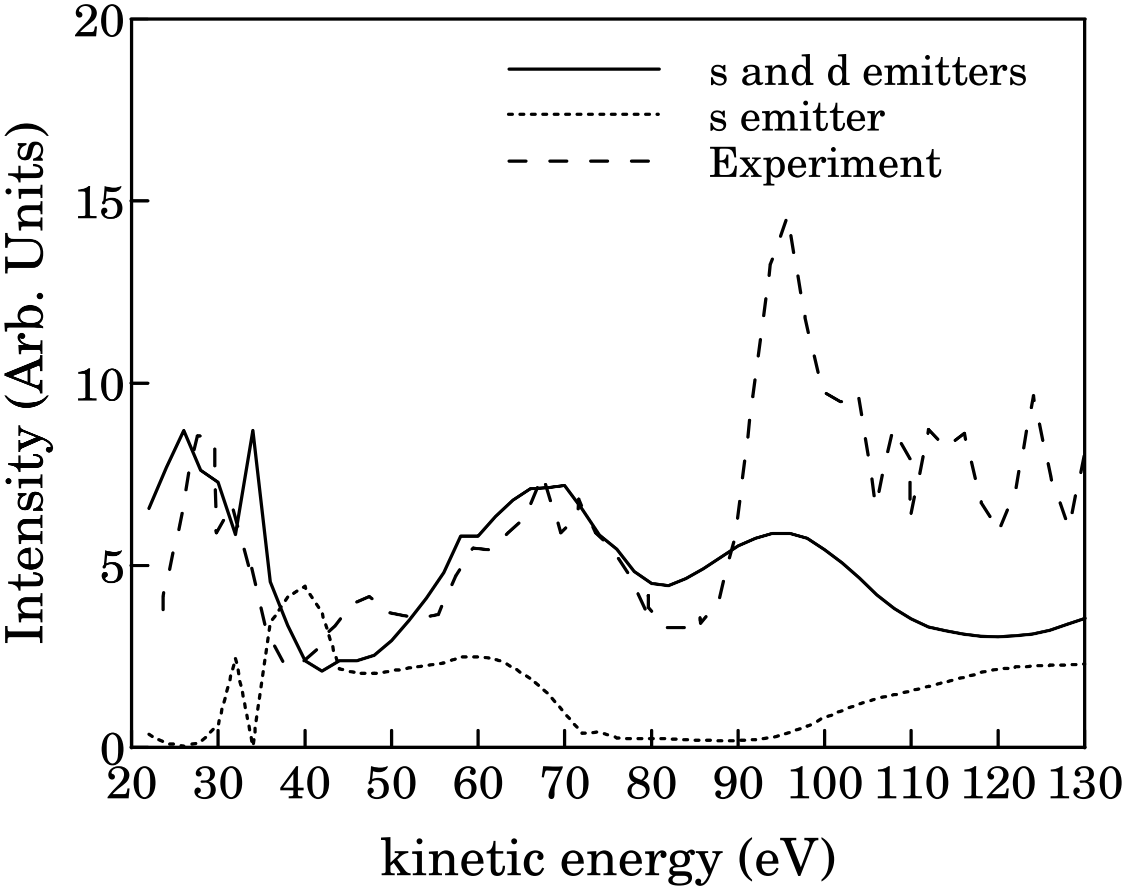

Figure 5.10: Simulations of I-ϵ curve of Si-2p photoemission from a $CoSi_2(111)$ surface with electron kinetic energy of ranging from 20 to 130 eV. There are Si Auger $L_3M_1M_{23}$ and $L_3M_{23}M_{23}$ transitions appearing in the spectrum above 90 eV, it will increase the intensity in the experiment due to greater numbers of Auger electrons involved in the diffraction. In this case the simulation and the experimental curve differ by a constant of proportionality for a good approximation.

90 eV) the intensity in the experimental curve increases sharply relative to that of the simulation. Also Co Auger emission around 50 eV could not be separated from the Si-2p peaks in that region, and gives rise to the extra small peak at 48 eV in the experimental curve on Fig. 5.10. Multiple scattering simulation with a simple s-wave emitter shows different features in this diffraction curve, and does not explain the results of the experiment.

5.5 Conclusions and summary

We have applied the concentric shell algorithm [32] for a core-level photoelectron diffraction calculations. One of the main quantities of the cluster calculation is the cluster scattering matrix $\mathbf{S}^{(N)}(\epsilon)$, which was stored and used later for diffraction intensity calculations under different experimental configurations. Different modes for the angle-resolved photoelectron diffraction include:

(1) a fixed x-ray incident beam, moving the electron analyzer in a plane which passes through the sample normal to scan the polar angles, and rotating the sample about its normal to obtain the azimuthal scan ϕ,

(2) a fixed angle between x-ray and electron analyzer, rotating the sample to obtain the polar and azimuthal angle scans,

(3) a fixed x-ray incident beam and sample position, moving the electron analyzer to scan the whole hemisphere, etc..

Other modes, such as Si-2p normal emission experiment, are also discussed and the simulations were done to compare with the experimental results.

At higher energies($\epsilon = 695$ eV), photoelectron has a longer inelastic-scattering length, and a larger size of cluster (430 atoms surrounding the emitter) was needed to achieve a convergent condition, while at low energies (20eV to 130eV in Si-2p normal emission) only a few shells of atoms were included in the cluster calculation to satisfy the convergence requirement.

A transition matrix $\mathbf{A}^{(0)}$, where matrix element $A^{(0)}_{LL_c}$ is transition amplitude for the transition from a bound core-state $|n, L_c\rangle$ to a final free state $|\epsilon, L\rangle$ is discussed. If the energy of the x-ray is high enough, selection rules for a dipole approximation will be invalid. Therefore higher order terms, such as quadrupole transition, must be considered. A roughly estimate of the ratio of transition amplitude for electric quadrupole $A^{(0)}_{qpole}$ and dipole $A^{(0)}_{dpole}$ radiation is [69]:

$$\frac{A^{(0)}_{qpole}}{A^{(0)}_{dpole}} \simeq \frac{3}{40}(\frac{\omega a_o}{c})^2$$

where ω is the angular frequency of the photon, c the velocity of the light, and a_o the radius of the emitter. In the Co-3p and Si-2p XPD experiments these ratios are about 0.015 and 0.00015, respectively, so the dipole transition theory is still a good approximation for those transitions. The above estimate indicates that in a higher x-ray energy range, the quadrupole transition may not be negligible and the quadrupole transition matrix should be included in the calculations. Then the final states of the photoelectron emitted from a p core-state will result in s, p, d, and even f wave-fields.

A formula for the rotation matrix in Eq. 5.7 is introduced to transform a spherical harmonic function between the sample and the laboratory reference frames. The relation between the transition matrix $\mathbf{A}^{(0)}$ in a sample reference frame and the transition matrix $\mathbf{A}'^{(0)}$ in a laboratory reference frame is given by Eq. 5.8. Dipole transition matrices show that emitted waves of s and d-states are involved in the core-level Co-3p or Si-2p x-ray photoexcitation process, and some of those emitted wave-fields are in mutually coherent channels if they originated from the same core-state, and some are in mutually incoherent channels if they are emitted from different states, such as the $|1\bar{1}>$, $|10>$, and $|11>$ core-level states.

Experimental angle-resolved Co-3p XPD from a $CoSi_2(111)$ surface is compared with the experimental configuration-dependent simulation. The result shows that the simulations reproduce most of the features of the experiment well, especially the central dip which is mainly contributed from a d-wave source. The Si-2p normal emission diffraction from a $CoSi_2(111)$ surface is also simulated, based on the fact that the scattering matrices are functions of kinetic energy of the photoelectron, and the transition matrices vary slightly with the energies. Excellent agreement has been found between the experimental curve and the simulated one using a multiple scattering algorithm with s and d wave emitters as the initial emitting wave-fields. It is very convincing to see that the simplified assumption of a final s wave in a low energy diffraction calculation fails to describe the results of the XPD experiments in this Si-2p normal emission diffraction and other low energy diffraction experiments[72].

CHAPTER 6

Photoelectron Holography

Holography was first proposed by Gabor in 1948 as a means of overcoming the barrier encounted by electron microscopy in the electro-optical lens' spherical aberrations which prevented the achievement of the atomic resolution images. He realized that if an unknown wave is made to interfere with a known wave, the resulting interference intensity pattern, a "hologram", contains most of the information needed to reproduce the unknown wave. He proposed a two-step hologram formation and reconstruction procedure, as shown on Fig. 6.1 on page 162. Firstly, a known spherical wave, called the "reference" wave, interferes with a wave scattered by the object, called "object" wave, and the interference modulations are recorded on a film. Secondly, the image reconstruction is done by shining an appropriate reference wave on the film to generate a three-dimensional holographic image of the object. Gabor's original idea was to use a diverging coherent electron source of low-energy spread to illuminate a sample. The scattered electron wave interferes with the reference wave from the electron source forming a hologram of the sample. This idea was later to lead to the large field of optical holography, which is now much better known in current science and technology than Gabor's original goal.

It was not until 1986, that Szöke [75], intrigued by x-ray flourescence "holograms" [74], suggested that a photoelectron and Auger electron diffraction pattern from a single crystal surface also have a holographic interpretation. In 1988 Barton proposed a computer algorithm [17], based on the Helmholtz-Kirchoff principle of optics, to reconstruct a three-dimensional image of the surface structure surrounding the emitter from such a diffraction. One of the important points demonstrated

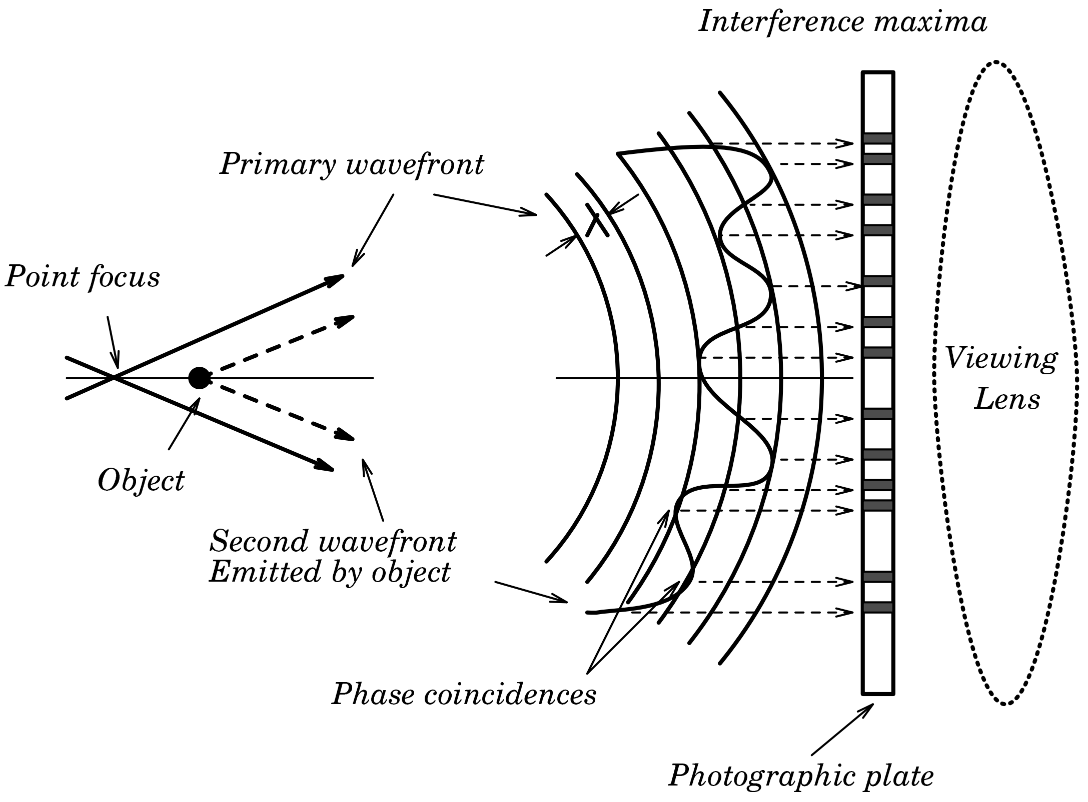

Gabor's holographic principle

Figure 6.1: Schematic diagram of Gabor's holographic principle. The known wave, the "reference" wave, is made to interfere with an unknown wave, or "object" wave. The resulting interference intensity pattern, a " hologram" contains most of the information needed to reproduce the unknown wave.

by this work is that the holographic reconstruction may not be hindered by the presence of strong electron multiple-scattering.

In 1990, Saldin and De Andres [76] proposed a direct method of reconstructing a similar three-dimensional image from a diffuse low-energy electron diffraction pattern. They pointed out that an external electron beam may generate effectively local reference waves, appropriate for atomic-resolution holography, by scattering from a disordered array of adsorbate atoms on a crystal surface. In this scheme the adsorbate was regarded as acting as its own beam splitter. Because of the disorder inherent in the lattice gas, electrons scattered by the adsorbate are spread out over the whole diffraction pattern and are not only directed into the LEED intensity spots of the crystalline substrate. The resulting diffuse electron diffraction pattern was given a holographic interpretation. Saldin and DeAndres also pointed out that the image can be improved by averaging several holographic images taken at different electron kinetic energies.

The first successful experimental result was achieved by Harp, Saldin, and Tonner [77] for the holographic analysis of experimental Kikuchi diffraction pattern from a Cu(001) surface. A Kikuchi pattern may be obtained by sending in an external electron beam into a sample, which may suffer substantial quasi-elastic scattering due to phonon creation and annihilation of the vibrating atoms with sufficiently high temperature on a surface. Electrons suffering such scattering appear as incoherent electrons from atomically-localized sources. Each of these atomically-localized sources may scatter elastically from its nearby atoms, and produce a holographic interference pattern.

Some other holographic algorithms, such as, the scattered-wave included Fourier transform (SWIFT) [79,**?**], referenced and scattered-wave included Fourier transform (RSWIFT) [79,?,?], small-window energy-extension process (SWEEP) [80], are aimed at correcting for the image shifts caused by the anisotropic emitting source wave and anisotropic scattered wave, as well as by multiple scattering.

In this chapter, we will describe the theory of hologram formation and reconstruction in Auger and photoelectron diffraction. The basic holographic reconstruction algorithm, Barton's Helmholtz-Kirchoff one, will be discussed together with several other algorithms that improve the reconstructed images. We will also demonstrate some examples of applying the holographic technique to solve the surface structures of Ni(001)-O, Si and $\mathrm{CoSi_2}(111)$.

6.1 Theory of photoelectron and related holographies

6.1.1 Diffraction intensity formed by a local source

Consider an electron wave, with an angular momentum L, emitted at the origin:

$$A_L h_l^{(1)}(kr) Y_L(\hat{\mathbf{k}}).$$

If a scatterer is assumed at the position $\mathbf{r}_j$, the resulting wave-field at the far field in the direction of $\hat{\mathbf{k}}$ is, as demonstrated in chapter 2, given by:

$$\psi(\mathbf{k}) = A_L \left(i^{-l} Y_L(\hat{\mathbf{k}}) + \sum_{L'} G_{LL'}(k\mathbf{r}_j) t_{l'} e^{-i\mathbf{k}\cdot\mathbf{r}_j} Y_{L'}(\hat{\mathbf{k}}) \right), \tag{6.1}$$

where the exact expression for the free propagator Green's function may be written as:

$$G_{LL'}(k\mathbf{r}) = 4\pi \sum_{L''} i^{l-l'-l''} (-)^{m'-m''} h_{l''}^{(1)}(kr) Y_{l'',-m''} \int Y_{lm} Y_{l''m''} Y_{l'',-m'} d\Omega.$$

The electron wavelength should be significantly smaller than the distances between the emitter and scatterers in order to resolve the atomic structures, and this requires:

$$kr \gg 1.$$

Under such circumstances the Green's function may be approximated by

$$G_{LL'}(k\mathbf{r}) = 4\pi i^{l'-1}\left(\frac{e^{ikr}}{ikr}\right)Y^*_{L'}(\hat{\mathbf{r}})Y_L(\hat{\mathbf{r}}).$$

This may be regarded as the lowest-order approximation to a "separable" Green's function as defined by Rehr *et al* [8]. Thus, we obtain from Eq. 6.1,

$$\psi(\mathbf{k}) = A_L\left(Y_L(\hat{\mathbf{k}}) + f(\hat{\mathbf{k}}\cdot\hat{\mathbf{r}}_j)\frac{e^{i(kr_j-\mathbf{k}\cdot\mathbf{r}_j)}}{r_j}Y_L(\hat{\mathbf{r}}_j)\right), \tag{6.2}$$

where the common factors of i^{-l}'s are dropped, and the atomic scattering factor takes the "plane-wave" form of:

$$f(\hat{\mathbf{k}}\cdot\hat{\mathbf{r}}_j) = \frac{4\pi}{ik}\sum_{L'}Y^*_{L'}(\hat{\mathbf{r}}_j)Y_{L'}(\hat{\mathbf{k}}).$$

More accurate approximations of $\psi(\mathbf{r})$ in Eq. 6.2 may be calculated using higher-order separable Green's functions [8], which result in more accurate atomic scattering factors, such as the "spherical-wave" form [79,?] of $f(\mathbf{k},\mathbf{r})$ as already discussed in Chapter 2.

If the emitted electron source takes a more complicated form, and is expanded as a linear combination of spherical harmonic functions in the angular momentum representation,

$$\phi(\mathbf{k}) = \sum_L a(k,L)Y_L(\hat{\mathbf{k}}),$$

where $a(k,L)$ is a complex function of k and L, and if several scatterers at position $\mathbf{r}_j$ are involved in the scattering, the resulting wave field may be expressed as

$$\psi(\mathbf{k}) = \phi(\mathbf{k}) + \sum_j\left(f(\mathbf{k},\mathbf{r}_j)\frac{e^{i(kr_j-\mathbf{k}\cdot\mathbf{r}_j)}}{r_j}\phi(\mathbf{r}_j)\right). \tag{6.3}$$

The first term is the reference wave of emitter that goes directly to the electron detector in the far field, and the summation term represents the scattered waves, or the object waves. In an experiment, only electron intensity modulations may be measured with an electron analyzer. This may be written as:

$$I(\mathbf{k}) = \left|\phi(\mathbf{k}) + \sum_j \left(f(\mathbf{k}, \mathbf{r}_j) \frac{e^{i(kr_j - \mathbf{k}\cdot\mathbf{r}_j)}}{r_j} \phi(\mathbf{r}_j) \right)\right|^2 . \tag{6.4}$$

Although the phase information is not recorded directly, such information is contained in the angular distribution of the diffraction intensity modulation throughout the hemisphere of measurement, and could be recovered by an appropriate algorithm.

6.1.2 Barton's Helmholtz-Kirchoff transform

Barton [17] suggested that one may use a Fourier transform formula to convert the intensity modulation into an image function, $A(\mathbf{r})$,

$$A(\mathbf{r}) = \int\int I(\mathbf{k}) e^{-i\mathbf{k}\cdot\mathbf{r}} d\mathbf{k}_{||}, \tag{6.5}$$

where $\mathbf{k} = (k_x, k_y, k_z)$ is a wave vector, $\mathbf{k}_{||} = (k_x, k_y)$ its component parallel to the surface, and k_z may be written as

$$k_z = \sqrt{k^2 - k_x^2 - k_y^2}.$$

Substituting Eq. 6.4 into Eq. 6.5, one obtains

$$A(\mathbf{r}) = \underbrace{\int\int dk_x dk_y e^{-i\mathbf{k}\cdot\mathbf{r}} \left|\phi(\mathbf{k})\right|^2}_{\text{Direct term}}$$

$$+ \underbrace{\int\int dk_x dk_y e^{-i\mathbf{k}\cdot\mathbf{r}} \phi(\mathbf{k}) \sum_j \left(f^*(\mathbf{k}, \mathbf{r}_j) \frac{e^{-i(kr_j - \mathbf{k}\cdot\mathbf{r}_j)}}{r_j} \phi^*(\mathbf{r}_j) \right)}_{\text{Image term}}$$

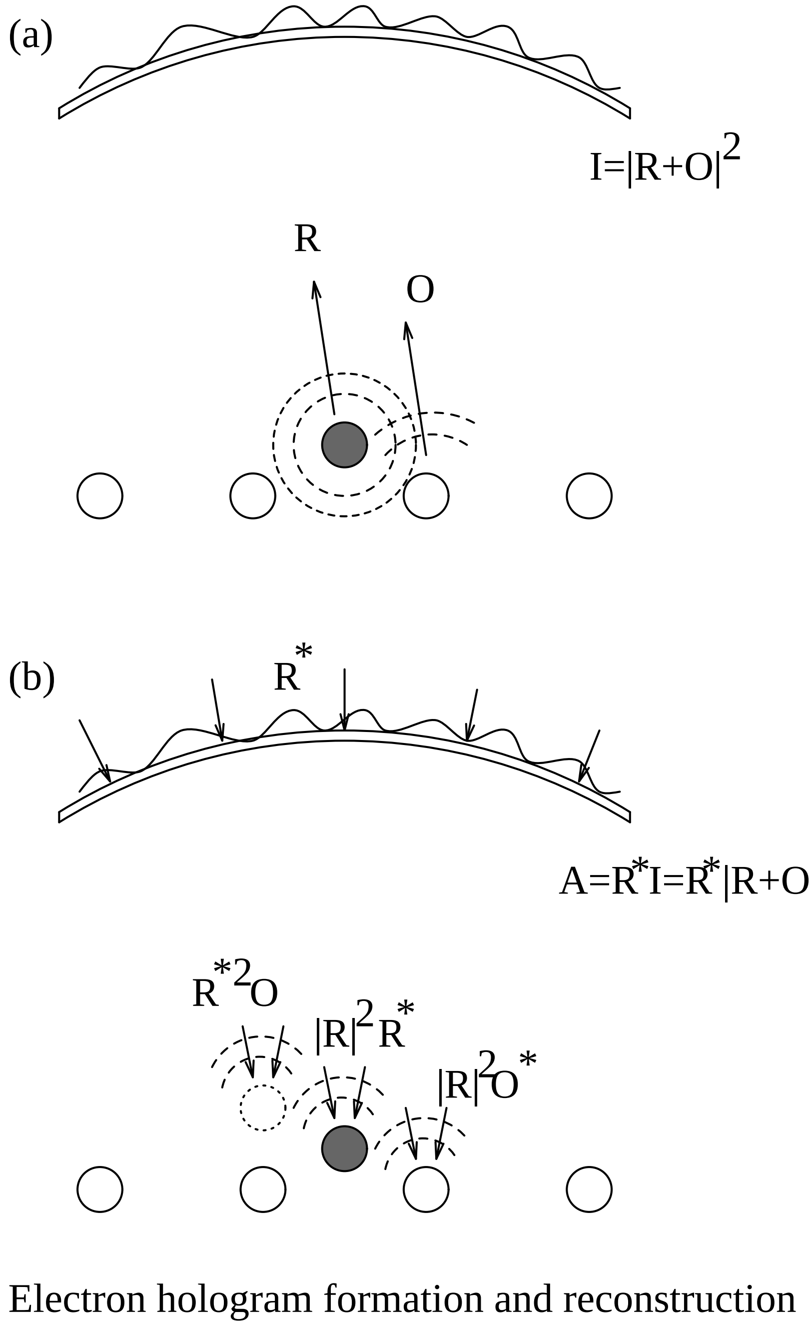

Figure 6.2: Schematic diagram of electron hologram formation and reconstruction with an atomic electron source. A reference wave, R, interferes with a scattered wave, O, and the resulting diffraction pattern is recorded on a film. An image may be reconstructed by shining a time-reversed wave, R^*, on the developed film. The $O^*|R|^2$ term forms the atom image near the scatterer, $R^{*2}O$ term froms its twin image, $|R|^2R^*$ converges at the emitter position, and squared term of the object wave, $|O|^2R^*$, is negligible if $O \ll R$.

$$+\underbrace{\int\int dk_x dk_y e^{-i\mathbf{k}\cdot\mathbf{r}}\phi^*(\mathbf{k})\sum_j\left(f(\mathbf{k},\mathbf{r}_j)\frac{e^{i(kr_j-\mathbf{k}\cdot\mathbf{r}_j)}}{r_j}\phi(\mathbf{r}_j)\right)}_{\text{Twin image term}}$$

$$+\underbrace{\int\int dk_x dk_y e^{-i\mathbf{k}\cdot\mathbf{r}}\sum_{j'}\sum_j\left(f(\mathbf{k},\mathbf{r}_{j'})f^*(\mathbf{k},\mathbf{r}_j)\frac{e^{i(kr_{j'}-\mathbf{k}\cdot\mathbf{r}_{j'})}}{r_{j'}}\frac{e^{-i(kr_j-\mathbf{k}\cdot\mathbf{r}_j)}}{r_j}\phi(\mathbf{r}_{j'})\phi^*(\mathbf{r}_j)\right)}_{\text{Self-interference term}} \tag{6.6}$$

A schematic diagram of electron hologram formation and reconstruction with an atomic source is shown in Fig. 6.2 on page 167. If we assume that the first term in Eq. 6.6, $\mid\phi(\mathbf{k})\mid^2$, does not vary very much with $\mathbf{k}$, i.e., that the emitter is quite isotropic, that the scattering factor $f(\mathbf{k},\mathbf{r})$ is a smooth function of $\mathbf{k}$, and that the fourth term is negligible, it may be seen that the image function of Eq. 6.6 will peak at the position of the scatterer $\mathbf{r}_j$:

$$\mathbf{r} = \mathbf{r}_j$$

due to the second term which is called the image term, and also peaks at

$$\mathbf{r} = -\mathbf{r}_j$$

due to the third term which is called twin image term. The latter term peaks at positions which are related to the atom positions by an inversion operation through the center of the emitter. The fourth term (the self-interference term) in Eq. 6.6 is similar to the Patterson function of x-ray diffraction, which represents the effects of the interference between the scattered waves. In the case of the backscattering geometry, this term is negligible, but will pose a serious problem in the forward-scattering geometry.

From the above strict conditions, it can be seen that Barton's transform would be expected to break down for an anisotropic emitter wave, a highly forward peaked atomic scattering factor at high electron kinetic energy and in the forward-scattering geometry hologram, etc. Generally speaking, due to the extra phase contributed from the atomic scattering factor, emitter wave function and the square term, the images are often shifted, spurious and dominated by an artifact near the origin. Therefore other image reconstruction algorithms were developed for dealing with such problems.

6.1.3 Other algorithms for the scattered and reference wave corrections and the multiple energy integral

The scattered-wave included Fourier transform (SWIFT) [22,**?**] was an algorithm developed to overcome the effects of anisotropic scattered and reference waves by introducing a kernel function that does not require any prior knowledge of the crystal structure. By looking at Eq. 6.6, it is easily seen that if one defines a kernel function

$$F(\mathbf{k},\mathbf{r}) = f^*(\mathbf{k},\mathbf{r})\phi^*(\mathbf{r})\phi(\mathbf{k}),$$

and modified Eq. 6.5 to

$$A(\mathbf{r}) = \int\int \frac{I(\mathbf{k})}{F(\mathbf{k},\mathbf{r})} e^{-i\mathbf{k}\cdot\mathbf{r}} d\mathbf{k}_{\|}, \tag{6.7}$$

the second term of Eq. 6.6 will become a $\delta(\mathbf{r}-\mathbf{r}_j)$ like function after the integral, and sharply peak at

$$\mathbf{r} = \mathbf{r}_j.$$

This image-correction technique compensates for the angular dependence of the scattered and emitter waves, and preserves the direct-inversion principle of holographic transforms, while not requiring a prior knowledge of atomic positions. However, it still does not solve the problem caused by the cross term of the interferences of the scattered waves amongst themselves, or the fourth term in Eq. 6.6.

The effect of this term is to give rise to satellite peaks lying between atom positions, and artifacts near the origin. The effect of this term is that each scattering atom acts somewhat like an independent emitter, and the final holographic image is composed of the environment of each scatterer superimposed on the image at the origin.

As first suggested by Saldin and De Andres [76] a simple average of the reconstructed image function can improve the *fidelity* of the image. Since the spurious images are generally energy dependent, it is possible to average them out, leaving only the atomic features which are energy independent, and the formula is as simple as:

$$|A(\mathbf{r})|^2 = \int_{k_{min}}^{k_{max}} |A_k(\mathbf{r})|^2 \, dk \tag{6.8}$$

where the k_{max} and k_{min} are the maximum and minimum wave vector ranges.

Similar multiple energy integrating algorithms put forward by, e.g., Barton [85],

$$A(\mathbf{r}) = \int_{k_{min}}^{k_{max}} dk \int dk_y \int dk_x \chi(\mathbf{k}) e^{i(kr - \mathbf{k}\cdot\mathbf{r})} \tag{6.9}$$

and by Tong *et al.* [86]:

$$A(\mathbf{r}) = \int_{k_{min}}^{k_{max}} dk \int dk_y \int dk_x \chi(\mathbf{k}) e^{i(kr - \mathbf{k}\cdot\mathbf{r})} g(\mathbf{k}) \tag{6.10}$$

were intended to eliminate the cross term and multiple scattering effects in the electron hologram, where $\chi(\mathbf{k})$ is the anisotropy of the diffraction intensity, and $g(\mathbf{k})$ is a window function which ensures that $\chi(\mathbf{k})$ begins and ends at nodal points. The distance r in the phase factor is measured from the electron emitter to the image point currently being calculated, instead of the distance to any particular scatterer's positions. Thus, the essence of the direct measurement of holography is still preserved.

6.2 Holographic image of Auger emission from O on Ni(001) surface

For adsorbate emitters, striking reconstructed images have been demonstrated from computer-simulated diffraction patterns by, e.g., Barton [17] and Saldin et al. [76], and the effectiveness of this technique in such configurations is now well established. Therefore, in what follows we reconstruct holographic images from our diffraction patterns, partly to confirm the correctness of our simulation of the diffraction pattern, but also to examine and comment on a much-debated topic, namely the effect of multiple-scattering on the holographic process.

As an example of an application of Barton's Helmholtz-Kirchoff algorithm, Auger electrons emitted by an O atom adsorbed on the four-fold hollow site on a Ni(001) surface is considered in the simulation. For simplicity, an s-wave emitter is assumed here. In this special case, a backscattering geometry satisfies the condition that the object wave is smaller than the reference wave. The energy of the emitted electrons was taken to be 504 eV, corresponding to a prominent O Auger line.

Fig. 6.3 (a) shows the resulting back-scattered diffraction pattern calculated by the full multiple-scattering version of concentric-shell algorithm [32] for polar angles ranging from zero at the center of the pattern to 70^o at the edges. For the purposes of our discussion of the effect of multiple-scattering on holographic reconstruction from such a pattern, we show on Fig. 6.3 (b) the corresponding diffraction pattern calculated in the single-scattering (kinematic) limit.

The latter pattern is achieved by neglecting the the back-scattering matrix product $\mathbf{T}_{q+1}^{OI}\mathbf{J}_{q}^{IO}$ as in the forward-scattering approximation of Sec. 2, but now additionally only the terms up to first order in the forward-scattering matrices

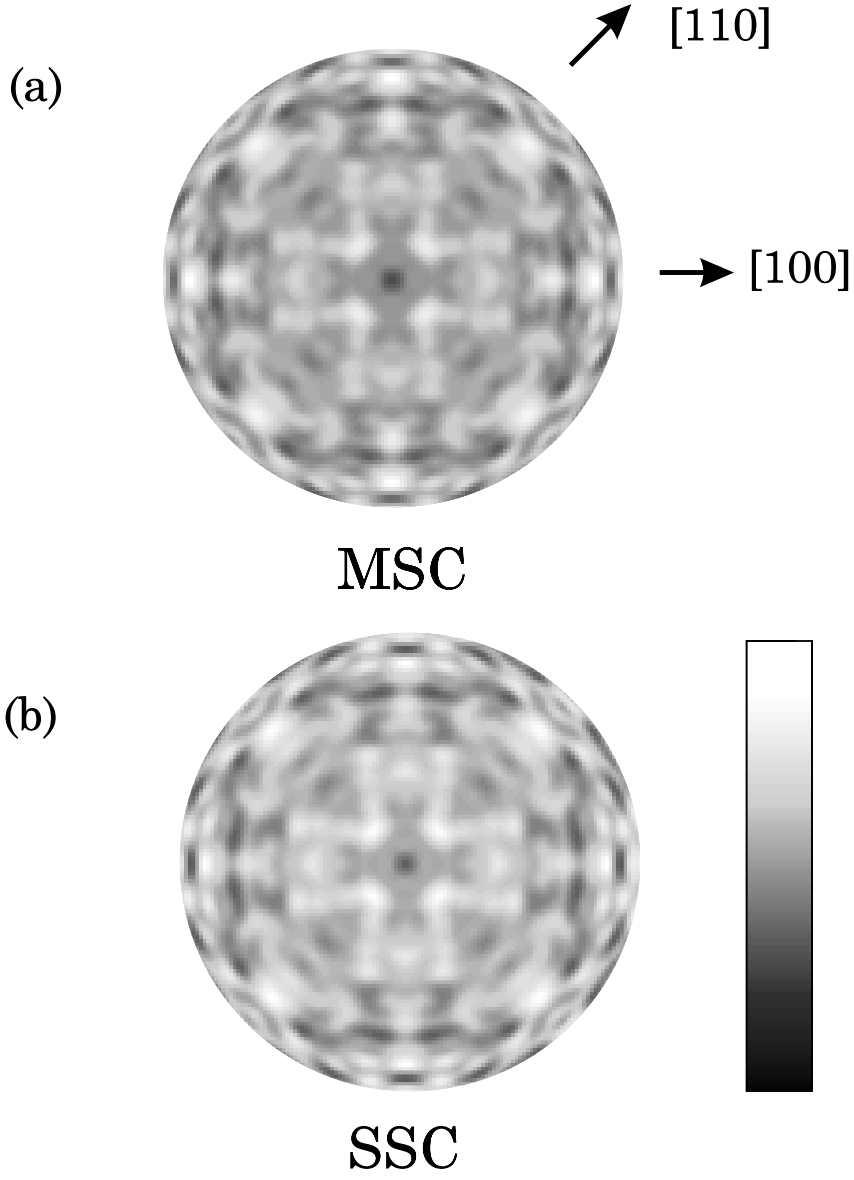

Figure 6.3: Calculated electron diffraction patterns for KVV Auger emission from an O adatom adsorbed on the fourfold hollow site of a Ni(001) surface, using (a) full multiple-scattering calculation (MSC), and (b) single-scattering calculation (SSC). Note that there are differences between these two patterns, indicating the necessity of including full multiple scattering from atoms in this geometry.

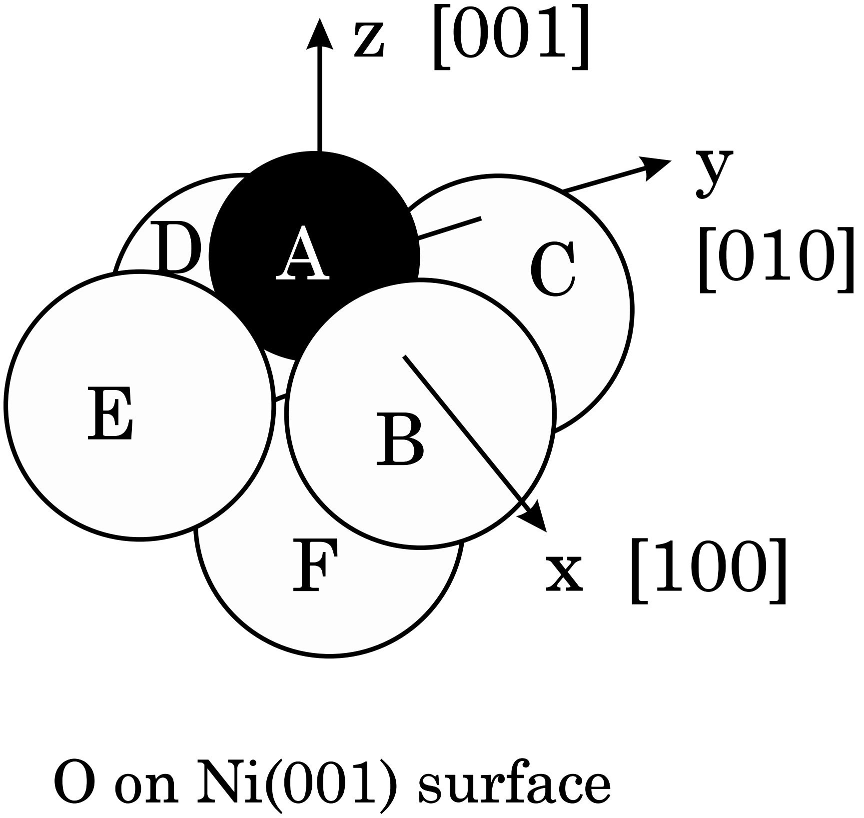

Figure 6.4: Model of the atomic geometry of O/Ni(001). The dark sphere, A, represents an O atom adsorbed on a fourfold hollow site of Ni(001) surface. The light spheres represent the Ni atoms.

$\mathbf{T}_q^{OO}$ in Eq. 2.18 on page 35 are retained. Then $\mathbf{S}^{(N)}$ may be further approximated by

$$\mathbf{S}^{(N)} \simeq \mathbf{I} + \mathbf{T}_1^{OO} + \mathbf{T}_2^{OO} + \cdots + \mathbf{T}_N^{OO}. \tag{6.11}$$

The two diffraction patterns of Fig. 6.3 show differences, demonstrating the importance of multiple scattering in calculations of backscattered diffraction patterns.

We then perform the holographic reconstruction by means of Barton's algorithm [17]

$$A(x,y,z) = \int I(k_x,k_y)\exp\left[-i\sqrt{(k^2-k_x^2-k_y^2)}\,z\right]e^{-i(k_x x+k_y y)}dk_x dk_y \tag{6.12}$$

which relates the amplitude of a reconstructed "image" at a real-space position with Cartesian coordinates (x,y,z) relative to the electron emitter, to the intensities $I(k_x,k_y)$ of a diffraction pattern, where k_x and k_y are the Cartesian components of the local wave-vector $\mathbf{k}$ of the detected electrons. The corresponding real-space intensity is taken to be $I_{rec}(x,y,z) = |A(x,y,z)|^2$.

Fig. 6.4 shows a model of the atomic geometry assumed in the cluster calculations of the electron diffraction pattern. An O atom (dark sphere) is assumed to be adsorbed on a four-fold hollow site of a Ni(001) surface. The light spheres represent the Ni atoms. Fig. 6.5 displays the variation $I_{rec}(x,y,z=-0.82\mathring{A})$ of the reconstructed intensity in the plane of the uppermost layer of Ni atoms on our surface. Part (a) of this Figure shows the reconstructed image from the full multiple scattering diffraction pattern of Fig. 6.3 (a), while part (b) shows that from the single scattering pattern of Fig. 6.3(b). Bright spots are seen very close to the positions of the substrate atoms B, C, D, and E of our model, and on both parts of the Figure. Fig. 6.6 (a) and (b) depict the corresponding intensities $I_{rec}(x=0,y,z)$ in a plane perpendicular to the surface and passing through two of the nearest-neighbor Ni atoms. Bright intensity streaks, perpendicular to the surface, are seen passing through the positions of the atoms C and E, as well as through their "twin-image" positions, C' and E', respectively, on the images reconstructed from the multiple scattering (a) and single scattering (b) diffraction patterns, as well the position of atom F in the second Ni layer, and its twin image F'.

It has been shown by Fig. 6.5 and Fig. 6.6 that there is relatively little degradation of the reconstructed image due to multiple scattering, despite the noticeable differences between the multiple and single scattering patterns on Fig. 6.3 (a) and (b), respectively.

6.3 Holographic image of ARXPD from Si(001)-[2×1] surface

Many recent results have shown that diffraction patterns produced by localized electron sources, such as those from Auger electron [89], photoelectron [90], and Kikuchi electron [77] diffraction patterns, can be interpreted as holograms. However, in the reconstruction of the holographic image from a diffraction pattern, one has first to measure a high quality hologram with fine interference fringes, which can be achieved by requiring a high angular resolution of the diffraction pattern. This restriction could be relaxed if several single-energy diffraction patterns were used for energy integrated holographic reconstruction.

6.3.1 The holographic and non-holographic features in an ARXPD

There are many factors that can affect the quality of a reconstructed image: some of these are due to the restrictions of the experiments, and some are due to

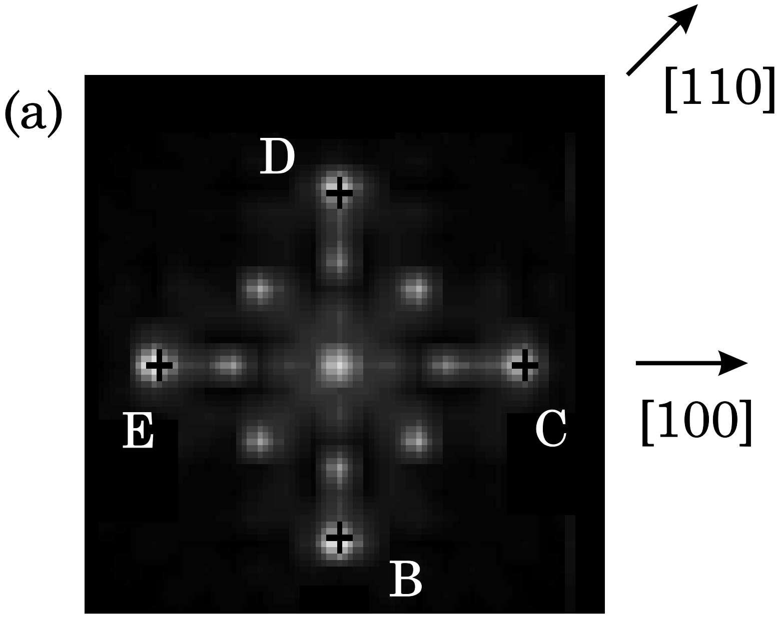

MSC

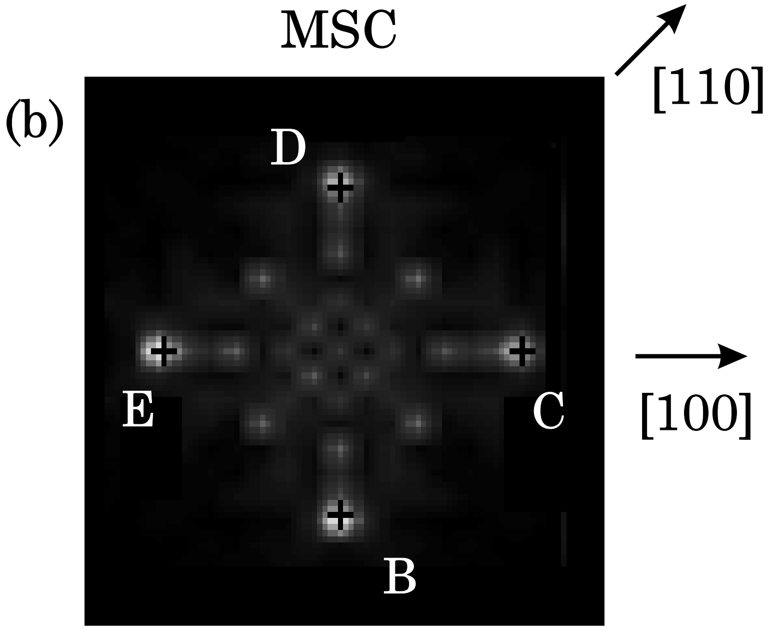

SSC

Figure 6.5: Holographic images obtained from the holograms of Fig. 6.3. The images are shown at $z = -0.82\mathring{A}$ plane, which passes through the outermost Ni surface layer. Image (a) was reconstructed from the MSC hologram, and (b) was from the SSC hologram. Both images show the bright spots near the positions of substrate Ni atoms.

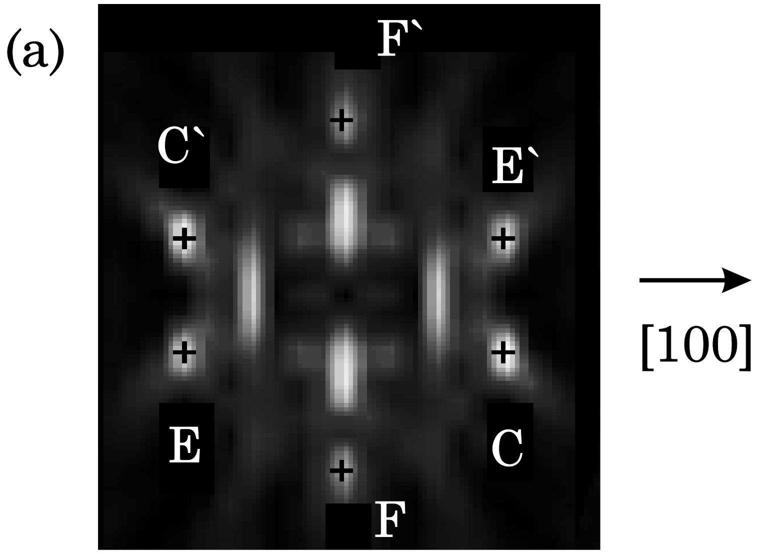

MSC

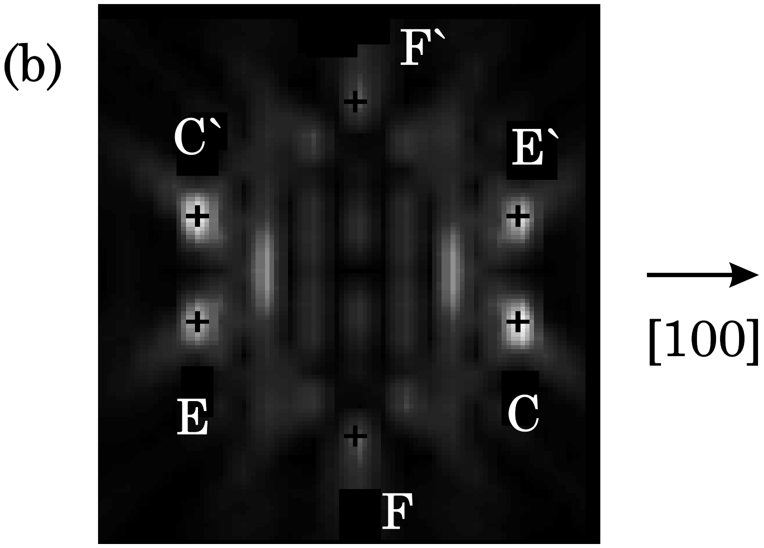

SSC

Figure 6.6: Holographic images obtained from the holograms of Fig. 6.3. The images are shown at $x = 0.0\mathring{A}$ plane, which passes vertically through emitter and two of the nearest-neighbor Ni atoms. Image (a) was reconstructed from the MSC hologram, and (b) from the SSC hologram. The prime's letters represent the twin images.

the reconstruction algorithm. The experimental limitations include the selectivity and quality of the transition peak in the XPS spectrum, the detector's spatial and energy resolution, the signal to noise ratio, the angular range of the diffraction pattern, the sample's condition including surface roughness (steps and defects on the surface). Given otherwise ideal experimental circumstances, the fundamental limit to spatial resolution using holographic inversion techniques is mainly determined by the electron energy, or wave vector k, and angular range (maximum collected angle θ) of the diffraction pattern. The spatial resolution parallel to the surface is

$$\Delta r_{||} = \frac{\pi}{ksin\theta},$$

and that for the vertical component is

$$\Delta r_{\perp} = \frac{2\pi}{k(1-cos\theta)}.$$

Given an electron kinetic energy of 1000 eV, and full range of diffraction pattern, $\theta = 90\ ^o$, the spatial resolution of $\Delta r_{||}$ and $\Delta r_{\perp}$ are equal to 0.8 $\AA$ and 1.6 $\AA$, respectively. Although, the improvement of the experimental conditions can provide a better quality diffraction pattern, an advanced holographic inversion algorithm is still needed for ARXPD. Such an algorithm should include corrections for the the electron wave that emitted from the photoemission process, which may be highly anisotropic in nature, the scattered electron wave, which is also highly forward peaked at high electron kinetic energy, and multiple-scattering processes, which also add some difficulties to the interpretation of the holographic image.

The intensity I_o of an experimental Si-2s core-level ARXPD diffraction pattern from a Si(001)-[2×1] surface, at an electron kinetic energy of 1337 eV, measured by B. P. Tonner and co-workers, is plotted versus the wave vectors parallel to the surface, k_x and k_y, as shown in Fig. 6.7 on page 180. The maximum polar angle of the diffraction pattern is 70 ^{o} and with the center of the pattern pointing along the sample normal, i.e., the [001] direction. The ARXPD was done in such a way that the incident x-ray beam and the direction of the outgoing photoelectron lie in a plane containing the sample normal. The sample normal is rotated in this plane to scan the polar angle θ. Rotation of the sample about its normal direction varies the azimuthal angle ϕ. Elastic scattered electrons from the Si-2s transition were recorded by separating the peak intensity with the background signals in an XPS spectrum.

We will use here the two-dimensional Fourier transform algorithm of Barton to reconstruct the holographic image. The third dimension, k_z, of this transform is determined by

$$k_z = \sqrt{k^2 - k_x^2 - k_y^2}.$$

The reconstruction algorithm can be written as:

$$A(\mathbf{r}) = \int_{k_{x_{min}}}^{k_{x_{max}}} dk_x \int_{k_{y_{min}}}^{k_{y_{max}}} dk_y \left\{ I_o(k_x, k_y) e^{-iz\sqrt{k^2-k_x^2-k_y^2}} e^{-ixk_x - iyk_y} \right\}, \qquad (6.13)$$

where the $k_{x_{min}}, k_{x_{max}}$ and $k_{y_{min}}, k_{y_{max}}$ are the minimum and maximum electron wave vectors in the x and y directions respectively, parallel to the surface. The diffraction pattern was digitized on a grid of 128 × 128 pixels with uniform steps of Δk_x, and Δk_y as the input to a two-dimensional fast Fourier transform (FFT) program [106]. With a fixed z_o value, the inversion routine returns an output array in a real space with the same size (in two dimension), but with a different order in the array. It, then, needs to be reordered in order to construct a *single* image plane $A(x, y, z_o)$. Continuing this process by changing the z_o value to cover a cubic volume will generate the reconstructed image function $A(x, y, z)$.

Consider the local geometry of a Si emitter in a Si(001) surface, as shown in

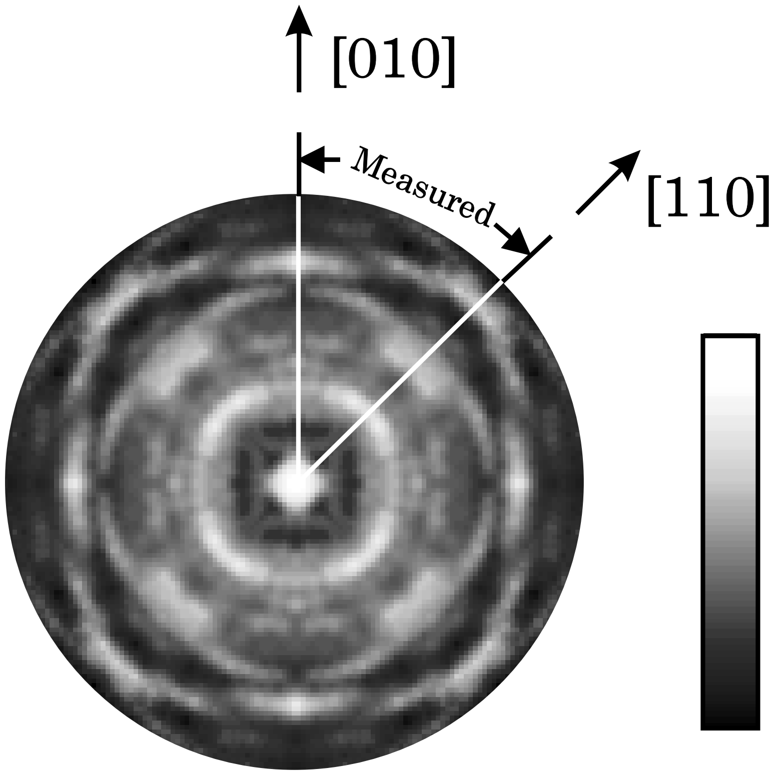

Si-2s ARXPD pattern from
Si(001) surface at 1337 eV

Figure 6.7: The experimental diffraction pattern from Si-2s core-level of a Si(001)-[2×1] surface with kinetic energy of 1337 eV as measured by B. P. Tonner and co-workers.

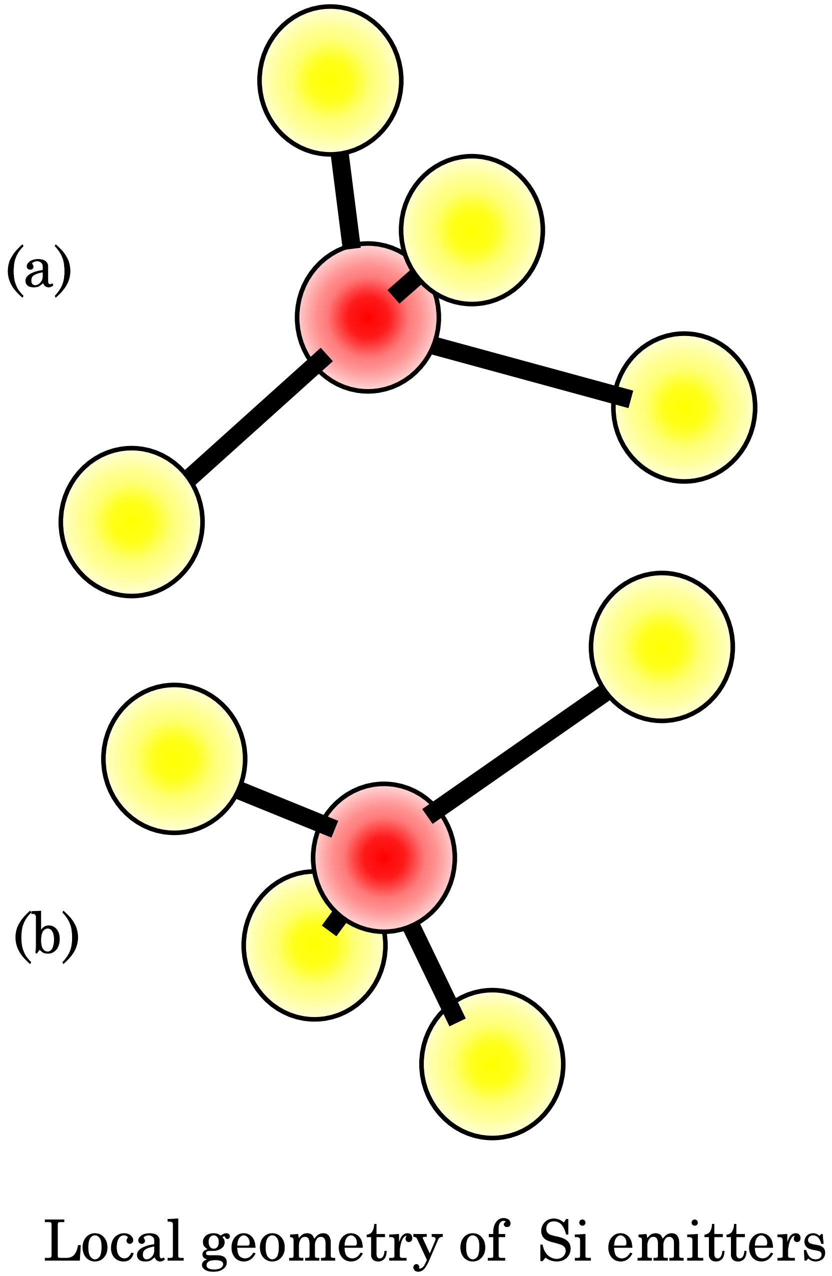

Figure 6.8: Local geometry of Si emitters in a Si(001) surface. Two orientations of Si emitter local geometries, tetrahedral structures, are shown by (a) and (b). Cluster (a) rotated about [001] by 90^o would generate cluster (b). The Si diamond lattice constant is 5.43 $\AA$ with the Si-Si bond length 2.406 $\AA$.

Fig. 6.8 on page 181. If we ignore the surface reconstruction on the grounds that the top layer atoms contribute little to the holographic fringes on the diffraction pattern, we need consider only the two orientations of tetrahedral structures in the crystal, one rotated by 90^o with respect to the other. The Si emitters in those two clusters produce two diffraction patterns, and rotating one pattern by 90^o about [001] direction would reproduce that generated by the other cluster.

A straightforward Fourier integral of diffraction pattern $I_o(k_x, k_y)$ with Eq. 6.13 results in a three-dimensional intensity distribution, $A(\mathbf{r})$, which is shown in Fig. 6.9 on page 183. The sides of the cubic volume that can be seen on this figure are the planes of $x = 2.55\mathring{A}$, $y = 2.55\mathring{A}$, and $z = 2.55\mathring{A}$ where atoms should be located (assuming an emitter at the origin), the expected atom positions are in near the corners of this cube. No clear indication of atom images are observed on those planes on Fig. 6.9. Strong artifact images are observed at the top of the cube, where no atom is located. The poor image function obtained by direct inverting the diffraction pattern of the Si-2s ARXPD pattern is due to the fact that there are many strong artifacts, which dominate the reconstructed image, appearing near the center of each face of the cube.

However, one may notice that Fig. 6.7 is dominated by the so-called forward-scattering peaks along the low-index Miller directions. Due to the strong forward-scattering feature of the electron scattering factor, the self-interference term in Eq. 6.6 cannot be neglected in this situation. Some other unknown features, such as the intensity background, might also contribute to the artifacts formed in the real space close to the origin. We know that the holographic information lies in the interference fringes which are spread over a large area of the diffraction pattern, it is obvious that some other features, such as the anisotropy of the source

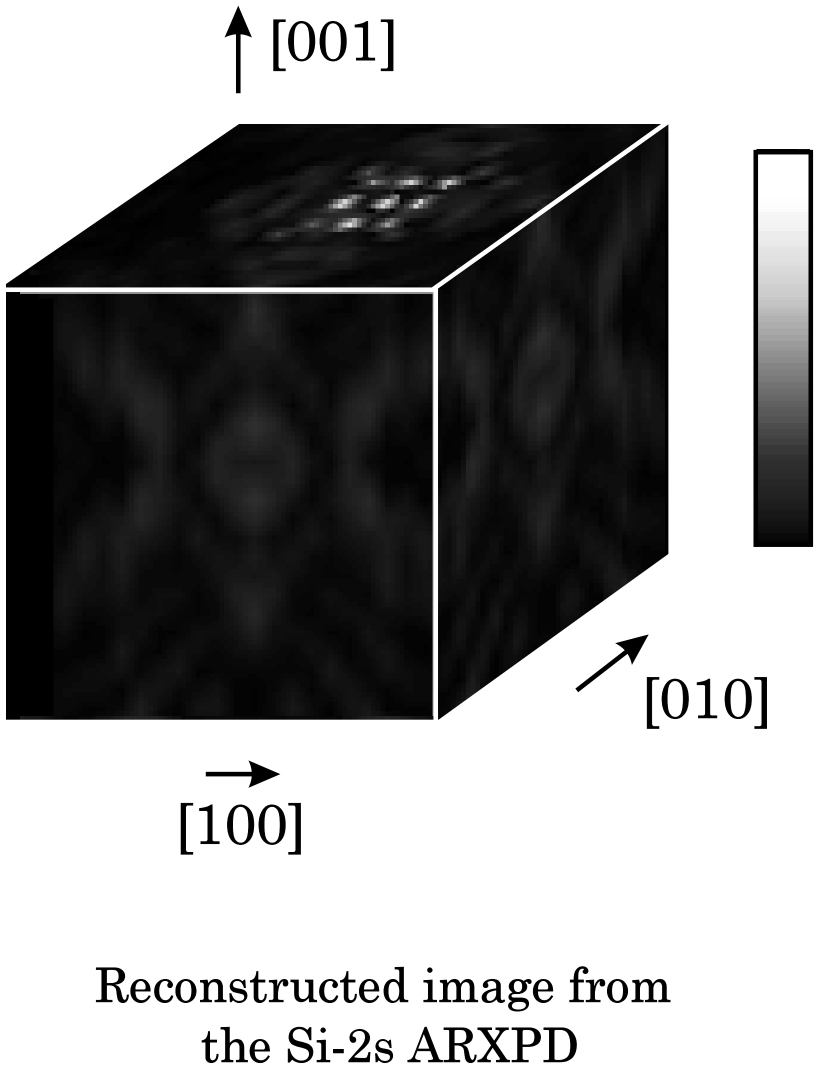

Figure 6.9: Reconstructed image of unfiltered Si-2s core-level ARXPD pattern from Si(001)-[2×1] surface. The sides of the cubic volume were formed by cutting through the planes of $x = 2.55\mathring{A}$, $y = 2.55\mathring{A}$, and $z = 2.55\mathring{A}$, where the true atom positions are located. No clear indication of atomic images are seen.

wave from the atomic transition, can also greatly affect the quality of the inverted holographic image even when good experimental conditions have been maintained. So we first try to eliminate those non-holographic features in the diffraction pattern by subtracting a smooth background from the hologram, and then carry out the holographic reconstruction.

6.3.2 Filtering process

In can be seen that by convolving the original diffraction anisotropy, $\chi(\mathbf{k}_{||})$, with Gaussian of sufficient large angular width, one may remove all the (fine) holographic fringes. If this smooth function, which is a non-holographic pattern, is removed from the original pattern, one is left only with the holographic information to be inverted into a holographic image.

In principle, a "local average" function may be subtracted with the formula:

$$\chi(\mathbf{k}_{||}) = I(\mathbf{k}_{||}) - \frac{\int_{\Delta k_x}\int_{\Delta k_y} I(\mathbf{k}_{||}^{'})d(\mathbf{k}_{||}^{'} - \mathbf{k}_{||})}{\int_{\Delta k_x}\int_{\Delta k_y} d(\mathbf{k}_{||}^{'} - \mathbf{k}_{||})},$$

where the Δk_x, Δk_y are the width of the local area for the average.

Our aim is to find a smooth function which can be used to suppress the background of the diffraction pattern consisting of forward-scattering peaks and other unknown non-holographic features. One way of finding the smooth function is by defining a function, $F_o(k_x, k_y)$, by

$$F_o(k_x, k_y) = A_1(k_x, k_y)k_x^{'2} + A_2(k_x, k_y)k_x^{'}k_y^{'} + A_3(k_x, k_y)k_y^{'2} + A_4(k_x, k_y)k_x^{'} + A_5(k_x, k_y)k_y^{'} + A_6(k_x, k_y) \qquad (6.14)$$

where $k_x^{'}$ and $k_y^{'}$ are the x and y components of the detected electron wave vectors over a limited region of the diffraction pattern, and the A's are real functions of k_x and k_y, determined by a best fit of the $F_o(k_x, k_y)$ to the experimental data $I_o(k_x, k_y)$,

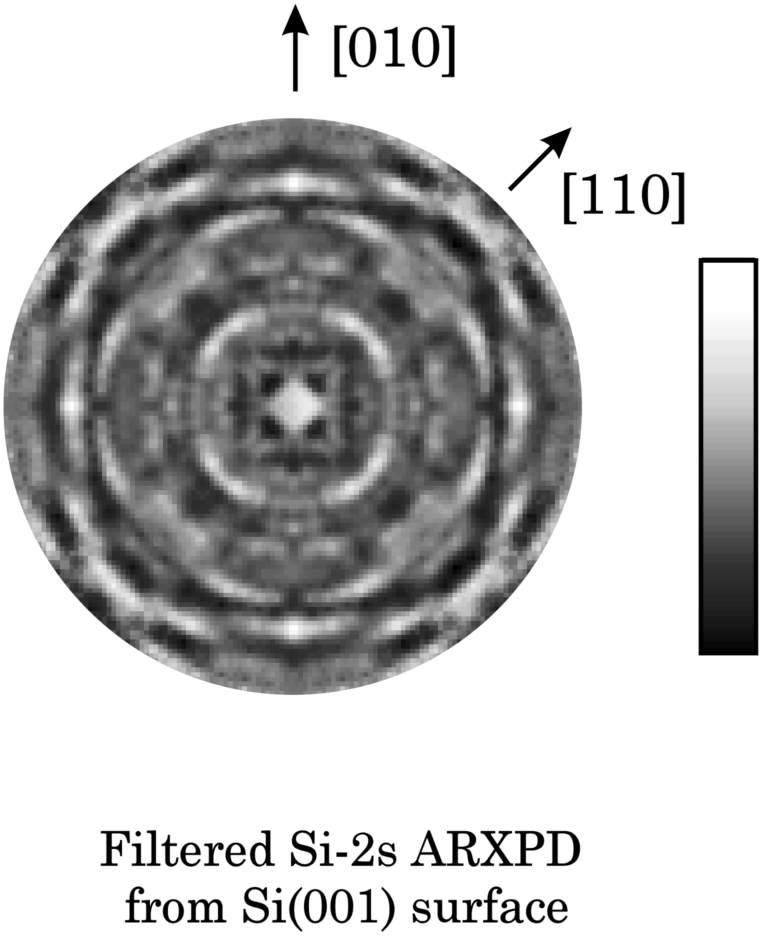

Figure 6.10: The filtered Si-2p core-level ARXPD from Si(001)-[2×1] surface. Note that after the filtering process, the fine fringes of the holographic interference are enhanced throughout the pattern, and the forward-scattering peaks are reduced.

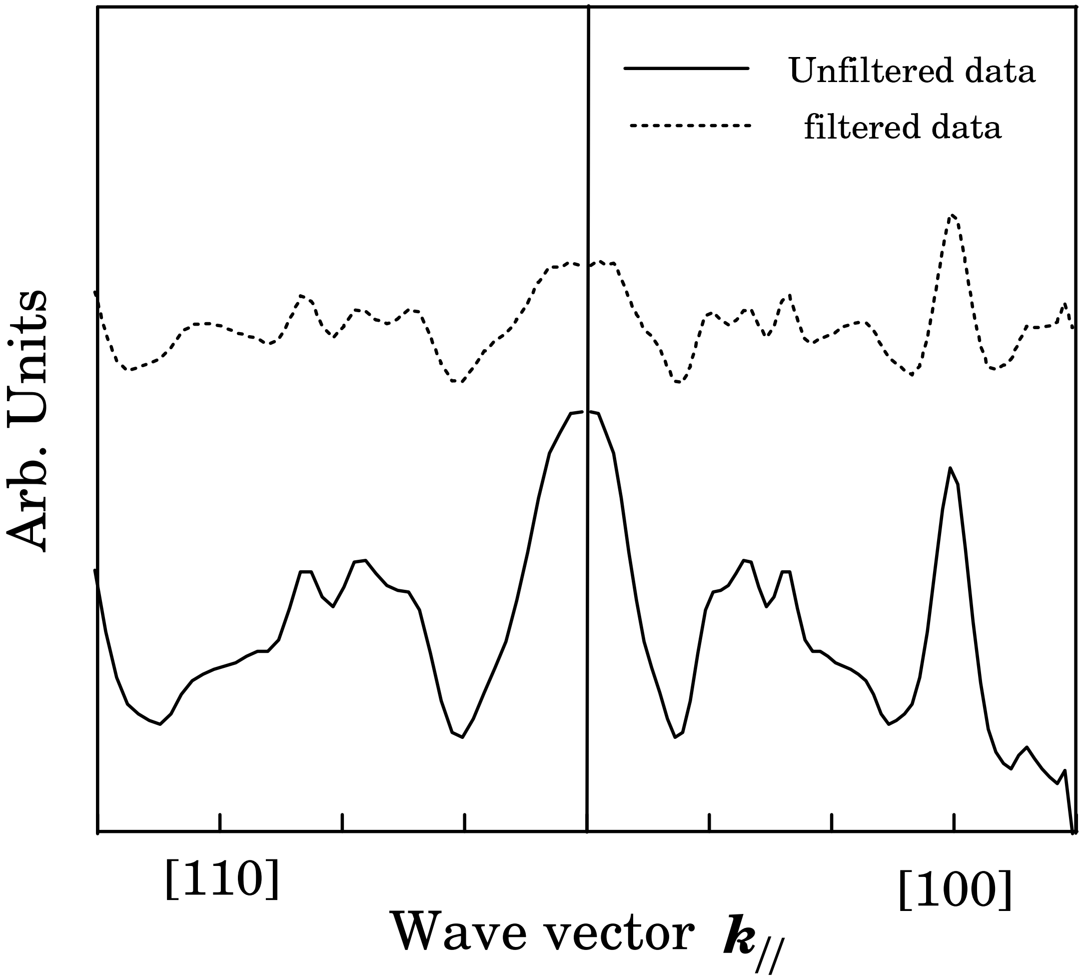

Figure 6.11: The filtered (dashed line) and unfiltered (solid line) diffraction intensity of Si-2p core-level ARXPD from a Si(001)-[2×1] surface along the [010] and [110] azimuths. Note that the filtered curve emphasizes the small fringes throughout the pattern while suppressing the strong forward-scattering peaks along the low-index directions.

in a small region centered at k_x and k_y. In this way, a smoothed background through the whole pattern may be determined. The "filtered" holographic data is, then, taken to be this smooth background function subtracted from the measured data, namely:

$$F(k_x, k_y) = I_o(k_x, k_y) - F_o(k_x, k_y).$$

This process is justified by the argument that the fine holographic interference fringes are spread all over the diffraction pattern and will not be removed by subtracting such a smooth function. The overall signal to noise ratio is also improved by this procedure.

The "filtered" diffraction pattern is shown in Fig. 6.10 on page 185. We also plot the "filtered" hologram intensity in two major azimuths [010] and [110], along with "unfiltered" data for comparison, in Fig. 6.11 on page 186. It is clearly seen on Fig. 6.11 that the "filtered" curve emphasizes the small fringes throughout the pattern while suppressing the strong forward-scattering peaks along the low-index directions. Then, replacing $I_o(k_x, k_y)$ in Eq. 6.13 by $F(k_x, k_y)$, we obtained the reconstructed image function, $A(\mathbf{r})$, which is shown in Fig. 6.12 on page 188. The faces of the cubic volume are taken to be the same as those of Fig. 6.9. It is very clearly seen that image function in Fig. 6.12 has been improved dramatically compared with the unfiltered reconstructed image. The nearest neighbor Si atom images clearly show up in the planes of $x = 2.55\AA$, $y = 2.55\AA$, and $z = 2.55\AA$, with small artifacts near the center of each face of the cube. The atom images on Fig. 6.12 are shifted by only several tenths of an Angstrom. These shifts could be due to the angular anisotropy of the waves scattered by the near neighbors of the emitter atom [91].

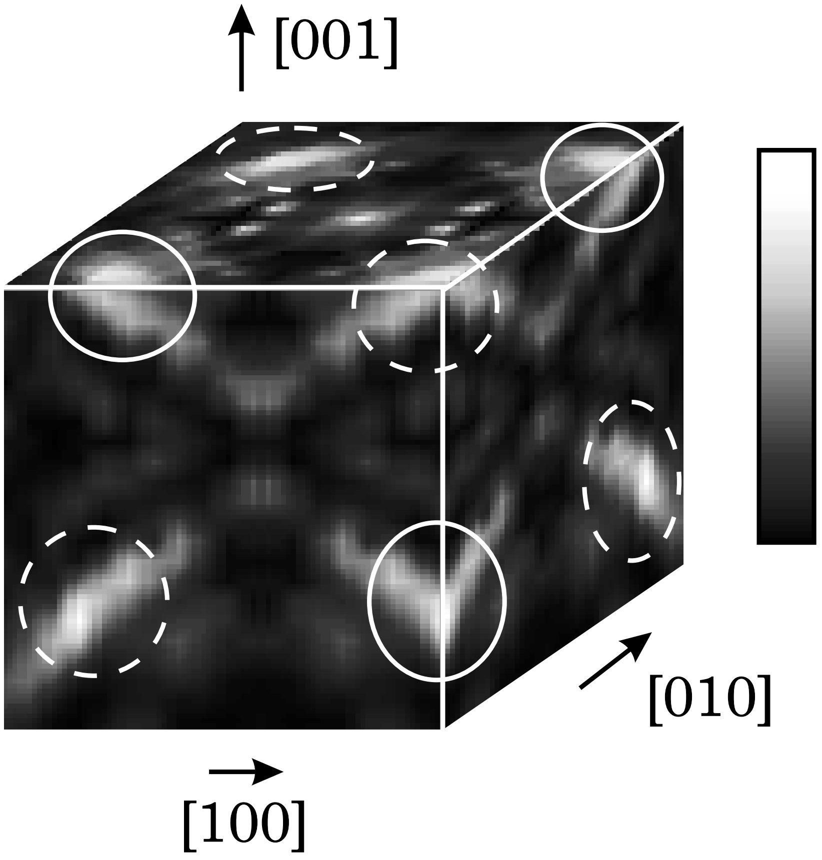

Reconstructed image from the filtered Si-2s ARXPD

Figure 6.12: Holographic reconstruction from the filtered Si-2s core-level ARXPD pattern from a Si(001)-[2×1] surface. The dashed circles represent the atom images from cluster (a), and solid circles for images from cluster (b) of Fig. 6.8.

6.4 Holographic image of Co-3p ARXPD from a $CoSi_2(111)$ surface

In this section, we will discuss the use of the direct inversion method of photoelectron holography for the study of the Co-3p ARXPD from a $CoSi_2(111)$ surface. A photoelectron diffraction pattern from a $CoSi_2(111)$ surface was recorded on the Argonne-Minnesota beam-line at Synchrotron Radiation Center, Madison, Wisconsin. A higher kinetic energy will result in a higher spatial resolution in directions both parallel and perpendicular to the surface, but on the other hand, atomic scattering factors tend to be more anisotropic at higher kinetic energy. Therefore, a photon energy of 750 eV and electron kinetic energy of 695 eV from Co-3p core-level photoemission was chosen as a compromise. Another reason that the Co-3p photoemission peak was measured was to make the XPD diffraction pattern more surface sensitive, as the Co emitters are located at the second, fifth, and eighth layers etc. Due to the limited electron mean free path, only the Co emitters in the second and fifth layer would contribute significantly to the diffraction intensity in far field. A detailed surface model showing the local geometry of the Co emitters at the second and fifth layers is shown on Fig. 6.13 on page 190. In a LEED study [68], surface reconstruction was not observed. However, the first interlayer spacing of the $CoSi_2(111)$ surface is contracted by 12%, the second expanded by 2.5%, and the third contracted by 1.2%.

6.4.1 Reference and Scattered-Wave Included Fourier Transform

Due to the complexity of the Co emitter source wave as determined by the dipole selection rules, and the anisotropic atomic scattering factor, a number of factors should be taken into account before performing the holographic recon-

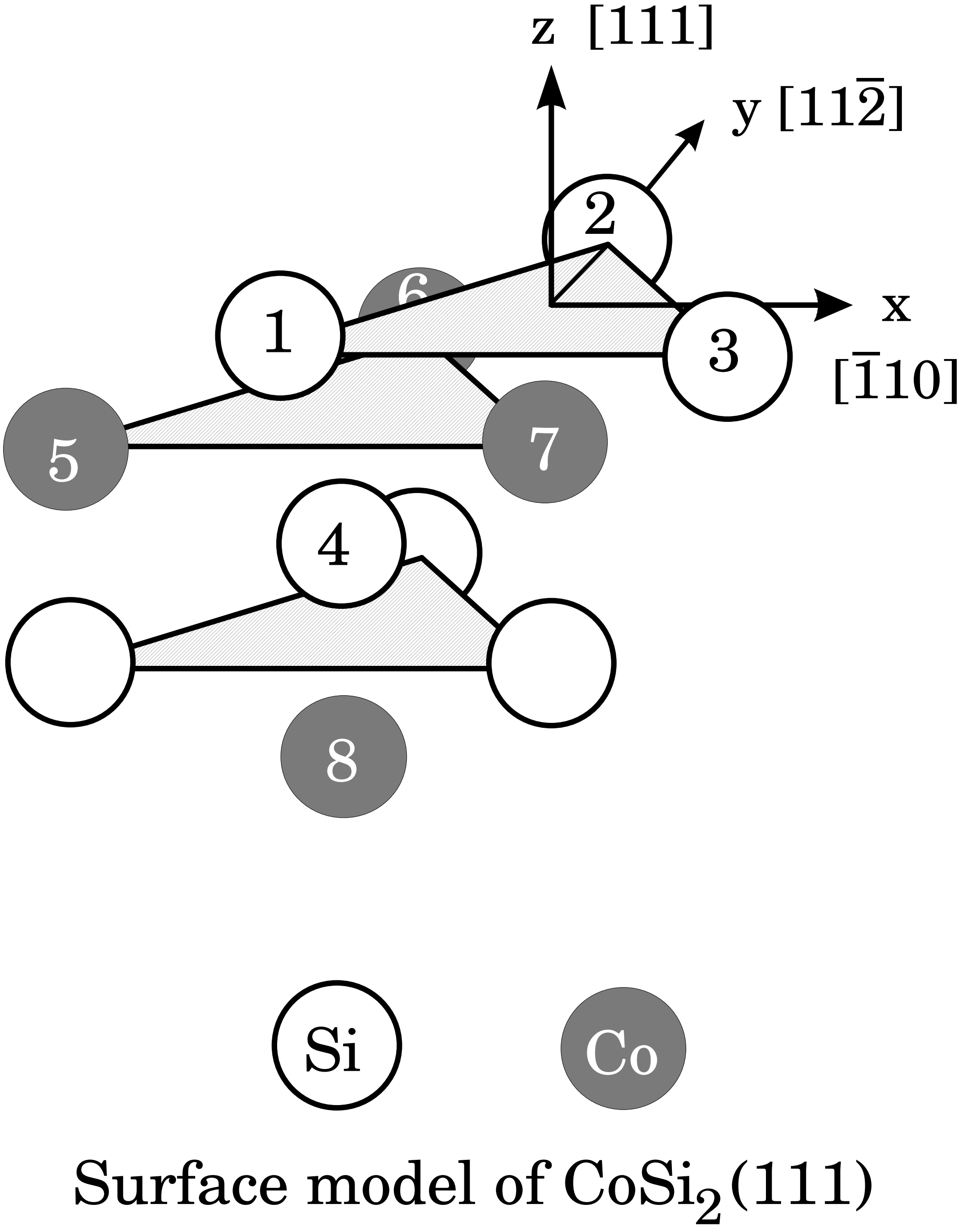

Figure 6.13: Perspective diagram of local geometry of the Co emitters in a $CoSi_2$(111) surface. The Co emitter in the fifth layer will produce a reconstructed image of the nearest-neighbor atoms, as well as those of the next-nearest-neighbor atoms.

struction, including background subtraction, correction for the anisotropic emitted wave, correction for the anisotropic atomic scattering factor, and eliminating the self-interference of the object waves which cause the forward-scattering peaks on the diffraction pattern.

Firstly, we applied the Barton's Helmholtz-Kirchoff algorithm to the diffraction pattern of Fig. 5.4. No clear indication in the reconstructed image function was found of the true atom positions in the $\mathrm{CoSi_2}(111)$ surface structure. As we have described in Sec. 6.3.2, this is because a smooth background function hampers the reconstruction process due to the self-interference terms along the low Miller-index directions and contributes to the artifact near the origin. These background artifacts may be removed through the filtering process introduced in Sec. 6.3.2. A "local average" intensity, which can be calculated using Eq. 6.14, was subtracted from the original intensity. The anisotropy function, $\chi(\mathbf{k})$, is shown on Fig. 6.14 on page 192 along the $[11\bar{2}]$ azimuth, together with diffraction intensity before the filtering for comparison. It may be seen in Fig. 6.14 that the filtering suppressed the forward-scattering peaks and enhanced the fine fringes in the pattern.

Now we introduce a reference and scattered-wave included Fourier transform (RSWIFT) algorithm to correct for both the anisotropic electron emitter source and the anisotropic atomic scattering factor. In the SWIFT algorithm

$$A(\mathbf{r}) = \int\int \frac{I(\mathbf{k})}{K(\mathbf{k},\mathbf{r})} e^{-i\mathbf{k}\cdot\mathbf{r}} d\mathbf{k}_{||} \tag{6.15}$$

the kernel function was defined to account of the contribution of the anisotropic emitted electron wave of Co-3p photoemission and the forward atomic scattering factor. In this specific experimental geometry, we employ the (inverse) kernel

$$K(\mathbf{k},\mathbf{r}) = \sum_{L_c}\sum_{L}\sum_{L'} M_{LL_c} M^*_{L'L_c} Y_L(\hat{\mathbf{k}}) Y^*_{L'}(\hat{\mathbf{r}}) f^*(\mathbf{k}\cdot\mathbf{r}) \frac{e^{-ikr}}{r}, \tag{6.16}$$

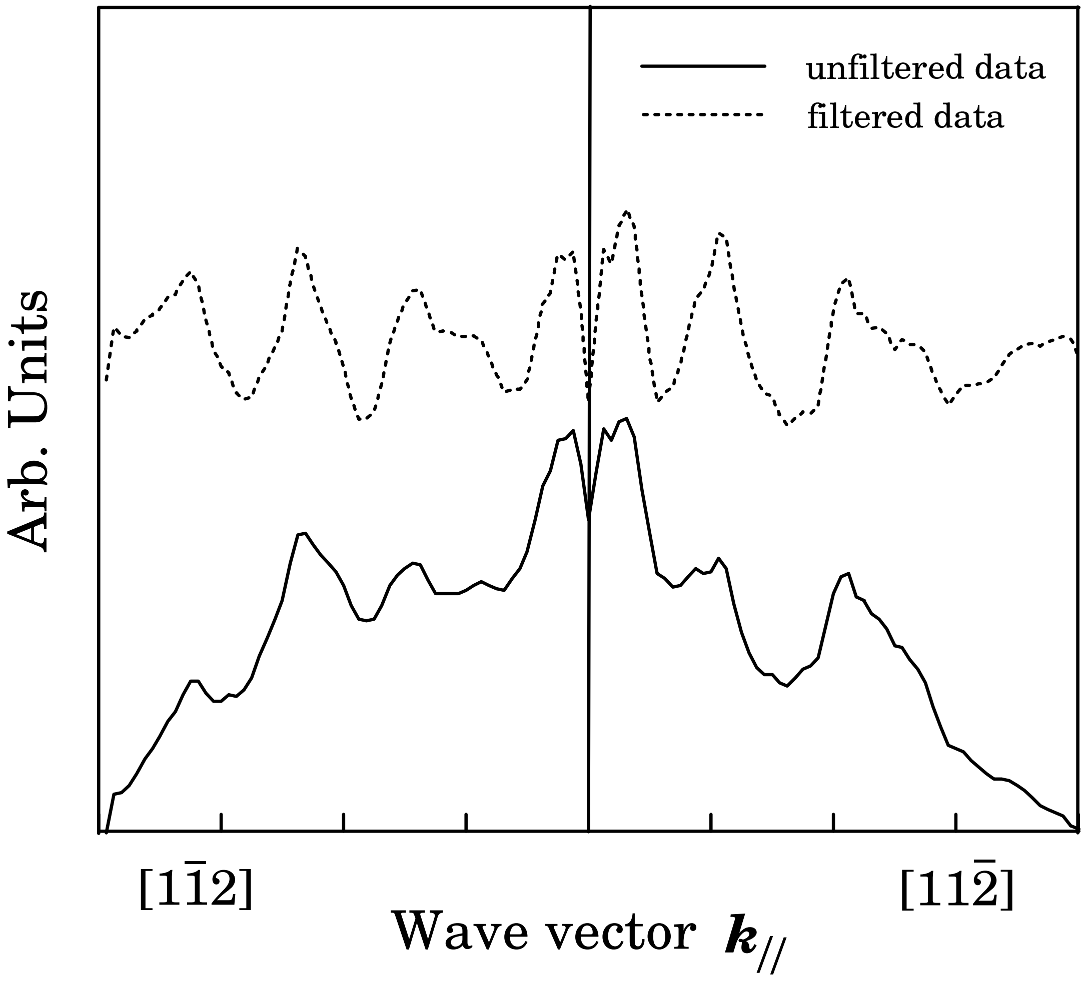

Figure 6.14: Filtered and unfiltered intensity from Co-3p core emission from a $CoSi_2$(111) surface. The plot is along the [11$\bar{2}$] direction. The “local average” of 27×27 points was used to subtract a smooth function which suppressed the self-interference terms caused by the forward-scattering peaks.

where L_c specifies the initial core state, L and $L^{'}$ are the angular momenta of the emitted free electron states, and the M's are the allowed transition matrix elements, defined by

$$M^{(0)}_{LL_c} =< L|cos(\theta)|L_c >< R(r,\epsilon,l)|r|R_{31}(r) > e^{i\delta_l}$$

where the polarization direction of the photon is taken along the z axis, and the core-state radial wave function of $R_{31}(r)$ is the solution of the radial Schrӧdinger equation of a cobalt atom for principal quantum number, $n = 3$, and angular momentum quantum number, $l = 1$. $R(r, \epsilon, l)$ is a solution of the radial Schrӧdinger equation within the muffin-tin sphere for an energy of ϵ, matching on to the function $j_l(kr)cos(\delta_l)$ - $n_l(kr)sin(\delta_l)$ at the muffin-tin radius, where j_l and n_l are the spherical Bessel and Hankel functions respectively, and δ_l is a phase shift of a Si atom. As have been calculated in chapter 5, the emitted states of a photoelectron in Co-3p photoemission are s and d states, and the non-zero transition amplitudes are:

$$M^{(0)}_{2\bar{1},1\bar{1}} = 3.153e^{i\delta_2}$$

$$M^{(0)}_{00,10} = 1.444e^{i\delta_0}$$

$$M^{(0)}_{20,10} = 3.641e^{i\delta_2}$$

and

$$M^{(0)}_{21,11} = 3.153e^{i\delta_2}$$

Eq. 6.15 can cause a serious problem as the reconstructed intensities for negative z in real space tend to be much higher than those for positive z. This could add difficulties in interpreting the image function obtained from Eq. 6.15. Since the phase part of the kernel function, $K(\mathbf{k}, \mathbf{r})$, is the major correction for the image shifting in the SWIFT algorithm, we can modify Eq. 6.15 for including only the phase part of the kernel function (6.16), thus

$$A(\mathbf{r}) = \int\int \frac{I(\mathbf{k})|K(\mathbf{k},\mathbf{r})|}{K(\mathbf{k},\mathbf{r})} e^{-i\mathbf{k}\cdot\mathbf{r}} d\mathbf{k}_{||} \tag{6.17}$$

Therefore, image function obtained by Eq. 6.17 will be quite "uniformly" distributed at both positive and negative z.

6.4.2 Reconstructed image

The image function, $A(\mathbf{r})$, was obtained by performing the reference and scattered-wave corrected Fourier transform of Eq. 6.17 with the kernel function of Eq. 6.16.

Fig. 6.15 on page 195 shows the reconstructed image function, $A(\mathbf{r})$, in the x = 0.0 $\mathring{A}$ plane, where two Si atoms (atoms (2) and (4) as indicated in Fig. 6.13), a Co atom (atom (6)), and their twin images are seen. The solid circles represent the true atom positions, dashed circle that of the emitter, and dotted circles those of the twin images in this plane. Fig. 6.16 on page 196 shows the plane y = -0.93 $\mathring{A}$, where two Si atoms ((1) and (3)) and two Co atoms ((5) and (7)) are indicated by solid circles representing the true atom positions. Fig. 6.17 on page 197 shows the plane z = -0.57 $\mathring{A}$, where three nearest-neighbor Si atom ((1), (2), and (3)) are seen. In this plane the background intensity is seen to be very low and the signal-to-noise ratio is relatively higher than that of the x and y plane cuts. The advantage of using a $CoSi_2$ crystal as a sample is that the emitter and the nearest scatterers are of different chemical species, which ensures that the photoelectrons of the same energy are not emitted by both the reference wave source and its nearest-neighbor scatterers. The high Debye temperature of a $CoSi_2$ sample provides a rigid lattice for the study. The layer spacing between the emitter and its nearest

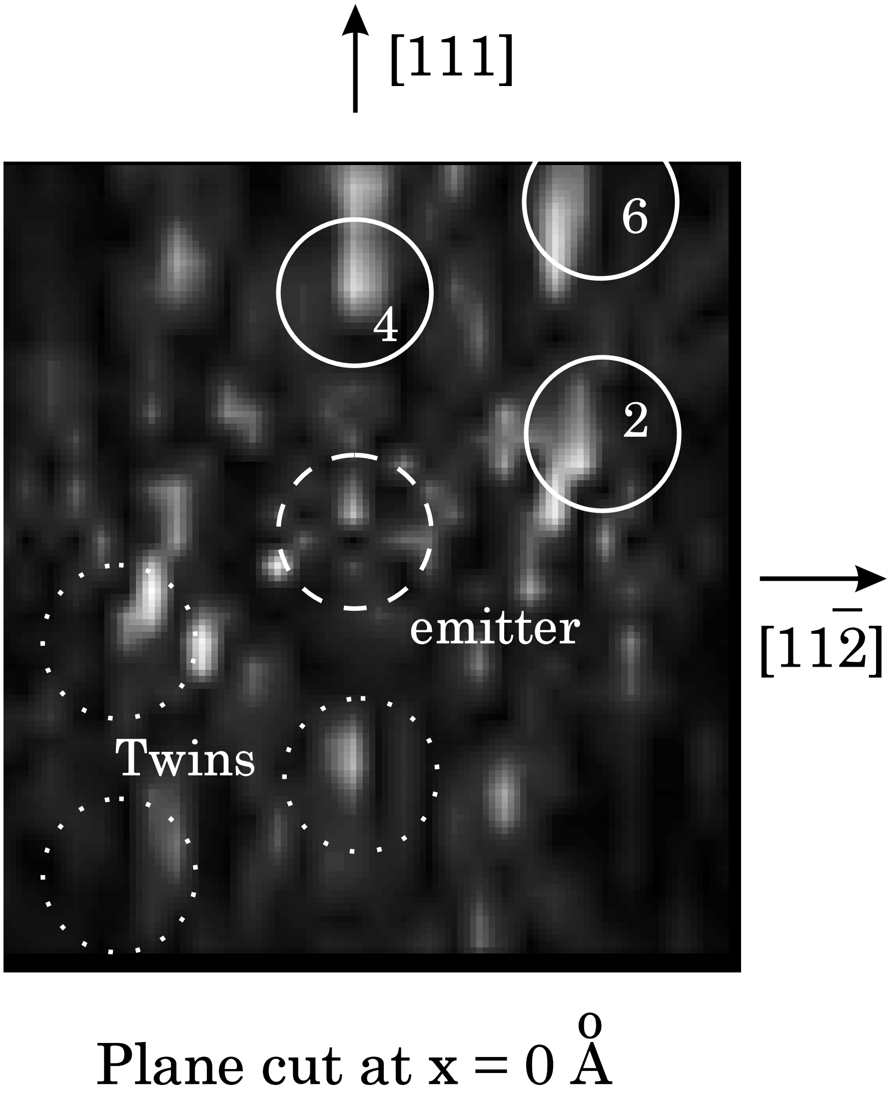

Figure 6.15: Plane cut at $x = 0\mathring{A}$ for holographic reconstruction from Co-3p ARXPD. Atom (2) is due to the second and fifth layer of Co emitters. Atoms (4) and (6) are due to the Co emitters in the fifth layer. The dashed circle is at the emitter position, and dotted circles represent the twin images of atoms (2), (4), and (6).

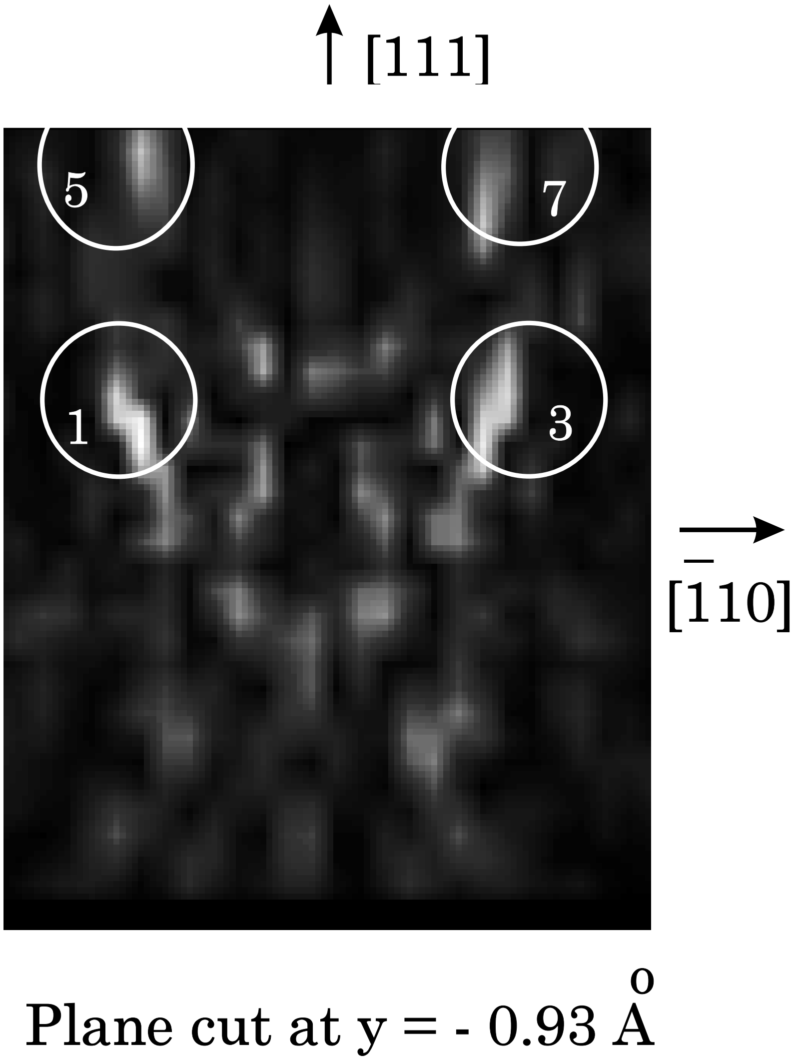

Figure 6.16: Plane cut at $y = 0.93\mathring{A}$ for holographic reconstruction from Co-3p ARXPD. Atoms (1) and (3) are due to Co emitters in the second and fifth layers. Atoms (5) and (7) are due to Co emitters in the fifth layer.

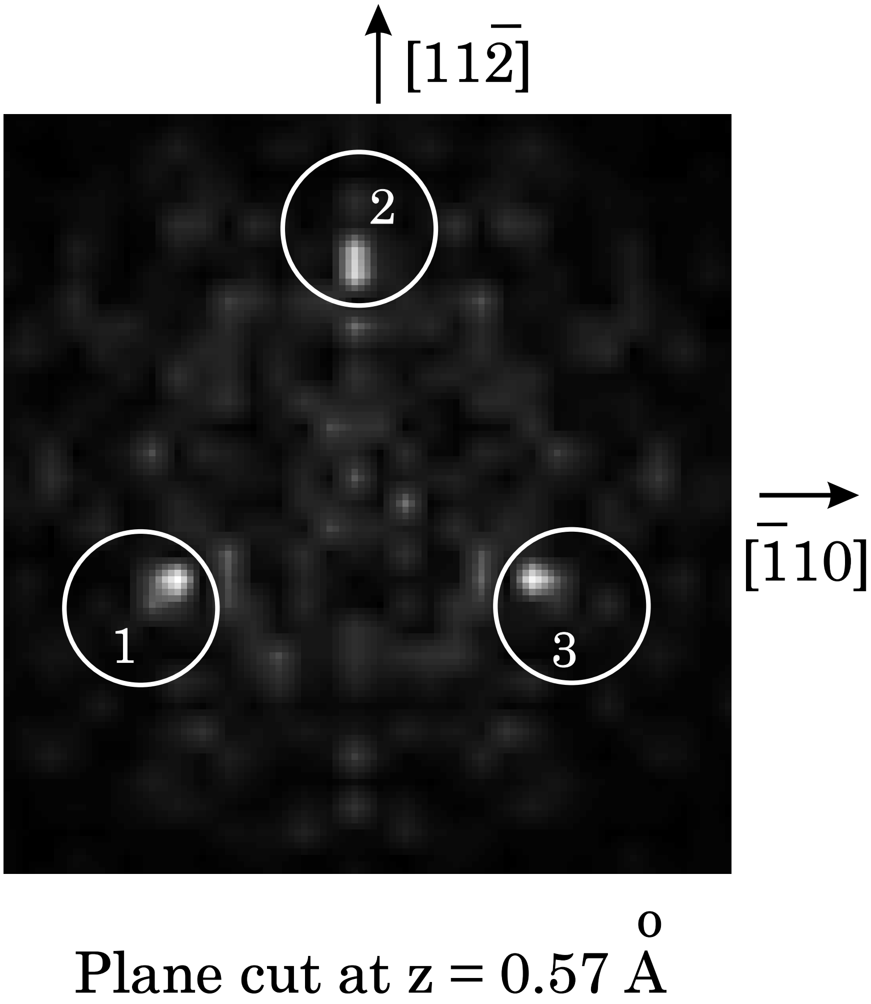

Figure 6.17: Plane cut at $z = 0.57 \mathring{A}$ for holographic reconstruction from Co-3p ARXPD. Bright spots represent the near-neighbor Si atoms (1), (2) and (3) as shown in Fig. 6.13.

neighbors is 0.57 Å along [111] direction, and this is smaller than the value of 0.68 Å obtained by a LEED dynamical analysis [68]. However, the Si atom (4) direct above the Co emitter at fifth layer is shown up at the expected position in Fig. 6.15. Furthermore, in the lateral direction, the Si images are moved closer to the emitter. The distance between the emitter and the nearest neighbor Si atoms is measured to be 2.00 Å which is reduced by about 0.29 Å from the corresponding LEED result. The estimated spatial resolutions parallel and perpendicular to the surface are 0.28 Å and 0.70 Å, respectively.

Most previous work in photoelectron holography has reported image reconstruction of mainly the nearest neighbors to an emitter. Encouragingly, in this study we are able to detect the next-nearest neighbors as well, although the quality of their images appear to be somewhat reduced. From Figs. 6.15 and 6.16, we are able to see images produced by the Co emitter located in the fifth layer. The image of atom (6) in the x-cut of Fig. 6.15 is produced by the Co emitter in the fifth layer, and is the next-nearest neighbor atom to this emitter. The images of atoms (5) and (7) shown in the y-cut of Fig. 6.16 are also the next-nearest neighbor atoms of the Co emitter in the fifth layer. Their measured vertical distance from the emitter is 2.94 Å, contracted towards the emitter by about 0.15 Å compared with the LEED result.

In order to display the significance of the RSWIFT algorithm, we compare our reconstructed image with the results obtained from on Barton's Helmholtz-Kirchoff transform, the SWIFT algorithm, x-ray crystallography, and dynamical LEED. The comparison of the results of the measured distance from the Co emitter to its nearest-neighbor Si atom are shown on Fig. 6.18 on page 200. From the Helmholtz-Kirchoff algorithm, the bond length is longer in vertical direction and shorter in the lateral direction. The SWIFT algorithm, without a reference-wave correction, drives the image even further away from its true atom position than that for the Helmholtz-Kirchoff inversion, although the vertical position of the image is at the right place. This is consistent with the observation of Saldin *et al.* [22] in the case of Auger electron holography. It will be seen, however, that the RSWIFT algorithm does move the holographic image much closer to the true atom positions, as measured by LEED and x-ray crystallography. The atom position obtained from the image function has been improved by approximately a factor of three in the RSWIFT result compared with that obtained by the Helmholtz-Kirchoff and SWIFT algorithms. The vertical distance from the emitter to the reconstructed image position of the nearest and next-nearest neighbor atoms are very close to the actual value, as shown in Figs. 6.15 and 6.16. However, the lateral distances between the emitter and the near-neighbor scatterers was about 12 % shorter than expected. The reason could be the assumption made in our reconstruction procedure that the electric field vector of the incident x-ray is normal to the sample surface, which is not exactly true, as explained in chapter 5. Another reason could be that only one-sixth of the diffraction pattern from the $CoSi_2(111)$ surface was measured with the rest of the pattern obtained by the symmetry operations. These symmetry operations were not entirely appropriate as we have already discussed in chapter 5.

6.4.3 Conclusions

In summary, we have discussed the practice of reconstructing a holographic image from a photoelectron diffraction pattern. Such an inversion procedure may be done easily by applying a Fourier transform integral to a system in a backscat-

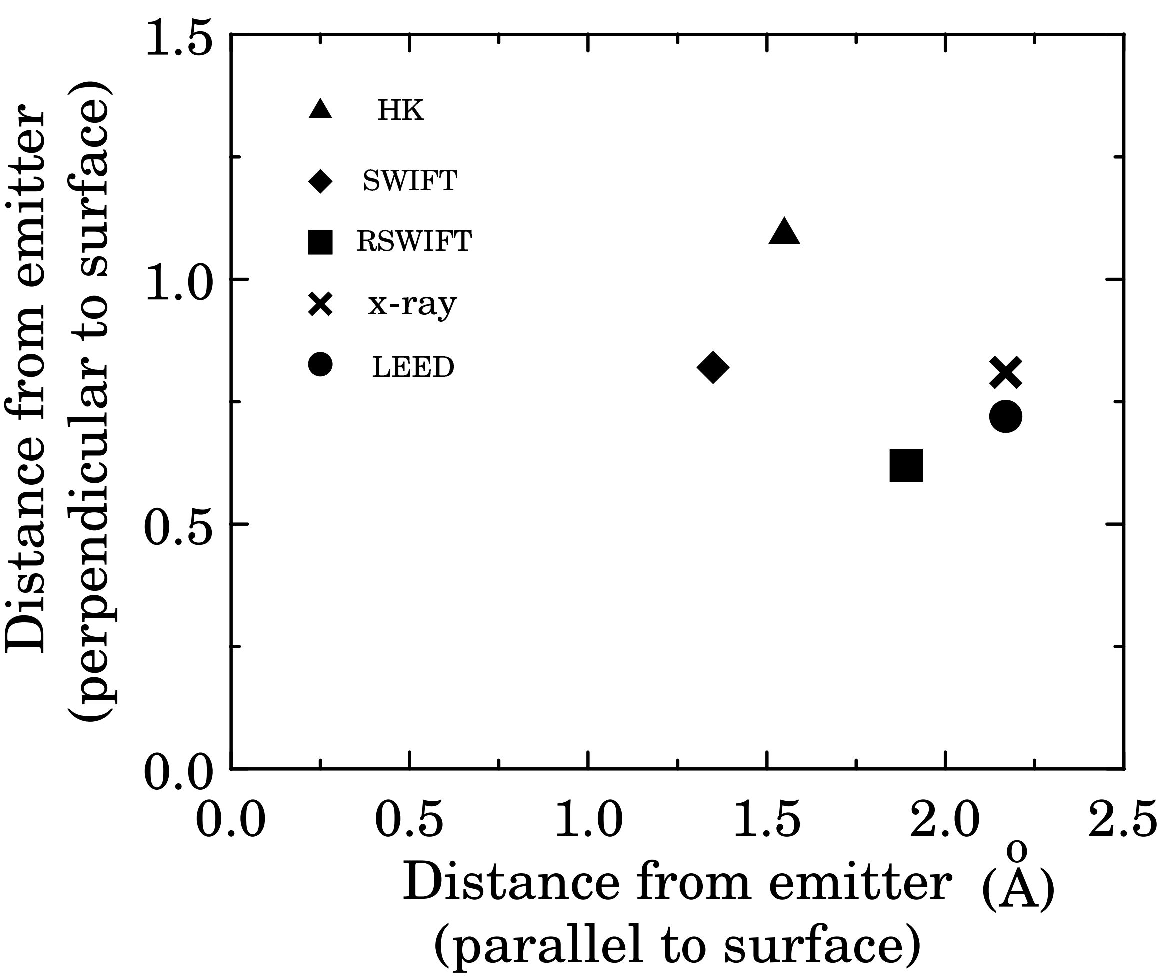

Figure 6.18: Comparison of the measured distance from Co emitter to its nearest-neighbor Si atom by using different methods. Symbols of diamond, triangle, square, cross, and circle represent the results for Helmholtz-Kirchoff algorithm (HK), SWIFT, RSWIFT, x-ray crystallography and LEED, respectively.

tered geometry, such as an O adsorbate (emitter) on a Ni(001) surface. In a forward-scattering geometry, the use of the Fourier transform integral as a reconstruction algorithm may fail to recover the actual crystal structure. Such a failure is due primarily to the appearance of the non-holographic features, such as self-interference terms of the forward-scattering intensity peaks, in the diffraction pattern. Those slowly oscillatory parts in a diffraction pattern might seriously hamper the reconstructed image, and need to be removed before holographic inversion.

We show that most of the above non-holographic features, especially those features that cause the artifacts around the origin, could be greatly reduced by a filtering process, and by this means better holographic images may be obtained with atomic resolution. Specifically, these non-holographic features may be modeled by a smooth background function of k_x and k_y, and then removed from the original diffraction pattern. The true holographic interference fringes, rapidly oscillating fine fringes in the diffraction pattern, are not affected by this procedure. Taking the "filtered" pattern as a "purer" hologram, and then carring out the Fourier transform inversion procedure, the quality of the holographic image may be greatly improved to yield atomic resolution. In other wards, most of the non-holographic features are the lower frequency parts of the diffraction pattern, and could be separated from the holographic interference fringes which correspond to the higher frequencies parts. After the filtering, the ratio of the holographic signal to noise will be increased significantly. By this means we have been able to reconstruct a much better holographic image from the ARXPD diffraction pattern from a Si(001)-[2×1] surface.

We have also demonstrated experimentally that a photoelectron diffraction pattern of an excited Co-3p electron from a $CoSi_2(111)$ surface may be inverted to form a holographic image without any prior knowledge of the crystal structure. An algorithm which corrects for both the reference wave and the anisotropy of the scattered wave was introduced and applied to the above diffraction pattern. In this algorithm, dipole transition theory is used to calculate the emitter reference wave, and the kernel function includes the source wave and the atomic scattering factor of the scattered atom at general position $\mathbf{r}$. Although some of the information, such as, the Co-3p photoemission matrix elements and the chemical identity of the scattered atoms, are known beforehand, the algorithm is still a direct method, which requires no prior knowledge of the crystal structure. A clear holographic image was obtained with reconstructed atom positions close to true atom position. Various holographic reconstruction algorithms have also been discussed, and used to reconstruct a holographic image from this photoelectron diffraction pattern. It was seen that the reference and scattered-wave included Fourier transform (RSWIFT) algorithm moves the reconstructed atom images much closer to the scatterer positions in the crystal, determined by standard LEED and x-ray crystallography methods. The remainly discrepancies could be due to the incorrect assumption that the x-ray photon polarization direction was along the surface normal in the experiment in question.

Chapter 7

Atomic Position Recovery by Iterative Optimization of Reconstructed Intensities (APRIORI)

7.1 Introduction to linear programming

7.1.1 Optimization

The basic concept of optimization is a principle underlying the analysis of many complex decision or allocation problems. It offers a certain degree of philosophical elegance, and often offers an indispensable degree of operational simplicity. By using this optimization philosophy, one may approach a complex decision by focusing attention on an objective function designed to quantify performance and measure the quality of the decision. This objective function is maximized or minimized subject to the constraints that may limit the selection of variables. If a suitable single aspect of a problem can be isolated and characterized by an objective function, e.g., profit or loss in a business setting, speed or distance in a physical problem, or searching for a set of variables to minimize an error function, optimization may provide a suitable framework for analysis.

Prior to the 1940's, optimization theories were mainly associated with differential calculus. These techniques, as we know, had been successfully applied to problems in economics, engineering, and pure sciences including physics for over 200 years. However, these methods were found to be inadequate for solving certain types of problems, such as linear programming problems (LP) as we will discuss in this section. It was during World War II that a systematic research program led by George B. Dantzig focussed on developing the theory of linear programming.

The specific solution developed by Dantzig is called the simplex algorithm [92]. It is a step-by-step procedure for solving all linear programming problems in a finite number of arithmetic operations. Since Dantzig's initial work in 1951, the development and application of linear programming has advanced very rapidly. Much work has been done to improve the computational efficiency of the simplex algorithm, thus enabling the solution of larger and larger problems with less effort and greater speed. Although many variants of the simplex algorithm for special uses have been developed, none of these new procedures has replaced the straightforward approach of the simplex algorithm.

A linear programming problem is characterized by linear functions of the variables; the objective function is linear in the variables, and the constraints are linear equalities or linear inequalities. Many problems found in practice are formulated as constrained problems. This is because in most instances a complex problem such as the detailed production policy of a corporation, the planning of a large government agency, or even the design of a complex device, cannot be treated directly in its entirety accounting for all possible choices, but instead must be decomposed into separate sub-problems, i.e, each sub-problem having constraints that are imposed to restrict its scope. Thus, in planning problems, budget constraints are commonly imposed in order to decouple that one problem from a more global one.

One obvious measure of the complexity of a programming problem is its size, measured in terms of the number of unknown parameters or the number of constraints. As might be expected, the size of problems that can be effectively solved has been increasing with advancing computing technology and with advancing theory. It is divided into three classes of problems: *small-scale problems* having about five or fewer unknowns and constraints; *intermediate-scale problems* having from about five to a hundred variables; and *large-scale problems* having more than a hundred and perhaps over thousands of variables and constraints. This classification is not entirely rigid, but it reflects at least roughly not only size but the basic differences in approach that accompany different size problems. As a rough rule, a small-scale problem can be solved by hand or on a small computer. Intermediate-scale problems can be solved on a main-frame computer. Large-scale problems require sophisticated codes that exploit special structure and usually require large main-frame computers.

Most algorithms designed to solve large optimization problems are iterative in nature in order to exploit the basic and important characteristic of high-speed digital computer, i.e., its ability to perform repetitive operations efficiently. Typically, in seeking a vector that solves the programming problem, an initial vector $\mathbf{x}_0$ is selected and the algorithm generates an improved vector $\mathbf{x}_1$. The process is repeated and a still better solution $\mathbf{x}_2$ is then found. Continuing this fashion, a sequence of ever-improving points $\mathbf{x}_0$ $\mathbf{x}_1$ ... $\mathbf{x}_k$ ..., are found that approach a solution point $\mathbf{x}^*$. For linear programming problems, the generated sequence is of finite length, reaching the solution point exactly after a finite (although initially unspecified) number of steps.

7.1.2 The fundamental theorem of linear programming

A linear programming problem is a mathematical program in which the objective function is linear in the unknown parameters and the constraints consist of linear equalities or inequalities. As shown below, any linear programming problem can be transformed into the following standard form:

Minimize an objective function of the form:

$$c_1x_1 + c_2x_2 + c_3x_3 + \cdots + c_nx_n$$

subject to the constraints

$$b_1^l \leq a_{11}x_1 + a_{12}x_2 + \cdots + a_{1n}x_n \leq b_1^u$$

$$b_2^l \leq a_{21}x_1 + a_{22}x_2 + \cdots + a_{2n}x_n \leq b_2^u$$

$$\cdot \qquad\qquad\qquad\qquad\qquad\qquad\qquad\qquad \cdot$$

$$b_m^l \leq a_{m1}x_1 + a_{m2}x_2 + \cdots + a_{mn}x_n \leq b_m^u$$

and

$$x_1^l \leq x_1 \leq x_1^u$$

$$x_2^l \leq x_1 \leq x_2^u$$

$$\cdot \qquad\qquad\quad \cdot$$

$$x_m^l \leq x_m \leq x_m^u$$

where the b_i^l's, b_i^u's, x_i^l's, x_i^u's, c_i's, and a_{ij}'s are the fixed constants and real numbers, and the x_i are the real numbers to be determined, or named as variables. In more compact vector notation, this standard problem becomes that of

minimizing

$$f(\mathbf{x}) \quad = \quad \mathbf{c}^T\mathbf{x}$$

subject to

$$\mathbf{b}^l \leq \mathbf{A}\mathbf{x} \leq \mathbf{b}^u$$

and

$$\mathbf{x}^l \leq \mathbf{x} \leq \mathbf{x}^u \tag{7.1}$$

where the variable array, $\mathbf{x}$, is an n-dimensional column vector, the objective function array, $\mathbf{c}^T$, is an n-dimensional row vector, $\mathbf{A}$ is an m by n matrix, $\mathbf{b}^l$ and $\mathbf{b}^u$ are m-dimensional vectors of the lower and upper boundary constraints arrays, and $\mathbf{x}^l$ and $\mathbf{x}^u$ are m-dimensional vectors of the lower and upper variable arrays.

Given an LP, the feasible set for this LP is a set of vectors (equivalently points) in the appropriate n-dimensional space R^n which satisfy the constraints for the given LP. Let K denote the feasible set for the LP. The basic properties of a feasible set for an LP can be summarized as follows:

1. The feasible set K is convex.
2. K has a finite number of corners.
3. Finite minimums and maximums of the objective function for the LP occur at corners of K.

Definition of a Convex Set:

A subset K of R^n is convex if whenever $\mathbf{x}$ and $\mathbf{y}$ belong to K, and u and t are non-negative numbers with $u + t = 1$, then $u\mathbf{x} + t\mathbf{y}$ belongs to K.

Definition of a Corner:

A point $\mathbf{x}$ of a convex set K in R^n is not a corner point of K if there are two points $\mathbf{y}$ and $\mathbf{z}$ in K and two positive numbers t and u, such that (1) $t + u = 1$ and (2) $\mathbf{x} = t\mathbf{y} + u\mathbf{z}$. Corner points are also called extreme points.

A graphic example of convex set, non convex set and corner points are shown in Fig. 7.1 on page 7.1. Geometric intuition should suffice to identify the convex set, non-convex set, and corner points of the feasible sets in a system where only a small number of variables are presented as in the case of Fig. 7.1.

A solution $\mathbf{x}$ to the LP should be a point in the feasible set K at which the objective function attains its minimum value on K, and it is called an *optimal* *solution.* Thus a solution $\mathbf{x}$ of $\mathbf{Ax} = \mathbf{b}$ is a feasible solution to the LP if and only if $\mathbf{x} \geq 0$. A solution $\mathbf{x}$ of $\mathbf{Ax} = \mathbf{b}$ is called a *basic solution* if the columns of the $\mathbf{A}$ matrix corresponding to the nonzero entries in $\mathbf{x}$ are linearly independent. A *basic feasible solution* (BFS) is a solution that is basic and feasible.

Fundamental Theorem of Linear Programming

Given a linear program in standard form of Eq. 7.1 where $\mathbf{A}$ is an m by n matrix of rank m,

1) if there is a feasible solution, there is a basic feasible solution;

2)if there is an optimal feasible solution, there is an optimal basic feasible solution.

The proof of the above fundamental theorem can be found in most elementary linear programming text books, e.g. [93].

The simplex algorithm is essentially a method of systematically examining the feasible solutions of a standard-form linear programming for optimality, i.e., select an initial extremum point which is a *basic feasible solution*(BFS), move algebraically from one BFS to another while trying to decrease the objective function each time. The final objective function obtained by the optimized basic feasible solution is called the optimized objective function.

7.1.3 Formulating a linear programming problem

Many problems in nature are not explicitly written in a linear programming format of (7.1). In most cases, the variables, constraints, and objective function are needed to be sorted out and identified. Formulating a linear program to model

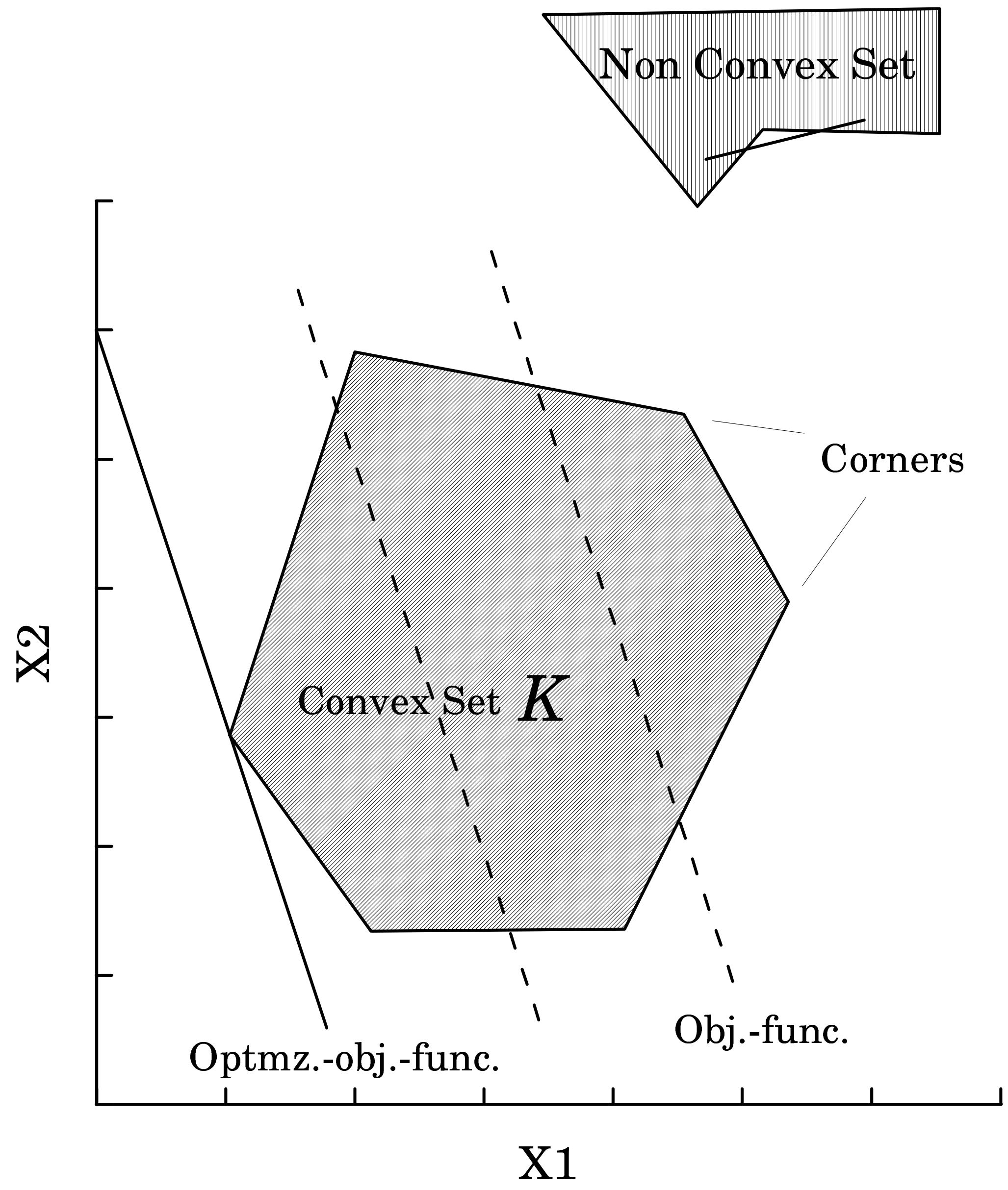

Figure 7.1: Schematic diagram of the simplex algorithm. The simplex algorithm is a method of systematically examining the basic feasible solutions and moves one BFS to another while trying to decrease the objective function.

a situation involves three basic steps:

1. Specify the unknown variables.
2. Specify the constraints.
3. Specify the objective function.

In the case of the APRIORI problem, a set of experimental data points, $\{I_i^{exp}\}$, is given. Suppose that a set of formulated equations, which are a set of linear functions of a set of variables, $\{X_j\}$, can be used to represent $\{I_i^{exp}\}$. We may write:

$$I_i^{exp} = \sum_{j=1}^{N_X} M_{ij} X_j, \quad \text{and} \quad i = 1, 2, \ldots, N_K \tag{7.2}$$

where M_{ij} is a matrix element of $\mathbf{M}$ and a real number. Noted that the number of equations, N_K, could differ from the number of unknown parameters, N_X. The variable set, $\{X_j\}$, is confined between the lower boundary set of $\{X_j^l\}$ and upper boundary set of $\{X_j^u\}$, where

$$X_j^l \leq X_j \leq X_j^u$$

We now define the error function, or optimization function, to be

$$E = \sum_{i=1}^{N_K} \left| \left(\sum_{j=1}^{N_X} M_{ij} X_j - I_i^{exp} \right) \right| \tag{7.3}$$

A feasible set of solution, $\{X_j\}$, is defined as an optimal feasible solution when the error function is at the minimum.

Now we focus our attention on reformulating the problem of minimizing the error function (7.3) into the standard linear programming format of (7.1) so that it can be solved by the simplex algorithm of linear programming for which computer routines are widely available.

7.1.3.1 1. Specification of the unknown variables

The variable set of $\{X_j\}$ can be defined as a column vector

$$\mathbf{X} = \begin{pmatrix} X_1 \\ X_2 \\ . \\ X_{N_X} \end{pmatrix}$$

In order to minimize Eq. 7.3, the number of variables in the set of $\{X_j\}$ is not sufficient to construct a linear programming model. Now we will introduce the positive error $E^{(+)}$ and negative error $E^{(+)}$ as following:

For a given feasible solution $\{X_j\}$,

if $\left(\sum_{j=1}^{N_X} M_{ij}X_j - I_i^{exp}\right) > 0$, define

$$\begin{cases} E_i^{(+)} = \left(\sum_{j=1}^{N_X} M_{ij}X_j - I_i^{exp}\right) \\ E_i^{(-)} = 0 \end{cases}$$

if $\left(\sum_{j=1}^{N_X} M_{ij}X_j - I_i^{exp}\right) < 0$, then define

$$\begin{cases} E_i^{(+)} = 0 \\ E_i^{(-)} = -\left(\sum_{j=1}^{N_X} M_{ij}X_j - I_i^{exp}\right) \end{cases}$$

Hence

$$E_i^{(+)} + E_i^{(-)} = \left|\left(\sum_{j=1}^{N_X} M_{ij}X_j - I_i^{exp}\right)\right|$$

where $E_i^{(+)} \geq 0$, $E_i^{(-)} \geq 0$, for $i = 1, 2, \ldots, N_K$, The absolute signs can be then removed according to the above definition of $E_i^{(+)}$ and $E_i^{(-)}$:

$$E_i^{(+)} - E_i^{(-)} = \left(\sum_{j=1}^{N_X} M_{ij}X_j - I_i^{exp}\right) \tag{7.4}$$

Since the values of $E_i^{(+)}$ and $E_i^{(-)}$ are the positive and need to be determined, so they are the new variables. The number of unknown variables becomes $N_X + 2N_K$. We, therefore, define the total linear variable column vector $\mathbf{x}$ to be:

$$\mathbf{x} = \begin{pmatrix} \mathbf{X} \\ \mathbf{E}^{(+)} \\ \mathbf{E}^{(-)} \end{pmatrix} = \begin{pmatrix} \cdot \\ X_i \\ \cdot \\ E_j^{(+)} \\ \cdot \\ E_k^{(-)} \\ \cdot \end{pmatrix} \tag{7.5}$$

where i goes from 1 to N_X, j from 1 to N_K, k from 1 to N_K, and $0 \leq E_i^{(+)}, E_i^{(-)} \leq \infty$.

The lower and the upper boundary of the variable sets are:

$$\mathbf{x}^l = \begin{pmatrix} \mathbf{X}^l \\ \mathbf{0} \\ \mathbf{0} \end{pmatrix} \quad \text{and} \quad \mathbf{x}^u = \begin{pmatrix} \mathbf{X}^u \\ \infty \\ \infty \end{pmatrix} \tag{7.6}$$

7.1.3.2 2. Specification of the constraints

Eq. 7.4 can be written in the more compact vector form,

$$\mathbf{E}^{(+)} - \mathbf{E}^{(-)} = \mathbf{M}\mathbf{X} - \mathbf{I}^{exp}$$

or

$$\mathbf{M}\mathbf{X} - \mathbf{E}^{(+)} + \mathbf{E}^{(-)} = \mathbf{I}^{exp}$$

where the column vector

$$\mathbf{I}^{exp} = \begin{pmatrix} I_1^{exp} \\ I_2^{exp} \\ . \\ I_{N_K}^{exp} \end{pmatrix} \tag{7.7}$$

and matrix

$$\mathbf{M} \quad = \quad \begin{pmatrix} M_{11} & M_{12} & \cdots & M_{1N_X} \\ M_{21} & M_{22} & \cdots & M_{2N_X} \\ . & . & & . \\ M_{N_K1} & M_{N_K2} & \cdots & M_{N_KN_X} \end{pmatrix}$$

It can also be written in the form:

$$\begin{pmatrix} \mathbf{M} \ , & -\mathbf{I} \ , & \mathbf{I} \end{pmatrix} \begin{pmatrix} \mathbf{X} \\ \mathbf{E}^{(+)} \\ \mathbf{E}^{(-)} \end{pmatrix} = \mathbf{I}^{exp}$$

where **I** is a unit matrix of rank N_K. Or we may write:

$$\mathbf{Ax} \quad = \quad \mathbf{I}^{exp} \tag{7.8}$$

where the constraint matrix **A** is:

$$\mathbf{A} = \begin{pmatrix} M_{11} & M_{12} & \cdots & M_{1N_X} & -1 & 0 & \cdots & 0 & 1 & 0 & \cdots & 0 \\ M_{21} & M_{22} & \cdots & M_{2N_X} & 0 & -1 & \cdots & 0 & 0 & 1 & \cdots & 0 \\ . & . & & . & . & . & & . & . & . & & . \\ M_{N_K1} & M_{N_K2} & \cdots & M_{N_KN_X} & 0 & 0 & \cdots & -1 & 0 & 0 & \cdots & 1 \end{pmatrix}$$

Now the constraint Eq. 7.8 fits the standard format of a linear programming model, Eq. 7.1.

7.1.3.3 3. Specification of the objective function

Our goal is to minimizing the error function (Eq. 7.3), so we define our objective function as the error, E, of Eq. 7.3. If we take the objective array as a row vector $\mathbf{c}^T$:

$$\mathbf{c}^T = (\underbrace{0,\ 0,\ \cdots,\ 0}_{N_X},\underbrace{1,\ 1,\ \cdots,\ 1}_{N_K},\underbrace{1,\ 1,\ \cdots,\ 1}_{N_K}) \tag{7.9}$$

then the objective function is:

$$f(\mathbf{x}) = \mathbf{c}^T\mathbf{x}$$

or

$$f(\mathbf{x}) = (\underbrace{0,\ 0,\ \cdots,\ 0}_{N_X},\underbrace{1,\ 1,\ \cdots,\ 1}_{N_K},\underbrace{1,\ 1,\ \cdots,\ 1}_{N_K}) \begin{pmatrix} X_1 \\ . \\ X_{N_X} \\ E_1^{(+)} \\ . \\ E_{N_K}^{(+)} \\ E_1^{(-)} \\ . \\ E_{N_K}^{(-)} \end{pmatrix}$$

$$= \sum_{i=1}^{N_K}(E_i^{(+)} + E_i^{(-)}) = \sum_{i=1}^{N_K} \mid \left(\sum_{j=1}^{N_X} M_{ij}X_j - I_i^{exp} \right) \mid = E$$

which is exactly the form of Eq. 7.3. Minimizing the objective function $f(\mathbf{x})$ in a linear programming procedure will result in a minimum error for Eq. 7.3 which is our goal.

7.1.3.4 Summary

We have constructed a set of variables, a series of linear equations, and an objective function in order to convert the problem of minimizing the error function of Eq. 7.3 into the standard linear programming model of Eq. 7.1.

We seek to minimize the objective function

$$f(\mathbf{x}) \quad = \quad \mathbf{c}^T\mathbf{x}$$

subject to the constraints

$$\mathbf{b}^l \leq \mathbf{A}\mathbf{x} \leq \mathbf{b}^u$$

and

$$\mathbf{x}^l \leq \mathbf{x} \leq \mathbf{x}^u \tag{7.10}$$

where vector $\mathbf{c}^T$ is defined by Eq. 7.9,

$$\mathbf{c}^T \quad = \quad (\underbrace{0,\ 0,\ \cdots,\ 0}_{N_X}, \underbrace{1,\ 1,\ \cdots,\ 1}_{N_K}, \underbrace{1,\ 1,\ \cdots,\ 1}_{N_K})$$

variable vector $\mathbf{x}$ by Eq. 7.5,

$$\mathbf{x} \quad = \quad \begin{pmatrix} \mathbf{X} \\ \mathbf{E}^{(+)} \\ \mathbf{E}^{(-)} \end{pmatrix} \quad = \quad \begin{pmatrix} X_i \\ E_j^{(+)} \\ E_k^{(-)} \end{pmatrix}$$

matrix **A** by Eq. 7.8,

$$\mathbf{A} = \begin{pmatrix} M_{11} & M_{12} & \cdots & M_{1N_X} & -1 & 0 & \cdots & 0 & 1 & 0 & \cdots & 0 \\ M_{21} & M_{22} & \cdots & M_{2N_X} & 0 & -1 & \cdots & 0 & 0 & 1 & \cdots & 0 \\ . & . & & . & . & . & & . & . & . & & . \\ M_{N_K1} & M_{N_K2} & \cdots & M_{N_KN_X} & 0 & 0 & \cdots & -1 & 0 & 0 & \cdots & 1 \end{pmatrix}$$

the lower and upper boundary constraints are specified by

$$\mathbf{b}^l \quad = \quad \mathbf{b}^u \quad = \quad \mathbf{I}^{exp} \quad = \begin{pmatrix} I_1^{exp} \\ I_2^{exp} \\ . \\ I_{N_K}^{exp} \end{pmatrix}$$

and the lower and upper boundary for the variables by

$$\mathbf{x}^l \quad = \quad \begin{pmatrix} \mathbf{X}^l \\ \mathbf{0} \\ \mathbf{0} \end{pmatrix} \quad \text{and} \quad \mathbf{x}^u \quad = \quad \begin{pmatrix} \mathbf{X}^u \\ \infty \\ \infty \end{pmatrix}$$

7.2 Atomic Position Recovery by Iterative Optimization of Reconstructed Intensities

In the last section, we have introduced the linear programming concepts and formulated the variables, linear equations, constraints, and objective function of Eq. 7.10 on page 215 to convert a physics optimization problem into a standard linear programming format. In this section, we will apply these equations to attempt to overcome some of the previous limitations of electron holographic crystallography.

7.2.1 Overcoming Limitations of Holographic Crystallography

A by-product of the proposal [75] to reconstruct structural data from a diffraction pattern by computer holography has been the stimulation of new thought about direct methods [94] in crystallography. The earliest [17] of the holographic reconstruction algorithms used in practice was based entirely on analogy with ideas current in optics, and which stem from the seminal work of Gabor [3]. More reliable algorithms for holographic crystallography [76,**?**,**?**,**?**,**?**,**?**] have been developed subsequently including corrections for the anisotropies of atomic scattering factors [87,**?**,**?**,**?**], and that of the reference wave [79,**?**].

A problem which was recognized earlier [87,**?**] was the fact that the object waves are not always much smaller in magnitude than the reference wave, giving rise to artifacts on reconstructed “images” [99,**?**]. Taking a Cu atomic scattering factor, as an example, the forward-scattering amplitude could be as high as 3.0 $\mathring{A}$ (estimated from Fig. 2.2) for an electron energy of 914 eV. This amplitude is even greater than that of the reference wave if a scatterer Cu atom is located at 2.55 $\mathring{A}$, the nearest-neighbor distance from an emitter in a Cu crystal. In other words, if the reference wave amplitude were assumed to be 1, the amplitude of the object wave is:

$$|O| = \frac{\left| f^{(l)}(\mathbf{k}, \mathbf{r}) \right|}{r}$$

which is around $3.0/2.55 = 1.18$ in the forward-scattering direction. So omitting the quadratic terms, i.e., the squares of object waves, in a traditional electron holographic reconstruction algorithm would result in poor image reconstruction when the forward-scattering peaks dominate the diffraction pattern (hologram).

Algorithms which combine data from diffraction patterns due to electrons of several different energies have been proposed [101,?,?,?] in part to overcome the problem of holographic twin-images [17]. However, with present technology, collection of photoelectron diffraction data over a large solid angle range at several regularly-spaced energies is a rather laborious task (and may be impossible with Auger electron diffraction).

We present in this Section a robust new reconstruction algorithm, which offers the prospect of overcoming all the above difficulties. It is a rapid iterative scheme for accurately reconstructing the relative positions of source and scatterers directly from the data of a mono-energetic point-source diffraction pattern. It makes use of the squared object-wave terms neglected in traditional holographic algorithms to reconstruct the holographic images. It also does not suffer from a twin-image problem, and even identifies the chemical species of the *scattering* atoms.

7.2.2 Photoelectron diffraction from a Ni-C-O linear chain model

We begin by drawing attention to some of the limitations of prior schemes [17,?,?,?,?,?], for the reconstruction of the positions of atomic scatterers of different chemical species, from a single diffraction pattern, when the scatterers lie on both sides of an emitter atom. We illustrate our point by considering a Ni-C-O linear chain model of a CO molecule adsorbed on the atop site of a Ni surface, as shown in Fig. 7.2 on page 219. If the carbon atom is excited through a photo-emission or electron-induced Auger process, the electron emitted by source atom C will produce a diffraction pattern at far-field. For simplicity, we assume that the emitted wave takes an isotropic form of an s-wave emitter. The interference between the s-wave electron emitted from the C atom (forming a reference wave $Ref.$) and that scattered from the nearby O and Ni atoms (the object waves $Obj.$) gives rise to a

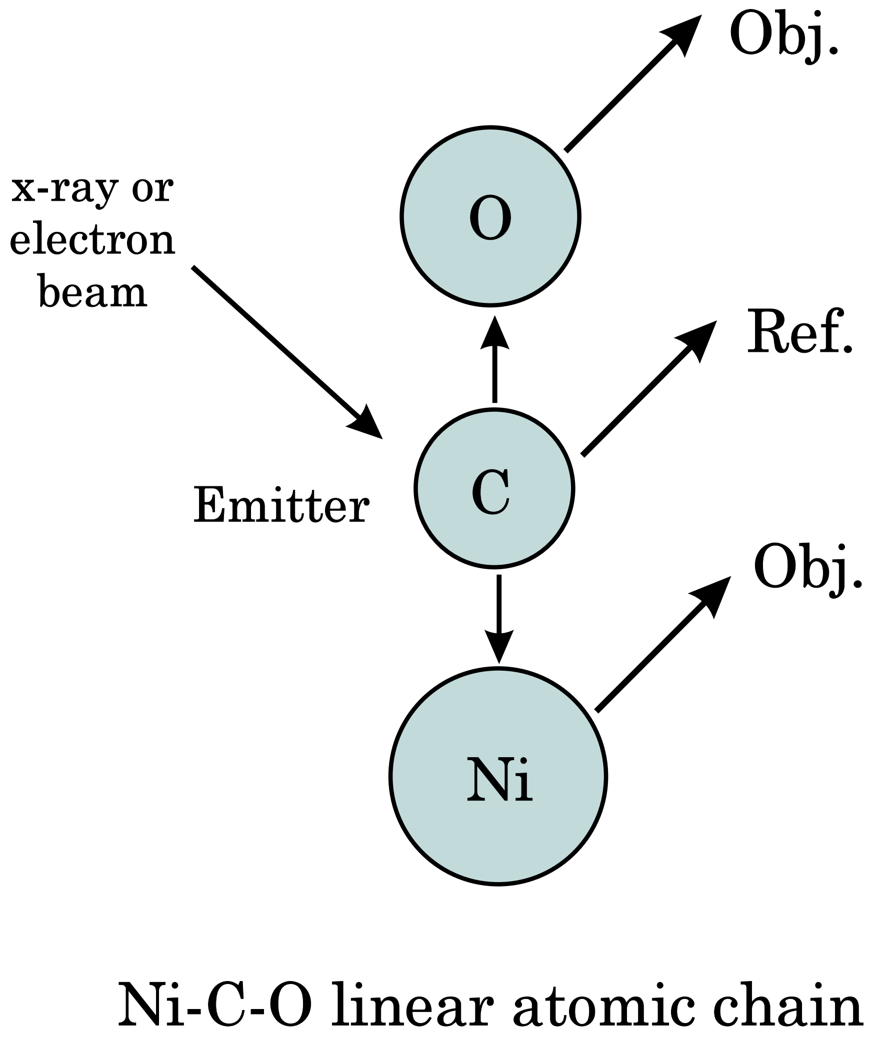

Figure 7.2: Ni-C-O atomic linear chain model. The Ni-C and C-O distances were taken to be 1.80 and 1.15 $\AA$. The carbon atom is assumed to be excited by an x-ray photon or an electron, emitting an electron wave from the carbon atom, and forming a photoelectron diffraction in far-field.

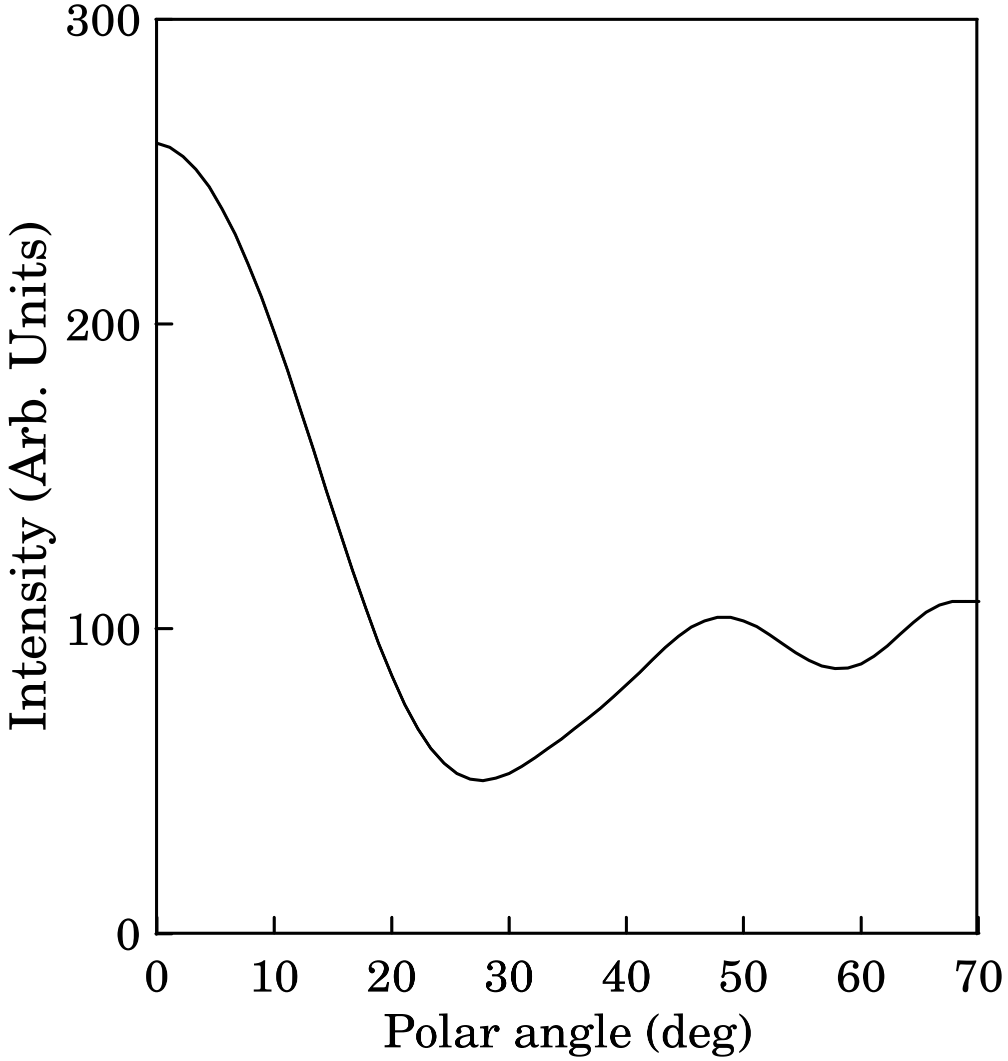

Figure 7.3: Polar angle variation of the diffraction intensity from the Ni-C-O linear chain, shown in Fig. 7.2, calculated by an exact multiple-scattering scheme [32], with the C atom emitting an isotropic electron wave, e.g. s-wave emitter, at kinetic energy of 504 eV. The polar axis is defined to lie in the direction from the C to the O atom.

far-field diffraction pattern which will have an azimuthal symmetry about a polar axis directed from the C atom towards the O atom. In Fig 7.3 on page 220 we show the polar-angle variation, $I(\theta)$, of the intensity of this diffraction pattern, for 500 eV electrons, and θ lying in the range from 0 to 70^o, as calculated by an exact full multiple-scattering cluster scheme [32].

Firstly, we use Barton's Helmholtz-Kirchoff algorithm [17] to reconstruct from the diffraction data of Fig. 7.3 real-space amplitudes in the region close to the emitter. In Barton's Helmholtz-Kirchoff algorithm the image function, $\mathbf{A}(\mathbf{r})$, is calculated from:

$$\mathbf{A}(\mathbf{r}) = \int\int I(\mathbf{k}) e^{-i\mathbf{k}\cdot\mathbf{r}} d\mathbf{k}_{||} \tag{7.11}$$

where the $\mathbf{k}$ is the wave vector, $\mathbf{k}_{||}$ the component that parallel to the surface. A radial image function (RIF) may be obtained by reconstring the image intensities along a line passing through the three atoms in the chain model. The resulting radial image function is shown on Fig. 7.4(a). The vertical dotted line on the positive side of the abscissa denotes the position of the O scatterer relative to the emitter (the C atom, at the origin), while that on the negative side represents the position of the Ni atom. Note the symmetry of the RIF about the origin as a consequence of the holographic twin problem. No particular indication of the O or Ni atoms is present on the RIFs.

We next utilize a scattered-wave included Fourier transform (SWIFT) [91,**?**,**?**,**?**] to calculate the corresponding RIFs, using the spherical-wave scattering factors (7.16) of O and Ni separately in the scattered-wave kernel. This image function is calculated from:

$$\mathbf{A}(\mathbf{r}) = \int\int \frac{I(\mathbf{k})}{f(\mathbf{k},\mathbf{r})} e^{-i\mathbf{k}\cdot\mathbf{r}} d\mathbf{k}_{||} \tag{7.12}$$

where the scattering factor $f(\mathbf{k},\mathbf{r})$ of O or Ni is the s(inverse) scattered-wave kernel.

The radial image is along the same direction as that of Fig. 7.4(a). The profiles on the positive side of the abscissa are multiplied by the scale factor shown in Fig. 7.4 to compensate for an inverse kernel containing large forward-scattering factors. The resulting RIFs are shown on Fig. 7.4(b) and 7.4(c), respectively. On Fig. 7.4(b) a peak is indeed seen close to the position of the O atom, but a quite spurious one is also seen on the opposite side of the emitter, where no O atom is present. The latter feature is either due to the incomplete removal of the twin image of the O, or else the incomplete filtering out of the image of the Ni atom. The profile shown on Fig. 7.4(c) shows a peak close to the Ni atom, but also an unwanted artifact on the other side of the scatterer.

Szöke [104] has recently pointed out that many of the spurious features on holographically reconstructed images, like those on Fig. 7.4(a)-(c) are a consequence of the use of the back-propagation algorithms, with their attendant diffraction limits and problems of wave interference. Since the aim of holographic crystallography is the determination of the *positions* of scatterers rather than their scattered wave-fields, he suggested introducing into the theory the idea of a spatial distribution function to be determined from the experimental data and a knowledge of the forms of the reference and scattered waves. We propose here a novel algorithm for determining such a function, which we term as Atomic Position Recovery by Iterative Optimization of Reconstructed Intensities (APRIORI) [88].

7.2.3 Iterative optimization of reconstruction

Consider first the kinematic expression for the amplitude of an electron wave of detected wave-vector $\mathbf{k}$, emitted at the origin of a coordinate system, and scat-

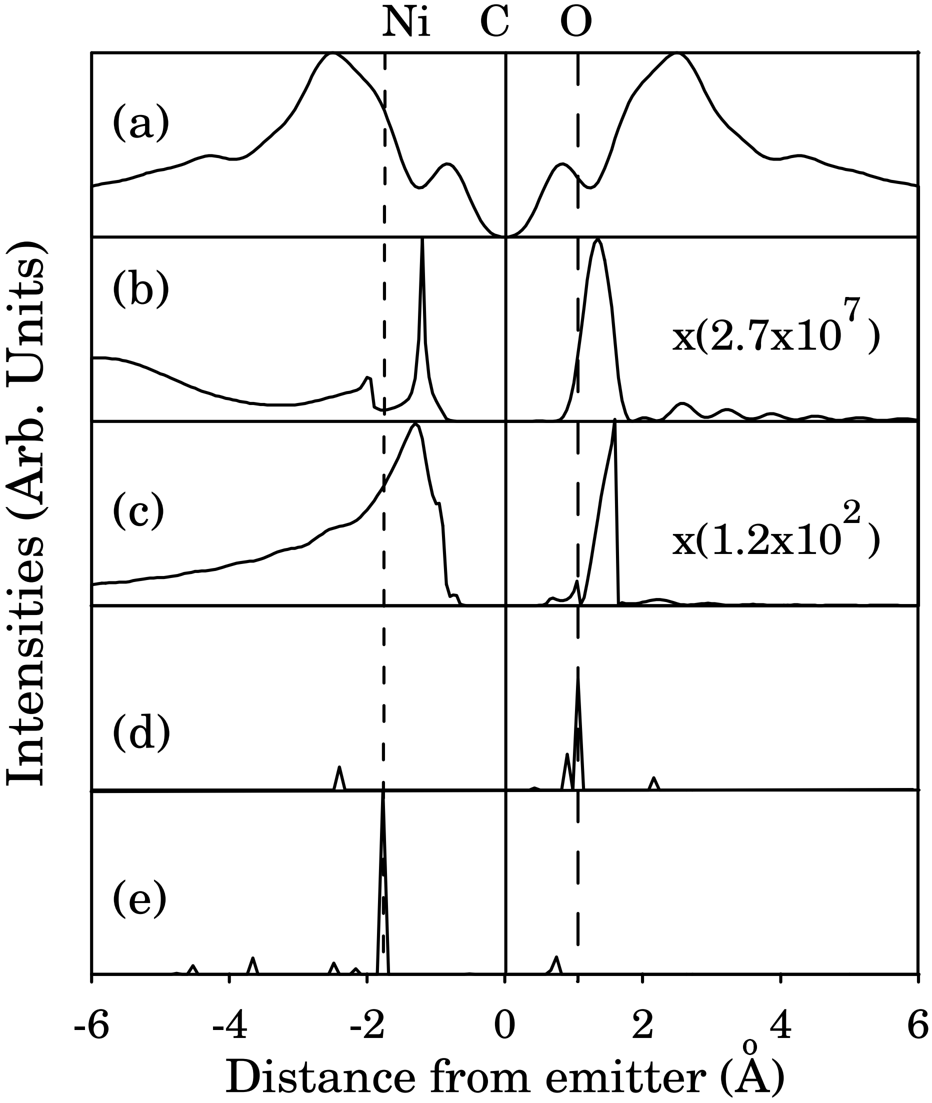

Figure 7.4: Radial image functions (RIFs) along the atom chain as reconstructed from the diffraction intensities of Fig. 7.3 by various methods. (a) Barton's Helmholtz-Kirchoff integral. (b) A scattered-wave-included Fourier transform (SWIFT) algorithm with a scattered-wave kernel containing a spherical-wave electron scattering factor of an O atom. (c) Same as (b) except using a scattered-wave kernel of Ni. (d) The distribution $p_O^{(4)}$ for O, as calculated by the APRIORI algorithm after 4 iterations. (e) The corresponding distribution $p_{Ni}^{(4)}$ for Ni, found by the same optimization process. The vertical dashed lines represent the positions of the Ni and O scatterers.

tered by atoms of chemical species X at positions specified by the vectors $\mathbf{r}_i$:

$$A(\mathbf{k}) = R(\mathbf{k}) + \sum_{X,i} p_X(\mathbf{r}_i) O_X(\mathbf{k}, \mathbf{r}_i), \tag{7.13}$$

where the (real) functions $p_X(\mathbf{r}_i)$ [104] represent the spatial distribution of atoms of chemical species X. We take the emitted wave-function as the reference wave R of angular momentum quantum numbers lm, i.e.

$$R(\mathbf{k}) = Y_{lm}(\hat{\mathbf{k}}), \tag{7.14}$$

and

$$O_X(\mathbf{k}, \mathbf{r}_i) = Y_{lm}(\hat{\mathbf{r}}_i) \frac{f_X^{(l)}(\mathbf{k}, \mathbf{r}_i)}{r_i} e^{i(kr_i - \mathbf{k} \cdot \mathbf{r}_i)} \tag{7.15}$$

as the object waves scattered by nearby atoms. Eq. 7.14 and 7.15 represent amplitudes measured on a distant spherical detector approximately centered on the emitter, so we have dropped some unimportant common factors. The atomic scattering factors in Eq. 7.15 take the spherical-wave form: [79]

$$f_X^{(l)}(\mathbf{k}, \mathbf{r}_i) = \frac{1}{k} c_l(kr_i) \sum_{l'} (2l' + 1) t_{l'}^X c_{l'}(kr_i) P_{l'}(\hat{\mathbf{k}} \cdot \hat{\mathbf{r}}_i) \tag{7.16}$$

where $t_{l'}^X$ is an atomic t-matrix element of angular momentum quantum number l' for the chemical species X, $P_{l'}$ a Legendre polynomial and $c_l(kr_i)$ the polynomial coefficient of the Hankel function $h_l^{(1)}(kr_i)$ [8]. Inelastic damping is taken into account in equations (7.14)-(7.16) by allowing the wavenumbers k to be complex. Using equations (7.13)-(7.15) we see that the intensity, $I(\mathbf{k}) (= |A(\mathbf{k})|^2)$, of the diffraction pattern, regarded as a function of the wave-vector $\mathbf{k}$ of the detected electron, can be written as

$$I(\mathbf{k}) = |R(\mathbf{k})|^2 + \sum_{X,i} p_X(\mathbf{r}_i) \left\{ [R^*(\mathbf{k}) O_X(\mathbf{k}, \mathbf{r}_i) + c.c.] + O_X^*(\mathbf{k}, \mathbf{r}_i) \sum_{Z,j} p_Z(\mathbf{r}_j) O_Z(\mathbf{k}, \mathbf{r}_j) \right\} \tag{7.17}$$

where *c.c.* denotes complex conjugation, and Z is another dummy index specifying a chemical element and r_j the cooordinate of chemical species Z.

We take as our task the determination of the spatial distributions $p_X(\mathbf{r}_i)$ (and $p_Z(\mathbf{r}_j)$). We describe below an iterative process for determining these quantities from experimental measurements of $I(\mathbf{k})$ and calculated values of $R(\mathbf{k})$ and $O_X(\mathbf{k}, \mathbf{r}_i)$ (and $O_Z(\mathbf{k}, \mathbf{r}_j)$). If we allow the position vectors $\mathbf{r}_i$ and $\mathbf{r}_j$ to take a set of values on an uniform grid of points [104] in a space large enough to include all expected positions of the scattering atoms, we may obtain an n-th order estimate $p_X^{(n)}$ of the distributions p_X, by the following method.

We define the error $E^{(n)}(\mathbf{k})$ in our n-th order estimate of the experimentally measured intensity $I^{exp}(\mathbf{k})$ at the position on the diffraction pattern specified by the detected wave-vector $\mathbf{k}$ as

$$E^{(n)}(\mathbf{k}) = |R(\mathbf{k})|^2 + \sum_{X,i} p_X^{(n)}(\mathbf{r}_i) M_X^{(n)}(\mathbf{k}, \mathbf{r}_i) - \mu I^{exp}(\mathbf{k}), \tag{7.18}$$

where μ is a constant of proportionality to be determined, and we take

$$M_X^{(n)}(\mathbf{k}, \mathbf{r}_i) = [R^*(\mathbf{k}) O_X(\mathbf{k}, \mathbf{r}_i) + c.c.] + O_X^*(\mathbf{k}, \mathbf{r}_i) \sum_{Z,j} p_Z^{(n-1)}(\mathbf{r}_j) O_Z(\mathbf{k}, \mathbf{r}_j), \tag{7.19}$$

as suggested by the terms within the curly brackets of (7.17). Note that $M_X^{(n)}$ contains the distributions $p_Z^{(n-1)}(\mathbf{r}_i)$ determined by the previous iteration.

For any particular iteration $n \geq 1$, we propose finding the best fit to $I^{exp}(\mathbf{k})$ by minimizing an "objective function" [105] defined by

$$\sum_{\mathbf{k}} \mid E^{(n)}(\mathbf{k}) \mid \tag{7.20}$$

subject to the constraints that

$$\mu \geq 0, \tag{7.21}$$

$$1 \geq p_X^{(n)}(\mathbf{r}_i) \geq 0, \qquad \text{for all X and } \mathbf{r}_i \tag{7.22}$$

and that

$$\sum_{\mathbf{r}_i} p_X^{(n)}(\mathbf{r}_i) = N_X \qquad \text{for all X}, \tag{7.23}$$

where N_X is the number of scattering atoms of type X. The problem has now been cast in a form from which it may be solved directly by e.g. an iterative application of the simplex algorithm [106]. By this means, we find the values of the constant μ and of the distributions $p_X^{(n)}(\mathbf{r}_i)$ which minimize the errors of Eq. 7.20 of our fit to the data points $I^{exp}(\mathbf{k})$, using the values of the distributions $p_Z^{(n-1)}(\mathbf{r}_i)$ from the previous iteration. The iterations are halted when $p_X^{(n)}(\mathbf{r}_i) \simeq p_X^{(n-1)}(\mathbf{r}_i)$, i.e. when the distributions have converged to self-consistency.

As a test of our algorithm, we simulated an "experimental" angular distribution of intensities $I^{exp}(\mathbf{k})$ equating these to a set of values of $I(\theta)$ from Fig. 7.3 at 64 equally-spaced polar angles θ in a measurable range from 0^o to 70^o, where the direction, $\hat{\mathbf{k}}$, is specified by the polar and azimuthal angles θ and ϕ. The spatial grid of test positions, $\mathbf{r}_i$, of the atoms were taken to be a uniform grid of 128 points in the range of ± 5 Å from the C atom along the polar axis (making a grid spacing of a little less than 0.08 Å). Since we have described a self-consistency cycle, the final distributions $p_X^{(n)}$ should be quite independent of the initial values of $p_Z^{(0)}$ used in (7.19) to start the process. However, in our test case, we have found that taking

$$p_Z^{(0)}(\mathbf{r}_j) = \delta_{Z,X}\delta_{\mathbf{r}_i,\mathbf{r}_j} \tag{7.24}$$

gave rise to the most rapid convergence. This includes the square moduli of the object waves from the same atom, but excludes the corresponding cross terms from different atoms in the initial estimates of $M_X(\mathbf{k}, \mathbf{r}_i)$ in (7.19).

The distributions $p_X^{(n)}$ were converged after just four iterations of the above algorithm, after which the constant of proportionality μ also converged to within a few percent of the correct value relating the "experimental" intensities, $I^{exp}(\mathbf{k})$, in the arbitrary units of Fig. 7.3, to the theoretical expression for $I(\mathbf{k})$ in Eq. 7.17. The resulting distributions $p_O^{(4)}$ and $p_{Ni}^{(4)}$ for the O and Ni scatterers respectively, are shown on Fig. 7.4(d) and 2(e). The largest spikes on these histograms are at the pixels closest to the positions of the O and Ni atoms respectively. The much smaller spikes are presumably due to the multiple-scattering neglected in the reconstruction algorithm. Nevertheless, the accuracy with which the positions of the scatterers are located relative to the C emitter appear in dramatic contrast to that from the panels (a)-(c) on the same Figure. Also notable is the complete absence of twin images on panels (d) or (e). This has been achieved without the need for multiple-energy diffraction data [101,**?**,**?**,**?**]. Perhaps most striking feature is the clear identification for the first time of the different chemical species. The computer time required for the reconstruction of profiles 7.4(d) and 7.4(e) by the new algorithm was comparable with those required for Fig. 7.4(b) and 7.4(c), from the SWIFT scheme.

7.2.4 Testing for the stability of the reconstruction images

Since the reconstruction of holographic images could fail due to the poor quality of the diffraction pattern data, we test the effects of perturbing the diffraction intensities of Fig. 7.3 by adding random Gaussian noise, ΔI, with a standard deviation of σ= 0.5%, 4%, and 8%, as shown on Fig. 7.5 on page 228. The RIF's for the O and Ni reconstructions using the APRIORI algorithm for these curves are shown on Fig. 7.6 on page 229. Curves (a) and (b) of Fig. 7.6 show the distribution $\mathrm{p}_O^{(5)}$ and $\mathrm{p}_{Ni}^{(5)}$ for the O and Ni respectively, as calculated by the APRIORI

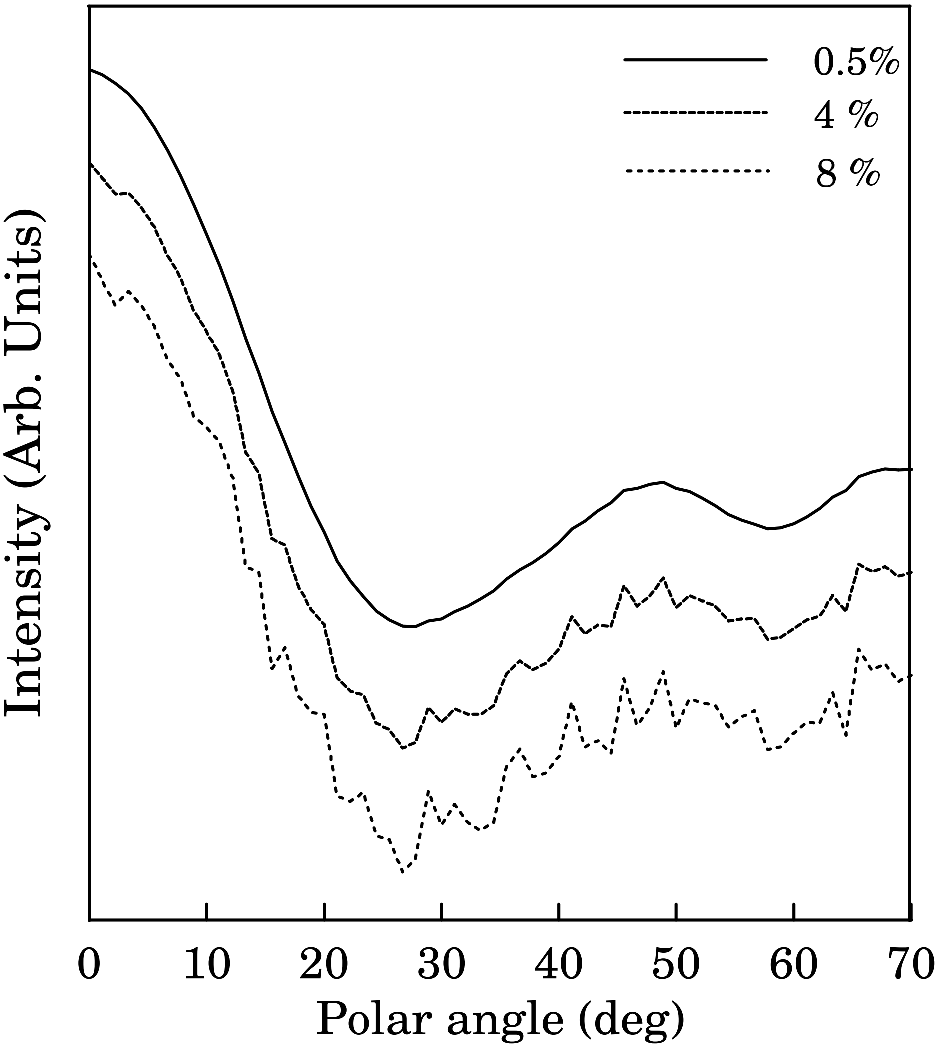

Figure 7.5: Polar angle variation of the diffraction intensity from Ni-C-O linear chain model, as shown in Fig. 7.2, calculated by an exact multiple-scattering scheme, and perturbed by adding Gaussian noise of 0.5%, 4% and 8 % standard deviation, respectively, with emitter of carbon atom emits an isotropical electron wave, s-wave emitter, at kinetic energy of 504 eV. The polar axis is defined to lie in the direction from the C to the O atom.

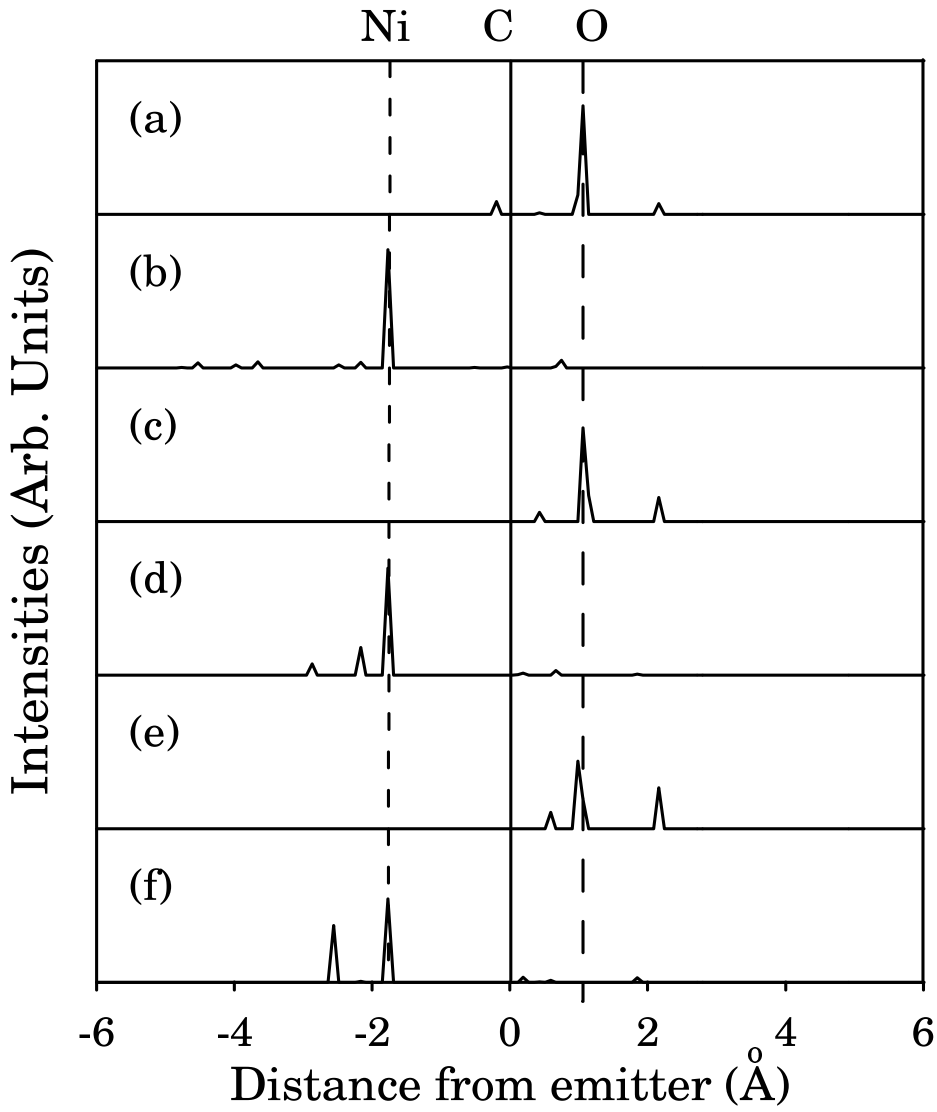

Figure 7.6: Radial image functions (RIDs) along the atom chain as reconstructed from the perturbed diffraction intensities of Fig. 7.3 as shown on Fig. 7.5. The distribution curve (a) for O and distribution curve (b) for Ni in the same optimization process for a Gaussian noise of σ=0.5%. (c) and (d) curves are the same RIFs for the noise of σ=4%. (e) and (f) curves are for the noise of σ=8%.

algorithm after five iterations for diffraction intensity with random Gaussian noise of $\sigma = 0.5\%$, as shown by upper panel curve on Fig. 7.5. Curves (c) and (d) on the one hand , and (e) and (f) on the other, are the results for the reconstruction from diffraction patterns of Gaussian noise of $\sigma = 4\%$ and 8% respectively, shown on the middle and lower curves on Fig. 7.5. It is seen that all the reconstructed RIFs are fairly clear and peaked at the right positions, and also that the species of the reconstructed images of the atoms are clearly distinguished on the RIFs, although more artifacts tend to appear on the RIFs from the data with greater noise.

On these RIF's, we found no perceptible shifts of the reconstructed peak positions for errors, ΔI, of $\pm\sigma$ of up to 4% of the mean intensity of the diffraction pattern, as shown on Fig. 7.6 by curves (a), (b), (c), and (d). On the reconstruction from the diffraction pattern of Fig. 7.5 with the 8% noise, we see that the RIF's on panels (e) and (f) on Fig. 7.6 are peaked at the right positions, but some spikes at larger distances from the emitter than the true atom position start to appear and increase in intensity as the noise becomes worse. For ΔI of up to as high as about 12%, we have found that the Ni atom peak was reproduced at the correct position, with the O atom shifted just three points of the spatial grid (i.e about 0.2 Å). This is an encouraging indication of the stability of this technique even in the presence of fairly noisy experimental data.

7.3 Three-dimensional image reconstruction from Si(111)-B surface model

In the previous Section we have reconstructed one-dimensional real-space images from the diffraction pattern from the Ni-C-O chain model. In this way, we could reconstruct the images along a fixed direction in order to reduce the real space grid points to speed up the program. In this Section we try to remove the constraints of fixing the reconstruction directions, and of course, as may be imagined, that this will increase the number of grid points in the image space. This will require more data points from the diffraction pattern to give a reliable result, and hence will need a longer computational time and larger memory size.

7.3.1 Si(111)-B surface model

The model used to test a three-dimensional APRIORI algorithm is a model of the Si(111) ($\sqrt{3}$x$\sqrt{3}$)B surface. A $\sqrt{3}$x$\sqrt{3}$ surface reconstruction on the Si(111) surface may be obtained when boron atoms diffuse from the bulk to the surface in heavily doped Si samples [109,?]. The structure has been studied by scanning tunneling microscopy(STM) [108,?], LEED [112], x-ray diffraction [110], photoemission [111], and a model of the surface by electron holography [87]. In this model a boron atom (termed B-S_5) is at a subsurface substitutional site in the second layer, directly underneath a Si adatom, as shown in Fig. 7.7 on page 233. There are five nearest neighbors of Si atoms around the emitter and four of them, termed as Si(1), Si(2), Si(3), and Si(4), are in forward scattering positions from the B emitter. The bond lengths of B-Si(1,2,3) and B-Si(4) are 2.15 and 2.32 $\mathring{A}$ respectively, with the bond angles between B-Si(1,2,3) and B-Si(4) being 63 ^{o}. The system also has a three fold rotation symmetry along [111]. A photoelectron diffraction pattern from such a cluster was calculated with a full multiple scattering program [32] for an electron kinetic energy of 500 eV with the boron atom considered as the emitter. The result is shown in Fig. 7.8 on page 234 with the center of the pattern at the projection of the [111] direction and the edge at a polar angle of 70^o. For simplicity, the emitted wave is assumed as an isotropic s wave. In this energy range the diffraction pattern is dominated by the forward scattering features which are the intensity enhancements along the B-Si directions.

7.3.2 APRIORI image reconstruction formalism

Because the boron atom is in the second layer, and the back-scattering contributions are less important in this energy range, multiple scattering effects are relatively small for this Si(111)-B system. The kinematic scattering formalism is considered for reconstructing the scatterer's positions around the B emitter. Let's start with the resulting wave-field of an electron source wave emitting at the origin:

$$A(\mathbf{k}) = R(\mathbf{k}) + \sum_{X,i} O_X(\mathbf{k}, \mathbf{r}_i), \tag{7.25}$$

where the emitting wave, $R(\mathbf{k})$, serves as the reference wave, and the scattered wave, $O_X(\mathbf{k}, \mathbf{r}_i)$, as the object wave of holography. The intensity of the far field diffraction pattern is

$$I(\mathbf{k}) = \mid A(\mathbf{k}) \mid^2 . \tag{7.26}$$

As has been proposed in the previous section since our purpose is to determine the positions of the scatterers rather than their scattered wave fields, we attempt to determine the spatial distribution of the scatterers as a three-dimensional image function. If the possible positions of the scatterers are represented by a grid of points in a cubic volume, a three dimensional function $p_X(\mathbf{r}_i)$ can be defined as the spatial image function of the scatterers of species X.

As it has been discussed before, the diffraction intensity may be written as Eq. 7.17 on page 224. In Eq. 7.17, the squares of the object waves are very important to the correct reconstruction of the positions of forward scattering atoms and cannot be omitted in the case where forward-scattering peaks are dominant

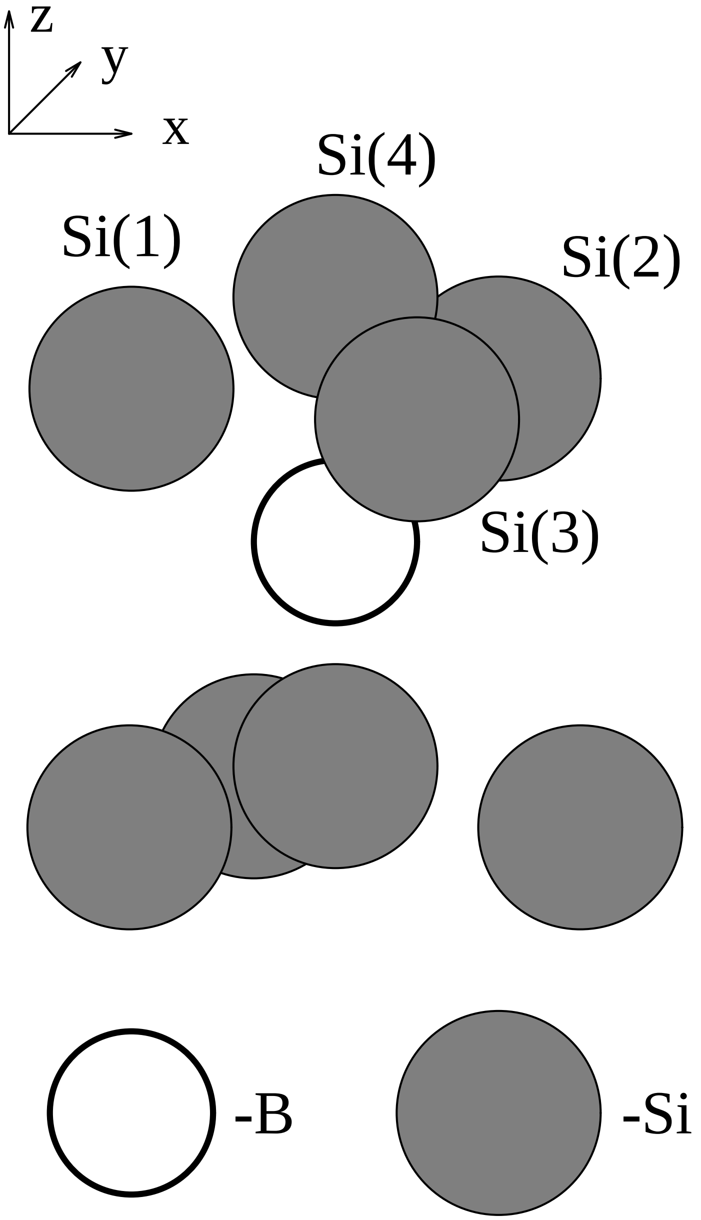

Figure 7.7: Schematic diagram of Si(111)($\sqrt{3}$x$\sqrt{3}$)B surface model. A boron atom at S_5 site is in a subsurface substitutional position in the second layer, directly underneath Si(4) adatom.

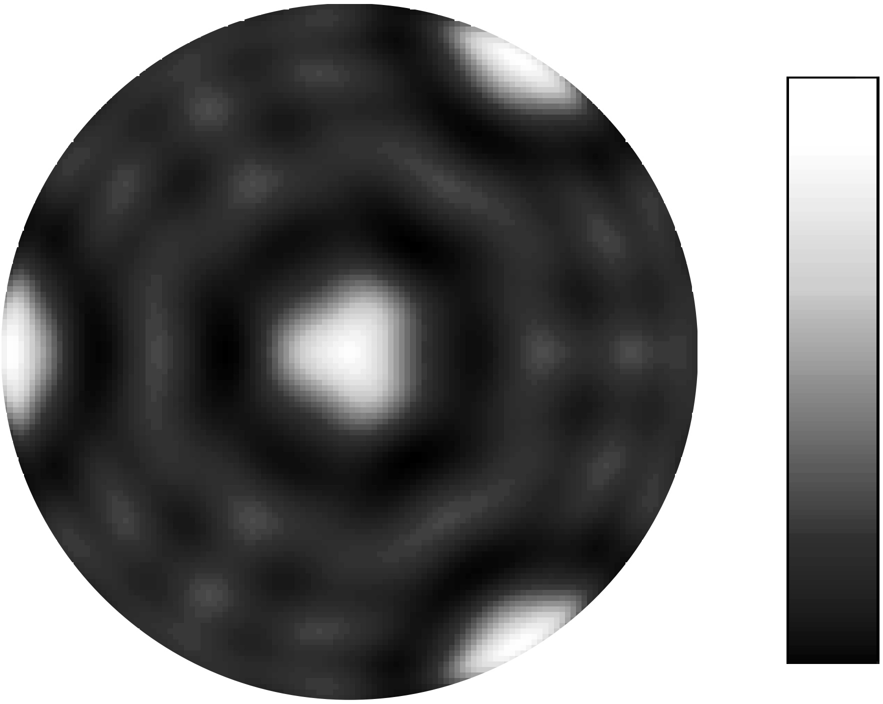

Figure 7.8: Multiple scattering calculation of the photoelectron diffraction from a Si(111)($\sqrt{3}$x$\sqrt{3}$)B surface at kinetic energy of 500 eV with a boron emitter at S_5 site.

in a diffraction pattern. In such cases, the amplitudes of the object waves are comparable with or even greater than that of the reference waves.

The error function, $E(\mathbf{k})$, is defined in Eq. errorfunction on page 225 for the estimation of the difference between the calculated $I(\mathbf{k})$ from Eq. 7.17 and the experimentally measured intensity $I_{exp}(\mathbf{k})$. In Eq. 7.18, μ is a constant of proportionality and needs to be determined, and the matrix element $M_X(\mathbf{k}, \mathbf{r}_i)$ takes the form of Eq. 7.19 on page 225, which is also a function of the spatial image function $p_X(\mathbf{r}_i)$ and needs to be determined. Therefore an iteration process is introduced in which $M_X^{(n-1)}(\mathbf{k}, \mathbf{r}_i)$ is calculated using the results $p_X^{(n-1)}(\mathbf{r}_i)$ of the previous iteration.

For any particular iteration $n \geq 1$, the problem of minimizing the sum of the absolute errors can be formulated as a linear programming problem as following:

We seek to minimize

$$\sum_{\mathbf{k}} \left(E_+^{(n)}(\mathbf{k}) + E_-^{(n)}(\mathbf{k}) \right) \tag{7.27}$$

subject to the constraints:

$$\mid R(\mathbf{k}) \mid^2 + \sum_{X,i} p_X^{(n)}(\mathbf{r}_i) M_X^{(n-1)}(\mathbf{k}, \mathbf{r}_i) - \mu I_{exp}(\mathbf{k}) = E_+^{(n)}(\mathbf{k}) - E_-^{(n)}(\mathbf{k}) \tag{7.28}$$

$$E_+^{(n)}(\mathbf{k}), E_-^{(n)}(\mathbf{k}) \geq 0 \text{ , for all } \mathbf{k} \tag{7.29}$$

$$0 \leq p_X^{(n)}(\mathbf{r}_i) \leq 1 \tag{7.30}$$

$$\sum_{\mathbf{r}_i} p_X^{(n)}(\mathbf{r}_i) = N_X \text{ , for all } X \text{ and } \mathbf{r}_i \tag{7.31}$$

and

$$\mu \geq 0, \tag{7.32}$$

where N_X is the number of scattering atoms of type X, and $E_+^{(n)}(\mathbf{k})$ and $E_-^{(n)}(\mathbf{k})$ are the positive and negative errors. Constraint (7.30) makes sure that the reconstructed distribution function has a positive value at all grid points. Constraint (7.31) ensures the sum of $p_X^{(n)}(\mathbf{r}_i)$ equals to the total number of atoms in the reconstructing cube, however, this constraint can be removed if one does not know the exact number of atoms in the cube. The distribution function $p_X^{(n)}(\mathbf{r}_i)$ can then be solved directly by an iterative application of a simplex algorithm.

Note that the matrix M_X in constraint (7.28) contains the function $p_X^{(n-1)}$ from the previous iteration. In the first iteration, we include the important contributions from the squared object wave terms by:

$$p_Z^{(0)}(\mathbf{r}_j) = \delta_{Z,X}\delta_{\mathbf{r}_j,\mathbf{r}_i}, \tag{7.33}$$

and the initial value of $M^{(0)}$ matrix becomes:

$$M_X^{(0)}(\mathbf{k},\mathbf{r}_i) = [R^*(\mathbf{k})O_X(\mathbf{k},\mathbf{r}_i) + c.c.] + \mid O_X(\mathbf{k},\mathbf{r}_i) \mid^2 . \tag{7.34}$$

Thus the spatial image function $p_X^{(1)}(\mathbf{r}_i)$ may be obtained by minimizing the "objective function" (7.27) subject to the constraints of (7.28), (7.29), (7.30), (7.31) and (7.32), and then used to calculate the matrices $M^{(1)}$, $M^{(2)}, \cdots$, up to $M^{(n-1)}$ recursively, using Eq. 7.19 and the simplex algorithm. This iterative procedure is continued until the image function is self-consistent, *i.e.*,

$$p_X^{(n)}(\mathbf{r}_i) \simeq p_X^{(n-1)}(\mathbf{r}_i). \tag{7.35}$$

7.3.3 Three dimensional holographic images of Si(111)-B surface

The reconstructed image function for Si, $p_{Si}(\mathbf{r}_i)$, is calculated on an uniform spatial grid of 33x33x33 points along the x, y and z directions in a 10x10x10

$\mathring{A}^3$ cube with its center at the origin (the emitter position). This will make a grid spacing of 0.313 $\mathring{A}$ which is at an atomic resolution scale. Since the simplex algorithm computer routine that we used was limited by the size of the M matrix, the number of the constraints have to be cut down in order not to sacrifice the resolution in real space. Thus, 64 points of the "experimental" diffraction intensity $I(\mathbf{k})$ in k space were taken as the input for the constraint (7.28), and the spatial image function, $p_{Si}(\mathbf{r}_i)$, was determined, then another set of 64 points data from $I(\mathbf{k})$ were used to obtain another image function, etc., and finally the resulting image functions were averaged for all the available $I(\mathbf{k})$.

The total number of points in k space on the Si(111)($\sqrt{3}$x$\sqrt{3}$)B electron diffraction pattern is 128x128, and the average image function $p_{Si}(\mathbf{r}_i)$ after four iterations is shown in Fig. 7.9 on page 238. The upper panel shows a cut through the y =0 plane on which the Si(1) and Si(4) atoms are expected to be, and the lower panel a cut through the z =0.98 plane where the Si(1), Si(2), and Si(3) atoms are located. Note that the intensities of all the images on these graphs are on the same absolute scale, and the images of Si(1), Si(2), Si(3), and Si(4) have the strongest intensities of the entire three-dimensional distribution $p_{Si}(\mathbf{r}_i)$ and located at exactly the atomic positions of our Si(111)($\sqrt{3}$x$\sqrt{3}$)B model. No strong artifact intensities appear in the image function $p_{Si}(\mathbf{r}_i)$ except some noise which might be due to multiple scattering contributions to the diffraction pattern.

7.3.4 Radial image functions of the Si(111)-B

In order to reduce the size of the M matrix, one may make use of certain available information of the system, such as the three-fold symmetry and the forward scattering features on the diffraction pattern, and attempt to reconstruct the

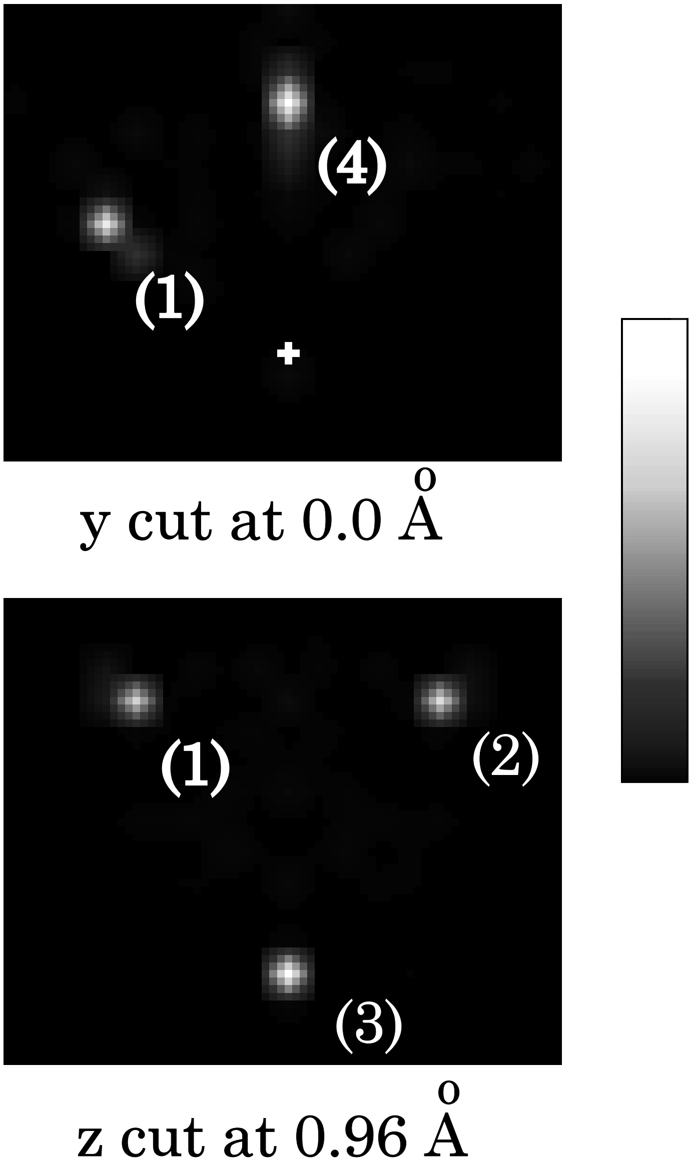

Figure 7.9: Three dimensional reconstruction image of Fig. 7.8 using APRIORI algorithm. The upper panel shows a cut of spatial image function $p_{Si}^{(4)}(\mathbf{r}_i)$ through the y =0 $\AA$ plane on which the Si(1) and Si(4) images are seen, and the lower panel a cut through the z = 0.98 $\AA$ plane where Si(1), Si(2), and Si(3) are located. Note that the intensities of all the images are on the same scale.

image function $p_{Si}(\mathbf{r}_i)$ only along all the forward scattering directions and obtain the radial image function (RIF) only along those directions. This will not only dramatically reduce the size of M matrix but also decrease the spacings between the grid points on the RIFs for a better image resolution, while reducing the number of grid points overall in real space to increase speed and reduce computer memory requirements.

The reconstructed RIFs $p_{Si}(\mathbf{r}_i)$ along the four forward-scattering directions are shown on the lower panels of Fig. 7.10 on page 240, and Fig. 7.11 on page 241, for radial axes along the normal and 63^o polar angles, respectively. It can be seen that the reconstructed images appear at the correct positions with no artifacts near the origin as usually seen with other holographic reconstruction methods. Another important feature is that our APRIORI method completely eliminates the twin image on the other side of the radial axis. Also shown on the upper panels of Fig. 7.10 and Fig. 7.11 are the holographic reconstructed RIFs by Barton's Helmholtz-Kirchoff integral method, which give arise strong artifacts near the origin and no particular indication of Si atom was present for both directions. A scattered-wave included Fourier transform (SWIFT) algorithm [79,**?**] which corrects for the phase shifts of the scattered wave is used to obtain the RIF plotted in the middle panels of Fig. 7.10 and Fig. 7.11 along the forward scattering directions. Although significant improvement in the Si images can be seen on the RIF compared with those from Barton's algorithm, strong artifact intensities still appeared near the origin: the Si images are broad with long tails, and the twin images were not eliminated.

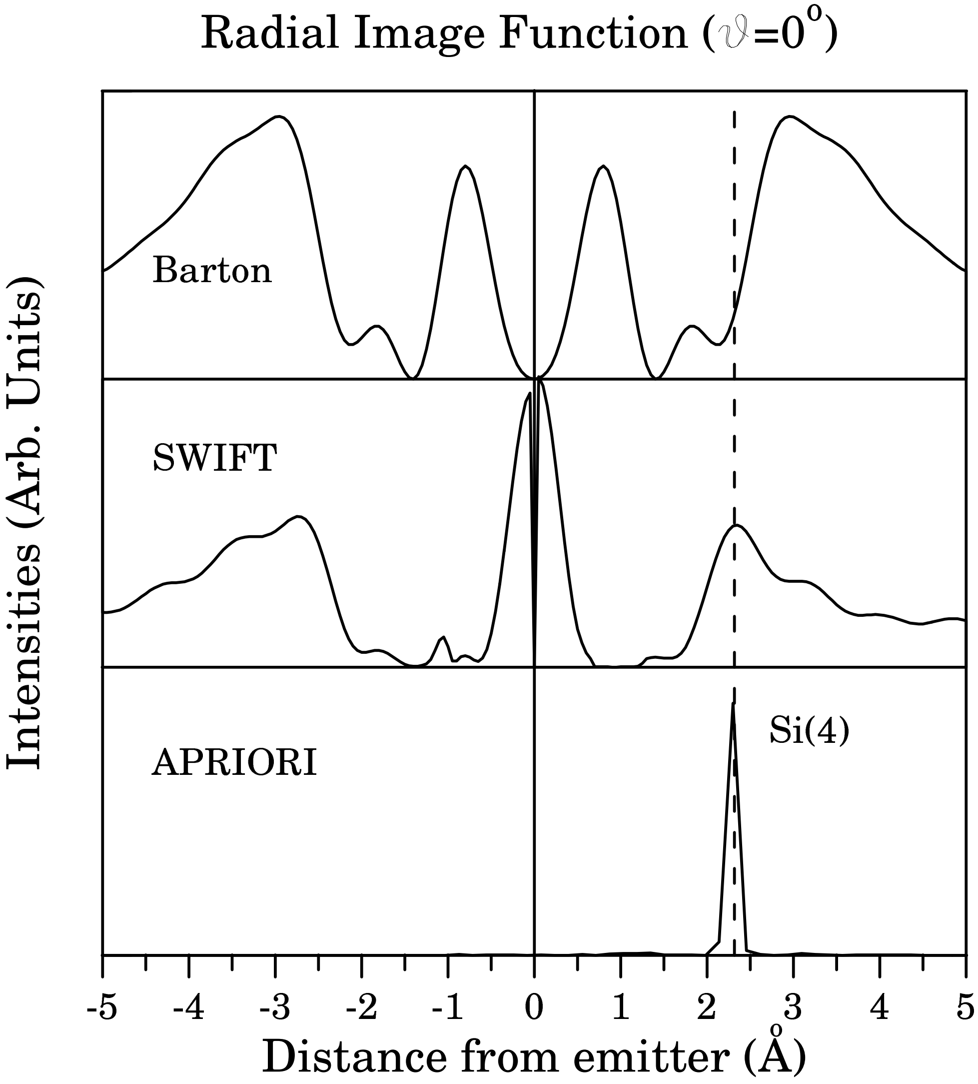

Figure 7.10: Radial image functions (RIFs) with radial axis along the normal direction, at θ=0^o, by different electron holographic reconstruction algorithms. Upper and middle panels show the results of the Barton's Helmholtz-Kirchoff Fourier transform and the Scattered-Wave Included Fourier transform (SWIFT) method. Lower panel curve is the APRIORI reconstruction image function $p_{Si}^{(4)}(\mathbf{r}_i)$ after four iterations.

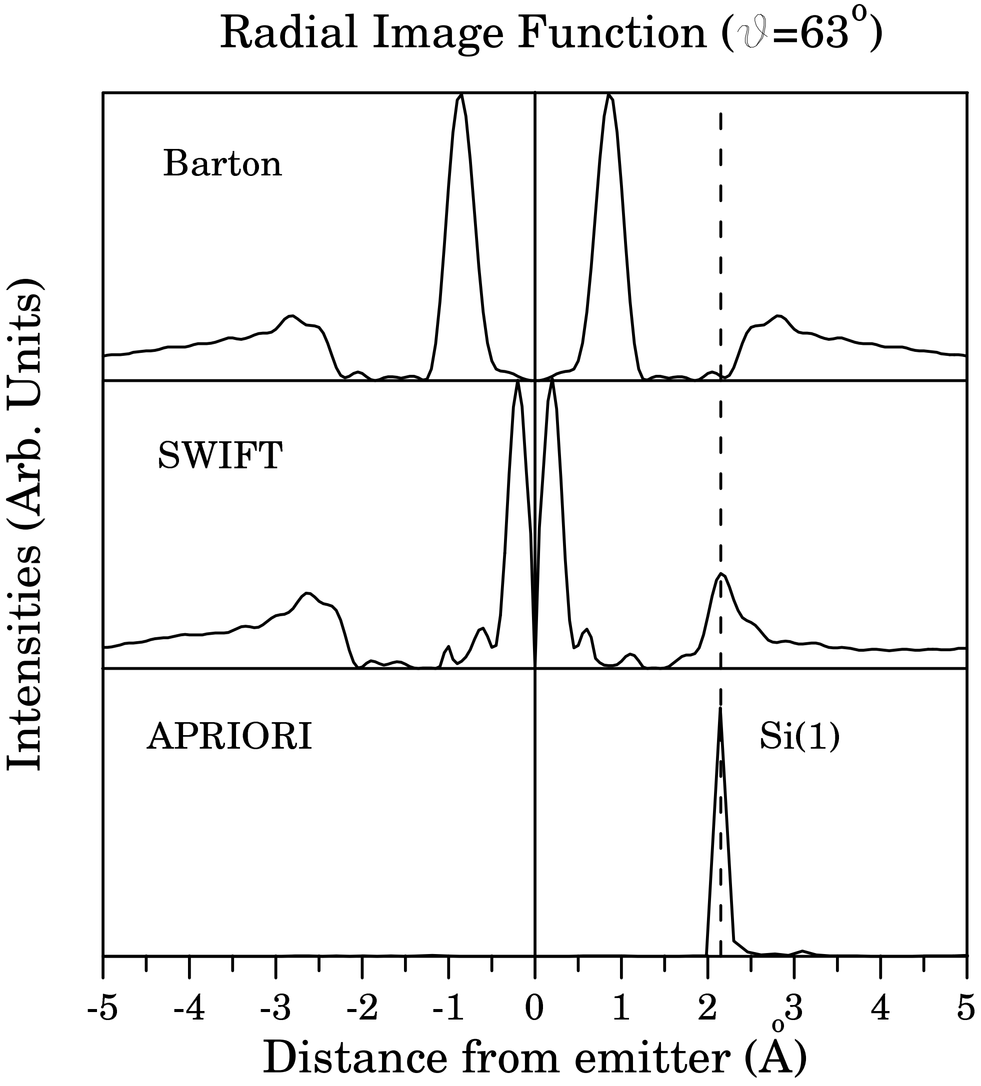

Figure 7.11: Radial image functions (RIFs) with radial axis along the polar angle θ=63^o by different electron holographic reconstruction algorithms. Upper and middle panels show the results of the Barton's Helmholtz-Kirchoff Fourier transform and the Scattered-Wave Included Fourier transform (SWIFT) method. Lower panel curve is the APRIORI reconstruction image function $p_{Si}^{(4)}(\mathbf{r}_i)$ after four iterations.

7.3.5 Conclusions

A robust new reconstruction algorithm [88], which offers the prospect of overcoming many difficulties encountered in the traditional photoelectron holography by making use of linear programming optimization procedures, has been presented. The rapid new iterative scheme appears to accurately reconstruct the relative positions of source and scatterers directly from the data of a mono-energetic point-source diffraction pattern. It makes use of the squared object-wave terms which are neglected in traditional holographic algorithms to reconstruct the holographic images. It also does not suffer from a twin-image problem, and even identifies the chemical species of the *scattering* atoms.

The first example for our new algorithm is to reconstruct radial image function from a simulated hologram from simple Ni-C-O chain model with C atom as the emitter. It was demonstrated that the linear programming procedures can reconstruct the Ni and O atom positions correctly with the twin images eliminated, while distinguishing the species of Ni and O atoms. In order to test the stability of the new algorithm, Gaussian noise of standard deviation $\sigma = 0.5$ %, 4.0 %, 8.0 %, and 12.0 % were added to our simulated experimental data. The results are encouraging for atom images can still be identified up to $\sigma = 12.0$ %.

The second test was performed for a model Si(111)($\sqrt{3}$x$\sqrt{3}$)B system, where a full dynamical simulation of a photoelectron diffraction diffraction pattern was carried out, and a three-dimensional image was reconstructed around the source atom (B emitter). This image strongly indicates the positions of the Si atoms in the forward-scattering positions, and the twin images were also eliminated in this case. Since a large number of data points, $\{I_i^{exp}\}$ i from 1 to 16384, needed to be used in the optimization procedure in order to secure a reliable reconstructed image while at the same time maintaining a reasonable size of program that fits the memory limit of our computer, we employed a strategy that uses only some of the data points, say i=1...64, for a run, and then, averages all the results to obtain the final image function.

In the above two examples the chemical species of the scatterers, and the number of atoms for each species, N_X, were known beforehand. In an application of the APRIORI algorithm to real experimental data, the sums over X and Z could be restricted to the chemical elements known to constitute the sample, as determined by, e.g., an Auger or photo-electron spectrum.

It might be argued that the particular example we have presented above to illustrate our method belongs to a class of atomic geometries, which includes the case of a source atom forming part of a simple adsorbate on a surface, in which the scattering is fairly kinematical, and that our technique may not be so applicable for example when the sources are buried deep beneath a surface, where the strong multiple-scattering effects may be unavoidable. However, we argue that it should be possible to handle the problem of structure *refinement* by an adaptation of the method even in such more general geometries. It should be noted that, in a typical problem in surface crystallography, the relative positions of most of the atoms affecting the measured intensities are assumed known, and effort is directed towards determining the positions (or small displacements from certain reference positions) of a few of them. We may then re-define the reference wave, $R(\mathbf{k})$, as being not just that emitted by a single atom, but that arising after the scattering of the emitted wave from some known reference structure [104], as calculated by a full multiple-scattering computer program. It is then often reasonable to regard the scattering of this reference wave from the small number, which we re-identify as N_X for species X, of atoms of unknown positions (or which deviate from their positions in the reference structure) as being kinematic, as assumed for example in the "tensor LEED" technique [107]. For such a problem a kinematic treatment of the object waves in a reconstruction algorithm would be no limitation.

More generally, it is also possible that this method may be extended to include some multiple scattering of even the object waves. For example, if we were to include double scattering, the matrix elements $M(\mathbf{k}, \mathbf{r}_i)$ would contain terms involving double and triple products of the distributions $p_Z(\mathbf{r}_j)$. A procedure can still be envisaged in which some initial guess of $p_Z^{(0)}$ of these distributions is refined by the same type of iterative optimization process.

Chapter 8

Summary

In this dissertation, theories and applications of three important techniques of surface structure determination have been addressed. They are x-ray photoelectron diffraction, Auger electron diffraction, and photoelectron holography.

We have described in chapter 2 the theories of both single scattering and multiple scattering schemes of an electron wave in a cluster, and introduced a concentric-shell algorithm [32] for the calculations of full multiple-scattering of the angular distributions of Auger electron, x-ray photoelectron, as well as Kikuchi electron diffraction patterns. This multiple-scattering cluster scheme is based on dividing a cluster into a series of concentric shells, with an origin chosen at the source atom, and a convenient computational algorithm for the intra- and inter-shell calculations. An advantage of a cluster calculation is the removal of the requirement of translational symmetry of the atomic structure near the surface. Once the cluster scattering matrix **S** is calculated, the angular distribution of the diffraction pattern may be computed for different real experimental conditions with little extra effort. We have also tested the convergence of the algorithm, and found that calculations with maximum angular momentum quantum number, $l_{out} > 60$, will result in similar diffraction patterns after smoothing by a finite aperture semi-angle. A forward-scattering approximation was also tested by neglecting intra-shell multiple scattering, and it was found that the resulting diffraction pattern was in good agreement with that using full multiple scattering for a high electron kinetic energy of 914 eV.

In chapter 3, we have implemented the full multiple scattering algorithm described in chapter 2 to simulate the 64 eV $M_{2,3}VV$ and 914 eV L_3VV Auger diffraction patterns from a Cu(001) surface, and have compared these simulations with the published experimental data and computer simulations of Frank *et al.* [1] who used a "blocking" model. With visual comparison and an R-factor calculation, it was found that the $M_{2,3}VV$ and L_3VV emissions are dominated by f-wave ($l = 3$) electrons. The Auger selection rule was also discussed and it was shown that final possible emitted electron states of the $M_{2,3}VV$ and L_3VV transitions are f-waves. The $M_{2,3}VV$ simulation shows that dips appear along most of the projections of atomic rows, except along the projections of the $< 101 >$ directions where intensity peaks shows up, while the L_3VV pattern is dominated by high intensity peaks along the low-index directions. These features on both patterns have been confirmed by the experiments of Frank *et al.* [1]. We have found that the angular momentum of the emitted electron is not the *sole* factor in determining whether the intensity forms a peak or a dip along a particular atomic row in a crystal. Other factors, such as the inter-atomic distances, could also be important in determining the feature along the projection of an atomic row on a diffraction pattern. This indicates that an electron diffraction pattern at low energy may not bear a simple and direct relation between the surface structure and the diffraction pattern. It is particular gratifying to see that *exactly* the same computer program reproduces the different diffraction features of both Auger electron diffraction patterns, while the "blocking" model has to be supplemented by including a "channeling" effect to obtain even a semblance of the high energy pattern.

In chapter 4, studies of Auger electron (Mg KLL 1180 eV) and photoelectron (O 1s 955 eV) diffraction angular distribution profiles from MgO(001) surfaces are described. Both diffraction patterns were measured in the same scan from cleaved and sputtered&annealed MgO(001) surfaces. It was found that there are coincidences between the low-index crystallographic directions and the forward-scattering maxima on the diffraction pattern. However, the anomalous phenomenon of peak shifts off the forward-scattering directions have aalso been observed. Theoretical multiple-scattering calculations have been performed on flat and rumpled MgO(001) surface models, as well as for neutral and ionic Mg and O atoms in the MgO, and the results show that the diffraction patterns from those different models do not differ very much, even for a highly reconstructed surface of 10% rumpling and 5% relaxation. This indicates that the peak shifts toward lower polar angles are not necessarily caused by rumpling in the surface structure of MgO(001). A series of simulations have been conducted, and it was found that a short inelastic scattering length of an electron in the MgO crystal seems to be responsible for such peak shifts. The good agreement between the experiments and the theoretical calculations for both diffraction patterns occurs when the imaginary part of the electron energy is 16 eV, which corresponds to a short inelastic scattering length at the lower end of the "universal" curve. It is also shown that the calculated electron diffraction patterns from a defect-free MgO surface model is in much better agreement with the photoelectron diffraction experiment performed on the cleaved MgO(001) surface, and gives less agreement with that from a sputtered&annealed MgO(001) surface. This might suggest that the cleaved MgO(001) surface has a smaller number of defects than the sputtered&annealed one.

In chapter 5, we have shown the details of carrying out the photoelectron diffraction simulations from a $CoSi_2(111)$ surface for Co-3p (695 eV) angle-resolved XPD and Si-2p (20 to 130 eV) normal emission modes by considering the real experimental conditions, such as the polarization direction of the x-ray photon, the emitted core-level photoelectron states, the electron analyzer position and the sample orientation. A formula for transforming the dipole transition amplitude in a laboratory reference frame (defined by the x-ray photon polarization) to that in a sample reference frame (defined by the sample orientations) is derived. We assumed that the emitted photoelectrons are mutually coherent if they come from the same core-level, and are mutually incoherent if they are emitted from different states. Simulation of the Co-3p XPD pattern from a $CoSi_2(111)$ surface does not show three-fold symmetry, although the surface has three-fold symmetry. This asymmetric pattern arises from the fact that the x-ray polarization direction is tilted along the (θ, ϕ)=$(67.5^o,0.0^o)$ direction (in polar coordinates), and that an electron from the core-level tends to be emitted along the polarization direction of the photon. The Si-2p normal emission diffraction simulation is carried out by calculating the energy dependent scattering matrix $\mathbf{S}(\epsilon)$, and assuming that transition probabilities for Si-2p final states remain the same. Excellent agreement has been found between the experiment and the simulation including both s and d-wave emitted by the Si atoms. However, poor agreement was found between the experiment and the theory if a simple s-wave emitter was used in the calculation.

In chapter 6, theories of photoelectron hologram formation and reconstruction are discussed. Several reconstruction algorithms, which are aimed at eliminating artifacts in the real space images and correcting image shifts due to phase shifts of the scattering atoms, have been addressed. It is shown by the reconstructed image from an O adatom on Ni(001) surface that Barton's Helmholtz-Kirchoff algorithm is suitable for the backscattering geometry, where the squared terms or the self-interference terms in Eq. 6.6, can be neglected, while for a forward-scattering dominated diffraction pattern, these terms are non-negligible in the forward-scattering directions. In an example of holographic reconstruction of Si-2p angle-resolved XPD from Si(001) [2×1], we have shown that the reconstructed image may fail to locate the correct atom image positions when simply applying a reconstruction algorithm to the unprocessed hologram. The failure of the reconstruction is due mainly to the appearance of non-holographic features of self-interference terms, which contribute a slowly oscillatory background to the diffraction pattern. This slow oscillatory background can be removed by a filtering process, and the reconstructed holographic image shows atomic images appearing at the true atom positions of a Si diamond structure with atomic resolution. The last example in chapter 6 is the holographic reconstruction of the Co-3p core-level angle-resolved XPD from a $CoSi_2$ surface. We use here a reference and scattered-wave included Fourier transform (RSWIFT) algorithm, which corrects for the anisotropic emitter waves and the anisotropic atomic scattering factors. A kernel function involving the atomic transition amplitudes for the final emitted electron waves and the atomic scattering factors of the scattered atoms is developed. Although in this algorithm we need to calculate the transition amplitudes from the Co-3p core-level, it is still a direct method in the sense that it requires no prior knowledge of the $CoSi_2(111)$ surface structure. The holographic reconstruction obtained by RSWIFT shows an improvement by a factor of three over the results from the Barton Helmholtz-Kirchoff and SWIFT algorithms.

In chapter 7, we introduced the basic concepts and fundamental theory of the linear programming, and then applied the method of linear programming to solve physics optimization problems in photoelectron holography. A three-step procedure of (1) specification of the unknown variables, (2) specification of the constraints, and (3) specification of the objective function, is carried out to convert an optimization problem into a standard linear programming format.

With the aid of a linear programming optimization routine, we developed the reconstruction algorithm of "atomic position recovery by iterative optimization of reconstructed intensities" (APRIORI). This method is sensitive to the dominant features of a diffraction pattern, e.g. the forward-scattering peaks, and takes account of the self-interference terms (squared terms) neglected in traditional holographic reconstruction schemes. Since we were more interested in determining the positions of the scatterers rather than their wave-fields, so we introduced a spatial function, $p_X(\mathbf{r})$, which represents the probability distribution of a scatterer of species X in the real space. An expression for the intensity of electron diffraction pattern is derived and optimized to the experimentally measured data subject to relevant constraints. An iterative scheme is proposed to optimize the error function of the absolute value of the difference between the experimental measured and the calculated data. Once an initial guess of spatial function is put in the intensity expression, a linear programming optimization process may be carried out and a new spatial function is obtained. The iterative optimization process is continued by using the new spatial function, and is halted when spatial function is self-consistent. The initial guess of the spatial function does not affect the final result. The first test of our new algorithm was to reconstruct a holographic radial image function from a photoelectron diffraction pattern due to a C emitter from a Ni-C-O chain model. We were able not only to reconstruct the correct positions of Ni and O atoms, but also to separately identify the Ni and O species, and to eliminate the twin images. The second test was to reconstruct a three-dimensional image from the photoelectron diffraction from a model of a B emitter on a Si(111)$(\sqrt{3} \times \sqrt{3})$B surface. The reconstructed image shows good agreement with the atom positions on the model, and no twin images or strong artifacts were found. In this case also, the test diffraction pattern was simulated by a full dynamical calculation. The stability of this algorithm was also tested with Gaussian noise of standard deviations σ=0.5%, 4.0%, 8.0%, and 12.0% on the Ni-C-O model, and the results show that the image reconstructions survive up to that noise level.

Bibliography

[1] D. G. Frank, T. Golden, Oliver M. R. Chyan, and A. T. Hubbard, J. Vac. Sci. Technol. **A 9**(3), 1254 May/Jun. (1991).

[2] D. Briggs, and M. P. Seah, Practical Surface Analysis, John Wiley & Sons 1983.

[3] D. Gabor, Nature (London) **161**, 777 (1948).

[4] M. P. Seah and W. A. Dench, Surf. and Interface Anal. **1**, 2(1979).

[5] A. G. McKale, G. S. Knapp, and S.-K. Chan Phys. Rev. B **33**, 841(1986).

[6] J. J. Rehr, R. C. Albers, C. R. Natoli, and E. A. Stern Phys. Rev. B **34**, 4350(1986).

[7] J. Mustre de Leon, J. J. Rehr, C. R. Natoli, C. S. Fadley and J. Osterwalder Phys. Rev. B **39**, 5632(1989).

[8] J. J. Rehr, and R. C. Albers Phys. Rev. B **41**, 8139(1990).

[9] A. Liebsch, Phys. Rev. Lett. **32**, 1203 (1974).

[10] J. B. Pendry, Surf. Sci. **57**, 679 (1976).

[11] J. B. Pendry, Low Energy Electron Diffraction, (Academic, London, 1974).

[12] C. H. Li and S. Y. Tong, Phys. Rev. Lett. **40**, 46 (1978).

[13] C. H. Li, A. R. Lubinsky, and S. Y. Tong, Phys. Rev. B **17**, 3128 (1978).

[14] S. Y. Tong and C. H. Li, in *Chemistry and Physics of Solid Surfaces*, Vol. **3**, edited by R. Vanselow and W. England (CRC Press, Boca Raton, 1982), p.287.

[15] S. Y. Tong, H. C. Poon, and D. R. Snider Phys. Rev. B **32**, 2096 (1985).

[16] J. J. Barton and D. A. Shirley, Phys. Rev. B **32**, 1906 (1985).

[17] J. J. Barton, M.-L. Xu, and M. A. Van Hove, Phys. Rev. B **37**, 10475 (1988).

[18] V. Fritzsche, J. Phys: Condens. Matter **2**, 1413 (1990); **2**, 9735 (1990)

[19] D. Friedman and C. S. Fadley, J. Electron Spectrosc. Relat. Phenom. **51**, 689 (1990).

[20] J. B. Pendry, in *Determination of Surface Structure by LEED*, edited by P. M. Marcus and F. Jona (Plenum, New York, 1984), p.3.

[21] D. K. Saldin and J. B. Pendry, Surf. Sci. **162**, 941 (1985).

[22] D. K. Saldin, G. R. Harp, and B. P. Tonner, Phys. Rev. B **45**, 9629 (1992).

[23] C. S. Fadley, Progress in Surface Science **16**, 275(1984).

[24] C. S. Fadley, Physica Scripta **T 17**, 39(1987).

[25] C. S. Fadley, in Synchrotron Radiation Research: Advances in Surface Science, (New York, Plenum), Chap.**11**, (1990).

[26] M. Sagurton, E. L. Bullock, and C. S. Fadley Surface Science **182**, 287(1987).

[27] M. L. Xu, J. J. Barton, and M. A. Van Hove, Phys. Rev. B **39**, 215 (1989).

[28] S. Kono, C. S. Fadley, N. F. T. Hall, and Z. Hussain, Phys. Rev. Lett. **41**, 117 (1978).

[29] S. Kono, S. M. Goldberg, N. F. T. Hall, and C. S. Fadley, Phys. Rev. Lett. **41**, 1831 (1978).

[30] L. -G. Peterson, S. Kono, N. F. T. Hall, C. S. Fadley, and J. B. Pendry, Phys. Rev. Lett. **42**, 1545 (1979).

[31] P. J. Orders, S. Kono, C. S. Fadley R. Trehan, and J. T. Lloyd, Surface Science **119**, 371 (1982).

[32] D. K. Saldin, G. R. Harp, and X. Chen, Phys. Rev. B **48**, 8234(1993).

[33] S. A. Chambers, Surf. Sci. Rep. **16**, 263 (1992).

[34] S. A. Chambers, Adv. Phys. **40**, 357 (1991).

[35] W. F. Egelhoff, Jr., Crit. Rev. Solid State Mater. Sci. **16**, 213 (1990).

[36] D. G. Frank, N. Batina, T. Golden, F. Lu, and A. T. Hubbard, Science **247**, 182 (1990).

[37] L. J. Terminello and J. J. Barton, Science **251**, 1218 (1991).

[38] J. J. Barton and L. J. Terminello, Phys. Rev. B **46**, 13548 (1992).

[39] Y. U. Idzerda and D. E. Ramaker, Phys. Rev. Lett. **69**, 1943 (1992).

[40] T. Greber, J. Osterwalder, D.Naumović, A. Stuck, S. Hüfner, and L. Schlapbach, Phys. Rev. Lett. **69**, 1947 (1992).

[41] Calculated Electronic Properties of Metals, by V. L. Moruzzi, J. F. Janak and A. R. Williams, (Pergamon Press Inc, New York 1978).

[42] F. Weissmann, Solid State Commun. **31**, 347 (1979).

[43] F. Weissmann and K. Müller, Surf. Sci. Rep. **105**, 251 (1981).

[44] H. L. Davis, in Proceedings of the 7th International Vacuum Congress and 3rd International Conference on Solid Surfaces, Vienna, 1977, edited by R. Dobrozenski, F. Rüdenauer, F. P. Viehböck, and A. Breth (Vienna, 1977) Vol. **3**.

[45] I. Cherkendorff, J. El. Spec. Relat. Phenom., **32**, 1 (1983).

[46] D. Aberdam, R. Baudoing, E. Blanc, and C. Gaubert, Surf. Sci. **71**, 279 (1978).

[47] E. L. Bullock and C. S. Fadley, Phys. Rev. B **31**, 1212(1985).

[48] J. Osterwalder, E. A. Steward, D. Cyr, C. S. Fadley, J. Mustre de Leon, and J. J. Rehr, Phys. Rev. B **35**, 9859(1987).

[49] A. Zangwill, Physics at Surfaces (Cambridge University Press, Cambridge, 1988).

[50] K. O. Legg, M. Prutton, and C. Kinniburgh, J. Phys. **C 7**, 4236(1974).

[51] M. R. Welton-Cook, and M. Prutton, Surf. Sci. **74**, 276(1978).

[52] T. Urano, T. Kanaji, and M. Kaburagi, Surf. Sci. **134**, 109(1983).

[53] P. A. Maksym, Surf. Sci. **149**, 157(1985).

[54] D. L. Blanchard, D. L. Lessor, J. P. LaFemina, D. R. Naer, W. K. Ford, and T. Guo, J. Vac. Sci. Technol. **A 9**, 1814(1991).

[55] P. R. Watson, J. Phys. Chem. Ref. Data **16**, 953(1987).

[56] H. Nakamatsu, A. Sudo, and S. Kawai, Surf. Sci. **194**, 265(1988).

[57] H. Nakamatsu, A. Sudo, and S. Kawai, Surf. Sci. **223**, 193(1989).

[58] C. Duriez, C Chapon, C. R. Henry and J. M. Rickard, Surf. Sci. **230**, 123(1990).

[59] S. Varma, X. Chen, J. Zhang, I. Davoli, D. K. Saldin, and B. P. Tonner, submitted to Surf. Sci. , (1994).

[60] V. E. Henrich, G. Dresselhaus, and H. J. Zeiger, Phys. Rev. B **22**, 4764(1980).

[61] F. Herman, and S. Skillman, Atomic Structure Calculation, (Prentice Hall, Englewood Cliffs, NJ, 1963).

[62] Karlheinz Schwarz, Phys. Rev. B **5**, 2466(1972).

[63] D. R. Penn, Phys. Rev. B **13**, 5248(1976).

[64] B. Cleff, and W. Mehlhorn, J. Phys. B **7**, 593(1974).

[65] M. A. Hove, and S. Y. Tong, Surface Crystallography by LEED, (Springer-Verlag Berlin Heidelberg New York, 1979).

[66] S. A. Chambers, S. B. Anderson, H. W. Chen, and J. H. Weaver, Phys. Rev. B **34**, 913 (1986).

[67] H. C. Poon, G. Grenet, S. Holmberg, Y. Jugnet, and T. Minh Duc, Phys. Rev. B **41**(18), 12735 (1990).

[68] Y. Zhou, J. C. Campuzano, P. Kaukasoina, M. Lindroos, and G. Jennings, Phys. Rev. B **47**(16), 10395 (1993).

[69] Atomic Physics of Lasers, by Derek Eastham, Yaylor & Francis, London and Philadelphia (1986).

[70] R. Leckey, J. D. Riley, R. L. Johnson, L. Ley, and B. Ditchek, J. Vac. Sci. Technol. **A 6**(1), 63(1988).

[71] G. Grenet, Y. Jugnet, S. Holmberg, H. C. Poon, and Tran Minh Duc, Surface and Interface Analysis, Vol. **14**, 367(1989).

[72] X. Chen, G. R. Harp, and D. K. Saldin, J. Vac. Sci. Technol. **A 11**(6), 428(1994).

[73] E. U. Condon, G. H. Shortley, The Theory of Atomic Spectra, Cambridge University Press (1951).

[74] J. T. Hutton, G. T. Trammell, and J. P. Hannon, Phys. Rev. B **31**, 743 (1985).

[75] A. Szöke, in **Short Wavelength Coherent Radiation: Generation and Applications**, Monterey, CA, 1986, Proceedings of the Topical Meeting on Short Wavelength Coherent Radiation: Generation and Applications, edited by D. J. Attwood and J. Boker, AIP Conf. Proc. No. 147 (AIP, New York, 1986).

[76] D. K. Saldin and P. L. De Andres, Phys. Rev. Lett. **64**, 1270 (1990)

[77] G. R. Harp, D. K. Saldin, and B. P. Tonner, Phys. Rev. Lett. **65**, 1012 (1990).

[78] D. K. Saldin, G. R. Harp, B. L. Chen, and B. P. Tonner, Phys. Rev. B **44**, 2480 (1991).

[79] B. P. Tonner, Zhi-Lan Han, G. R. Harp, and D. K. Saldin, Phys. Rev. B **43**, 14423 (1991).

[80] H. Huang, Hua Li, and S. Y. Tong, Phys. Rev. B**44**, 3240 (1991).

[81] Y. Zhou, X. Chen, D. K. Saldin, and J. Campuzano, Mat. Research Soc. Symposium Proc., Vol. **307**, 279 (1993).

[82] H. C. Poon, D. Snider, and S. Y. Tong, Phys. Rev. B **33**, 2199 (1986).

[83] P. J. Durham, J. B. Pendry, and C. H. Hodges, Comput. Phys. Commun. **29**, 193 (1982).

[84] D. D. Vvedensky, D. K. Saldin, and J. B. Pendry, Comput. Phys. Commun. **40**, 421 (1986).

[85] J. J. Barton, J. Elect. Spec. Rel. Phenom. **51**, 37 (1990).

[86] S. Y. Tong and H. Huang, Phys. Rev. B **46**, 2452 (1992).

[87] S. Y. Tong, C. M. Wei, T. C. Zhao, H. Huang, and Hua Li, Phys. Rev. Lett. **66**, 60 (1991).

[88] D. K. Saldin, X. Chen, N. Kothari, and M. Patel, Phys. Rev. Lett. **70**(8), 11122 (1993).

[89] Hong Li and B. P. Tonner Phys. Rev. B **40**, 10241(1989).

[90] H. Hilferink, E. Lang, and K. Heinz, Surf. Sci. **93**, 398 (1980).

[91] S. Hardcastle, Z.-L. Han, G. R. Harp, J. Zhang, B. L. Chen, D. K. Saldin, and B. P. Tonner, Surf. Sci. **245**, L190 (1991).

[92] Daniel Solow, "Linear Programming", (North-Holland, New York, Amsterdam, Oxford 1984.)

[93] R. B. Darst, “Introduction to Linear Programming”, (New York : M. Dekker, 1991.)

[94] M. M. Woolfson, *Direct Methods in Crystallography*, (Oxford Univ. Press, Oxford, 1961).

[95] S. Thevuthasan et al., Phys. Rev. Lett. **67**, 469 (1991).

[96] P. Hu and D. A. King, Nature **353**, 831 (1991).

[97] A. Stuck et al., Surf. Sci. **274**, 441 (1992).

[98] M. A. Mendez et al., Phys. Rev. B **45**, 9402 (1992).

[99] Z.-L. Han, S. Hardcastle, G. R. Harp, H. Li, X. D. Wang, J. Zhang, and B. P. Tonner, Surf. Sci. **258**, 313 (1991).

[100] G. Harp, D. K. Saldin, X. Chen, Z. Han, and B. Tonner, J. Electron Spectrosc. Relat. Phenom. **57**, 331 (1991).

[101] J. J. Barton and L. J. Terminello, *The Structure of Surfaces III*, edited by S. Y. Tong et al. (Springer, Berlin, 1991).

[102] S. Y. Tong, H. Li and H. Huang, Phys. Rev. Lett. **67**, 3102 (1991).

[103] J. J. Barton, Phys. Rev. Lett. **67**, 3106 (1991).

[104] A. Szöke, Phys. Rev. B **47**, 14044 (1993).

[105] See e.g. H. A. Taha, *Operations Research: An Introduction* (Macmillan, New York, 1992).

[106] E.g. W. H. Press, B. P. Flannery, S. A. Teukolsky, and W. T. Vetterling, *Numerical Recipes: The Art of Scientific Computing* (Cambridge Univ. Press, Cambridge, 1986).

[107] P. J. Rous et al., Phys. Rev. Lett. **57**, 2951 (1986).

[108] I. -W. Lyo, Efthimios Kaxiras, and Ph. Avouris, Phys. Rev. Lett. **63**, 1261 (1989).

[109] P. Bedrossian, R. D. Meade, K. Mortensen, D. M. Chen, J. A. Golovchenko, and D. Vanderbilt, Phys. Rev. Lett. **63**, 1257 (1989).

[110] R. L. Headrick, I. K. Robinson, E. Vlieg, and L. C. Feldman, Phys. Rev. Lett. **63**, 1253 (1989).

[111] Efthimios Kaxiras, K. C. Pandey, F. J. Himpsel, and R. M. Tromp, Phys. Rev. B **41**, 1262 (1990).

[112] H. Huang, S. Y. Tong, J. Quinn, and F. Jona, Phys. Rev. B **41**, 3276 (1990).

Appendix

Calculation of the shell scattering matrices

The incident and outgoing waves around central atom can be expanded about an atom at position, $\mathbf{r}_i$, in the qth shell around the emitter using the formulae:

$$h_l^{(1)}(kr)Y_{lm}(\hat{\mathbf{r}}) = \sum_{l'm'} g_{LL'}^{oi} j_{l'}(k|\mathbf{r}-\mathbf{r}_i|)Y_{l'm'}(\frac{\mathbf{r}-\mathbf{r}_i}{|\mathbf{r}-\mathbf{r}_i|}) \tag{8.1}$$

$$h_l^{(1)}(kr)Y_{lm}(\hat{\mathbf{r}}) = \sum_{l'm'} \tilde{g}_{LL'}^{oi} h_{l'}^{(1)}(k|\mathbf{r}-\mathbf{r}_i|)Y_{l'm'}(\frac{\mathbf{r}-\mathbf{r}_i}{|\mathbf{r}-\mathbf{r}_i|}) \tag{8.2}$$

$$j_l(kr)Y_{lm}(\hat{\mathbf{r}}) = \sum_{l'm'} g_{LL'}^{oi} h_{l'}^{(1)}(k|\mathbf{r}-\mathbf{r}_i|)Y_{l'm'}(\frac{\mathbf{r}-\mathbf{r}_i}{|\mathbf{r}-\mathbf{r}_i|}) \tag{8.3}$$

$$j_l(kr)Y_{lm}(\hat{\mathbf{r}}) = \sum_{l'm'} \tilde{g}_{LL'}^{oi} j_{l'}(k|\mathbf{r}-\mathbf{r}_i|)Y_{l'm'}(\frac{\mathbf{r}-\mathbf{r}_i}{|\mathbf{r}-\mathbf{r}_i|}) \tag{8.4}$$

where

$$g_{LL'}^{ij} = 4\pi(1-\delta_{ij}) \sum_{l''m''} i^{l-l'-l''}(-1)^{m'+m''} h_{l''}^{(1)}(k|\mathbf{r}_i-\mathbf{r}_j|)$$
$$Y_{l''-m''}(\frac{\mathbf{r}_i-\mathbf{r}_j}{|\mathbf{r}_i-\mathbf{r}_j|}) \int Y_{lm}Y_{l''m''}Y_{l'-m'}d\Omega$$

and

$$\tilde{g}_{LL'}^{ij} = 4\pi(1-\delta_{ij}) \sum_{l''m''} i^{l-l'-l''}(-1)^{m'+m''} j_{l''}(k|\mathbf{r}_i-\mathbf{r}_j|)$$
$$Y_{l''-m''}(\frac{\mathbf{r}_i-\mathbf{r}_j}{|\mathbf{r}_i-\mathbf{r}_j|}) \int Y_{lm}Y_{l''m''}Y_{l'-m'}d\Omega$$

are the propagator from atom i of position vector $\mathbf{r}_i$ to atom j of position $\mathbf{r}_j$ in the qth shell. $\tilde{g}_{LL'}^{ij}$ is the same as $g_{LL'}^{ij}$ except that $j_{l''}$ is substituted for $h_{l''}^{(1)}$. The superscript o represents the atom at the origin.

The "out-in" scattering matrix, $\mathbf{T}_q^{OI}$, of the qth shell consists of elements $T^{OI}_{q,lm,l'm'}$ and form the coefficients in the expansion of the scattered wave field

$$\sum_{l'm'} T^{OI}_{q,lm,l'm'} j_{l'}(kr) Y_{l'm'}(\hat{\mathbf{r}}) \tag{8.5}$$

generated by an outgoing wave,

$$h_l^{(1)}(kr) Y_{lm}(\hat{\mathbf{r}}), \tag{8.6}$$

centered on the absorbing atom.

To evaluate $\mathbf{T}_q^{OI}$, first consider a scattering atom at position $\mathbf{r}_i$, with t-matrix $\mathbf{t}_i$. The wave field, (8.6), can be re-expressed by Eq. 8.1 as

$$\sum_{l'm'} g^{oi}_{LL'} j_{l'}(k|\mathbf{r}-\mathbf{r}_i|) Y_{l'm'}(\frac{\mathbf{r}-\mathbf{r}_i}{|\mathbf{r}-\mathbf{r}_i|})$$

a sum of standing waves about the atom at $\mathbf{r}_i$. The wave initially-scattered by the atom at $\mathbf{r}_i$ can be written

$$\sum_{l'm'} t_{i,l'} g^{oi}_{LL'} h^{(1)}_{l'}(k|\mathbf{r}-\mathbf{r}_i|) Y_{l'm'}(\frac{\mathbf{r}-\mathbf{r}_i}{|\mathbf{r}-\mathbf{r}_i|})$$

$$= \sum_{L'} B^{(0)}_{i,L'} h^{(1)}_{l'}(k|\mathbf{r}-\mathbf{r}_i|) Y_{l'm'}(\frac{\mathbf{r}-\mathbf{r}_i}{|\mathbf{r}-\mathbf{r}_i|})$$

where $B^{(0)}_{i,L'} = t_{i,l'} g^{oi}_{LL'}$. But we know that

$$B_{i,L'} = B^{(0)}_{i,L'} + \sum_{j,L''} B_{i,L''} g^{ji}_{L''L'} t_{i,l'}$$

then

$$\sum_{j,L''} B_{j,L''} \{\delta_{ij}\delta_{L'L''} - g^{ji}_{L''L'} t_{i,l'}\} = B^{(0)}_{i,L'}$$

or

$$\sum_{j,L''} B_{j,L''} t_{i,l'} \{\delta_{ij}\delta_{L'L''} t^{-1}_{i,l'} - g^{ji}_{L''L'}\} = B^{(0)}_{i,L'} = t_{i,l'} g^{oi}_{LL'}$$

We end up with

$$\sum_{j,L''} B_{j,L''}\{\delta_{ij}\delta_{L'L''}t^{-1}_{i,l'} - g^{ji}_{L''L'}\} = g^{oi}_{LL'}$$

thus

$$\sum_{j,L''} B_{j,L''}H^{ij}_{L'L''} = g^{oi}_{LL'}$$

where

$$H^{ij}_{L'L''} = t^{-1}_{i,L'}\delta_{ij}\delta_{L'L''} - g^{ij}_{L'L''} \tag{8.7}$$

are the elements of the real-space Korringa-Kohn-Rostocker (KKR) matrix **H** and $t_{i,L'}$ is an element of the (diagonal) t-matrix of atom i, and thus

$$B_{j,L''} = \sum_{i,L'} T^{ij}_{L'L''}g^{oi}_{LL'} \tag{8.8}$$

where we define the matrix **T** as the inverse of **H**, where the matrix elements satisfy

$$\sum_{k,L'''} H^{ik}_{L'L'''}T^{kj}_{L'''L''} = \delta_{ij}\delta_{L'L''}$$

where **H** has a linear dimension of the number of atoms in the cluster multipled by the number of lm components considered in the scattering by a single atom. Thus the final scattered wave field due to the incidence of wave (8.6) on the cluster is

$$\sum_{j,L''} B_{j,L''}h^{(1)}_{l'}(k|\mathbf{r}-\mathbf{r}_j|)Y_{l'm'}(\frac{\mathbf{r}-\mathbf{r}_j}{|\mathbf{r}-\mathbf{r}_j|}) \tag{8.9}$$

with $B_{j,L''}$ is given by Eq. 8.8. The final step in the evaluation of $\mathbf{T}^{OI}$ is to re-express Eq. 8.9 as a sum of spherical standing waves centered at the origin. Each of the waves in Eq. 8.9 can be re-expressed in terms of such wave as

$$\sum_{j,L'',L'''} B_{j,L''}g^{jo}_{L''',L''}j_{l'''}(kr)Y_{L'''}(\hat{\mathbf{r}})$$

Thus the outgoing spherical wave (8.6) has generated the set of standing waves scattered back towards the origin:

$$\sum_{j,L'',L'''} T^{OI}_{q,L,L'''} j_{l'''}(kr) Y_{L'''}(\hat{\mathbf{r}})$$

where

$$T^{OI}_{q,L,L'''} = \sum_{j,L',L''} g^{jo}_{L,L'} T^{ij}_{q,L',L''} g^{jo}_{L'',L'''}$$

as given by Eq. 2.23.

It is not difficult to see that similar arguments also lead to the forms of the elements of the "out-out", "in-in", and "in-out" scattering matrices $\mathbf{T}^{OO}_q$, $\mathbf{T}^{II}_q$, $\mathbf{T}^{IO}_q$ of qth shell given by Eqs. 2.22, 2.24 and 2.25 respectively.

Xiang Chen

Degrees

- 1986, M.S., Peking University
- 1983, B.S., Peking University.

Position held

- 1986-1990, Engineer at North China Electro-Optics Institute.

Publications

- S. Varma, X. Chen, I. Davoli, J. Zhang, D. K. Saldin, and B. P. Tonner. "The structure of MgO(100) surfaces by photoelectron diffraction", Surface Science, in press.

- X. Chen, G. R. Harp, and D. K. Saldin. "On the controversies regarding the 64eV $M_{2,3}VV$ and 914eV L_3VV Auger conclusions from full multiple-scattering simulations", Journal of Vac. Sci. Technol. A **12**, 428(1994).

- D. K. Saldin, G. R. Harp, and X. Chen. "Concentric shell algorithm for Auger and core-level photoelectron diffraction: Theory and applications", Phys. Rev. B **48**(11), 8234 (1993).

- D. K. Saldin, X. Chen, N. C. Kothari, and M. H. Patel. "Atomic position recovery by iterative optimization of reconstruction intensities: Overcoming limitations of holographic crystallography", Phys. Rev. Lett. **70**(8), 11122 (1993).

- Y. Zhou, X. Chen, D. K. Saldin, and J. C. Campuzano. "Reconstruction of the 3-D atomic structure of $CoSi_2$(111) by photoelectron holography", Mat. Research Soc. Symposium Proc., Vol. **307**, 279 (1993).

- B. P. Tonner, J, Zhang, X. Chen, Z. Han, G. R. Harp, and D. K. Saldin. "Photoelectron holography of Si(100)-[2x1] and other surface and thin-film structures", Journal of Vac. Sci. Technol. B **10**(4), 2082 (1992).

- G. R. Harp, D. K. Saldin, X. Chen, Z. Han, and B. P. Tonner. "The effects of various experimental parameters on the accuracy of photoelectron holography", Journal of Electron Spectroscopy and Related Phenomena, Vol. **57**, 331-355 (1991).

Presentations

- Oral presentation on "Anomalous shifts of forward-scattering peaks in photoelectron diffraction patterns from MgO(001) surfaces" on APS Meeting 1994 in Pittsburgh, PN.

- Poster on "Atomic position recovery by iterative optimization intensity(APRIORI)" algorithm on APS Meeting 1993 in Seattle, WA.
- Poster on photoelectron diffraction from $CoSi_2(111)$ surface on American Vacuum Society Meeting Nov. 1992 in Chicago, IL.
- Poster on "Concentric-shell Algorithm for electron multiple scattering calculations" on American Vacuum Society Meeting Nov. 1992 in Chicago, IL.
- Oral presentation on "Forward-scattering or blocking in Auger electron diffraction?" on APS Meeting 1992 in Indianapolis, IN.

Honors and Awards

- Graduate School Dissertation Fellowship of University of Wisconsin-Milwaukee, Sept. 1993 - May 1994.
- The best paper and presentation award of the 1994 Graduate Student Symposium of the Laboratory for Surface Studies, University of Wisconsin-Milwaukee.

Dilano K. Saldin Date